

AUTOMATED ROBOTIC TRACKING OF GELATINOUS ANIMALS IN THE  
DEEP OCEAN

A DISSERTATION  
SUBMITTED TO THE DEPARTMENT OF MECHANICAL ENGINEERING  
AND THE COMMITTEE ON GRADUATE STUDIES  
OF STANFORD UNIVERSITY  
IN PARTIAL FULFILLMENT OF THE REQUIREMENTS  
FOR THE DEGREE OF  
DOCTOR OF PHILOSOPHY

Jason H. Rife  
December 2003



I certify that I have read this dissertation and that, in my opinion, it is fully adequate in scope and quality as a dissertation for the degree of Doctor of Philosophy.

---

Stephen M. Rock (Principal Adviser)

I certify that I have read this dissertation and that, in my opinion, it is fully adequate in scope and quality as a dissertation for the degree of Doctor of Philosophy.

---

Claire J. Tomlin

I certify that I have read this dissertation and that, in my opinion, it is fully adequate in scope and quality as a dissertation for the degree of Doctor of Philosophy.

---

J. Christian Gerdes

Approved for the University Committee on Graduate Studies.

2

---

# *Abstract*

---

The expense and challenge of accessing the deep ocean continue to limit long-duration observations of gelatinous marine animals. Studies commonplace in the research of terrestrial and flying animal behaviors are largely impractical in the deep ocean with current technology. Behaviors of gelatinous species, collectively referred to here as jellies, are remarkably complex given the relatively simple physiology of these animals. Most jellies do not have a centralized nervous system, yet these animals demonstrate intricate foraging, migration, evasion and aggregation behaviors. New technologies are required to discover previously unobserved behaviors, to study behavioral distributions over time, and to investigate the links between behaviors and environmental stimuli.

Automating the jellyfish-tracking task will give biologists the capability to acquire more data over significantly longer observation periods than is possible with current-generation technology. In particular, automation addresses the two key limitations associated with current techniques for data collection: pilot fatigue and infrastructure cost. This dissertation develops a core automated jellyfish-tracking technology and discusses its successful demonstration as a pilot-assist for a remotely-operated vehicle (ROV). This system, which successfully tracked gelatinous animals for periods as long as 89 minutes during field trials, can also serve as a control component for future deployments of untethered robots, called autonomous underwater vehicles (AUVs).

A key challenge in enabling jellyfish-tracking involves the development of a vision-processing algorithm to measure the position of the tracking vehicle relative to the animal subject. In automated jelly-tracking, the burden for reliable vision-processing lies primarily in image segmentation, the process of clustering video-frame pixels into target and background regions. A large number of segmentation algorithms have been developed for other applications; however, no design tool exists to relate the performance of these algorithms to a new application. This disserta-

tion introduces a new design tool, called segmentation efficiency, that narrows the set of prospective segmentation algorithms by analyzing a database of reference images. In the context of a jellyfish database, the segmentation efficiency tool leads to the development of a gradient-based algorithm that reliably tracks a wide range of gelatinous animal species under varied lighting conditions.

Successful field demonstrations of reliable tracking also rely on a control law design tailored to the jelly-tracking application. The control component interprets vision position measurements to create ROV thruster commands. As a primary goal, these thruster commands regulate the position of the target in a small volume at a fixed distance from the cameras. The control law also balances two secondary considerations: the risk of artificially disturbing animal behavior through excessive control action and the contrary risk of losing the target outside the viewing cone due to overly-delicate thruster actuation.

Field demonstrations validate the utility of vision and control software to enable reliable tracking as a core technology for an ROV-based pilot assist or as a control component for an AUV-based jelly tracker. The major additional challenge associated with transitioning the demonstrated ROV-based system to an AUV application involves power consumption, since AUVs, unlike ROVs, rely entirely on portable, internal energy storage. This dissertation analyzes the energy budget for the illumination component of the visual sensing system in order to establish the feasibility of applying core jelly-tracking technologies to an AUV implementation. In the future, AUV-based jelly trackers are expected to observe gelatinous animals in their native habitats for periods as long as 24 hours or more.

---

## Acknowledgements

---

This dissertation benefitted immeasurably from the efforts of my colleagues and friends.

I would like to extend a first acknowledgement to the entire Monterey Bay Aquarium Research Institute (MBARI). Along with the Packard Foundation, MBARI provided the financial support to make this dissertation possible. MBARI scientists, furthermore, provided the conceptual seeds for this work. I offer my gratitude, in particular, to biologists Bruce Robison, who initially proposed the concept of automated robotic jellyfish tracking, and Rob Sherlock, who helped establish the biological context for jellyfish tracking. Thank you, too, to the engineers at MBARI, and particularly to Rob McEwen and Mike Risi, who both dedicated many hours of preparation to research dives with *Ventana* and *Tiburon*. Of course these research dives could never happen without the *Point Lobos* crew. I extend a special thanks to them and to the *Ventana* pilots: Craig Dawe, D.J. Osborne, Knute Brekke, Mark Talkovic, and Stuart Stratton. Whenever I think of MBARI, the *Ventana* pilots are the first people that leap to mind. These men have consistently supported Stanford research and have provided many poignant insights that shaped the course of the jelly-tracking research project.

I offer further thanks to the Stanford engineering school for the role it has played in assisting my development as a student, a scientist, a writer, and a critical thinker. So many individuals within this school have made a positive impact on my Stanford experience. Thanks to Professor Bob Cannon for helping to found the supportive and stimulating environment that is the Stanford Aerospace Robotics Lab (ARL). Thanks also to the other members of my thesis defense committee, including Professors Claire Tomlin, Chris Gerdes, and Howard Zebker, for their perceptive commentary. Thanks also to the support staff in the aeronautics and astronautics department: Sherann Ellsworth, Dana Parga, Jane Lintott, Godwin Zhang, and Aldo Rossi. I cannot imagine

life at Stanford without the assistance of these individuals to guide me through the many challenges, technical and bureaucratic, associated with research in a large university setting. Thanks, too, to all the ARL lab members, whose experience and constructive criticism during group meetings have helped to keep my research directions focused and on-track. In particular, I'd like to acknowledge the efforts of the ARL underwater robotics group, including Steve Fleischer, whose code provided the basis for the experimental jelly-tracking system; Andreas Huster, whose wisdom and intelligence have touched every aspect of life in the ARL; Kortney Leabourne, whose research originally drew me to the field of underwater robotics; and finally to Aaron Plotnik, Kristof Richmond, and Jeff Ota, whose close support has been instrumental to the success of our *Ventana* dive experiments. Aaron, Kristof, and Jeff, I wish you the best of luck in your continuing research in the ARL's underwater robotics program.

Ultimately, a Ph.D. advisor is the individual most responsible for supporting the development of dissertation research. I want to extend my deepest thanks to my advisor, Professor Stephen Rock. His accurate comments, his hands-off management style, and his deep loyalty to his students have made my time at the ARL both a pleasure and a rich learning experience.

Finally, thank you to my family. Allison, my wife, your companionship and love have changed my life. Mom and Dad, you firmly believe that love and an education are the two most precious gifts any parents can bestow upon their children. These gifts from you have made me who I am today.



---

# *Contents*

---

<b>Abstract</b> .....	v
<b>Acknowledgements</b> .....	vii
<b>Contents</b> .....	ix
<b>List of Figures</b> .....	xiii
<b>List of Tables</b> .....	xvii
<b>Nomenclature</b> .....	xix
<b>1 Introduction</b> .....	1
1.1 Motivation .....	1
1.1.1 Robotic Exploration of the Deep Ocean .....	2
1.1.2 Gelatinous Animal Tracking: Scientific Motivation .....	4
1.2 Project Goals .....	5
1.2.1 Problem Statement .....	5
1.2.2 Challenges .....	7
1.2.3 Areas of Related Research .....	8
1.3 Contributions .....	10
1.3.1 Enabled Reliable Tracking for an ROV Pilot Assist .....	11
1.3.2 Analyzed Low-Power Tracking for AUV Applications .....	13
1.4 Reader's Guide .....	13
<b>2 Biological Context</b> .....	15
2.1 Ethology of Gelatinous Zooplankton .....	15
2.2 Jelly Classification .....	17
2.2.1 Cnidaria .....	18
2.2.2 Ctenophora .....	20
2.2.3 Appendicularia .....	22
2.3 Experiments Using a Jelly Tracking Robot .....	22
2.3.1 Basic Visual Studies .....	23
2.3.2 Quantitative Motion Studies .....	24
2.3.3 Response to Stimuli .....	25
2.4 Jelly Habitats .....	26

2.4.1	Ocean Properties	26
2.4.2	Engineering Implications of Animal Habitat	27
2.5	Jelly Motion Behaviors	29
2.5.1	Foraging Behaviors	31
2.5.2	Diel Vertical Migration (DVM)	32
2.5.3	Horizontal Migrations	33
2.5.4	Evasive Actions	34
2.5.5	Aggregation Behaviors	35
2.5.6	Engineering Implications of Motion Behaviors	36
2.6	Morphology and Mechanisms of Jelly Motion	37
2.6.1	Medusa System Dynamics	37
2.6.2	Medusae Morphology and Swimming Patterns	40
2.6.3	Medusa Buoyancy Regulation	45
2.6.4	The Motion of Other Gelatinous Animals	46
2.6.5	Engineering Implications of Jelly Morphology	47
2.7	Sensory Physiology	48
2.7.1	Mechanoreceptors	48
2.7.2	Chemical, Pressure, Temperature Receptors	49
2.7.3	Optical Receptors	50
2.7.4	Light Induced Behavioral Responses among Cnidarians	51
2.7.5	Engineering Implications of Light Sensitivity	55
2.8	Summary	58
<b>3</b>	<b>Experimental System</b>	<b>61</b>
3.1	Introduction	61
3.2	ROV Ventana	63
3.3	R/V Point Lobos	64
3.4	Computer Hardware	65
3.4.1	The Ventana Control Computer (VCC)	65
3.4.2	The Pilot-Assist Computer (PAC)	65
3.5	Human in the loop	67
3.6	Vision Sensor	67
3.6.1	Vision Software	67
3.6.2	Stereo Camera Configuration	69
3.6.3	Lighting	70
3.7	Secondary Sensors	71
3.7.1	Camera Angle Sensors	71
3.7.2	Navigation Pack	72
3.7.3	Pilot Joystick Feedback	72
3.7.4	Doppler Velocity Log (DVL)	72
3.8	Feedback Control	72
3.9	Summary	75
<b>4</b>	<b>Vision System Design</b>	<b>77</b>
4.1	Introduction	77
4.1.1	Background	78
4.1.2	Related Work	80
4.2	Segmentation Efficiency	85
4.2.1	Modeling Segmentation Algorithms	86
4.2.2	Segmentation Efficiency Defined	91
4.2.3	Ensemble Averaged Segmentation Efficiency	95

4.3	A Segmentation Method for Jelly Tracking .....	98
4.3.1	Application of Segmentation Efficiency to Jelly Tracking .....	98
4.3.2	Constraining Algorithm Choice Based on System Requirements .....	103
4.3.3	Segmentation Method for Field Experiments .....	104
4.3.4	Recognition Method for Field Experiments .....	106
4.4	Reliability of the Recognition Subcomponent for Very Long-Duration Jellyfish Tracking ...	107
4.4.1	Recognition Number .....	108
4.4.2	Improving Target Segmentation with the Background Difference Filter .....	115
4.5	Summary .....	117
<b>5</b>	<b>Control System Design .....</b>	<b>119</b>
5.1	Introduction .....	119
5.1.1	Related Work .....	122
5.1.2	A Baseline Control Law .....	124
5.2	Defining the Control Objective .....	129
5.2.1	Decomposition of Vehicle Equations .....	130
5.2.2	Specifying a Consistent Control Reference and Error State .....	136
5.3	Null Space Applications .....	140
5.3.1	Applying the Null Space to Minimize Thrust .....	141
5.3.2	Applying the Null Space to Noninterfering Shared Control .....	146
5.3.3	Thrust Signal Pathway .....	146
5.4	Countering Large Disturbance Forces .....	149
5.4.1	Acceleration of the Animal Target .....	150
5.4.2	Other Disturbance Forces .....	152
5.4.3	Augmenting the Baseline Control to Counter Large Disturbances .....	157
5.5	Summary .....	164
<b>6</b>	<b>Integrated-System Experiments .....</b>	<b>167</b>
6.1	Introduction .....	167
6.1.1	Dive Sites and Timeline .....	169
6.1.2	Experimental Equipment .....	170
6.1.3	Experimental Procedures .....	170
6.2	Vision-Only Experiments .....	171
6.3	Tracking Experiments .....	174
6.3.1	Boundary Control .....	175
6.3.2	Low-Frequency Disturbance Accommodation .....	181
6.3.3	Shared Control Using the Control-Objective Null Space .....	185
6.3.4	The Long Duration Ptychogena Run .....	197
6.4	Biology Applications .....	202
6.4.1	System Reliability Statistics .....	203
6.4.2	The Study of Gelatinous Animal Subjects .....	211
6.5	Summary .....	219
<b>7</b>	<b>AUV Power Budget: Lighting .....</b>	<b>221</b>
7.1	Power Budget for AUV-based Tracking .....	222
7.1.1	Overall AUV Power Budget .....	222
7.1.2	Actuator Power .....	223
7.1.3	Sensor Power .....	225
7.1.4	Comparison of AUV and ROV .....	226
7.2	Optimizing Lighting Configuration .....	226

7.2.1 Radiometry .....	227
7.2.2 Power Optimization .....	230
7.3 The Impact of Strobed Lighting on Biology Data .....	238
7.3.1 A Behavioral Response Model for a Photosensitive Medusa .....	238
7.3.2 Tuning and Validating the Light-Response Model .....	244
7.3.3 Applying the Light-Response Model to the Design of a Strobed Lighting System .....	248
7.3.4 Choice of an Illumination Wavelength .....	252
7.4 Summary .....	252
<b>8 Conclusion .....</b>	<b>255</b>
8.1 Core Research Contributions .....	255
8.1.1 System Reliability for ROV-Based Tracking .....	256
8.1.2 System Energy Consumption for AUV-Based Tracking .....	258
8.2 Engineering Development to Support Operational ROV-Based Tracking .....	258
8.2.1 Interface .....	259
8.2.2 Limit Cycles .....	259
8.2.3 Stereo Camera Calibration .....	259
8.2.4 Smooth Transfer to Shared Control .....	260
8.3 Topics for Future Research .....	260
8.3.1 Vision .....	260
8.3.2 Control for Low Sample-Rate AUV Tracking .....	263
8.3.3 Biology Applications .....	264
8.4 Summary .....	265
<b>Appendix A: ROV Parameters .....</b>	<b>267</b>
<b>Appendix B: Code Structure .....</b>	<b>269</b>
<b>Bibliography .....</b>	<b>271</b>

---

## *List of Figures*

---

1.1	ROV Ventana aboard the Deck of R/V Point Lobos. ....	3
1.2	Artist Concept for a Jelly-Tracking AUV .....	4
1.3	Limitations of Human-Piloted, ROV-Based Jellyfish Tracking .....	6
1.4	Related Topics .....	8
2.1	Cnidarian Medusa. ....	19
2.2	Beroid Ctenophore. ....	21
2.3	Recently Abandoned Larvacean House. ....	21
2.4	One-Dimensional Motion Trajectories of Several Medusae .....	40
2.5	Swim Frequency Depends on Medusa Size. ....	41
2.6	Motorneuron Voltage during Shadow Reflex .....	53
2.7	Medusa photoreponse model. ....	56
2.8	Spectral Photoresponse of Two Medusa Species .....	57
3.1	System Hardware Block Diagram .....	62
3.2	ROV Ventana with R/V Point Lobos .....	62
3.3	Vision-Processing System .....	68
3.4	Stereo Triangulation Geometry .....	69
3.5	ROV Ventana's Lighting System .....	71
3.6	Control Component .....	73
3.7	Viewing Cone Boundaries and Nonlinear Boundary Control .....	74
4.1	The Two Subcomponents of Visual Tracking: Recognition and Segmentation ....	79
4.2	Comparison of Performance Assessment Methods for Visual Tracking .....	84
4.3	A Luminance Histogram for a Jellyfish Image .....	92
4.4	Segmentation Efficiency for a Jellyfish Image .....	96
4.5	Segmentation Efficiency for a Ctenophore Image .....	97

4.6	Ensemble-Averaged Segmentation Efficiency Confidence Limits .....	101
4.7	Luminance Contours under Nonuniform Illumination .....	103
4.8	Block Diagram for Recognition Component .....	107
4.9	Model of Image Plane Projection .....	111
4.10	Probability of Recognition Success .....	113
4.11	Success Probability with Improved Occlusion Handling .....	114
4.12	A Two-Step Segmentation Strategy for Long-Sample Interval Jelly Tracking ....	116
5.1	Baseline Control Law .....	120
5.2	Extensions to the Baseline Control Law .....	121
5.3	Coordinate Frames .....	127
5.4	Camera Viewing Cone .....	129
5.5	The Viewing Cone and ROV Overactuation .....	130
5.6	Jelly-Tracking Coordinate Systems .....	133
5.7	Defining the Error State .....	137
5.8	Geometry for a Dedicated Jelly Tracking AUV .....	145
5.9	Block Diagram Algebra: Control Block for Experimental System .....	148
5.10	Tether Tension Measurements .....	153
5.11	The Magnitude of Curvilinear Disturbance Forces for the Experimental System	156
5.12	Zone of Influence for Boundary Control .....	159
5.13	System block diagram (individual axis). .....	163
6.1	Monterey Canyon .....	168
6.2	Ptychogena Specimen .....	174
6.3	Benthocodon 1: Raw Measurements, Boundary Control .....	176
6.4	Benthocodon 2: Vehicle Control Input .....	177
6.5	Benthocodon 3: Position Error State .....	178
6.6	Benthocodon 4: Velocity Error State, Chatter and Limit Cycles .....	179
6.7	Biases through Time 1 .....	182
6.8	Double Bias Compensation .....	184
6.9	Initial Range Response .....	186
6.10	Shared Control 1: Circumferential Control Signals .....	188
6.11	Shared Control 2: Disturbance-Accommodation (DA) Control .....	189
6.12	Shared Control 3: Position Error .....	191
6.13	Shared Control 4: Velocity Error .....	192
6.14	Shared Control 5: 4-Axis Automatic Control .....	193

6.15	Shared Control 6: Boundary Control .....	195
6.16	Shared Control 7: Three-Dimensional Position, Relative to the Target .....	196
6.17	Ptychogena Run 1: Automated Control over Entire 89 Minute Duration .....	198
6.18	Ptychogena Run 2: Position Error Signal over 89 Minute Run .....	199
6.19	Ptychogena Run 3: Jelly Swimming and Tether Traction .....	200
6.20	Ptychogena Run 4: .....	201
6.21	Duration of Tracking .....	204
6.22	Four Specimens Tracked in the Deep Ocean by Ventana .....	205
6.23	Larvacean Run: Comparison of Automatically Acquired Data to Previous Data .....	212
6.24	Ptychogena Run 5: Motion of Ptychogena over the Sea Floor .....	214
6.25	Ptychogena Run 6: Motion of Ptychogena over the Sea Floor, End-on View .....	215
6.26	Ptychogena Run 7: Motion of the Ptychogena over the Sea Floor, Time Traces .....	216
6.27	Ptychogena Run 8: Altitude and Depth .....	217
7.1	Radiometry Definitions .....	227
7.2	The Spectral Effects of Absorption and Camera Sensitivity .....	229
7.3	Multiple Light Source Geometry .....	233
7.4	Scattering Function of Water .....	234
7.5	Power Reduction as a Function of Sample Rate .....	237
7.6	Definition of Medusa Light Response Model .....	239
7.7	Training a Model for Polyorchis Data .....	245
7.8	Validating the Polyorchis Model in Response to a Train of Light-off Events .....	246
7.9	Frequency Domain Description of Pulsed-Light Sequences .....	249
7.10	Applying Light-Response Model to Proposed Low-Energy Strobe Pattern .....	250





---

## *List of Tables*

---

2.1	Classification of Gelatinous Zooplankton .....	17
2.2	Measured Depth Range for Various Gelatinous Zooplankton .....	28
2.3	Animal Speed Variations .....	30
2.4	Changes in Medusa Speed During a Pulse Cycle .....	43
3.1	Serial String Variables .....	66
4.1	Types of Filtering .....	87
4.2	Topology Processing Algorithms .....	90
4.3	Segmentation Efficiency for Jellyfish Database .....	100
4.4	Target Size Distribution .....	105
6.1	Dive Timeline .....	169
6.2	Summary for Four Extended Tracking Experiments .....	205
6.3	Run Termination Statistics .....	207
7.1	Summary of the energy budget for a hypothetical jelly-tracking AUV .....	222
A.1	Approximate Parameter Values for Ventana .....	267
B.1	Approximate Parameter Values for Ventana .....	269



---

# Nomenclature

---

In this dissertation, state and position vectors are expressed in a particular form that explicitly indicates both the reference frame's origin and coordinate system. As an example, the vector  ${}^{\circ j}p_v$  indicates the state of the vehicle (v) relative to a target jelly (j) expressed in a cylindrical coordinate system (o). The two-term leading superscript thus permits the specification of alternative coordinate systems for a given reference frame. This dissertation uses four distinct frame origins and three distinct coordinate systems. The four frames are:

$j$	Jelly-centered frame: axes aligned with water frame, $w$
$s$	Camera sensor frame: z-axis aligned with camera optical axis
$v$	Vehicle frame: Society of Naval Architects and Marine Engineers (SNAME) convention for axes
$w$	Water-fixed, inertial frame: z-axis aligned with gravity

The three coordinate systems are Cartesian, cylindrical, and tracking (or null-space decoupled) coordinates. Where no coordinate system is indicated, as in the state vector  ${}^j p_v$ , the default coordinate system is assumed Cartesian.

- ... Default (Cartesian) coordinate system:  $p = [x \ y \ z \ \psi]^T$ ; vector consists of three translational coordinates and one rotation (yaw heading) coordinate.
- Cylindrical coordinate system:  ${}^{\circ}p = [r \ \gamma \ z \ \psi]^T$ ; vector consists of a cylindrical position coordinate (radius, circumferential angle, and depth) and yaw heading.
- ⊙ Cylindrical control-objective coordinate system:  ${}^{\odot}p = [r \ {}^{\odot}\psi \ z \ n]^T$ ; vector decouples those coordinates used in tracking control (range, depth, and yaw bearing relative to the radial unit vector) from the tracking law null space coordinate,  $n$ .

In addition to their use in defining 3-component position vectors,  $q$ , and 4-component state vectors,  $p$ , these reference frames conventions also describe other vectors used in analysis of the control system. In each of the following cases, the  $k$  and  $l$  superscripts and subscripts refer to combinations of reference frames ( $j, s, v, w$ ) and coordinate systems.

${}^k q_l \in \Re^3$	Vector describing the position of an object $l$ with respect to the reference frame and coordinate system $k$
${}^k p_l \in \Re^4$	Vector expressed in the reference frame and coordinate system $k$ that describes both the location and yaw orientation of the frame $l$
${}^k R_m \in \Re^{3 \times 3}$	Rotation matrix transforming a position vector from one cartesian coordinate system, $k$ , to a new cartesian coordinate system, $m$
${}^k S_m \in \Re^{4 \times 4}$	Linear transformation between two arbitrary coordinate systems or reference frames, i.e. from ${}^k p_l$ to ${}^m p_l$
${}^k \bar{S}_m({}^k q_l)$	Nonlinear transformation between two coordinate systems or reference frames, i.e. from ${}^k q_l$ to ${}^m q_l$
${}^k A_l \in \Re^4$	Inertial pseudoforce on object in frame $l$ accelerating relative to a second frame $k$
${}^k D \in \Re^4$	Vehicle drag in $k$
${}^k T \in \Re^4$	Tether tension in $k$
${}^k \tau \in \Re^4$	Vehicle thrust in $k$
${}^k u \in \Re^3$	Reduced dimensional vehicle thrust vector, expressed in $k$
${}^k F \in \Re^4$	Force bias on ROV in $k$
${}^k \mathcal{M} \in \Re^{4 \times 4}$	Diagonal mass and inertia matrix, including added mass, in $k$
${}^k b \in \Re^{4 \times 4}$	Diagonal drag coefficient matrix, in $k$

*The fundamental value of undersea vehicles as platforms for deep-sea research is that they provide an in situ point of view in a discipline that has been dominated historically by indirect methods.*

- B.H. Robison, 1999 [8]

---

This dissertation describes a new robotic capability for long-term observation of a gelatinous animal in the deep ocean. The project originates from a continuing collaboration between the Stanford University Aerospace Robotics Lab (ARL) and the Monterey Bay Aquarium Research Institute (MBARI). The research introduces and performs field tests of novel technologies that will enable new experiments in marine biology.

---

## 1.1 Motivation

The purpose of this work is to create tools for improved understanding both of gelatinous marine animals and of their role within the larger marine ecosystem. At the dawn of the 21st century, the Earth's oceans remain largely unexplored and poorly understood. Nonetheless, human populations have come to rely on this vast but fragile resource. Oceans play a critical part in feeding human populations, in promoting shipping, in supplying oil demands, and in regulating global climate. These waters also play a vital role in the lives of nonhuman species. In fact, the oceans contain ninety-five percent of the biosphere, the volume of space available to life on Earth [2]. The significance of the oceans to human populations and to other living creatures motivates continuing research into the complex, interconnected systems that make up this vital resource.

Driven in part by the by-products of an increasingly dense and industrial global population, dramatic changes have occurred in the ocean environment over the century just past. The human roots of these sea changes augment the urgency and importance of ocean research. Large-scale events that continue to transform the ocean include oil slicks, melting ice caps, collapsed fisheries, and algal blooms induced by agricultural runoff. Each incident impacts the ocean directly and

indirectly, through the interconnected web of ocean systems that link weather, currents, pollutant concentrations, chemical cycles and animal populations. Tracking changes in the ocean environment requires detailed study of ocean properties over a range of spatiotemporal scales, from the global and millennial down to the micron and millisecond scales.

Marine animals serve as one important mesoscale marker of changes in the ocean environment. Agents of change influence animal population density, migration patterns and behaviors. By studying animals through direct and indirect observations, scientists can answer fundamental questions about both the animals under study and the changing ocean environment.

### 1.1.1 Robotic Exploration of the Deep Ocean

Over the past century, scientists have harnessed a wide range of new tools to study the deep ocean. These tools offer scientists the growing capability for both direct and indirect observations of the ocean's physical properties and its ecology. Indirect observation methods have evolved from basic net-trawling techniques to more modern technologies relying on sonar and satellite imagery. Indirect observation methods give scientists convenient access to data over large patches of the ocean but do not, generally, provide detail about phenomena occurring at scales below a meter. Direct observation techniques prove indispensable in studying mesoscale ocean properties and, furthermore, in studying individual animals that inhabit the ocean depths.

The past century has also witnessed continual innovation of direct observation techniques. Many such technologies trace historically from Beebe and Barton's bathysphere, a five foot diameter pressure vessel that, during the 1930s, carried its operators as deep as 923 m [3]. The bathysphere relied on a tethered connection to the surface for both life support and movement. To overcome the limitations associated with this tether, submersible designers sought to add on-board life support and thrusters to a subsequent generation of vehicles, called bathyscaphes. Of these vehicles, the most celebrated was the bathyscaphe *Trieste*, which in 1960 traveled to the deepest known point of the ocean floor at 11,700 m below the surface. As submersible vehicles continued to improve access to the deep ocean, the popularization of scuba gear, based on the 1943 invention of the aqualung by Jacques-Yves Cousteau and Emile Gagnan, afforded scientists the capability for convenient personal access to the ocean's upper reaches. Scuba gear and improved submarine designs, including Woods Hole Oceanographic Institute's famed *Alvin* (1964), Harbor Branch Oceanographic Institute's *Johnson-Sea-Link* vehicles (1971 and 1975), and the Canadian Fisheries



**Figure 1.1** ROV *Ventana* aboard the Deck of *R/V Point Lobos*.

Institute's Pisces IV (1985), emerged as the primary technologies for direct ocean observation and remained dominant in this role into the early 1990s.

Robotic agents arrived to the field of ocean science in the late 1980s with the first dives of MBARI's *Ventana*, pictured in Figure 1.1, and WHOI's *Jason* [8]. These box-shaped robots, originally designed for the off-shore industry, function via teleoperation, with scientists and pilots seated remotely aboard a support ship. Their teleoperation capability earned these robots the monicker "remotely operated vehicle," or ROV. The scientific community quickly adopted ROVs as a primary tool for deep-ocean exploration. Although teleoperated vehicles cannot yet recreate the full sensory presence available from within a manned research submarine, safety and financial considerations, coupled with the desire to observe greater depths for longer durations, have motivated a shift from manned submersibles to unmanned, robotic platforms. In the year 2003, ROVs serve as the primary platform for direct observation of the deep ocean.

The autonomous underwater vehicle, or AUV, emerged in the 1990s as a new class of unmanned submersible vehicle with potential applications for marine science. The AUV paradigm, which continues in 2003 to transition between academic research and commercial manufacture, forgoes a tether, the defining characteristic of an ROV. In the absence of a tether, the AUV gains tremendous mobility advantages. At the same time, the AUV sacrifices the steady power flow and high-bandwidth communications connection available through an umbilical to a surface ship. The absence of off-board energy severely limits the power available to AUVs. Also, the absence of a human in the control loop makes AUVs sensitive to varying ocean conditions and to unforeseen events. In the context of these challenges, the creation of reliable and versatile AUV software remains a topic of active research.

### 1.1.2 Gelatinous Animal Tracking: Scientific Motivation

The field of deep-ocean ecology requires, as an essential capability, new technology for long-duration observation of individual animals. Studies of gelatinous animal biology, in particular, would benefit from these new technologies.



**Figure 1.2** Artist Concept for a Jelly-Tracking AUV



Marine biologists, unlike the terrestrial variety, cannot easily observe the behavioral routines of animal subjects living in their native habitats. This problem of limited access has led scientists to apply manned submersible and unmanned ROV technologies to observe deep-ocean species. These human-controlled submersible vehicles have revolutionized marine biology by providing a new window into the lives of deep-ocean animals. Current technologies are best suited, however, to observation periods lasting only a few minutes. Although biologists have made substantial contributions given these short-duration observations, further scientific advances will require new capabilities to enable study of animal behaviors over many hours or days. These new technologies will provide the large quantities of extended-duration data required to detect and analyze subtle patterns of growth, feeding, migration and aggregation.

The need for such technology is particularly important in the study of gelatinous marine animals. Their slow pace of motion drives the need for long-duration observation. Only through extended length *in situ* experiments can biologists compile meaningful statistics describing gelatinous animal behavior. This data cannot otherwise be acquired through aquarium studies or remote observation. The fragile nature of gelatinous specimens makes them challenging to collect and difficult to nurture in aquaria. As for remote observation, the water-filled bodies of gelatinous animals do not provide structural support for the attachment of transmitter beacons, nor do they strongly reflect sonar pulses propagated from a remote source. For these reasons, direct *in situ* observations are a biologist's primary tool for studying behavioral patterns and linking them to environmental stimuli and to evolutionary trends.

---

## 1.2 Project Goals

This section discusses the limitations of current technologies for observing jellyfish and the research requirements to enable automated solutions that address those limitations.

### 1.2.1 Problem Statement

Human-piloted ROVs remain the state-of-the-art technology for observing gelatinous animals in the deep ocean. The ROV platform is well suited to the study of jellyfish and other gelatinous animals, generically labeled as *jellies* within this dissertation. ROV actuators produce more than adequate thrust to follow most gelatinous animal movements, even though they do not provide

sufficient acceleration to follow many faster swimmers like fish and squid. The ROV tether provides immediate transmission of video data to scientists on a surface support ship; as a consequence, scientists can interactively direct an experiment in progress. By equipping an ROV with sampling chambers, a scientist can even request that a pilot collect a particular specimen after a period of observation.

In the study of gelatinous animals over long durations, these positive aspects of ROV-based observation are balanced by two significant limitations: (1) pilot fatigue and (2) infrastructure cost.

The first limitation to long-duration ROV operation under human-pilot control is fatigue. Regulation of ROV position relative to a gelatinous animal subject requires precise, servo-level control. Skilled human pilots can perform these control actions continuously, but the process is a demanding one that tires the pilot and restricts his ability to perform simultaneous higher-level control functions. These fatigue restrictions discourage the acquisition of large quantities of long-duration data.

A second limitation, that of infrastructure cost, further restricts collection of the long-duration datasets needed to characterize gelatinous animal behaviors. In ROV operations, a support ship must hold station above the submersible to supply continuous power and control commands. The expense of holding the support ship and its crew on station during long experiments makes ROV-



**Figure 1.3 Limitations of Human-Piloted, ROV-Based Jellyfish Tracking**

*The two major limitations of the state-of-the-art technology for observing jellyfish are (1) pilot fatigue and (2) infrastructure cost.*

based tracking impractical for periods longer than 2-3 hours. To achieve even longer observation lengths, untethered technologies will be required.

This thesis proposes robotic autonomy as a mechanism to address both limitations associated with human-piloted ROV observation of gelatinous animals. The use of computerized sensing and control systems will enable, in fact, two new classes of improved technology for deep-ocean observation of gelatinous animals: (1) an automated pilot assist for ROVs and (2) a control component for untethered AUVs. Both of these automated solutions address the problem of pilot fatigue. The pilot-assist system shifts the servo-level tracking task to a computer controller and thereby frees the pilot to focus on higher-level control activities. The AUV control component enables jelly-tracking on an untethered vehicle, with no human in-the-loop. In the sense of automating certain control behaviors previously performed by a human pilot, a new technology for jelly tracking provides a common-core for both the ROV-based and AUV-based systems.

Of the two solutions, only the AUV approach addresses the second limitation of high infrastructure cost. Although the AUV tracking approach may give up some of the capabilities of human-piloted jellyfish tracking, such as the capability for manual specimen collection, the AUV-based system gains, in exchange, a capability to perform very long observations, of hours or days, without requiring the continuous presence of a nearby support ship. Thus, a single support ship could, in the future, deploy a large number of low-cost jelly-tracking AUVs to collect large quantities of long-duration data. Because they perform different types of task, both automated ROVs and AUVs are expected to play significant, complementary roles in future scientific investigations of gelatinous animals.

### 1.2.2 Challenges

Two major challenges arise in the development of new automated technologies to enable long-duration experiments (many hours or days) observing gelatinous animals: (1) a requirement for reliable tracking (for ROVs and AUVs) and (2) a requirement for low-power tracking (for AUVs). To achieve reliable tracking, sensing and control technologies must perform robustly for an extended duration while tracking a variety of animals under unstructured lighting conditions. For AUV-based tracking, limited energy storage imposes the second, low-power constraint. To achieve the low-power requirement, an automated tracking system for an AUV must consume

energy at a sufficiently low rate to enable actuation, sensing, and signal processing given a fixed amount of energy storage.

This dissertation focuses primarily on the reliable-tracking challenge. This reliability challenge motivates both a custom control strategy tailored to jelly tracking and a new strategy for vision-system design. Experimental tests using an ROV validate that these new developments enable extended-duration tracking. Also, the dissertation briefly addresses the requirement for low-energy tracking to establish the feasibility of porting the ROV-based pilot-assist capability to an AUV platform.

### 1.2.3 Areas of Related Research

The jelly-tracking project sits at the intersection of several distinct fields of research. These topics include marine biology, vision processing, and underwater vehicle control. As its goal, this dissertation seeks to supplement these existing areas of research by developing new technological capabilities which overcome the research challenges of reliability and power consumption so as to enable effective operational jellyfish tracking.

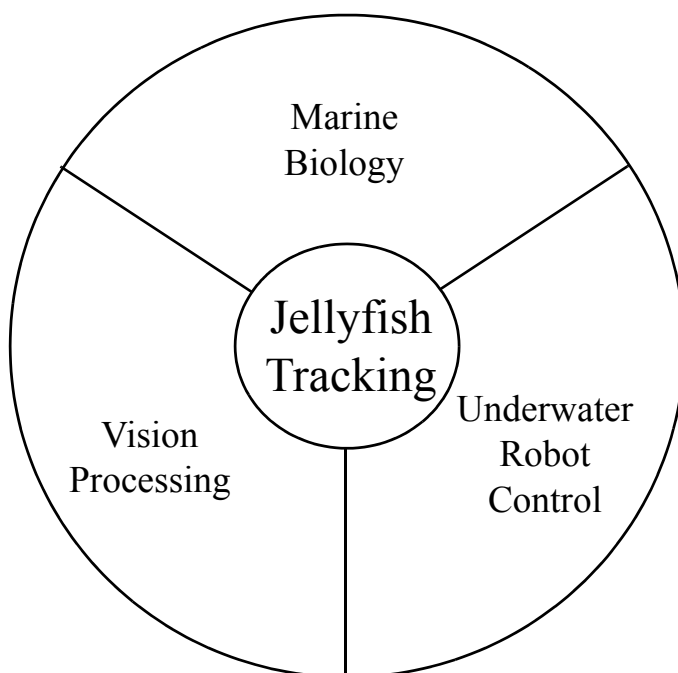


**Figure 1.4 Related Topics**

**Marine Biology**

No prior biology experiments have employed an automated submersible to collect data regarding an individual animal. Previous biological research using human-piloted ROVs to observe gelatinous animals does, however, provide a baseline for automated jellyfish tracking. Quantitative science acquired through these observation serves in generating specifications for the design of an automated jelly-tracking robot. Relevant specifications include information regarding the depth inhabited by various gelatinous animals of interest, their speed relative to the surrounding medium, and their sensitivity to stimuli such as the hydrodynamic disturbances and visible light emissions produced by the tracking robot. Marine biology also provides the motivation for future experiments enabled by the automated jelly-tracking capability. Chapter 2 will detail prior research concerning the biology of gelatinous animals and will apply this knowledge to the design of an automated jelly-tracking robot.

**Visual Sensing**

A large body of literature studies the topic of visual sensing methods to detect target position. A smaller subset of previous research investigates vision-processing methods for tracking and classifying marine animals. None of this work considers the localization of a transparent animal target in a deep-ocean environment subject to unstructured lighting, as provided by the standard light sources mounted on an operational ROV.

Sensing problems are among the most challenging issues in enabling field robot technologies. Without a representation of its relationship to the physical world, a robot possesses no guidance for motion or interaction. In a laboratory setting, robots often rely on artificial cues for localization, such as infrared LEDs detected by an overhead vision system or fiduciary marks placed on walls or ceilings. In an outdoors environment, terrestrial, floating and aerial vehicles may use the Global Position System (GPS) for navigation. Because GPS signals do not penetrate deep below the ocean surface, submersible vehicles must rely on other types of sensor for navigation and relative position.

In the jelly-tracking application few sensors are capable of producing a position measurement relative to a target animal. Because visual sensing has a proven track record for human-piloted ROV-based jellyfish observation and because scientists desire vision data as the primary scientific output of a jelly-tracking mission, this project relies on a visual signal to localize the jelly target. Although acoustics might provide an alternative non-intrusive method of localizing the jelly for

long-duration observations, prior experiments have demonstrated that the sonar target strength of typical gelatinous animals is very weak [4,5].

The primary challenge in the design of a vision sensor for jelly-tracking involves the segmentation process, which identifies pixel clusters possibly corresponding to the projection of the target animal into the image plane. Although a large number of segmentation algorithms have been described in the vision processing literature, no practical design tools exist to aid in matching one of these algorithms to a new tracking application. Chapter 4 introduces a new tool to aid in the synthesis of tracking algorithms and applies the tool to develop a vision processing strategy to track gelatinous animals.

### **Underwater Vehicle Control**

A large amount of prior research has investigated the control of underwater robots. However, much of this work has been performed in theory, with simulation or with laboratory experiments. Relatively little previous work has applied control theory to field operation of deep-ocean submersible robots. Moreover, no work has investigated target tracking using a visual sensor to control a hovering underwater robot operating in a deep-ocean environment.

Field experiments serve as the critical element in realizing this class of system. To demonstrate utility under realistic ocean conditions, the jelly-tracking research project uses the ROV *Ventana*, a vehicle operated by MBARI on a daily basis to perform marine science. For the jelly-tracking application actuator thrust should remain low to avoid disturbing the environment around the observed animal. Control law design balances this desire for low thrust with the need to enforce the camera sensor's viewing cone, outside which the visual sensor cannot localize the target's position. Additionally, the control law design must consider the extra degree-of-freedom (DoF) present in the task of regulating camera position relative to an animal (3 DoF) using a vehicle actuated in yaw and three orthogonal translational axes (4 DoF). Chapter 5 introduces a control law tailored to these characteristics of jelly-tracking using a hovering submersible in the deep-ocean environment.

---

## **1.3 Contributions**

Fundamentally, the jelly-tracking problem is one of system-engineering research in a novel application area. This research project develops core technologies that enable automated jelly tracking

for an ROV-based pilot-assist system or for an untethered AUV-based system. Research contributions build on prior work in the fields of marine biology, vision processing and underwater robotics in order to address the two major challenges associated with autonomous jelly tracking: the requirements to achieve high system reliability and low power consumption.

### 1.3.1 Enabled Reliable Tracking for an ROV Pilot Assist

As its major goal, this dissertation develops techniques that make possible long-duration jelly tracking in the context of an automated ROV pilot-assist system. For this ROV-based implementation, the primary research challenge involves tracking reliability. Specific contributions in the fields of vision processing and control were instrumental in achieving reliable, long-duration jellyfish tracking. These developments enabled field demonstrations of automated jellyfish tracking using the ROV *Ventana*. The following bullets summarize these contributions toward reliable jellyfish tracking.

- **Performed first-ever field demonstrations of long-duration automated jelly tracking:**

No prior research project has used an automated robot to follow a marine animal in its native environment. The primary contribution of this research is the first-ever demonstration of automated robotic animal tracking in the deep ocean. In these field experiments, the automated system successfully tracked a range of animal species dwelling at depths between 100 and 750 meters. Automated tracking commenced with a single button click once a human pilot located a tracking target. After initialization, the automated pilot assist ran continuously, with no human-pilot intervention, for periods as long as 89 minutes.

In addition to their role in validating the reliability of the tracking system, preliminary experimental dives collected data to characterize *in situ* jellyfish tracking. Useful data for refining the jelly-tracking system included information about target behavior in the presence of a tracking robot, characterization of disturbances on the tracking ROV, and characterization of the imaging environment for visual tracking.

- **Introduced a new approach for design of visual tracking algorithms for unstructured environments:** This project develops a new design tool, called segmentation efficiency, that streamlines the synthesis of visual tracking algorithms for field robotics applications.

In designing a vision sensor for a new application, an engineer must match an appropriate algorithm to the information content available in the video stream. For any tracking application, many existing algorithms may track only certain targets for only some of the time. Very few algorithms operate successfully and consistently for a broad range of natural targets. To help identify robust algorithms, the segmentation efficiency method assesses application-specific images in terms of a model of segmentation processing. This quantitative approach offers two benefits over conventional empirical evaluation methods. First, the segmentation efficiency method reduces the application-specific search space by focusing on the pixel-grouping, or segmentation, subcomponent of the vision tracking algorithm. This approach suppresses the analysis of the temporal-matching, or recognition, subcomponent of the tracking algorithm under the assumption that a general-purpose recognition algorithm can provide adequate performance for slowly evolving scenes (such as those in the jelly tracking application). Second, the segmentation efficiency technique frees the human designer from the burden of implementing a large number of candidate segmentation algorithms for testing purposes. Instead, the segmentation efficiency approach uses a general model of segmentation processing to evaluate the ability of various filtering and topological grouping strategies to provide a high ratio (or efficiency) of correctly classified pixels. This segmentation efficiency tool was applied to the jelly-tracking task and resulted in the design of a gradient-based tracking algorithm that runs reliably without requiring in-the-field parameter selection by a human operator. This visual jelly-tracking sensor enabled successful long-duration tracking of a variety of animal species under unstructured lighting conditions during a series of experimental trials in the deep ocean.

- **Designed a jelly-tracking control law tailored to visual animal observation using a hovering submersible robot:** The success of field demonstrations relied both on robust visual tracking and on reliable ROV control. The control law operates on the visual position signal to maintain the target inside the camera sensor's viewing cone. For an animal-observation application, the control law ought to disturb the environment of the tracked specimen as little as possible. In the design of the tracking law, the use of a redundant vehicle degree of freedom permitted a minimization of the thrust vector magnitude to reduce, in effect, hydrodynamic disturbances on the surrounding environment that might interfere with natural animal behavior. Control gains were chosen to match the bandwidth of jelly-



fish swimming, a specification derived from a survey of relevant biological literature. An aggressive boundary-control term sums with the basic regulation law to prevent target loss when the subject animal approaches the edge of the camera's field of view during a large transient disturbance.

### 1.3.2 Analyzed Low-Power Tracking for AUV Applications

As a secondary goal, this dissertation considers the optimization of the lighting system used for visual jelly tracking in order to demonstrate the feasibility of transitioning the core ROV pilot assist technologies to an untethered AUV application. For an AUV system, research challenges include requirements for both reliable tracking and low-energy consumption.

To achieve low-energy tracking, this dissertation investigates the optimization of light source geometry and strobing parameters. The lighting system used in ROV experiments was designed for broad-area coverage and consumed approximately 50% of the hotel energy budget during jelly-fish tracking (ROV Hotel Load: 8 kW, ROV Maximum Hydraulic Output: 30 kW). Significant reductions in lighting system power are necessary to deploy the core jelly-tracking concept with an AUV platform. Using radiometric analysis, this dissertation develops an energy scaling method that permits optimization of lighting design for the energy-constrained application. Light source strobing plays an important role in reducing the system energy budget to a level consistent with long-duration AUV tracking. Further analysis, based on a survey of the biology literature, suggests that strobed lighting may, in fact, reduce the impact of optical stimuli on photosensitive gelatinous animal specimens over long (24-hour) tracking durations.

---

## 1.4 Reader's Guide

The remainder of this thesis is organized as follows. Chapter 2 examines the behavior and physiology of gelatinous animals to provide a context for the jelly-tracking capability and to establish constraints on its design. Chapter 3 details the experimental system employed for ocean trials.

The subsequent three chapters detail contributions that enable and demonstrate reliable jelly-fish tracking. Chapter 4 derives the segmentation efficiency design tool and employs it to construct a vision processing technique tailored to the jelly-tracking task. Chapter 5 examines the development of a control law for the experimental system, a law which enforces the viewing field

constraint while minimizing the overall thrust vector required for tracking. Chapter 6 presents experimental results that validate the utility of vision and control software in reliably tracking gelatinous animal targets for extended time periods. These experiments, using a prototype ROV-based pilot assist to control the ROV *Ventana*, demonstrated the first-ever instance of animal tracking using an automated submersible robot in the deep ocean.

The ensuing chapter, Chapter 7, considers the challenge of transitioning the core jelly-tracking technologies to an energy-constrained AUV platform. This chapter considers the effects of light-source design parameters on system energy consumption and their potential impact in artificially biasing observed animal behaviors. Finally, Chapter 8 summarizes the dissertation and suggests several avenues for related future research.

*In the field of plankton biology, ignorance of the living organism has resulted in a host of strange publications, of which my favorite is van Der Spel's book, "The Euthecosomata: a group with remarkable developmental stages." These remarkable developmental stages ... are in fact fixation artifacts caused by tissue contraction when the animals were put in formaldehyde.*

- W.M. Hamner, 1985 [41]

---

Biological science both motivates automated jelly-tracking research and shapes the design of the prototype experimental system. Establishing an interdisciplinary common ground between engineering and zooplankton research thus provides a foundation for the design of a jelly-tracking robot. Toward this goal, the current chapter reviews gelatinous zooplankton research to construct a biological context for automated jelly tracking. In examining the state of zooplankton science, the chapter extracts specifications for the automated tracking vehicle. In particular, the chapter identifies the types of animals to be studied and the habitats of those animals. Motion physiology and behaviors bound the dynamic and endurance specifications for the jelly-tracking platform. The sensitivity of animals to stimuli produced by the tracking robot further shapes engineering specifications, as the platform should not significantly impact natural behavioral patterns under observation. Sensors on board the jelly-tracking robot will collect data to address questions at the frontier of gelatinous zooplankton research. The requirements for new biology applications thus determine the sensor payload requirements and mission profiles required to perform future jelly-tracking experiments.

---

## 2.1 Ethology of Gelatinous Zooplankton

Animal behavior and anatomy have evolved in a complementary fashion. Behavioral biology (or Ethology) seeks to understand an animal's actions and their connection to the animal's physical makeup across a range of scales, from the molecular to the cellular level and from the organism to the population level. Laboratory experiments have answered many difficult questions about animal physiology and behavior. Nevertheless, animal specimens under lab conditions often exhibit

behavioral patterns distinct from those exhibited under natural conditions. For this reason, an important step in understanding expressed animal behaviors involves the study of the natural actions of animals dwelling in their native habitats.

Field behavioral studies require a sustained presence in an animal's habitat. While this requirement for long term observation does not significantly impede terrestrial studies, it poses a major constraint for deep ocean ethology. To date, scuba gear, manned submersibles and ROVs have permitted scientists to study deep water animals for short periods, generally no longer than a few minutes. Longer studies have not been practical given current technology, costs, and the limitations of human fatigue. To facilitate long-term jelly tracking and to enable tracking for as long as a day or more, automation will be required.

In the future, automated robotic tracking of individual animals may enhance biological understanding of a wide range of species. Gelatinous zooplankton have been chosen as the first animal subjects for automated robot tracking. Gelatinous animals are relatively large, abundant, and slow moving, factors which restrict the complexity required of the tracking system. The behavior of gelatinous animals, moreover, remains a subject of great interest to ethologists. Lab study of gelatinous animal specimens proves challenging, as these fragile animals may degrade quickly or act unnaturally under laboratory conditions. Traditional remote-sensing methods, furthermore, provide relatively little information about jelly movements. Net tows, for example, mangle gelatinous zooplankton beyond recognition. Sonar signals reflect poorly from water-based gelatinous animal tissues [4,5]. Transmitter-beacon tagging methods may weaken or damage a specimen when the transmitter mass is attached to its surface [62]. By contrast, local observation methods, as demonstrated by prior ROV and manned submersible experiments, can provide high-resolution, non-contact examination of gelatinous animal behavior. Automating the jelly-tracking capability could address the cost and practicality issues associated with long-duration animal tracking using current-generation vehicle platforms. In consequence, an automated jelly-tracking vehicle could greatly increase the frequency and duration of experiments to investigate gelatinous animal behavior.

In addition to enhancing the understanding of individual animal species, the data collected by a jelly-tracking robot could also enable studies linking gelatinous animals to the environment. These connections may, in fact, act at global scales that impact human activities. For instance, jellies, by their sheer abundance, play an important role in maintaining fisheries. Because many jel-

---

Kingdom Animalia		
Phylum Cnidaria		
Class Anthozoa		Coral, sea anemone
<b>Class Cubozoa</b>		<b>Medusae (cubomedusae)</b>
<b>Class Hydrozoa</b>		
Subclass Hydromedusae		<b>Medusae (hydromedusae)</b>
Subclass Siphonophora		<b>Siphonophores</b>
<b>Class Scyphozoa</b>		<b>Medusae (scyphomedusae)</b>
<b>Phylum Ctenophora</b>		<b>Comb jellies</b>
Phylum Mollusca		
Class Gastropoda		Heteropods, pteropods, etc.
Phylum Chordata		
Subphylum Urochordata		Animals with “spinal column”
<b>Class Appendicularia</b>		<b>Larvaceans</b>
Class Thaliacea		Salps, doliolids

---

TABLE 2.1. Classification of Gelatinous Zooplankton

*Bold type indicates those species considered as promising targets for autonomous tracking activities.*

lies prey on fish eggs or on food sources shared with fish, fast-growth of jelly populations may slow or prevent the recovery of depleted fisheries [73,78]. Also, because of their environmental sensitivity and rapid reproductive rate, jellies serve as important markers of changing ecosystems. Dramatic increases in jelly biomass, as large as twenty-fold over two decades in the Bering Sea [21], may result from global warming. The collection of jelly data *in situ* may thus have wide-ranging application, both for fundamental and applied scientific investigations.

---

## 2.2 Jelly Classification

The term *jellies* refers, in this dissertation, to gelatinous animals classified as medusae, siphonophores, comb jellies or larvaceans. Morphology and motion, two factors which directly impact jelly tracking, vary substantially among these gelatinous species. This section offers an overview of the subset of gelatinous animals designated as research targets for future tracking activities.

Except where otherwise noted, the sources for Section 2.2 and Section 2.4 are [51,66,82,94].

Jellies are generally described as *zooplankton*, a term whose Greek origin connotes a wandering animal that drifts under environmental forces. In marine biology zooplankton are contrasted with *nekton*, a term describing aggressive swimmers like squid, fish, and marine mammals. The reputation of gelatinous animals as wanderers is not entirely accurate. Although ocean winds, currents, and tides, greatly affect the motion of gelatinous zooplankton, many species swim actively and migrate significant distances through the water column.

The bodies of gelatinous zooplankton consist of as much as 95% water. This adaptation provides gelatinous animals with a number of important evolutionary advantages [94]. Seawater serves as a biologically inexpensive construction material which permits jellies, when nutrients become available, to grow quickly and to produce offspring through budding or sexual reproduction. Gelatinous tissue also aids in thwarting predation, both through transparency, which makes jellies hard to detect, and through low nutritional content, which makes jellies a poor food source for larger ocean animals. In addition to these direct advantages for natural selection, water-filled tissue also makes jellies approximately neutral buoyant, which reduces propulsion requirements, and provides a hydrostatic skeleton, which supports complex physical shapes with large surface area for gas exchange and prey capture.

The commonality of gelatinous tissue among marine zooplankton does not imply that these species all share a common ancestor; rather, gelatinous tissue represents the result of convergent evolution on a successful survival strategy [46]. The majority of gelatinous species observed in Pacific coastal waters belong to two phyla of radially symmetric animals, the cnidaria (or true jellies) and the ctenophores (or comb jellies). Other gelatinous animal groups prominent in the mid-water include the heteropods and pteropods (members of Phylum Mollusca) and the salps and larvaceans (members of Subphylum Urochordata). Salps and larvaceans share nearly as much in common with humans as with jellyfish; salps, larvaceans, and human embryos all possess a rigid structure, called a notochord, along the length of their back at some stage during development.

Among the wide array of gelatinous zooplankters, the present study focuses only on cnidarians, ctenophores and larvaceans.

### 2.2.1 Cnidaria

The true jellyfish, bell-shaped and frequently large in size, belong to Phylum Cnidaria. Biologists identify animals as cnidaria if they possess stinging cells, called nematocysts or cnidocytes. Flow-

ing clusters of tentacles are a salient feature of most medusae, as their name, which evokes the snake-haired gorgon of Greek mythology, implies. The life cycle for most cnidarians alternates between a motile medusa stage and a sessile polyp stage, although a number of cnidarian species lack either the free-swimming or the attached stage. Coral and anemones are notable examples of cnidarians that spend the majority of their life cycles attached to a solid substrate. Free-swimming medusae are divided into three classes. First, the scyphomedusae are the jellies most commonly visible at the ocean surface and in aquaria. Large at maturity and colorful, these jellies may be recognized by a scalloped pattern around their bell margins. Cubozoans represent a second class of medusa, similar enough to the scyphozoans that some biologists lump the two groups as a single class. Cubozoans, uncommon along the central California coast, have cube shaped bell interiors that earn them the name box-jellies. Box jelly stings are particularly painful and sometimes deadly to humans. A third class of jellyfish are the hydrozoa. Class Hydrozoa, with nearly 10,000 living members, is much larger and more diverse than Class Scyphozoa (with approximately 200 members) or Class Cubozoa (with only 17 members). Generally small in size, hydromedusae possess a thin flap, called the vellum, around the bell margin. Although some hydromedusae have a deep



**Figure 2.1 Cnidarian Medusa.**

*This Solmissus specimen was photographed from Ventana during the Stanford-MBARI dive on October 11, 2002.*

red color to help them hide in the ocean depths, the vast majority of hydrozomedusae rely on transparent gelatinous tissue as an adaptation to promote foraging and discourage predation.

Also grouped within Class Hydrozoa are the chain shaped organisms known as siphonophores. Members of Subclass Siphonophora range from short, at only a few centimeters in length, to longer than a blue whale, at 40 meters in length. These chains function, ecologically, as a single, large organism. From an evolutionary point of view, however, siphonophore chains have developed as colonies of individual animals. These individual elements of the siphonophore chain are called zooids. Siphonophores chains grow by budding new attached zooids, which all share a common stem housing a digestive cavity and nervous system. In many siphonophore species, zooids develops into a specialized form, morphologically similar to either the medusal or polypoidal forms observed among other hydrozoa. These differentiated segments serve specific functions within the colonial superorganism, acting as mouths, reproductive organs, tentacle bearers, swimming bells and floats. To the casual observer, umbrella-like swimming bells, when present, clearly indicate the common heritage between siphonophores and other medusae. Like all cnidarians, siphonophores possess stinging nematocysts. These stings are frequently painful to humans and have earned the portuguese-man-of-war (*Physalia physalis*), a siphonophore with a large gas float but without swimming bells, a particularly infamous reputation as a hazard to swimmers.

### 2.2.2 Ctenophora

Comb jellies, which do not possess stinging nematocysts, are classified in Phylum Ctenophora. Like true jellyfish, the comb jellies display radial symmetry and possess gelatinous, transparent tissue. In aquaria and in video images, the casual observer can recognize ctenophores by the parallel, multi-hued flashing stripes along their body. The flashes result from the refraction of light impinging on eight rows of waving cilia, also called ctenes, which ctenophores employ for propulsion. This ciliated propulsion mode, different from the pulsed jet motion of medusae, is one of the many distinctions between typical ctenophores and the cnidarians. In addition to their lack of a hollow swimming bell, ctenophores differ from cnidarian medusae in their tentacle count. Adult ctenophores possess no more than two tentacles. Many adult ctenophores, like the beroid ctenophores, lack tentacles altogether. Also unlike cnidarians, many of which alternate between motile and sessile forms throughout their life cycle, ctenophores produce fully motile offspring that do not pass through an intermediate sessile stage.





**Figure 2.2 Beroid Ctenophore.**  
*From MBARI archives.*

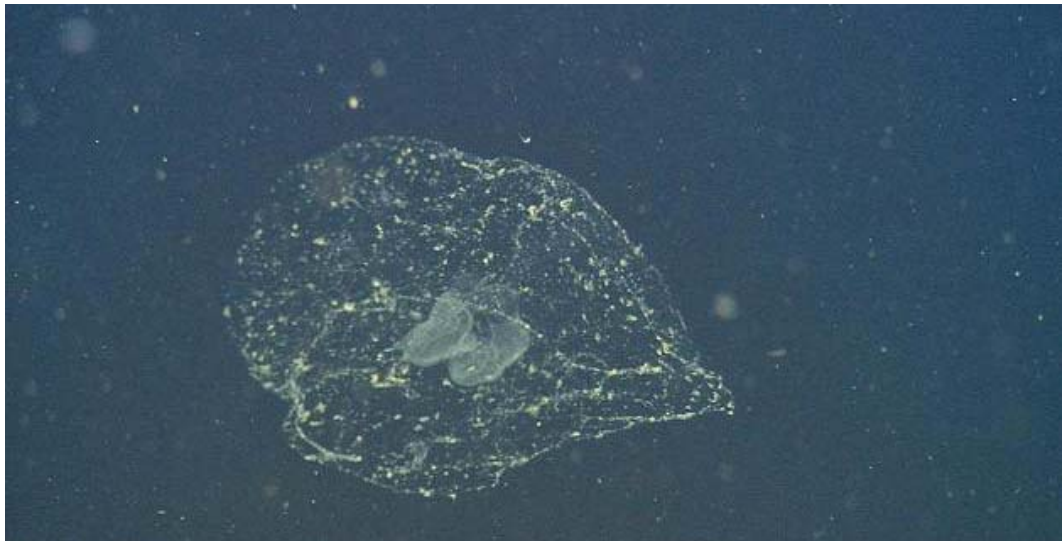


**Figure 2.3 Recently Abandoned Larvacean House.**  
*Photographed during a Stanford-MBARI dive, on 10/11/2002.*

### 2.2.3 Appendicularia

Along with the radially symmetric members of Phylum Cnidaria and Phylum Ctenophora, the automated jelly tracking project focuses on one other group of gelatinous animals, the subset of urochordates belonging to Class Appendicularia. Appendicularians, also referred to as larvaceans, are tadpole-shaped animals, typically a millimeter to a few centimeters in length. In spite of their small body size, larvaceans build mucous feeding structures, called houses, many times their body length. The houses of the giant larvacean, *Bathochordaeus charon*, may grow as large as 2 m in diameter. Houses act as filters to separate food from a large volume of water and to direct it to the larvacean's mouth. Continual undulating motions of the larvacean's tail circulate fluid through the house. When entrapped particles clog the mucous filter, the larvacean leaves its house and constructs a new one. Larvaceans may also leave their house through a special trap-door when they detect vibrations from a nearby predator. Discarded larvacean houses collapse on themselves and sink toward the ocean floor. Ecologists believe that descending larvacean houses, also called sinkers, play an important roles in nutrient cycling and in the community structure of some zooplankton species that congregate on abandoned houses [10].

---

## 2.3 Experiments Using a Jelly Tracking Robot

The motivation for automated jelly tracking lies in the unanswered questions at the fringe of gelatinous zooplankton biology. As such, this section examines the frontiers of biological research and the future utility of automated jelly-tracking experiments.

The experimental goals for long-duration tracking fall into three broad categories based on sensor requirements. The first category consists of ethological studies which use video data to analyze the actions of gelatinous animals over time. The second category quantifies animal motion behaviors using special instrumentation to measure jelly movement relative to the water column. A third category studies sensory responses of jelly specimens to naturally occurring environmental stimuli. These experiments require specific sensors to measure environmental parameters as well as general video data to record animal behavior.

### 2.3.1 Basic Visual Studies

The following research topics use vision both as a sensor for scientific data collection and for robot motion control.

- **Long Duration Behaviors and Time Budgeting:** Ethology provides the primary inspiration for a jelly tracking robot. A jelly tracker would enable ethologists to observe, for the first time, animal behavior over long durations [77]. This data could aid in discovery of new behaviors and provide a field context for behaviors previously observed only in laboratory studies [69,81]. To date, few studies have attempted to observe a single specimen in its native environment for longer than a half hour [42,7,88]. Consequently, almost no data exist to describe the behavior of individual gelatinous animals over longer periods. Video data would provide a good record of behavioral time budgets (divided among such activities as foraging, resting, evasion and reproductive pursuits) through day and night. Such data could be examined in the context of optimal foraging theories [42] or in the construction of accurate bioenergetic models [61].
- **Variation Among Individuals:** Evolution shapes animal populations by acting on individual organisms. For this reason, study of variations in behaviors within an animal population provides an important cornerstone in developing an understanding of the evolution of a species [43]. For example, individual medusa of the same species may perform migrations out of phase [77]. These variations may have important consequences for the population and for the individual medusae; however, no quantitative data exists to permit study of this phenomenon.
- **Variations Among Species:** A jelly tracking robot could also enable comparative studies of different species. For example, jelly species exhibit different, highly specialized feeding behaviors which may not occur under laboratory conditions [39,68]. Automated collection of field data, especially for animals living deep in the ocean, could provide insight to explain these differences. Multiple instantiations of the jelly-tracking robot, moreover, could provide researchers the capability to acquire simultaneous data at various locations throughout a biological hotspot.
- **Predation Experiments:** Visual data can provide direct evidence of predator-prey interactions. These observations are currently difficult to perform *in situ* [27]. Such observations

would show medusa both as predators and prey [88]. Video footage would provide data about the probabilities of prey encounter and prey capture [26,27,36,57,88]. Since little information is currently available concerning the feeding rations of most gelatinous animals, video data could aid in refining notions of diet and prey selectivity [68]. Transparent gelatinous bodies and stomachs might even permit study of animal digestion *in situ*.

### 2.3.2 Quantitative Motion Studies

A capability to measure the motion of an animal target relative to the water would enable additional experiments to quantitatively measure jelly motion behaviors.

- **Horizontal and 3D Migrations:** With the exception of a few experiments conducted at the ocean surface, no attempts have been made to measure the horizontal motion of gelatinous zooplankton species [40,38]. In comparison with vertical motions, which may be quantified using a pressure-depth gage, horizontal motions are more difficult to quantify *in situ*. Limited observations suggest, however, that some animals travel substantial horizontal distances. (The ctenophore *Leucothea*, for example, may spend as much of 60% of its daylight hours swimming horizontally [42]; *Chrysaora quinquecirrha* may also spend a large fraction of its time swimming laterally against currents [28].) Specialized instrumentation, like a doppler velocity log (DVL) might permit a jelly-tracking robot to measure three-dimensional jelly motion accurately. Acquisition of this data would be a significant contribution to gelatinous zooplankton biology [113,77]. Water-relative motion data could also be combined with depth gage or altimeter data to understand jelly motion with respect to its environmental boundaries.
- **Particle Flux:** Biogeochemical cycling through the ocean has been identified as an important investigation topic by numerous researchers [18]. A jelly tracking robot could provide data concerning the flux of organic particulates through the water column. In particular, a robot would be useful in collection of data concerning large particulates like larvacean houses [44]. These gelatinous structures are believed to be an important component of organic particulate cycling. Studies of larvacean houses might also provide data for understanding planktonic communities, which may form on the nutrient rich surface as houses sink [10]. Comparative studies of numerous sinking houses could provide data regarding the distribution of sinking speeds for larvacean houses of various species and information

about the evolution during sinking of house shape, which affects drag coefficient and terminal velocity [82]. Although jelly houses are quite fragile, a carefully controlled jelly-tracking robot might also provide the *in situ* capability to watch larvaceans build and abandon houses.

### 2.3.3 Response to Stimuli

By equipping a tracking robot with specialized sensors to detect environmental stimuli, experiments could be performed to understand the links between sensors, stimuli, and jelly reactions.

- **Light Stimuli:** Given an appropriately designed illumination system, a long duration jelly-tracking experiment could study the *in situ* motion of an individual zooplankter with respect to ambient sun light. No experiment has ever studied the lighting environment and motion patterns of an individual animal *in situ*. A photosensor would be required in these experiments to measure ambient lighting.
- **Chemical Cues:** As chemical stimuli have been observed to affect jelly motion patterns [13,17,89], a chemical detector could provide important information relating jelly behavior to chemoreception. Alternatively, a robot could collect water samples for subsequent analysis in a laboratory setting.
- **Mechanical Stimuli:** Shear flows exist in areas of strong current, at the ocean surface and the ocean floor. The impact of such gradients on gelatinous zooplankton behavior are unclear [38]. It is possible however, that some animals orient themselves based on shear measurements; this behavior might, for example, explain the preference for horizontal swimming into an oncoming current observed among *Chrysaora* by Ford *et al.* [36]. Studying the behavioral impact of shear flows would require an appropriate sensor to measure fluid gradients as well as careful positioning of the tracking robot, to avoid wake affects on the subject animal.
- **Effect of 3D Structure of Ocean Properties:** Measurements of local ocean properties could help explain patterns of animal behavior and reveal animal preferences for particular ambient conditions. Such measures could include pressure, temperature, salinity and oxygen concentration, as measured by a standard CTDO instrument. Measures could also include gradients of these properties. For instance, the aggregation of medusae around a

salinity discontinuity has been studied in a laboratory setting, but never in the open ocean [12].

---

## 2.4 Jelly Habitats

The zones inhabited by gelatinous animals affect mission design and platform specification for the automated jelly tracking task.

### 2.4.1 Ocean Properties

The habitats of a marine zooplankton species, in terms of latitude and depth range, reflect the tolerance of that species for variations in the properties of the water column. Environmental salinity, for instance, has an important effect on gelatinous animals, since jellies take on water volume in low salinity environments and lose water volume in higher salinity environments. Although most jellies osmoregulate well enough to tolerate typical variations in ocean salinity, many species apparently prefer salinity concentration in the typical ocean range of 30-35 parts per thousand. Jellies also display sensitivity to their thermal environment. Metabolic processes, including growth rates, swimming speeds, and muscle actions, depend on temperature for these ectothermic animals. Typical ocean temperatures decrease asymptotically with depth from the surface, but deeper waters show little temperature variation over time. Deep ocean animals thus dwell in environments with relative thermal stability, with typical temperatures between 1 and 8°C. Some medusae have wider salinity and temperature tolerances than others; *Aurelia* tolerates salinity as low as 6 parts per thousand and temperatures as low as -0.6°C and as high as 30°C. Dissolved oxygen concentration appears to have a weaker affect on the choice of habitats for gelatinous animals. Oxygen respiration rates depend on specimen mass and on swimming activity (0.02-0.025 ml/hour/g for *Aurelia* [51,66], 0.05 ml/hour/g for *Stomolophus meleagris* [55], 0.005-0.08 ml/hour/g for *Gonionemus vertens* and *Stomatoca atra* [30]). Many gelatinous species thrive even in the ocean's oxygen minimum zone, between 500 and 1000 m in depth, where oxygen concentration dips as low as 0.1 ml/l.

Whereas the ocean's local properties place physiological bounds on jelly habitats, larger-scale properties, like food availability and predation, place ecological bounds on habitats. The ocean's ecological properties, unlike its local physical properties, change dramatically over time, often dis-

playing repeated patterns on a diurnal or annual basis. Over the course of the day, the most common motion pattern displayed by zooplankton is a migration toward surface waters at night. This pattern, called diel vertical migration (DVM) is described in more detail in the following section on motion behaviors (Section 2.5). Over the scale of months, jelly habitat and population cycles follow seasonal changes in the ocean environment. Ocean hydrodynamics define the two most pronounced ecological seasons in Monterey Bay, the upwelling season, which lasts between March and September, and the non-upwelling season, which persists through the remainder of the year. Upwelling brings cold, nutrient-rich water from the deep ocean toward the surface and initiates a surge in animal populations. The latency of the population surge for a given species depends on its place in the food chain. Sharp increases in primary production excite the population dynamics for predator animals. Gelatinous zooplankton populations may peak in size a month or more after the primary production peak [80,83]. The spatiotemporal evolution of primary production thus acts as a leading indicator for the geographic range, depth range, and dynamic growth of gelatinous animal populations during the upwelling season.

At present, only limited data exist to characterize the depth changes and seasonal habitat and population changes for pelagic gelatinous animal species. Table 2.2 captures some depth range data collected from *in situ* observation. Only a few of the studies summarized in the table capture diurnal migration [72,83] or seasonal variations [80,83] in the depth ranges inhabited by particular animal species.

### 2.4.2 Engineering Implications of Animal Habitat

Ocean conditions and depth ranges favored by particular gelatinous animal species guide the deployment of the jelly-tracking robot. Seasonal abundance variations affect the probability of observing a particular animal species. Under certain environmental conditions, jellies of the same species may cluster in groups. In general, however, deep-ocean jellies can be considered as solitary creatures. This assumption plays a significant role in the design of the vision system for measuring target location (Chapter 4).

The most significant aspect of animal habitat that affects the mechanical design of the jelly-tracking robot is the hydrostatic pressure at the animal's preferred depth range. This pressure determines the requirements for seals and pressure vessels interior to the robotic vehicle. The depth ranges listed in Table 2.2 indicate that a jelly-tracking robot could perform a wide range of

Species	Principal Range (1 $\sigma$ )	Full Depth Range (3 $\sigma$ )	Measurement Location	Measurement Season	Source
<b>Medusae (Hydrozoa and Scyphozoa):</b>					
All medusae	600-900 m	400-900+ m	Bahamas	Oct-Nov (Day)	[57]
“	700-900 m	400-900 m	South Florida	Aug-Sep (Day)	[57]
“	600-800 m	400-800+ m	New England	Aug-Sep (Day)	[57]
Aegina citrea	150-300 m	100-600+ m	British Columbia	Aug-Apr (Day)	[59]
Aglantha digitale	75-150 m		British Columbia	Aug-Apr (Day)	[59]
Colobonema sericeum	400-600 m		Monterey Bay	Random Samples	[82]
Foersteria pupurpea		200+ m	Monterey Bay	Random Samples	[94]
Phialidium gregarium		< 25 m	Friday Harbor, WA	Yearlong	[68]
Proboscoidactyla flavicirrata		< 25m	Friday Harbor, WA	Yearlong	[68]
Solmissus albescens	400-700 m	150-1400 m	Western Medit.	Yearlong (Day)	[72]
“		0-100 m	Western Medit.	April (Night)	[72]
Deepstaria enigmatica		600-1750 m	U.S. West Coast	Random Samples	[94]
Tiburonia Granrojo		750-1500 m	Pacific Ocean	Random Samples	[65]
<b>Siphonophores:</b>					
Calcyophoran siphonophores	300-400 m	0-1000 m	Monterey Bay	Non-upwelling (Day)	[83]
“	400-800 m	0-1000+ m	Monterey Bay	Upwelling (Day)	[83]
“	200-300 & 600-700 m	0-800 m	Monterey Bay	Upwelling (Night)	[83]
Nanomia bijuga	200-400 m	0-700 m	Monterey Bay	Yearlong	[80]
<b>Ctenophores:</b>					
Beroë cucumis		< 500 m	U.S. West Coast	Random Samples	[94]
Bolinopsis sp.	150-400 m	100-600 m	British Columbia	Aug-Apr (Day)	[59]
Leucothea pulchra		< 200 m	California	Random Samples	[94]
Leucothea sp.	10-25 m	0-35 m	Catalina, CA	Jun-Jul (Day)	[42]
<b>Larvaceans:</b>					
Bathochordaeus charon		100-500 m	U.S. West Coast	Random Samples	[94]
Mesochordaeus erythrocephalus	300-500 m	200-750 m	Monterey Bay	Random Samples	[49]
Oikopleura spp.		< 200 m	U.S. West Coast	Random Samples	[94]

TABLE 2.2. Measured Depth Range for Various Gelatinous Zooplankton



tasks (particularly night-time studies) with only 200 m of depth capability. A 1000 m capability would permit study of the vast majority of known gelatinous species through their entire range of vertical migration. Only a few jelly species have been identified at depths greater than 1000 m. A jelly-tracking robot with the capability to plunge to these great depths could, however, help study recently identified deep-ocean species like *Tiburonia granrojo*, a gumdrop shaped jellyfish first described by MBARI and JAMSTEC scientists in the current year, 2003 [65].

---

## 2.5 Jelly Motion Behaviors

For animals that do not possess brains, ctenophores and cnidarians demonstrate richly varied behavioral patterns. Larvaceans, which do have a centralized nervous system, also display complex behaviors. Although some behavior patterns, like the house-building and filtering behaviors among larvaceans or the tentacle and mouth bending behaviors of medusae, involve no translational animal motion, other behaviors, like patterns of foraging, migration, evasion and aggregation, do involve significant bodily motion. This section reviews the latter category of behaviors involving translational animal motion, as target translational motion determines the energy and actuator requirements for automatic robotic tracking.

Although some field-based experiments have quantitatively described animal motion, most animal motion data comes from laboratory experiments. Behavioral lab studies have, for instance, measured medusa cruise swimming speeds and pulsation frequencies [25,26,27,36,37], as well as their escape response speeds [35]. By comparison, the same quantities are more difficult to measure *in situ*; field experiments have recorded only limited quantitative swimming data, using a droplet of dye to mark water-relative translation over short distances [42] and using pressure-depth gages to collect vertical motion data over longer distances [44]. In the long term, however, difficulty recreating environmental conditions in the lab makes the open ocean a more suitable setting for accurate observation of complex motion behaviors. An automated jelly-tracking platform will provide a new means of acquiring such data in the field.

Table 2.3 collects experimental data on cruise swimming and escape swimming speeds for several jelly species, as measured both in the lab and in the ocean.

	Avg. Period Speed (cm/s)					
Species	@ Cruise	@ Max	Size (cm)	Gait (Hz)	Measurement Location	Source
<b>Scyphozomedusae:</b>						
P. camtschatica	1-2	2	5-40	0.11-0.33	British Columbia	[88]
Stomolophus meleagris	4-12	16	1.4-13	1.7-3.6	Laboratory	[55]
<b>Cubomedusae:</b>						
Chironex fleckeri	1-2.5	8.0	3-10	--	Laboratory	[45]
<b>Hydromedusae:</b>						
Aeginura grimaldii	1.5-2.8	--	2-3	0.5-1.0	NW Atlantic +	[56]
Aglantha digitale	2-5	30-40	0.7-1.3	--	Laboratory	[25,35]
Gonionemus vertens	--	5-6	0.5-1.5	0.3	Laboratory	[30]
Phialidium gregarium	2 sink 3 swim	--	< 2	--	Friday Harbor, WA	[68]
Polyorchis penicillatus	0.2-0.3 sink 1.7-3.0 swim	--	2.5-5	--	Friday Harbor, WA	[68]
Solmaris corona	--		1-2	0.75-1.67	NW Atlantic +	[56]
Solmissus albescens	2-4	--	2-5	1.3-2.0	Western Medit.	[72]
Solmissus incisa and Solmissus marshalli	1.0-2.7	--	3-6	0.31-0.79	NW Atlantic, Western Medit.	[56,72]
Stomtoea atra	1.1 sink 0.7-1.5 swim	4-5	0.5-2.5	0.33	Friday Harbor, WA & Laboratory	[68,30]
<b>Siphonophores:</b>						
Nanomia bijuga	--	30	3-25	--	Monterey Bay	[80]
Sulculeolaria sp.	--	30	80	--	Open Ocean	[61]
<b>Ctenophores:</b>						
Leucothea sp.	1.3 horiz. 5.2 vertical		12 mean 26 max	0.07 lobes	California	[42,64]
<b>Larvaceans:</b>						
Oikopleura longicauda	--	30-50	0.1-0.2		Open Ocean	[39]

TABLE 2.3. Animal Speed Variations

*This chart compiles data for mean animal speed during sustained cruise (typical of foraging behaviors) and during bursts of rapid swimming (typical of escape behaviors). Animal size, pulse frequency at cruise, and the location of the measurement are included in subsequent columns.*

### 2.5.1 Foraging Behaviors

Jellies spend a large percentage of their lives hunting. As such, energy requirements for robot propulsion depend heavily on the experimental target species. Generally, gelatinous zooplankton engage in passive foraging (slowly trawling through the water column) rather than in active hunting (pursuing individual prey) [57]. This simple generalization, however, fails to capture the broad diversity of specialized foraging styles observed *in situ* for different gelatinous species.

In most cases, jelly behavior and physiology act in concert to enlarge the encounter volume for prey capture [61]. Motion increases the foraging encounter volume, but at the expense of a metabolic energy cost for propulsion. This trade-off means that some animals, depending on their physiology, either hover in place, hoping to ambush passersby, or swim continuously, accepting increased propulsion costs to augment the probability of encountering slow-moving prey. Among those animals that hover in place, tentacle arrangement is extremely important. Pre-ambush maneuvers help to spread tentacles over the maximum possible area. The scyphozoan *Phacellophora camtschatica*, for example, may swim horizontally back and forth to spread its tentacles both in front of and behind its bell [88]. Siphonophores, many of which hover in motionless ambush, enter into a turn before coming to a rest, thereby imparting a curved shape to their chain-like bodies and splaying their tentacles outward over a large-area two-dimensional sheet [61].

Among those animals that swim to forage, some species move predominantly in a single dimension, carving out a cylindrical foraging volume with diameter equal to the span of the animal's tentacles. In many cases, these animals minimize their drag by directing their tentacles straight back along the axis of motion [86]. Some narcomedusae, however, absorb the drag penalty and hunt with their tentacles splayed radially outward or directed forward from the bell, so as to augment their encounter diameter. Nematocysts are distributed according to hunting style to increase the likelihood of prey capture. Among medusae like *Solmissus*, that hunt with tentacles splayed radially outward, stinging cells develop preferentially on the forward (aboral) tentacle face [56].

Several species augment their capture volume with two-dimensional periodic motion. The coastal medusa *Polyorchis*, for instance, alternates between bouts of upward swimming and periods of negatively buoyant sinking [68]. The medusa *Stomotoca atra* modifies this basic pattern into a sawtooth trajectory with peak-to-peak amplitude of one to two meters and a period of 2-3 minutes [68]. These periodic motions carry *Stomotoca*'s two long tentacles sideways, substan-

tially increasing encounter area. Other examples of periodic two and three-dimensional foraging behaviors have been observed in the scyphomedusa *Phacellophora camtschatica* [88] and in the ctenophore *Beroë* sp [89].

Empirical evidence suggests that jellies may also exhibit non-periodic motion patterns focused around volumes of dense prey concentration [42]. This kind of reactive planning may increase the likelihood of encountering prey and decrease the likelihood of falling victim to a predator. In balancing energy requirements and predation risk for optimal foraging, animals must select which patches to visit, how long to remain in each patch, which food to consume in each path, and what trajectory to follow through that patch [79]. A jelly-tracking robot might aid in collecting data to compare animal motion to optimal foraging predictions. At present, few data exist to characterize how often jellies maneuver to stay within prey patches or what sensory mechanisms they use to detect prey concentration.

### 2.5.2 Diel Vertical Migration (DVM)

Along with foraging, a second behavioral pattern that impacts the propulsion energy budget for a jelly-tracking robot is vertical migration. A large number of zooplankton species perform diel vertical migrations (DVM), a periodic motion pattern synchronized with the 24 hour clock cycle. The standard DVM approaches the ocean surface at night and retreats to deeper waters in the daytime. A few zooplankton species exhibit phase-shifted or fully reversed DVM cycles, with minimum depth occurring during the day [48]. Of the phyla considered for jelly tracking, both pelagic cnidaria and ctenophora perform DVM [72,83,88]. Larvaceans do not migrate in this fashion.

Biologists hypothesize that the evolutionary origins of DVM lie in the advantages of foraging under the cover of darkness. The sun supplies ample energy to phytoplankton near the surface. A large number of species rise at night to feed on primary production or on the other animals that have migrated to surface waters for nighttime feeding. The cover of night removes the advantage of visual predation (by fish, squid, birds and turtles) and levels the playing field for foragers. In this sense, nighttime gives trawlers and ambush hunters the time to feed without substantial risk of capture by active visual hunters [48,72]. Nighttime surface hunting also helps gelatinous zooplankton avoid radiation damage caused by UV light [72]. Because protective pigments that block UV light would make jellies more visible to UV-sensitive, upwards-looking predators, many jel-

lies have evolved without these pigments and instead flee to the depths during daytime to avoid sun damage [53].

Biologists continue to pose many questions about the phenomenon of DVM. In particular, biologists desire more data regarding the variation in migration timing and depth range for individual animals, as natural selection acts on individuals and not on populations. Some laboratory experiments in large confined tanks have observed migration phase shifts of individuals in comparison with the population mean migration [76]. Biologists have not yet studied such shifts with *in situ* experiments, however.

The specific nature of the sensory cues which signal jellies to terminate ascent and descent also remain unknown. Ambient lighting is widely believed to play a major role in triggering DVM. Behavioral observations suggest that absolute light levels play some role in depth selection. Mills and Goy noted, for instance, that animals in the deep ocean rose closer than normal to the surface under reduced moonlight conditions caused either by heavy cloud cover or by a phytoplankton bloom [72]. Other observations in the open ocean suggest that zooplankton follow an isolume, thereby regulating depth to maintain constant ambient illumination through ascent and descent [19,90]. In some animals, relative light changes, rather than absolute changes, may be responsible for vertical migration [48].

At the deep end of migration, illumination may not provide an effective stimulus to trigger upwards DVM, as the natural light level may fall below a jelly's sensitivity threshold. For these deep diving animals, chemoreception of food sources, sensitivity to ambient pressure levels, or the rhythm of an internal clock may provide the signal for ascent [57]. A few experiments have specifically probed for evidence of jelly circadian rhythms; Mills did not find evidence in hydromedusae [69], but Schuyler *et al.* did notice continuing DVM patterns among specimens of the scyphomedusa *Chrysaora quinquecirrha* when they were shifted from natural lighting into full darkness [81].

### 2.5.3 Horizontal Migrations

Horizontal migration patterns among jellyfish were first recognized in the 1980s [38]. Prior to the occurrence of these ethological observations, many biologists believed that jellies migrated only in the vertical direction. Horizontal motion probably plays a smaller role in the energy budget for a

jelly tracking robot than vertical migration; nonetheless, little information is available concerning possible horizontal migration patterns for deep ocean zooplankters.

The most extensive description of horizontal jelly migration involves the translation of medusae through the surface waters of the marine lakes of Palau [40]. These marine lakes formed when geological activity severed them, and their animal populations, from the larger ocean. In Jellyfish Lake, Eil Malk, the population of the medusa *Mastigias* travels 400 m from west to east in the morning and 400 m back in the afternoon. Medusae in Jellyfish Lake, Koror, and in Goby Lake, Koror, travel 500 m and 200 m, respectively, over the course of the day.

Empirical observations suggest that many pelagic jellies perform moderate-scale horizontal motions. Observation by Matsumoto and Hamner, for instance, noted that the ctenophore *Leucothea* spent 60% of its time foraging horizontally [64]. Similar observations have been made by Robison *et al.* concerning the deep-ocean medusa, *Colobonema sericeum* [82]. *Colobonema* is a highly active swimmer, yet appears to maintain its depth in a narrow band, between 400 and 600 m below the ocean surface. Still other experiments provide further evidence of large horizontal migrations. Observing *Aurelia aurita* in Saanich Inlet, Strand and Hamner noted that local currents separate *Aurelia* at night but that the animals actively aggregate during the following day [88]. In the same study, injured specimens swam continuously in the horizontal plane, with no directional preference toward nearby aggregations.

From an evolutionary viewpoint, horizontal migrations patterns may have developed to promote foraging, to assist reproduction, or to avoid collision with the coastline [42,48]. The sensory mechanisms that have evolved to trigger horizontal migration are not known. Some instances of horizontal migration, such as those of *Mastigias* in Jellyfish Lake, however, appear to correlate strongly with changes in daylight and shadow.

### 2.5.4 Evasive Actions

Many jellies respond evasively to contact and hydrodynamic disturbances. Responses generally fall into two categories: hiding responses, in which jellies remain motionless, and swimming responses, in which jellies accelerate rapidly away from a stimulus. Gelatinous animals achieve their highest speeds during darting escape responses. These rapid motion behaviors thus introduce an important specification for the design of a jelly-tracking robot. To track a broad range of gelat-

inous species successfully, the tracking robot must have the capability to match target motion through rapid transients during evasive actions.

Escape swimming responses accelerate jellies to their maximum speed in four-five pulses (one or more seconds) [86]. Animals rarely maintain these high velocities for more than a few seconds, however. Table 2.3 summarizes the escape speeds for several gelatinous animals. Many jellies achieve escape speeds of 30 cm/s or more, including the hydromedusa *Aglantha*, the siphonophore *Nanomia*, and the larvacean *Oikopleura*. Rapid escape responses are common among larvaceans and siphonophores; some siphonophore species even shed tentacles or release a cloudy fluid to obscure pursuit [61]. Rapid escape responses are less common among medusae. A few hydromedusae, primarily the relatives of *Aglantha*, exhibit darting escape responses with velocity substantially greater than cruise (foraging) velocity [35]. Most other medusae that swim away from disturbances simply increase the speed of their normal swimming, by tucking back their tentacles to reduce drag (*Aeginura grimaldii* [56]) or by increasing contraction frequency (*Aurelia aurita* [88]). Rapid swimming escapes have also been observed among ctenophores. During *in situ* observation, Madin noted the ctenophore *Callianira bialata* swam rapidly downward when disturbed and that the ctenophore *Mertensia ovum* escaped with a quick burst of aboral swimming followed by a 180° turn and rapid swimming in the oral direction.

Most medusae attempt to hide from predators rather than trying to escape. Among hydromedusae, hiding behaviors typically take the form of a crumpling response. During crumpling, a medusa stops swimming, retracts its tentacles under its bell, and slightly contracts to reduce its volume [86]. This behavior cannot protect against a determined visual predator, but it does improve a jelly's odds of evading a passive forager [60]. Scyphomedusae, in contrast, may simply stop swimming rather than crumple. Strand and Hamner observed several specimens of the scyphomedusa *Aurelia aurita* that stopped pulsing while in contact with the tentacles of a predatory medusa, *Phacellophora camtschatica* [88].

### 2.5.5 Aggregation Behaviors

Relatively little information is available concerning jelly aggregations, as gelatinous animals typically swim apart from other members of the same species [51]. Certain environmental conditions or active jelly behaviors may result in dense aggregations, however. For instance, medusa blooms observed at the ocean surface result from concentrated reproductive activity, from the convergence

of ocean currents, or from jelly migration behaviors [38]. In the deep ocean, jellies may also aggregate along discontinuities of salinity or temperature [12,43]. In many cases, increased predator and prey concentrations occur together, sympatrically. Quantitative studies have observed denser-than-average populations of the medusa *Phacellophora* preying on aggregated *Aurelia* [88] and of the siphonophore *Nanomia* in waters concentrated with prey species like krill, *Solmissus*, and *Bathochordaeus* [80].

Locations of above average zooplankton activity and density, sometimes referred to as zooplankton hot spots, have been recognized as an important topic for future zooplankton research [18]. Observations of individual animals within hot spots will serve an important role in building a theory for patch dynamics [43]. Additional data will also help confirm hypotheses about the evolutionary advantages of aggregation, which may include defense against predation, improved spawning efficiency, and the exclusion of competitors from limited resources [38,88].

### 2.5.6 Engineering Implications of Motion Behaviors

The range of motion behaviors exhibited by gelatinous animals affects the design of the propulsion and energy storage systems for the jelly-tracking vehicle. Animal speed, for instance, plays an important role in predicting propulsion energy requirements for the tracking vehicle. Data from Table 2.3, along with knowledge of foraging behaviors and DVM, enable a rough estimate of animal speed. Motion data suggests that few of the animals described in this chapter, with the possible exception of siphonophores, continuously swim for extended durations at speeds faster than 2 cm/s. Chapter 7 applies this nominal cruising velocity of 2 cm/s in constructing an energy budget for a hypothetical jelly-tracking AUV.

The direction of animal motion influences the choice of propulsion strategy for the jelly-tracking vehicle. Buoyancy engine propulsion systems offer an energy efficient mechanism for generating vertical forces. For an energy-constrained AUV, the buoyancy engine offers potential advantages for tracking vertical DVM motions, which represent a prevalent behavior among gelatinous animals. Unfortunately, little information is available concerning the horizontal migration patterns of deep-ocean jellies. In order to enable horizontal migration experiments, a jelly-tracking vehicle requires some form of lateral thrust. The pursuit of animals during an escape response also demands high performance omni-directional thrust.



Escape responses set the bandwidth requirements for the vehicle control system. For medusae, acceleration generally occurs over 4-5 pulses. Assuming that pulsing frequency, during escape, does not change significantly from cruising pulsation frequency (0.1-3.0 Hz according to Table 2.3), the acceleration duration lasts approximately 1.3 seconds for the fastest medusa species. From this estimate of acceleration duration, Chapter 5 derives a robot bandwidth requirement of 1.7 rad/s to track these rapidly accelerating jellies. The bandwidth of the experimental jelly-tracking system was set to approximately 0.7 rad/s, somewhat lower than this limit, but sufficient to track most animal specimens encountered.

## 2.6 Morphology and Mechanisms of Jelly Motion

Although scientists have collected relatively little data to quantify patterns of motion behavior among jellies, they have closely examined many of the physical mechanisms that enable gelatinous animal propulsion. This section reviews these mechanisms and discusses the relationships between propulsion strategies and animal morphology. These details enable further refinement of engineering specifications for the automated jelly-tracking robot. In particular, medusa morphology and dynamics place additional constraints on the tracking law and on the propulsion energy budget.

### 2.6.1 Medusa System Dynamics

Despite their relative simplicity within the animal kingdom, gelatinous animals are elegant, highly integrated systems. The motion of a medusa, like the motion of any other mechanical system, can be modeled using an appropriate set of differential equations. This section overviews the modeling efforts of Daniel [29-31] and Demont and Gosline [32-34], who have applied basic concepts from mechanics to describe the motion of gelatinous medusae.

Fundamentally, a medusa may be modelled as lumped inertial mass subject to propulsive forces ( $u$ ) and hydrodynamic resistance ( $F_h$ ).

$$m\ddot{x} + F_h = u \quad (2.1)$$

Muscles are the primary force generators in medusa propulsion. Where higher species often employ opposed muscle pairs to control the direction of force production, medusa muscles act

only in one direction, to contract the bell. The internal tissue of the medusa, called the mesoglea, acts as a flexible, hydrostatic skeleton that restores medusa shape after contraction [37]. In essence, mesoglea and muscle perform together as an approximately linear, second-order system with harmonic forcing [34].

$$m\ddot{x}_m + \eta\dot{x}_m + kx_m = F_m \quad (2.2)$$

Here mesoglea deflection,  $x_m$ , is excited by muscle forcing,  $F_m$ . The spring constant,  $k$ , depends on animal geometry and mesoglea elastic modulus, the latter which has been measured at 400-1000 N/m<sup>2</sup> for the species *Polyorchis penicillatus* [32]. Damping, accounted for by the coefficient  $\eta$ , is a requirement for the system energy balance. To provide net forward propulsion and net output work during the bell's pressure-volume cycle, damping must extract energy during the recovery phase [33]. In *P. penicillatus*, energy recovery by the mesoglea is approximately 58%. Experimental evidence suggests that some species pulse near the resonant frequency of their swimming bells. By exploiting the resonance frequency of (2.2), like *P. penicillatus* reduces its overall energy requirements as much as 24-37% [34].

Although bell elasticity acts in an approximately linear fashion in a global sense, local variations in elastic modulus permit differential bending. These local changes in bell shape determine the kinematics of bell contraction [37]. In hydromedusae, bell kinematics are supplemented by the kinematics of velum contractions [86]. Together these changes in bell and velum geometry interact with the surrounding water to create jet propulsion. Medusa thrust is positive during contraction and negative during the recovery phase. Even though net mass flux is zero over the complete pulsation period, net thrust is positive. In effect, the jelly acts as a synthetic (periodically pulsed) jet. In engineering applications, synthetic jets typically use constant area orifices and sinusoidal excitation; these devices rely on the differences between potential-sink-like inflow and jet-like outflow to produce a net momentum flux. Jellies, in contrast, exploit variations in cycle timing and in orifice area to augment thrust production.

A medusa propulsive thrust equation was developed by Daniel [29], with thrust,  $u$ , as a function of water density,  $\rho$ , velar cross-sectional area,  $A_v$ , and rate of change of internal bell volume,  $V$ . Given an appropriate state function relating volume to bell deflection, the following equation for thrust is driven by the bell forcing equation (2.2).

$$u = -\rho A_v^{-1} \left| \frac{dV}{dt} \right| \frac{dV}{dt} \quad (2.3)$$

The thrust equation explains variations in medusa kinematics between the contraction and recovery phase that result in net thrust production. Averaged jet cross-sectional area,  $A_v$ , is larger during recovery than contraction. Also, the volume derivative is much higher during contraction than during the recovery phase, as recovery takes 1.3-2.5 times longer than contraction [29, 37]. The larger jet area and slower volume change during recovery reduce negative thrust, according to (2.3).

Frequency tuning may further improve the efficiency of jet propulsion. Although Daniel neglects this effect for small, rapidly pulsing animals [29], it is possible that intermediate sized medusae may take advantage of frequency tuning. In engineering applications, tuned synthetic jets produce 50% more thrust than continuous jets of the same dimensions

Hydrodynamic forces oppose periodic thrusting. This resistance,  $F_h$ , is the sum of unsteady drag and added mass forces. The drag force is proportional to density, frontal area ( $S$ ), drag coefficient ( $C_d$ ), and the square of velocity ( $u$ ); the added mass force is proportional to density, acceleration, volume and added mass coefficient ( $\alpha$ ).

$$F_h = C_d \left( \frac{\rho S u^2}{2} \right) + \alpha \left( \rho V \frac{du}{dt} \right) \quad (2.4)$$

The added mass force, which results from the acceleration of the flow field surrounding the medusa, accounts for the majority of animal momentum loss. The coefficients  $C_d$  and  $\alpha$ , as well as the frontal area  $S$ , depend strongly on medusa shape. Narrow, or prolate, medusae have more favorable hydrodynamics and accelerate to higher speeds than wide, or oblate, medusae.

Despite early questions about the efficiency of jelly propulsion [30], medusa propulsion appears highly effective when considered at a system level. Indeed, jellies are less efficient than fish from a purely hydrodynamic viewpoint. Efficiency in their propulsion strategy, however, results in a low overall energy requirement for medusa transport. In fact, [55] suggests that prolate jellies in the 10-1000 g mass range have lower overall transport costs than fish. Fish are fast swimmers, but their streamlining offers less of an advantage at the slower speeds traveled by medusae. Moreover, the jelly propulsion system requires less “overhead” than the fish propulsion

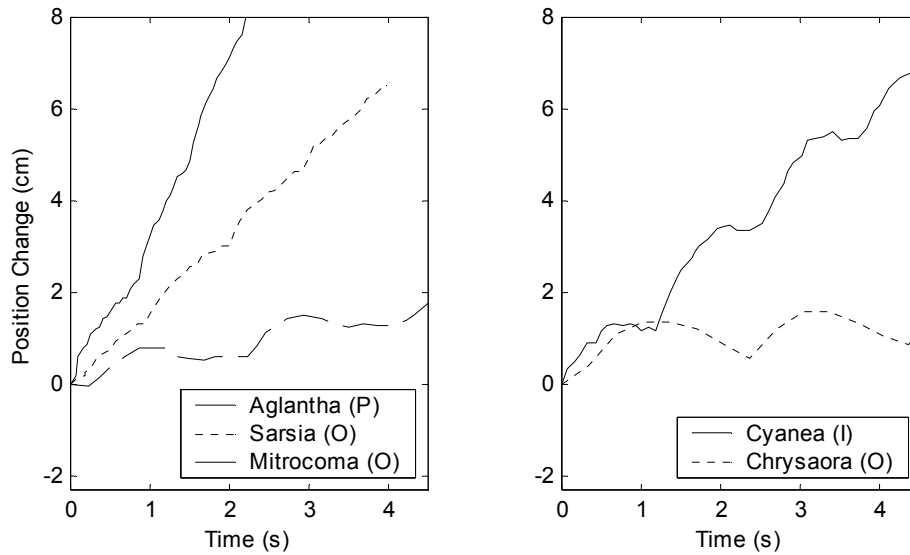


**Figure 2.4 One-Dimensional Motion Trajectories of Several Medusae**

Data collected from [25,27,36]. *Aglantha*, *Sarsia* are prolates (P). *Mitrocoma* and *Chrysaora* are oblates (O). *Cyanea* fineness puts it at an intermediate level (I), between the two extremes.

system. The muscle-to-body mass ratio for a typical jelly is only 1%, as contrasted with 50% for fish. Oxygen consumption, which reflects metabolic energy consumption, is correspondingly lower for medusa as compared to fish [55].

## 2.6.2 Medusae Morphology and Swimming Patterns

Medusa shape strongly affects swimming behavior. Swimming efficiency, for instance, is a strong function of medusa shape; however, swimming efficiency is only one aspect of the medusa survival strategy. To maintain propulsion, a medusa needs to renew its energy supply by continuously acquiring oxygen and nutrients from the water column. Though a large frontal area increases drag, the same large area also promotes oxygen transport and food capture. Thus, medusa geometry represents a trade-off between mobility (for escape, reproduction, etc.) and effective feeding. Different medusa behavioral patterns have evolved in different species to best exploit morphology for survival.

The simplest descriptor for medusa shape is the fineness ratio, which expresses the ratio of bell height to bell width. Although fineness ratio varies throughout contraction and recovery, a

jelly is typically classified by its fineness ratio in the relaxed state, prior to contraction. Those jellies with long bodies (fineness  $> 0.8$ ) are called prolate medusae. Those with short height along the radially symmetric axis (fineness  $< 0.5$ ) are called oblate medusae.

Oblate jellies generally move slower than prolate jellies during bouts of swimming, as shown by Figure 2.4. Among oblates, speed is not a strong function of bell size [25]. By contrast, speed is directly proportional to bell height for smaller prolate jellies [25,55]. At larger sizes, this proportionality flattens out and prolate swimming speeds become invariant with size. Presumably, the extreme drag penalties associated with higher speeds and larger sizes, as captured by (2.4), overwhelm propulsive advantages for these larger prolate medusae.

Pulsation frequency (swim cycles per second) also depends strongly on bell size. For a given species of medusa, pulsation frequency appears to vary exponentially with bell diameter. The dependence is stronger for oblate medusae than for prolate medusae. These differences are displayed by Figure 2.5, which compares pulsation frequencies for the oblate medusa, *Phacellophora*

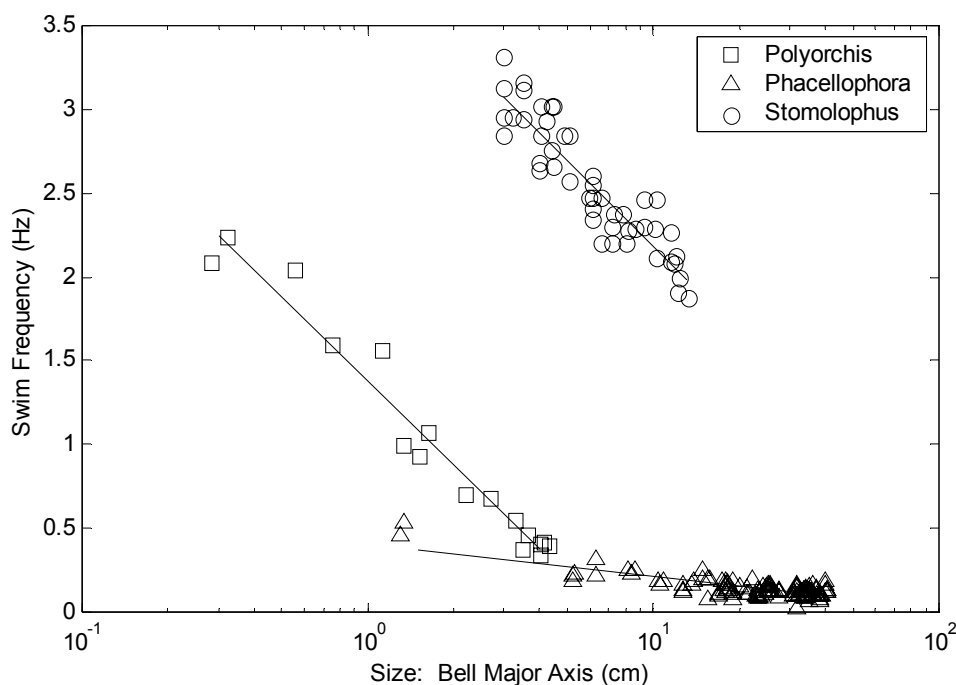


**Figure 2.5 Swim Frequency Depends on Medusa Size.**

Data for swim pulses per second have been compiled for three medusa species: *Polyorchis* [14], *Phacellophora* [88], and *Stomolophus* [55].

*camtschatica*, with the prolate medusae *Stomolophus meleagris* and *Polyorchis penicillatus*. These data were acquired under fixed environmental conditions. In general, ambient pressure [38], temperature [76] and lighting [11] can all affect medusa swimming frequency.

Contrast in swimming speed and bell pulsation rate evidence the strong hydrodynamic differences between oblate and prolate medusae. Table 2.4 collects data for jelly speed and pulsation frequency for animals of differing fineness ratio. A useful generalization for jelly tracking, based on these data, maintains that oblate medusae do not travel farther than one bell diameter during a second, whereas medusae of intermediate to high fineness ratio (fineness greater than 0.5) may travel as far as twice their bell diameter in a second during bouts of steady swimming. Not only does better streamlining mean that prolate jellies swim faster, in general, than oblate jellies, but streamlining also permits prolate jellies to maintain a relatively constant speed throughout repeated pulsation cycles. By contrast, speed oscillations through the pulsation cycle are large for typical oblate medusae. Both Figure 2.5 and in Table 2.4 indicate significantly larger peak-to-trough velocity differences for animals of low fineness ratio.

In fact, the hydrodynamic differences between prolate and oblate medusae are so pronounced that thrust model (2.3), which applies well to measurements of prolate medusae kinematics, breaks down when applied to measurements of oblate medusae kinematics. Colin and Costello suggest that, for oblate jellies, the bell contraction as much pushes water in a rowing motion as it ejects water in a jet motion [25]. Thus, in an accurate motion model for oblate jellies, a rowing term [30] would supplement the jet-propulsion term of (2.3).

The poor hydrodynamic efficiency of oblate jellies does not imply overall system inefficiency. Large frontal area increases the probability of encountering prey [61]. Moreover, “sloppy” hydrodynamics in the separated region behind the bell produce higher intensity turbulence and stronger vortex rings. These fluid motions increase transport of prey toward medusa tentacles and counteract prey escape responses. Examples of complicated flow fields that enhance feeding are described for *Chrysaora* in [36] and for *Aurelia* in [26]. As a generalization, feeding efficiency for medusae decreases as swimming efficiency increases.

The time budgets of the prolate jellies, the more efficient swimmers, thus contrast with the budgets of oblate jellies, the more efficient feeders [25]. Because swimming enhances feeding for oblates, these medusae move continuously. Field experiments by Costello *et al.* suggest oblate scyphomedusa species, like *Aurelia aurita* and *Chrysaora quinquecirrha*, may spend as much as

Species	Mean Speed (cm/s)	Min Speed (cm/s)	Max Speed (cm/s)	Body Size (cm)	Pulse Freq. (Hz)	Run Time (s)	Fineness Ratio	Source
<b>Scyphomedusae:</b>								
Aurelia aurita	0.3	-0.2	1.1	1.6	1.5	3.4	0.4	[26]
C. quinquecirrha	0.2	-1.0	1.7	5.5	0.5	9	0.3	[36]
Cyanea capillata	1.2	-1.0	4.6	3.9	0.8	6.5	0.6	[27]
Linuche unguiculata	1.4	0.3	2.9	1.6	2.9	1.7	1.1	[27]
S. meleagris	2.3	0.7	3.8	3.3	3.0	1.7	0.7	[27]
<b>Cubomedusae</b>								
Charybdea sp.	6.2	3.8	9.3	3.5	--	Many	0.6	[37]
<b>Hydromedusae:</b>								
Aequorea victoria	1.1	0.3	2.0	5.0	0.8	6	0.5	[25]
Aglantha digitale	2.2	-0.1	5.2	2.0	1.4	2	2.2	[25]
Bougainvillia sp.	1.3	0.2	3.3	0.8	--	Many	0.9	[37]
Euphysa flammea	1.3	0.0	3.8	1.1	--	Many	1.7	[37]
Gonionemus vertens	4.5	0.0	11.8	2.4	--	Many	0.6	[37]
Liriope tetraphylla	3.6	1.3	6.6	1.5	--	Many	0.7	[37]
Mitrocoma cellularia	0.4	-0.5	1.6	6.5	0.5	10	0.5	[25]
Phialidium gregarium	1.5	0.6	2.3	2.1	1.5	3	0.6	[25]
P. flavicirrata	1.1	0.5	2.2	0.6	1.6	3	0.9	[25]
Sarsia sp.	1.8	1.1	3.5	0.9	1.1	4	1.1	[25]
Stomotoca atra	1.5	0.5	4.0	1.2	--	Many	0.8	[37]
<b>Siphonophorae:</b>								
Diphyes dispar	10.7	9.6	11.7	3	2.8	2.3	3.0	[37]

TABLE 2.4. Changes in Medusa Speed During a Pulse Cycle

Minimum and maximum instantaneous speed are listed. Data are either for single animals (several consecutive pulses) or for many animals of similar size (phase averaged pulses).

93-100% of their time swimming [28]. Oblate medusae of Family Solmissus [72] and many oblate members of Order Leptomedusa [86] also spend the vast majority of their time swimming.

Prolate jellies, whose morphology inhibits feeding while swimming, remain motionless during foraging periods, relying on ambush tactics to capture moving prey. From time to time, these animals pulse briefly to keep their tentacles spread effectively through a capture volume. The neutrally buoyant, prolate hydromedusa *Proboscoidactyla flavicirrata*, for example, exhibits this hovering ambush behavior [68]. Some negatively-buoyant prolate jellies alternate between sinking and upwards pulsing to promote efficient foraging. Examples include the prolate Anthomedusans *Stomotoca atra* [14], which pulses upward for 1-3 s and then rests, sinking, for 10 s and *Polyorchis penicillatus* [30], which pulses upward quickly for 15-300 s and then rests for long periods, sinking while pulsing slowly at only 5-15 contractions per minute. This alternation between sinking and swimming is often called maintenance swimming, as it carries a medusae a significant absolute distance through the water column without appreciably changing absolute depth [14].

Thus prolate jellies are more likely to alternate between bouts of swimming and periods of rest, while oblate jellies are more likely to swim continuously. While swimming, both categories of medusa may demonstrate forms of spatially periodic motion. The prolate jelly *Stomotoca atra*, for instance, moves in a sawtooth wave pattern, travelling horizontally upward during its swimming bouts and vertically downward during its sinking bouts [68]. The oblate medusa *Phacellophora camtschatica* sometimes swims vertically in a helical pattern [88]. These behaviors, which increase the encounter frequency between medusa tentacles and prey species, involve turning motions. In order to effect a turn, medusae vary contraction strength around the bell margin.

In hydromedusae and cubomedusae, the velum deforms to act as a thrust vectoring nozzle. Scyphomedusae, in contrast, contract strongly on the inner turning edge of the bell to scoop water in the lateral direction. Gladfelter quantified the turning ability of several medusae species in the laboratory [37]; observations included a 70° turn by *Polyorchis* in a single pulse, a 114° turn by *Euphysa* over a 5 contraction maneuver, a 125° turn by *Gonionemus* in a 3 contraction maneuver over 1.6 seconds, and a 44° turn by *Cyanea* in a single contraction over 2 seconds.

A final difference between oblate and prolate medusae involves escape behavior. Because of their poor hydrodynamics, oblate animals cannot perform rapid escapes. Although some oblate scyphomedusae continue to pulse after contact with a predator, others cease pulsation immediately. Among the oblate hydromedusae, many species perform a crumpling action when touched by a



predator. During crumpling, animals cease swimming and draw their tentacles inside their bells to decrease their size and likelihood of capture by a foraging predator (see Section 2.5.4).

Prolates contrast with oblates in that their design, from a hydrodynamics viewpoint, favors rapid escape. Although some prolate hydromedusae crumple, many display dramatic escape responses with speeds far exceeding their foraging speeds. The most dramatic hydromedusan escape responses are seen in *Aglantha* and its close relatives, including *Colobonema* and *Benthocodon* [35].

### 2.6.3 Medusa Buoyancy Regulation

In addition to bell propulsion, the buoyancy of jellyfish plays an important role in their motion. Many nearshore species maintain negative buoyancy for feeding purposes, including *Phialidium gregarium*, *Polyorchis penicillatus*, and *Stomtoxa atra* [68]. Gravity propels these animals nearly as fast downwards as bell contractions propel them upwards (see Table 2.3). Pelagic, or open water, medusae generally maintain neutral buoyancy. Passive osmotic accommodation allows these medusae to match the ion concentration of the surrounding medium [70]. Some medusae may also use active means to effect changes in internal ion concentration.

The work of Mills suggests that medusae do not, in all likelihood, use active buoyancy control to change their position upward and downward in the water column. In particular, Mills investigated DVM and concluded that active buoyancy adjustment does not play a role in supporting vertical migration [71].

Even if jellies do use active buoyancy for propulsion, ion regulation occurs sufficiently slowly that it may be neglected for the purposes of automated jelly tracking. Laboratory experiments that swapped medusae between mediums of differing salinity, and hence differing density, showed that specimens regained neutral buoyancy over periods as long as 6-24 hours for large salinity changes (8 ppt or more) and no shorter than 10-30 minutes, even for small salinity changes (1-2 ppt) [67,70,93]. The only possibility for a rapid change in jelly motion resulting from a buoyancy related phenomenon involves a sharp salinity discontinuity. Were a target medusa to contact a salinity discontinuity, its progress might accelerate, decelerate or halt entirely.

### 2.6.4 The Motion of Other Gelatinous Animals

Typical siphonophore motion resembles that of medusae. With the exception of members of Order Cystonecta, which have no capability for self-propulsion, siphonophores possess swimming bells (nectophores) that pulse periodically, pulling their long bodies through the water column. When multiple nectophores are present in siphonophore colonies, they pulse out of phase, effectively smoothing siphonophore velocity. The dual bells of the siphonophore *Diphyes dispar*, pulse individually at 2.8 Hz, out-of-phase, to keep instantaneous speed variations within 10% of the mean colony speed, 10.7 cm/s. As a result of reduced acceleration losses, siphonophore propulsion is somewhat more efficient than medusa propulsion.

Unlike medusae, siphonophores colonies, with the exception of the calcyphorans, use gas filled floats to supplement their buoyancy. Gas filled pneumatophores allow easy siphonophore detection using sonar [80]. Siphonophores also differ from medusae in their ability to orient their bells relative to their bodies. *Nanomia*, and related siphonophores, are the only animals besides squid which can manipulate jet-propulsion to swim in two opposing directions [58].

Ctenophore propulsion contrasts strongly with that of medusae and siphonophores. Ctenophore propulsion relies on swimming cilia that occur in eight rows, distributed in pairs around the animal circumference. Cilia create propulsion with a paddling motion. Along the row, cilia trigger slightly out of phase to generate synchronized wave pulses. These paddling motions move the animal in the mouth-forward (oral) direction. Ctenophores, in rare cases, may also swim backwards, in the aboral direction [61,89]. In order to maneuver, ctenophores differentially actuate comb rows on opposite sides of their bodies and, for more rapid maneuvers, curve their ellipsoidal bodies [89]. Because comb rows pulse continuously, ctenophores move more smoothly and efficiently than medusae.

The group of lobate ctenophores use large, wing-like lobes to assist with propulsion. Ctenophores like *Leucothea* may forage with their lobes flapping periodically. Lobes can also be used to change swimming mode. With *Leucothea*, for example, lobe configuration changes dramatically from the horizontal foraging mode which glides forward at 1.3 cm/s, lobes flapping, to the vertical jet-propulsion mode, in which *Leucothea* curls its lobes into ducts around its rapidly beating cilia rows and accelerates to 5.2 cm/s [64]. Rapid buoyancy-driven propulsion has not been observed among ctenophores. Rather, ctenophores osmoconform to the ionic concentration of surrounding water in order to maintain neutral buoyancy, much like cnidarian species [71].

Larvaceans share little in common, in terms of their motion, with cnidarians and ctenophores. For the most part, larvaceans flap their tails continually to circulate water through their mucous filters. This flapping motion appears to cause little variation in the position of the house within the water column [44]. As such, larvaceans orient themselves arbitrarily relative to the gravity vector [20]. Larvaceans periodically abandon their houses and construct new ones. While free from their houses, larvaceans are capable of extremely rapid movement. Graham *et al.* measured the escape response for a free-swimming *Oikopleura longicauda* at approximately 30-50 cm/s [38]. Whether because larvaceans leave their houses when they become heavy or because the houses change density after abandonment, empty larvacean houses sink downward toward the ocean floor. Abandoned houses, which typically sink at 1 cm/s but often sink at 2-3 times this rate, play an important role in nutrient cycling through the water column.

### 2.6.5 Engineering Implications of Jelly Morphology

Variations in jelly morphology and propulsion strategies influence the specifications for an automated jelly-tracking robot. Earlier specifications for control bandwidth and energy consumption neglected oscillations in the jelly cruise speed; these oscillations may be significant, especially for oblate jellies. To account for these effects, the control bandwidth can be designed to partially attenuate velocity variations associated with jelly pulsing without significantly affecting tracking response for sudden acceleration. Chapter 5.3.1 discusses the design of a jelly tracking control law tuned to track escape responses while damping oscillations at the pulsation frequency. Disturbances at the pulsation frequency may still result in additional thruster action. Chapter 7.1.2 discusses the impact of speed oscillations (associated with tracking an oblate medusa) on the energy budget for a jelly-tracking AUV.

The relationship between motion and morphology presents many further opportunities for additional engineering research. For post-processing applications, like classification, motion data may help identify the morphology, and perhaps the species, of a tracked animal [122]. For real-time applications, morphology data may help predict patterns of motion for a particular animal specimen. In an energy-constrained AUV application, for instance, morphology information could be used to tune control gains and sensor sampling rates to balance energy minimization and the risk of target loss.

---

## 2.7 Sensory Physiology

This section discusses the capabilities of jellies to detect external stimuli. In mechanical robots, external stimuli both enable continuous feedback control and trigger discrete state transitions among various programmed behaviors. The same is true for jellies. Most jellies have sensors to detect touch and the gravitational direction. Many jellies also sense light and chemical concentrations. Jellies act on these stimuli both to trigger feedback behaviors, such as attraction toward the chemical signal produced by food source, and to trigger behavioral state changes, such as the transition between swimming and defensive crumpling.

The design of long duration observation experiments involving gelatinous specimens must consider the sensory capabilities of the observed specimen. As a scientific measurement device, the automated jelly tracking platform should not significantly affect jelly behavior. Anecdotal evidence suggests that robotic system for short-duration jelly tracking can be deployed without major impact on the behavior of the observed animal [42,57,72,77,7,80]. A more thorough analysis of animal sensory capabilities, however, helps identify potential problem areas that might arise for longer duration automated tracking.

### 2.7.1 Mechanoreceptors

Sensory cells in gelatinous animals are less specialized than those in higher animals. Ciliated epithelial cells in cnidaria are receptive to many stimuli, including touch, light and chemicals [66]. These cells are the primary means for detecting physical contact and hydrodynamic disturbances. When these receptors sense a mechanical disturbance, they may evoke a behavioral response for feeding, if in contact with prey, or for escape, if in contact with a predator. Ctenophores [89] and larvaceans [20] react similarly to cnidarians in response to mechanical stimuli.

Another class of mechanoreceptor allows jellies to detect gravitational direction. Called statocysts, these balance organs are found in a large percentage of cnidarian species, either in isolation or, in scyphomedusae, as part of bulbous sensory structures called rhopalia [47]. Statocysts also appear in larvaceans [20] and in ctenophores [66]. These tiny gravity sensors typically consist of a club-like appendage in a cilia-lined pit, that behaves in a manner similar to a cantilever-beam inclinometer [50,85]. Many cnidarians and ctenophores have been observed to perform closed loop feedback regulation to preserve the alignment between their axes of symmetry and the gravity

vector [37,89]. When statocysts are removed from a group of these animals, the distribution of orientation among the population becomes random. Statocysts may support other functions besides gravity alignment. Some medusae with statocysts do not consistently align with gravity, and others are passively stabilized by a buoyancy moment. Also, larvaceans have not been observed to actively regulate their orientation. In the field, larvaceans and their houses appear to be randomly oriented with respect to gravity.

Few studies have been conducted involving mechanical sensitivity of jellies to acoustic vibrations. Some anatomical evidence suggests that medusae possess crystalline structures possibly sensitive to sound [22]. In [58], Mackie indicates that the hydromedusa *Eutonia* turned and swam rapidly downward in response to a high frequency vibration; the vibration frequency was not, however, specified. Numerous experiments with manned submersibles and ROVs suggest that jellies do not generally react to intense nearby sound sources.

The mechanoreceptivity of gelatinous animals to water disturbances limits the proximity with which a tracking robot may approach its subject [42,77]. In previous experiments, observational platforms have been held at a minimum distance of one meter from the subject.

### 2.7.2 Chemical, Pressure, Temperature Receptors

A tracking robot is unlikely to trigger a jelly reaction based on chemical, pressure, or temperature sensitivity. The ability to measure these scalar properties during an observation experiment, however, might help explain low-frequency animal behavior. Specific physiological mechanisms for chemoreception remain unidentified; however, behavioral evidence suggests that some cnidaria and ctenophores sense prey through chemical detection [47,89]. Chemoreception may mediate tactile responses, as jellies perform different actions when they contact predators and prey. Chemoreception may also influence foraging patterns, as gelatinous hunters exhibit a preference for waters with trace concentrations of prey-related chemicals. One study by Arai showed that tank-confined *Aequorea* clustered near a screen which separated them from brine shrimp, a preferred prey species for these hydromedusae [13]. Other studies have shown attraction of the scyphomedusa *Aurelia* to herring eggs [17] and increased swimming activity of the ctenophore *Beroë* in seawater conditioned by exposure to *Bolinopsis* [89]. It is possible that the chemicals detected by these predators are nitrogen wastes or other excretory products of the prey species.

Jellies also respond to changes in temperature and pressure. Again, no physiological mechanism has been identified to explain these phenomena. Pressure sensitivity may nonetheless play a role in regulating DVM for deep-swimming animals [38]. Experimental evidence shows that some hydromedusae increase pulse frequency when ambient pressure increases by as little as 0.3-0.5 bars, a pressure change approximately equal to that experienced during a depth change of 3-5 m. Similarly, thermal sensitivity may cause jellies to move toward habitats of a preferred temperature. Temperature changes as small as 1 degree Celsius can influence swim frequency [76]. Environmental stimuli act together may augment jelly response. Hamner suggests that combinations of gradients in chemical concentration, pressure, temperature, and possibly also in turbulence, gravity or light may serve to guide jelly navigation through long migration patterns [38, 47].

### 2.7.3 Optical Receptors

Light sensitivity is common among gelatinous zooplankton. Among the cnidaria, many species possess light sensing organs, called ocelli. Ocelli vary in form from simple eyespots, to pigmented cups, to complex cups [63] and in number from four (*Sarsia tubulosa*) to hundreds (*Spirocodon Saltatrix*) [92]. Researchers have also discovered extraocular mechanisms for light detection. These receptors include photosensitive neurons [11,15] and also, possibly, photosensitive muscle and epithelial cells [63].

Ocelli govern a set of behavioral responses distinct from those governed by extraocular mechanisms. Whereas extraocular receptors and flat ocelli detect only ambient light intensity, cup-shaped ocelli can detect both the intensity and direction of spot lighting [66]. Correspondingly, cup ocelli initiate rapid directional lighting responses like the shadow response, a brief burst of swimming observed in some species when a bright light is switched off. Extraocular receptors, by contrast, invoke longer-term behaviors, such as DVM.

Among the most advanced cnidarian vision systems are those belonging to cubomedusae like *Tripedalia Cystophora*, whose complex ocelli, consisting of a cornea, retina and lens, are able to form images [23]. Even without brains, cubomedusae equipped with complex ocelli display behavioral responses to patterns of illumination; in a white-colored laboratory tank, *Chironex fleckeri* swam around vertically oriented black pipes but knocked over otherwise identical white pipes [45]. Other sophisticated vision-based behaviors have been observed among cnidarians, including sun-compass navigation [38,40]. Researchers have not yet identified the physiological

mechanism for sun-compass navigation, but hypothesize sensitivity to solar motion, to the angle of the sun above the horizon, or to the directional polarization of sunlight refracted through the ocean surface.

Although ocelli occur commonly among cnidarians, ctenophores do not possess ocelli [66]. Ctenophore DVM activity suggests possible extraocular photosensitivity; however, researchers have yet to identify a physiological mechanism for extraocular light reception in ctenophores [89]. Likewise, larvaceans do not possess specialized light sensing organs [20]. Although other urochordates develop eyes, researchers have not identified eyes or extraocular photoreceptors among larvaceans, nor observed behavioral patterns, such as DVM, which might suggest photosensitivity.

#### 2.7.4 Light Induced Behavioral Responses among Cnidarians

Because many cnidarians have sophisticated optical sensing capabilities, these animals place the most stringent constraints on the design of a jelly-tracking platform. For long duration visual observation, artificial illumination should be designed to minimize impact on animal behavioral patterns.

Some evidence exists, based on short duration *in situ* studies, that deep-ocean cnidarians do not respond dramatically to artificial illumination used by scientific submersibles. Mills and Goy, for instance, observed that the orientation of *Solmissus* under artificial lighting appeared random, and that *Solmissus* specimens did not begin downward migration, as might be expected, in the presence of bright ambient lighting [72]. The experiments of Robison, likewise, have detected no direct correlations between submersible lighting and gelatinous animal behavior. In one series of trials, Robison observed animal specimens both under full ROV lighting and with ROV lighting reduced by 90% [7]. These experiments found no appreciable differences in animal behavior during these short-term observations. In another series of experiments, Robison *et al.*, watched for motion of the siphonophore, *Nanomia bijuga*, in response to the lights of an approaching ROV [80]. These experiments exploited sonar, which reflects strongly from the gas-filled pneumatophores of *Nanomia*, to verify that the siphonophores remained stationary as the ROV approached within visual range.

Although field experiments have not noted gross behavior changes corresponding to artificial illumination, laboratory experiments under controlled conditions do indicate subtle changes of medusa behavior in response to light. Through such lab experiments, researchers have investi-

gated the physiological pathways, consisting of photoreceptive sensors, neural connections, and muscles, that mediate light responses. Photoresponses vary substantially with lighting duration, from rapid voltage spikes recorded in ocelli (light duration in tenths of seconds), to changes in jelly swimming frequency (duration of minutes), to light-induced vertical migration patterns (duration of hours). From these experiments, it is clear that any sensor based on active illumination may produce a response in a gelatinous animal under observation. Whether the response involves only a brief voltage spike in the photosensor or a full-blown swimming response depends on the nature of the lighting event and the species under observation. For this reason, it is important to match the jelly-tracking lighting system to the behavioral phenomena under study.

Even very brief lighting changes, as short as 10 ms, may evoke a response in the ocellus. Weber measured ocellus voltage spikes following step changes between artificial lighting and darkness. A 10 ms light or dark pulse excited an ocellus voltage spike with a duration of 200-300 ms. The spike latency, relative to initiation of the light stimulus, was 35-45 ms in *Sarsia tubulosa* [92] and 50-60 ms in *Polyorchis penicillatus* [91]. For longer light pulses, additional activity followed the initial ocellus voltage response. For illumination durations between 0.1 and 1 s, the light response was biphasic (rising above then falling below the cell's resting potential); for illumination lengths longer than 1s, persistent high frequency oscillations followed after the biphasic pulse. Although these voltage patterns demonstrate a definite ocellus response, even to very brief light stimuli, ocellus responses do not alone imply changes in the overall behavior of the medusa system. For an observable behavioral change to occur, the photoresponse pathway must transmit the ocellus activity and trigger a nervous response which, in turn, triggers muscle contraction.

Such a photosensitive pathway has been studied in detail for the shadow reflex, a motion response exhibited by some jellies following rapid decreases in light level. Arkett and Spencer discovered a subset of neurons in the outer nerve ring of *P. penicillatus* that respond directly to light-off events and that trigger, in turn, action potentials in the swimming motor neuron (SMN) system [14,15,16]. Action potentials are binary (all-or-nothing) changes in the potential of excitatory cells, that, in the case of the *P. penicillatus* SMN, correspond one-to-one with the contraction of bell muscles. Figure 2.6 shows SMN voltage changes in response to light-off events of varying length. Voltage begins to rise in small increments, after an initial latency of 150-200 ms. Eventually the SMN reaches a voltage threshold and an action potential spike occurs. These action poten-



tials, which correspond to muscle contractions, do not occur unless the shadow duration exceeds a minimum length of about 0.6 s.

The shadow response, which serves for escape and possibly for DVM initiation, has been observed in a number of hydromedusan species, including *Polyorchis penicillatus* [14,91], *Spirocodon saltatrix* [75], *Bougainvillia principis* [84], and *Gonionemus sp.* [74]. In none of these species has a swimming reflex been observed during a light-on event. In fact, a light-on event following a light-off event will inhibit a shadow reflex in progress, ceasing the burst of action potentials and returning the medusa to a spontaneous swimming mode. The shadow reflex and its inhibition are significant for jelly-tracking design, in that they are instances of observable medusa behavior that occur following changes in lighting level. It is further significant that reflexes only occur after a minimum exposure length, on the order of 100s of ms, even if the ocellus responds to much shorter exposure times, on the order of 10s of ms.

Over long durations of light or darkness, medusae exhibit habituation behaviors. A period of dark adaptation follows the *P. penicillatus* shadow reflex, for instance. At the beginning of this dark adaptation period, following the reflex burst of 1-4 action potentials, SMN voltage remains

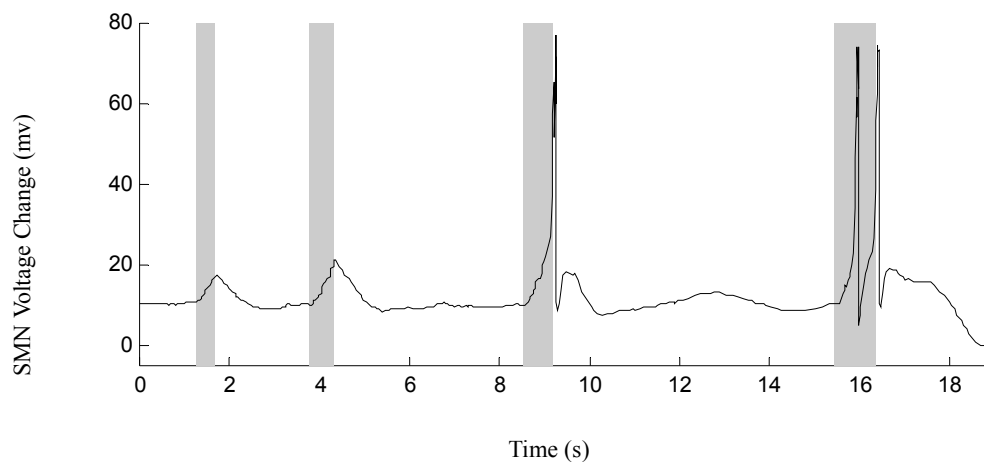


**Figure 2.6 Motorneuron Voltage during Shadow Reflex**

Voltage levels were measured in the swimming motorneuron of *Polyorchis penicillatus* when the animal is exposed to shadows of varying duration (Data source: [86]). The animal is exposed to a sequence of four light-off events of 0.44, 0.55, 0.64, and 0.92 seconds in period. The motorneuron depolarizes during each light off event and hyperpolarizes when the light turns on again. Action potentials occur for light-off events longer than 0.6 s.

elevated near the threshold potential. After approximately 8 seconds, SMN voltage declines toward the rest potential as the photoreceptor and nervous system habituate to the darkness [11]. Although regular swimming contractions may not resume for as long as 2 minutes after light-off [87], the medusa adapts more quickly and can, in some cases, resume spontaneous swimming within as little as 15-20 seconds after light-off [14].

Some hydromedusae also exhibit habituation responses to extended periods of increased lighting. In *P. penicillatus*, for instance, a step increase in illumination leads to an increase in swim frequency [11]. After the initial increase, the swim frequency decays asymptotically toward its original level over a 2-3 minute period of light adaptation [14]. This increased swim frequency phenomenon has also been observed among some scyphomedusae, like *Aurelia*, but not among others, like *Cyanea* [51]. Extraocular photoreception appears to govern this phenomenon, which occurs even in specimens with their ocelli surgically removed.

In addition to their reflex responses to brief lighting stimuli and their adaptive responses to stimuli of several minutes, medusae also exhibit light-mediated behavioral patterns over much longer time periods. Examples of these patterns include DVM and sun-mediated horizontal migrations, which both occur on a 24-hour cycle. These migration behaviors depend strongly on changes in natural lighting over time. Studies by Mills *et al.*, for instance, showed clear links between light changes and vertical migrations for hydromedusae in confined tanks [69]. These hydromedusae ceased DVM cycles after Mills introduced a tank cover that blocked out external light. Similar studies by Schuyler and Sullivan observed DVM patterns among confined *Chrysaora quinquecirrha* under natural lighting [81]. The introduction of a tank cover interrupted regular DVM motion for these scyphomedusae, which collectively swam to the top of the aquarium within the first fifteen minutes of darkness.

In general, medusae do not exhibit directed motion toward a light source (positive phototaxis) or away from it (negative phototaxis). While darkness did initiate motion in the case of Schuyler's *Chrysaora* experiments, passive stability and statocyst balance organs controlled swimming orientation. Experiments by Murbach demonstrated, similarly, that *Gonionemus* swims in apparently random directions, uncorrelated with an applied lighting gradient, until it arrives and stops in a zone of a preferred lighting level [74]. An exception to the trend are the cubomedusae, many of which display evident phototaxis toward strong point light sources [63].

### 2.7.5 Engineering Implications of Light Sensitivity

In designing a jelly-tracking robot for long-duration visual observations, the impact of artificial lighting on observed animal behavior is a critical issue. Three principle techniques may be considered to reduce the impact of artificial illumination on an ethological investigation. These techniques involve (1) strobing the light source, (2) altering the illumination wavelength, and (3) reducing the illumination intensity.

This dissertation recommends the use of strobed red lighting for jelly tracking. The use of a strobed light system to minimize the optical disturbance environment for the long-duration observation of gelatinous animals has not previously been proposed. Continuous artificial illumination over long durations threatens to interfere with slow behaviors, like DVM, that are mediated by natural lighting. Strobed illumination, in contrast, may allow the animal to adapt to natural ambient lighting to enable observation of DVM and other light-mediated behaviors. On the downside, pulsed lighting may trigger neural responses and, under some conditions, muscle responses. A pulsed lighting system must be designed, therefore, to avoid triggering light or dark reflexes in an observed specimen. Chapter 7 introduces a new light-response model to assess the effect of a pulsed lighting pattern on a reference medusa (*P. penicillatus*). Figure 2.7 illustrates the basic premise of the light-response model, a hybrid model that captures the various light-mediated medusa responses described in the previous section including ocellus (nervous) responses, reflex (muscle) response, adaptation, and DVM responses. Application of the model suggests that a particular strobed lighting pattern (designed for energy optimality in an AUV application) may reduce the optical disturbances generated by the tracking vehicle.

Strobing illumination is just one of the three ways of reducing the impact of artificial lighting on observed animal behaviors; a second technique involves modulating lighting frequency to wavelengths away from the peak sensitivity band for the specimens under observation. For most medusae, spectral sensitivity favors the blue wavelengths. Ocelli of the cubomedusa *Tripedalia cystophora*, for instance, respond most strongly to wavelengths between 440 and 470 nm [24]. The hydromedusae *Bougainvillia principis* [84] responds most strongly to wavelengths of 446-544 nm, while *Spirocodon saltatrix* respond strongly from 480-500 nm [63]. Although maximum sensitivity falls near the blue, many medusae have a relatively broad sensitivity throughout the visual range. For the species described by Figure 2.8, ocellus sensitivity drops by 75% of its peak value in the red, near 650 nm. Red sensitivity appears weaker among deeper swimming individuals.

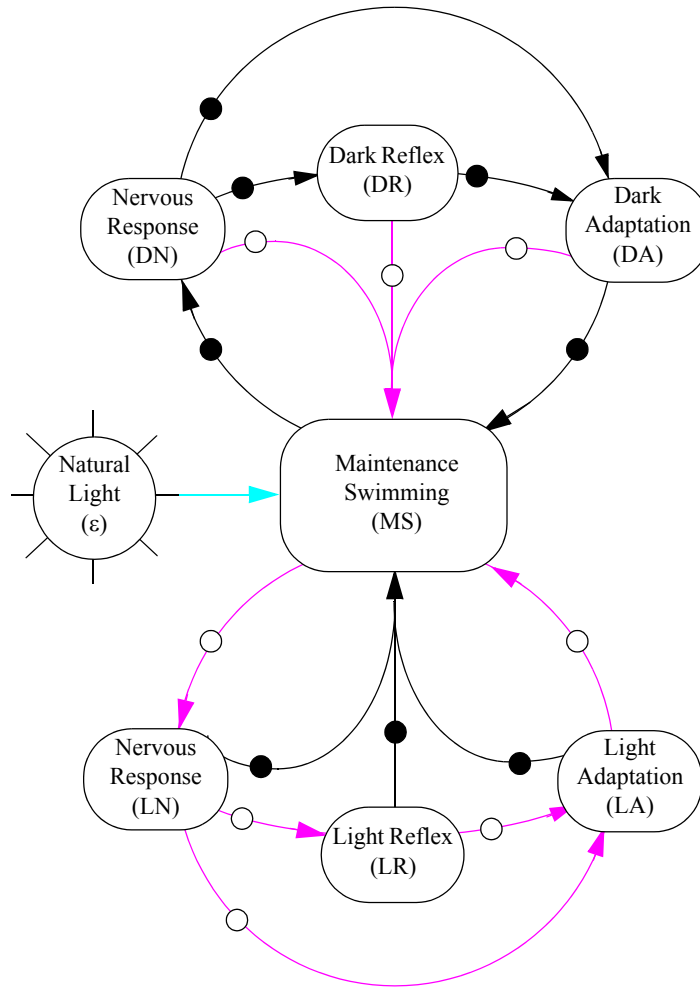


**Figure 2.7 Medusa photoresponse model.**

The model contains seven discrete states. Transitions occur based on the nature of the artificial lighting input. Open circles correspond to light-on events and closed circles to light-off (darkness) events. A change in lighting immediately triggers a mode switch. For continued lighting, mode switches occur only at thresholds of the light progress variable,  $x_l$ , or the dark progress variable,  $x_d$ . Further details of the model are described in Chapter 7.

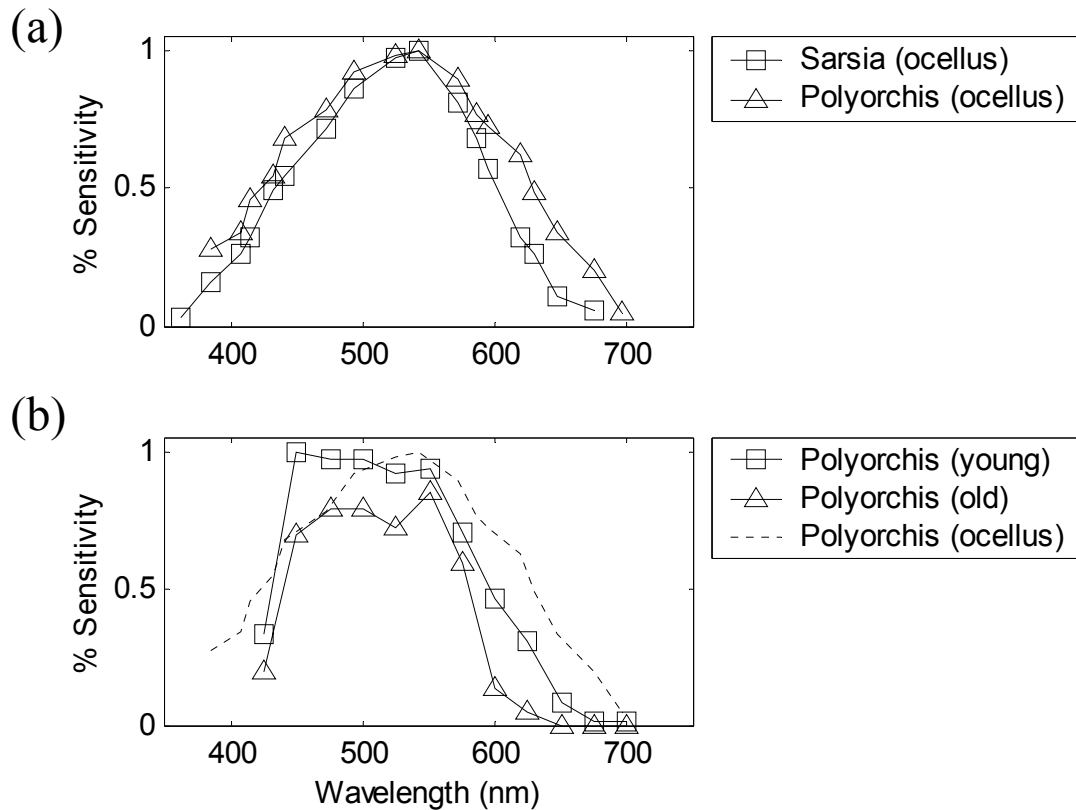


**Figure 2.8 Spectral Photoresponse of Two Medusa Species**

*Spectral responses for two hydromedusa species are compared, based on the data presented in [14,91,92]. (a) Voltage change in the ocellus upon application of a 30 ms monochromatic light pulse. Voltages are normalized by the maximum response across the spectrum. Both the *Polyorchis* and *Sarsia* ocelli respond to a broad range of wavelengths, with peak response around 550 nm. (b) Percentage of *Polyorchis* specimens that exhibited a shadow response to an 0.5 second blockage (100% shadow) of ambient monochromatic light. The plot compares young medusae (bell height < 2.0 cm) with older medusae (bell height > 2.0 cm). Shadow response sensitivities for *Polyorchis* correlate strongly with the ocellus response from part (a), replotted as a dashed line.*

According to the data depicted in Figure 2.8(b), shadow reflexes in response to red light occur more frequently for young *P. penicillatus* medusae, which prefer surface waters, than for older medusae, which swim at greater depth with less available red light. It is possible that deep swimming jellies, which consistently remain below 1000 m, may have very narrow bandwidth photoreception capabilities, if any. Based on these data, a strobed visual tracking system could employ red illumination to further reduce the chance of disturbing its jelly subject.

A third technique, that of reducing artificial illumination levels and employing a low-light camera, might also reduce the risk of artificially generating medusa behaviors. However, the effect of illumination reductions on medusa response is relatively weak. Weber found, for example, that the ocellus of *P. penicillatus* responds proportionally to the log of intensity, at about 25% per decade [91]. Thus, a reduction of light intensity by a factor of one thousand resulted in a reduction in ocellus response by only 75%. Arkett and Spencer demonstrated, furthermore, that photoresponses of *P. penicillatus* depend primarily on relative lighting changes, rather than absolute lighting level changes [16]. In tests alternating between full and partial lighting, the shadow reflex weakened with smaller relative lighting changes. In tests alternating between partial lighting and darkness, the shadow response always remained strong, even for very low partial lighting levels. From an engineering viewpoint, these studies indicate that reducing lighting intensity may be less effective than strobing or red-shifting the light source as a means of preserving natural animal behavior during visual observation.

---

## 2.8 Summary

This chapter has examined the biological basis that motivates the jelly-tracking activity and that constrains the design of a tracking robot. The study of the behavior of animals in their native habitats, proves difficult to conduct in the underwater environment. The desire for such studies provides the principle motivation for a jelly-tracking robot. In order to follow a broad range of important gelatinous species, including cnidarian medusae and siphonophores, ctenophores and larvaceans, a jelly-tracking robot must meet a range of specific design constraints:

- The robot must achieve depths of at least 200 m, for nighttime studies in the upper oceans, or 1000 m, for studies of gelatinous animals through their full diurnal migration patterns.

- Tracking duration is a key performance metric. Any improvements in the duration of automated tracking are useful. Ultimately, an AUV is desired that can track an individual animal for more than 24 hours.
- The robot energy budget must account for DVM. Many jellies transit as far as 200-500 m in both directions during their vertical migration cycles.
- The robot energy budget must account for target foraging behaviors. Oblate jellies often forage continuously, at nominal speeds in the 1-3 cm/s range. Prolate jellies move sporadically, but at higher speeds.
- During an escape response, a prolate jelly may accelerate to its maximum speed in as little as 1.3 s. To track the most rapid of these escape responses, a closed-loop vehicle bandwidth of approximately 1.7 rad/s is required. Choosing bandwidth to attenuate lower frequency disturbances can reduce oscillations and energy costs associated with tracking target speed changes during the period thrust-recovery cycle of medusa swimming.
- Robot actuation should not produce hydrodynamic disturbances that disturb the subject. As a rule of thumb for reducing hydrodynamic disturbances, the tracking robot should maintain a range of at least one meter from the target animal.
- The visual sensor should account for multiple jellies in proximity; however, deep-ocean jellies are generally found solitary and not in large aggregations.
- Artificial illumination required for visual observation should minimally impact jelly behavior. To enable long-duration observation without influencing jelly migration patterns requires a careful lighting design that considers strobing, light wavelength, and light intensity.

From a philosophical point of view, many of the design issues for automated jelly tracking are not unlike the “design issues” solved by evolution for gelatinous animals. Jellies represent systems of sensors, actuators, and control behaviors that function under limited processing and power constraints. In this sense, gelatinous animals serve as an inspiration and example for the design of highly integrated, efficient robot systems.





*The evolution of undersea vehicles and the research they enable have been mutually interactive ever since the first research submersible appeared in the 1930s.*

- B.H. Robison, 1999 [8]

---

This dissertation describes the first-ever field demonstration of jellyfish tracking using an operational robotic system. These experiments deployed a computer-controlled remotely operated vehicle (ROV) to track gelatinous animals at depths of hundreds of meters below the surface of Monterey Bay, California. This chapter overviews the hardware and software for the experimental jelly-tracking system. The primary hardware component for field testing is the ROV *Ventana*, a vehicle owned and operated by the Monterey Bay Aquarium Research Institute (MBARI). Additional equipment includes the sensor suite, mounted on the ROV, and the jelly-tracking computer, which sits remotely in the surface support vessel, R/V *Point Lobos*. The jelly-tracking computer runs two software components, a vision-processing algorithm, that determines target location from camera sensors, and a control-component, that maps the target location into actuator commands for the ROV thrusters. The hardware overview presented here provides context for system software development, which the subsequent two chapters describe in detail.

---

### 3.1 Introduction

Experiments demonstrate an ROV-based jelly-tracking pilot assist. As tethered platforms, generally controlled by human pilots, ROVs are versatile unmanned submersibles, useful for complex tasks in unknown environments. Certain ROV missions, like jellyfish tracking, require extended periods of pilot concentration to perform fine servo-level tasks. Pilot-assist systems combine the capabilities of a computer, which automates servo-level tasks, with a human pilot, who handles complex tasks and unexpected events. In the case of jellyfish tracking, the introduction of automation relieves pilot fatigue to promote more frequent, longer duration animal observation.

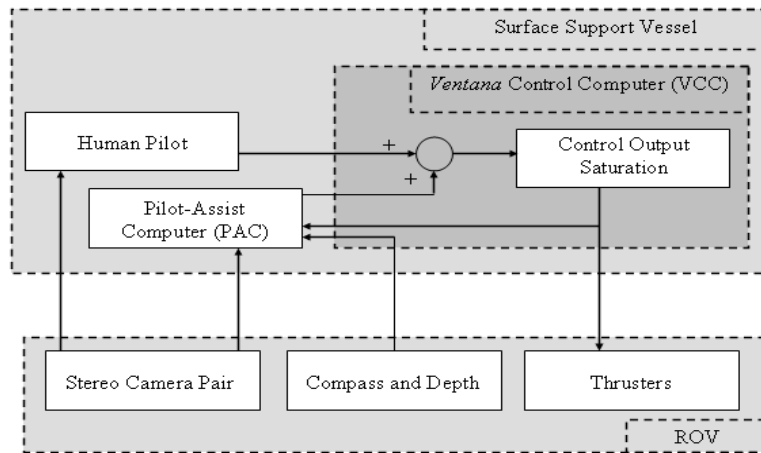


**Figure 3.1** System Hardware Block Diagram

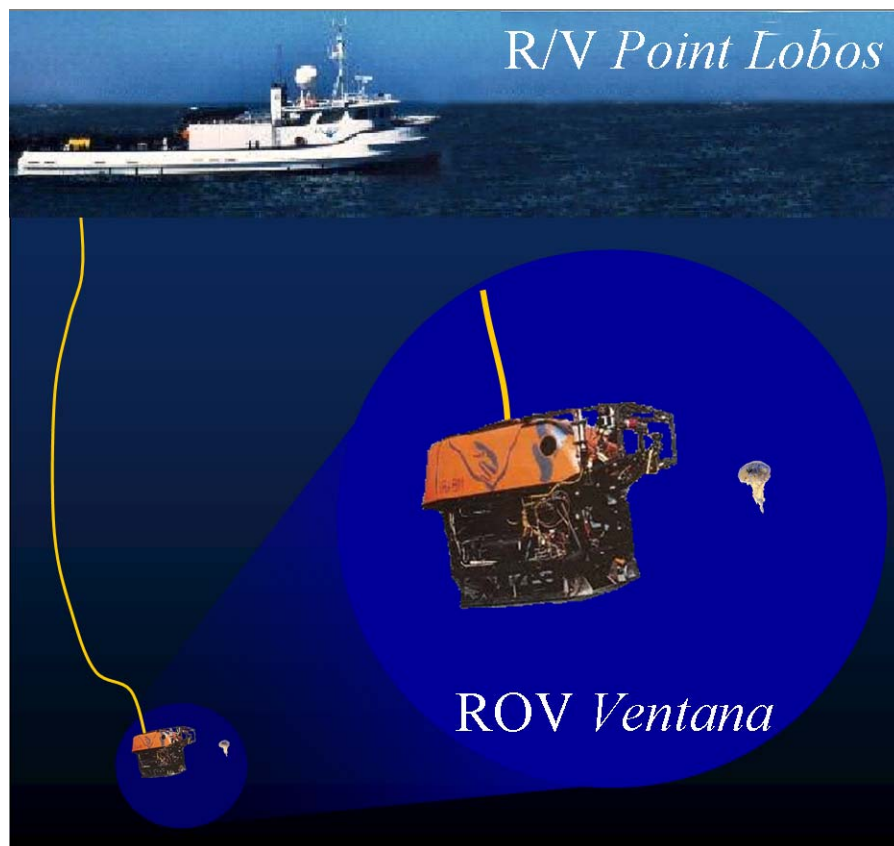


**Figure 3.2** ROV *Ventana* with R/V *Point Lobos*

Figure 3.1 summarizes the hardware structure of the ROV-based jelly-tracking system using a block diagram. The two largest blocks represent vehicle platforms: the ROV *Ventana* and its support ship, the R/V *Point Lobos*. While the ROV operates in the deep ocean, its cameras and other sensors collect data and send it to the surface support ship via a fiber-optic connection embedded in the ROV tether. In the standard control mode, the human pilot views video data and issues control commands via a joystick interface. In the automated jelly-tracking mode, the Pilot-Assist Computer (PAC) also acquires camera data and issues control commands, via a serial cable, to the main *Ventana* Control Computer (VCC). The VCC conditions control commands, summing human and autopilot commands when necessary and saturating them as required. The control computer sends these conditioned thrust requests down the tether to the submerged ROV. On board the submersible, these control signals actuate hydraulic valves which regulate the output for each of the ROVs ducted thrusters.

---

## 3.2 ROV *Ventana*

The ROV *Ventana* is a custom unmanned submersible, originally built by International Submarine Engineering in 1988 and since modified by MBARI for scientific use [9]. The submersible measures 2.2 m in height and 3.0 m in length. The vehicle mass, dry, is approximately 2600 kg. The submersible's nominal depth rating of 2000 m is limited to 1600 m by the length of the current tether. The kevlar-jacketed tether carries five power conductors that support an 8 kW hotel load (3.4 kW lighting, 1.1 kW system, 3.5 kW science) and as much as a 30 kW actuator load. The tether also incorporates ten fiber optic connections that transport video data and telemetry signals to the surface support vessel and control signals back to the ROV.

Vehicle actuation consists of three pairs of hydraulic thrusters. One pair points vertically, a second pair (aligned coaxially in a single tunnel) points laterally, and a third pair points in the fore-aft direction. The two fore-aft thrusters operate differentially to spin the vehicle in yaw. Thrusters do not actuate the ROV's pitch and roll degrees of freedom. Rather a strong, passive buoyancy moment counters pitch and roll motions. Deviations from equilibrium pitch and roll angles are small; effectively the ROV acts as a system constrained to four degree of freedom motion.

Control commands issued by the surface vehicle actuate hydraulic valves on board the ROV. These valves control the flow rate of hydraulic fluid to each thruster, thereby controlling rotor velocity and thrust output. Thrust commands, issued from the surface vessel, vary between +5 and

-5 V. Thrust saturates at either end of this scale. Thrusters operate at a hydraulic pressure of 3000 psi in standard mode. A bypass mode reduces pressure to 1000 psi to permit fine-tuned control. Pilots generally activate bypass mode for human-controlled jelly-tracking experiments. In cases when multiple actuators operate simultaneously, the flow rate of hydraulic fluid may drop, effectively reducing the force produced by each thruster below the requested level.

The open-frame construction of ROV *Ventana* enables it to be customized for different science experiments. For jelly-tracking experiments, the benthic toolsled was used. Vehicle buoyancy was trimmed to neutral by attaching or removing 25 lb (11.4 kg) lead bricks to the sled. The vehicle was also configured with one pair of detritus samplers, cylindrical containers used by biologists to collect gelatinous animal specimens. The high degree of system reconfigurability implies that ROV dynamic parameters change somewhat from dive to dive. Reconfiguration may also introduce communication errors among system components. A thorough vehicle checkout was performed prior to each experimental dive to verify communication between sensors and actuators and the jelly-tracking computer.

---

### 3.3 R/V *Point Lobos*

The R/V *Point Lobos* serves as the surface support vessel for the ROV *Ventana*. The ship measures 33.5 m (110 ft) in length and 7.9 m (26 ft) in beam. Originally commissioned as an oil-field supply vessel, the *Point Lobos* underwent renovation when acquired by MBARI in 1981. Renovations included the addition of an ROV control center and a deck crane, mounted at the ship's stern, that launch and recovers the ROV. The ship requires a crew of seven (master, first mate, engineer, two deck hands and two pilots) for ROV operations.

Pilots command the ROV from the control center located below deck in the ship's bow. Television monitors in the control room display video signals from the submerged ROV. A video multiplexer maps any of a variety of video inputs to each monitor. For jelly tracking under human pilot control, three monitors display video streams from the main camera and from the stereo camera pair mounted on the ROV's upper pan-tilt unit. Alongside these monitors, a touch-screen graphical user interface displays telemetry signals. These signals from the ROV include compass heading, depth, inclinometer angles, and thrust commands.

Based on video and telemetry data, the pilot issues thrust commands to the ROV. A joystick device takes inputs for fore-aft, lateral, and yaw thrust commands. A slider bar accepts vertical

thrust commands. Springs in the joystick mount return it to a neutral setting in the absence of contact with the pilot's hand. The slider bar, however, retains its setting in the absence of contact in order to allow the pilot to trim the ROV to compensate for non-neutral buoyancy.

---

## 3.4 Computer Hardware

The two computer systems depicted in Figure 3.1 both reside in the *Point Lobos* control room.

### 3.4.1 The *Ventana* Control Computer (VCC)

The *Ventana* control computer (VCC) serves as a permanent component required for ROV operation. This computer runs a Linux application that manages telemetry to the submerged ROV. Joystick and other pilot commands pass through this machine, which packages these signals and routes them to the ROV. The VCC also receives all ROV sensor data, except video and doppler velocity logger (DVL) signals. A touchscreen graphical user interface associated with the VCC displays this information to the pilot in an interactive fashion.

### 3.4.2 The Pilot-Assist Computer (PAC)

The pilot-assist computer (PAC) is a second machine, dedicated to software for automated station-keeping tasks. The PAC communicates with the VCC via a serial communication link at 20 Hz. The VCC reads the serial port string, consisting of control commands issued by the PAC, and writes a second string, consisting of telemetry data. These strings are summarized by Table 3.1.

The physical separation of the PAC from the VCC addresses three significant concerns: processing power, development flexibility, and safety during emergencies. First, the separation parallelizes computationally expensive processing tasks so that they do not interfere with the real-time requirements of the VCC. Second, the separation decouples the pilot assist-software from the main control software used for all *Ventana* operations. This characteristic is critical during development, so that arbitrary changes to the pilot-assist software are guaranteed not to affect the core operational software used for general ROV operation. Finally, the separation provides a convenient method of implementing an emergency stop button. The VCC sums and then saturates the control commands issued by the human pilot and the automated controller. If the pilot detects any problem with the automated system, the press of a single button interrupts all serial communica-

PAC Input Variables	Type	Nominal Zero	Units	Sign
Ambient Pressure	Integer	0 @ surface	Millibar	Positive at depth
Port Thruster Command	Integer	2047	0-4095 Full Scale	Increases forward
Starboard Thruster Command	Integer	2047	0-4095 Full Scale	Increases forward
Lateral Thruster Command	Integer	2047	0-4095 Full Scale	Increases starboard
Vertical Thruster Command	Integer	2047	0-4095 Full Scale	Increases down
Teleos Enabled	Integer	0	0/1	Positive enabled
Dive Number	Integer	0	Integer	Positive
Spare Integer	Integer	--	--	--
Heading	Float	0	Degree off North	Increasing east
Pitch	Float	0	Degree off Vertical	Positive nose up
Roll	Float	0	Degree off Vertical	Pos. starboard high
Altitude	Float	0	Meters	Positive
Summed Yaw (Pilot + PAC)	Float	0	-5 to 5 Full Scale	Increases starboard
Summed Axial Command	Float	0	-5 to 5 Full Scale	Increases forward
Summed Lateral Command	Float	0	-5 to 5 Full Scale	Increases starboard
Summed Vertical Command	Float	0	-5 to 5 Full Scale	Increases down
Depth	Float	0	Meters	Positive
Sony Camera Tilt Angle	Float	0	Degree off $x_v$ -axis	Increases down
Sony Camera Shoulder Angle	Float	0	Degree off $z_v$ -axis	Increases down
Sony Camera Pan Angle	Float	0	Degree off $x_v$ -axis	Increases port
Auxiliary Camera Tilt Angle	Float	0	Degree off $x_v$ -axis	Increases up
Auxiliary Camera Pan Angle	Float	0	Degree off $x_v$ -axis	Increases starboard
System Time	Float	Midnight	Seconds	Positive
Spare Float	Float	--	--	--

PAC Output Variables	Type	Nominal Zero	Units	Sign
PAC Yaw Command	Float	0	-5 to 5 Full Scale	Increases starboard
PAC Axial Command	Float	0	-5 to 5 Full Scale	Increases forward
PAC Lateral Command	Float	0	-5 to 5 Full Scale	Increases starboard
PAC Vertical Command	Float	0	-5 to 5 Full Scale	Increases down
Spare Float (x 8)	Float	--	--	--

TABLE 3.1. Serial String Variables

*This table details the input PAC variables (read by the pilot-assist computer) and the output PAC variables (issued by the pilot-assist computer). Sign conventions for these variables are listed, as they do not always match the standard sign conventions used internally by the pilot-assist software, as depicted by Figure 5.3.*

tion between the PAC and the VCC, effectively returning complete control authority into the pilot's hands.

The PAC for jelly-tracking experiments uses a 700 MHz Intel Pentium III processor. Twin Matrox Meteor cards acquire video signals in NTSC format. The jelly-tracking software consists of two components, a video processing component that measures target position and a control component that converts the visual-position signal into a thruster command. These two software components will be described in more detail in Chapter 4 and Chapter 5, respectively.

---

## 3.5 Human in the loop

The human pilot plays a very important role in the jelly-tracking pilot-assist system. Most significantly, the human pilot aids in initialization of the jelly-tracking system by (1) performing scanning transects in search of a target, (2) slowing the ROV to assess potential targets, and (3) holding station on the target during a brief, 1-2 second training period for the jelly-tracking recognition algorithm. A simple button push triggers the jelly-tracking algorithm to begin training and subsequently to assume fully automated tracking. The human pilot retains the ability to sum control with the automated tracker at any time. This capability permits the human pilot to adjust the target position, relative to the vehicle, at the request of a scientist or to immediately assume control in the event of an emergency.

---

## 3.6 Vision Sensor

Human pilots use video signals as their primary sensor for manual jelly tracking. The pilot-assist computer (PAC) mimics this technique, also employing vision to detect and localize jellyfish. The design of the vision software algorithm represents a significant contribution of this research project.

### 3.6.1 Vision Software

Vision-processing software, customized for the jelly-tracking task, runs on the PAC. Vision software operates on two input video streams to construct a relative-position measurement between a camera pair and an animal specimen. The vision software consists of three processing compo-

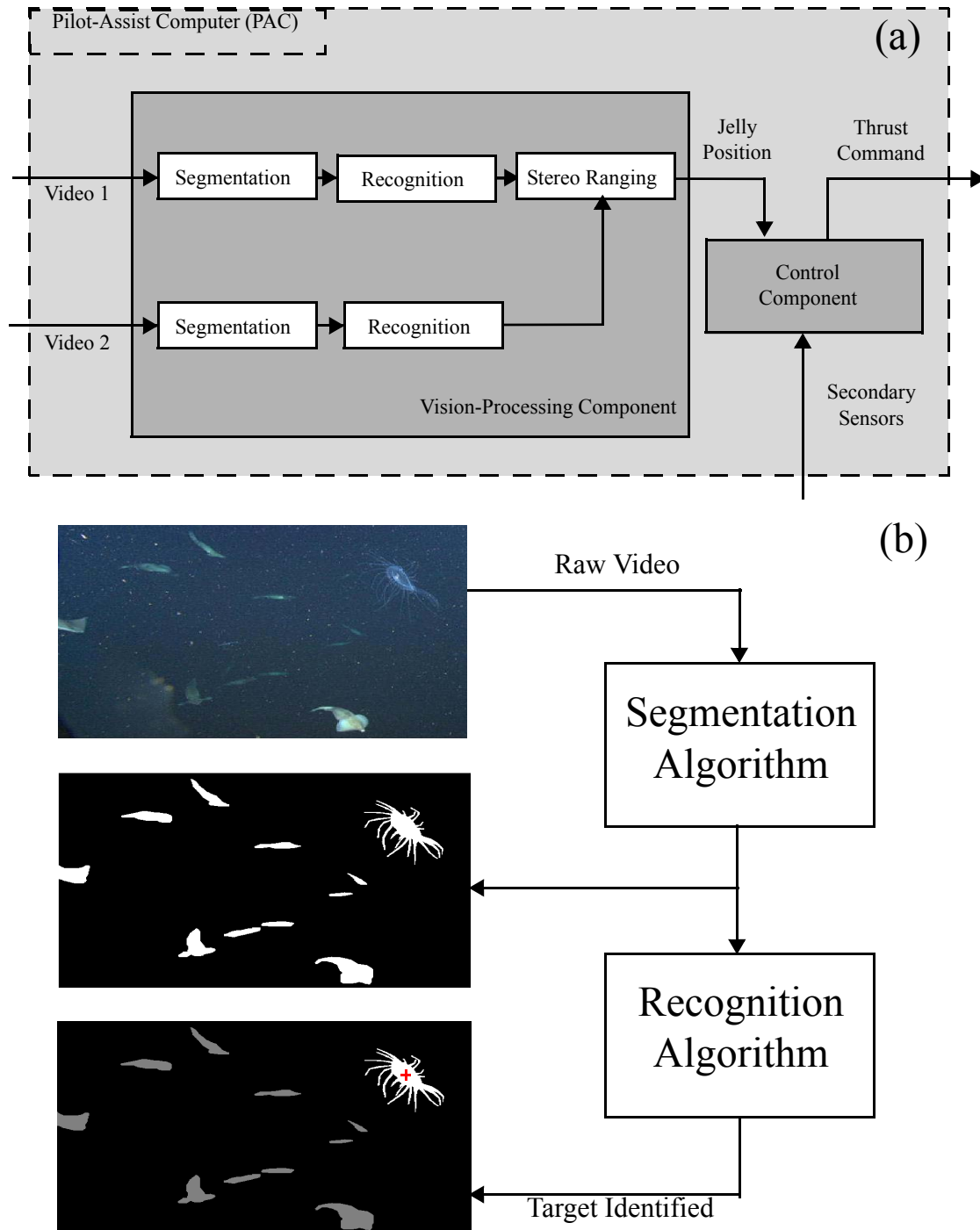


**Figure 3.3 Vision-Processing System**

(a) Block diagram for the PAC, with details of the vision-processing component. (b) Graphical depiction of vision-processing. The segmentation algorithm clusters pixels into associated regions, while the recognition algorithm identifies the region (indicated by a crosshair) that best matches a target profile.



nents, which operate sequentially on incoming images (see Figure 3.3). The first component, called the segmentation component, identifies clusters of image pixels sharing similar characteristics. The second component, the recognition component, scans these clusters to identify the best match to a target profile. The centroid of this best-match region defines the bearing vector from the camera origin to the tracked target. The third processing step, the stereo geometry step, applies camera calibration data to transform the two measured bearing vectors into a relative position vector that relates the animal's position to the camera rig.

Chapter 4 describes a new design tool used to synthesize segmentation and recognition algorithms for jelly tracking. The stereo geometry step is not task specific and is briefly summarized in the following section.

### 3.6.2 Stereo Camera Configuration

Video cameras provide the input for the vision-processing software; this software returns a three-dimensional target position which serves as an input to the motion control software. As discussed in the previous section, a stereo-triangulation method was used to compute target range by combining bearing vectors observed simultaneously by a pair of cameras.

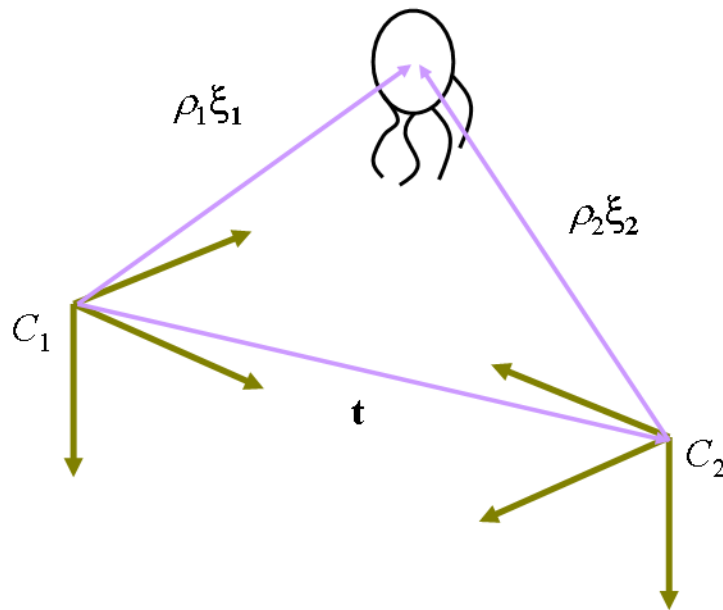


**Figure 3.4 Stereo Triangulation Geometry**

*C1 and C2 are camera reference frames, separated by the translation vector  $t$  and the rotation matrix  $R$ .*

Two different stereo configurations were used for jelly-tracking experiments. The first configuration consisted of a converging camera pair separated by a large-baseline (1 m); the second configuration, of a parallel camera pair separated by a short-baseline (10 cm). The large-baseline system used the main ROV science camera, a Sony model HDC-750a, along with an auxiliary camera, an Insite Orion mounted on the ROV's upper pan/tilt unit. The short-baseline configuration used two auxiliary cameras, the Insite Orion and a MSC 2000, both mounted on the upper pan/tilt unit. In the event of the temporary loss of the target from one of the two camera images, the system defaulted to single camera ranging, based on the assumption of constant target pixel area over brief periods of time [6].

The equation used for stereo ranging calculates the least-squares minimum distance between rays defined by the target location in each stereo image [54].

$$\rho_1 = \frac{t^T \xi_1 - \xi_1^T R \xi_2 t^T R \xi_2}{1 - (\xi_1^T R \xi_2)^2} \quad (3.1)$$

Here the variables  $\xi_i$  are the bearing vectors for the target, as viewed from each of the cameras, labeled camera 1 and camera 2. The translation vector  $t$  and the rotation matrix  $R$  are the extrinsic parameters that relate camera 2 to camera 1. Extrinsic camera parameters were calibrated in advance using a calibration target. Radial lens distortion, an intrinsic camera parameter, was modeled using a third order radial distortion curve, assuming square pixels and a centered pixel array. The intrinsic camera calibration was performed in dry air; the calibration did not account for the refraction effects of water. This difference was assumed, to first order, to introduce a simple scaling factor on the estimated target range.

### 3.6.3 Lighting

Although photons penetrate as deep as 1000 m into the ocean, very little light passes beyond the first 100 m. The ROV carries its own light sources for all video applications. The primary light sources are six SeaArc 2 Daylight High Intensity Discharge (Metal Halide) arclamps. These lights were arranged either for midwater viewing, with all lights pointed forward (Figure 3.5), or for mixed benthic-midwater operations, with two lights pointed forward and four pointed downward. Orientation of each light source was adjusted by hand prior to an ROV dive. Because light source

orientation was not carefully calibrated (and, in general, is not carefully calibrated before most midwater dives), the lights form an unstructured illumination pattern. In addition to the six arclamps attached to the vehicle frame, a seventh incandescent light source was attached to the upper pan/tilt unit, beside the Orion Insite and MSC 2000 cameras.

---

## 3.7 Secondary Sensors

In addition to the primary visual sensors, the jelly-tracking system makes use of several secondary sensor signals.

### 3.7.1 Camera Angle Sensors

The pilot can manually adjust the angles of the main camera and the auxiliary cameras. A set of Hall effect sensors measure the offset of the main Sony HDTV camera from a straight-forward position. Potentiometers in the upper pan/tilt unit likewise measure the angle of the auxiliary cam-

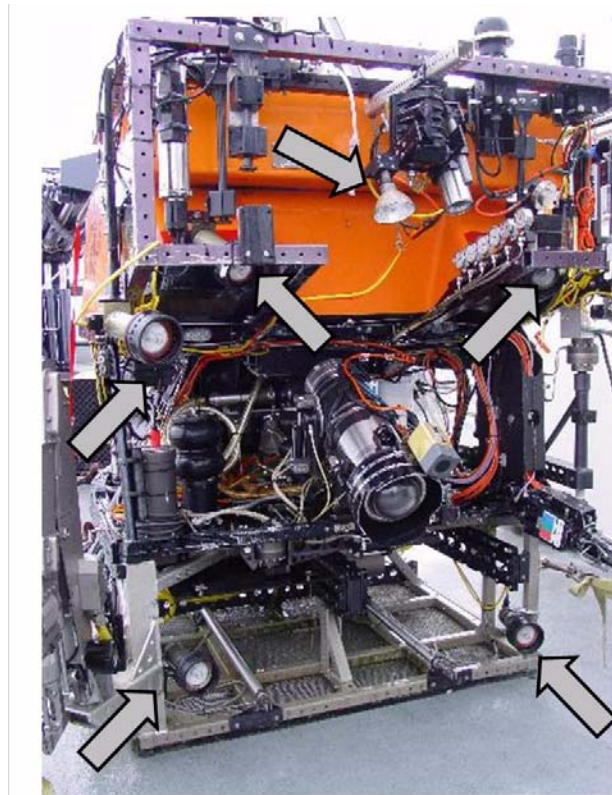


**Figure 3.5 ROV *Ventana*'s Lighting System**

eras' optical axes relative to the vehicle's fore-aft axis. Angles sensors are required for control. They permit a transformation of target position measurements from the camera frame into the vehicle frame. Camera angle sensors also enable large-baseline stereo calculations. Because this configuration uses cameras mounted on two separate pan/tilt units, both sets of angle sensors are used to compute the rotation matrix,  $R$ , in (3.1).

### 3.7.2 Navigation Pack

A compass and a pair of inclinometers measure angles relative to magnetic north and to gravity, respectively. These angle define the rotation between the inertial frame and the vehicle frame.

### 3.7.3 Pilot Joystick Feedback

The VCC serial string also feeds back the total control signal issued to the thrusters. This signal is the sum of human and autopilot control commands along four axes: yaw, axial, lateral, and vertical. The low-frequency disturbance estimator (Figure 3.6) uses these signals to measure and compensate for the quasi-steady bias, introduced primarily by the ROV tether force.

### 3.7.4 Doppler Velocity Log (DVL)

The Ventana ROV sensor package includes an RDI Workhorse Doppler Velocity Log (DVL). The DVL signal was not used as a sensor for control during jelly-tracking experiments. The DVL signal does have use, however, for future science missions. The DVL senses the doppler shift of an acoustic ping bounced off particles suspended in the water column or, if it is within range, off the ocean floor. The doppler shift, in turn, indicates the vehicle's velocity relative to the scatterer, either the ocean bottom or the water column.

---

## 3.8 Feedback Control

An important contribution of this research project involves the introduction of custom controller for the jelly-tracking application. Whereas Chapter 5 develops the control design in detail, this section offers a brief overview of the control software component.

Control software operates on the vision signal to keep the animal target centered on the camera axis at a reference range. Figure 3.6 presents a block diagram for the control software and shows the relationship of the control component to sensor input signals, including both the primary vision sensor and the secondary sensors. As a reasonable approximation, the ROV behaves as a damped second order inertia. Classical control techniques, therefore, address the primary requirements for the design of an ROV-based tracking law. Practical details of the control-law implementation, however, augment software complexity. Specifically, three important issues motivate enhancements to a generic baseline control law: (1) the definition of a control objective for a sensor that measures only 3 DoF motion relative the target animal, (2) optimization of the 4 DoF thruster map to exploit the null space orthogonal to the control-objective, and (3) the rejection of large disturbance forces that threaten to carry the target outside the boundaries of the camera viewing cone.

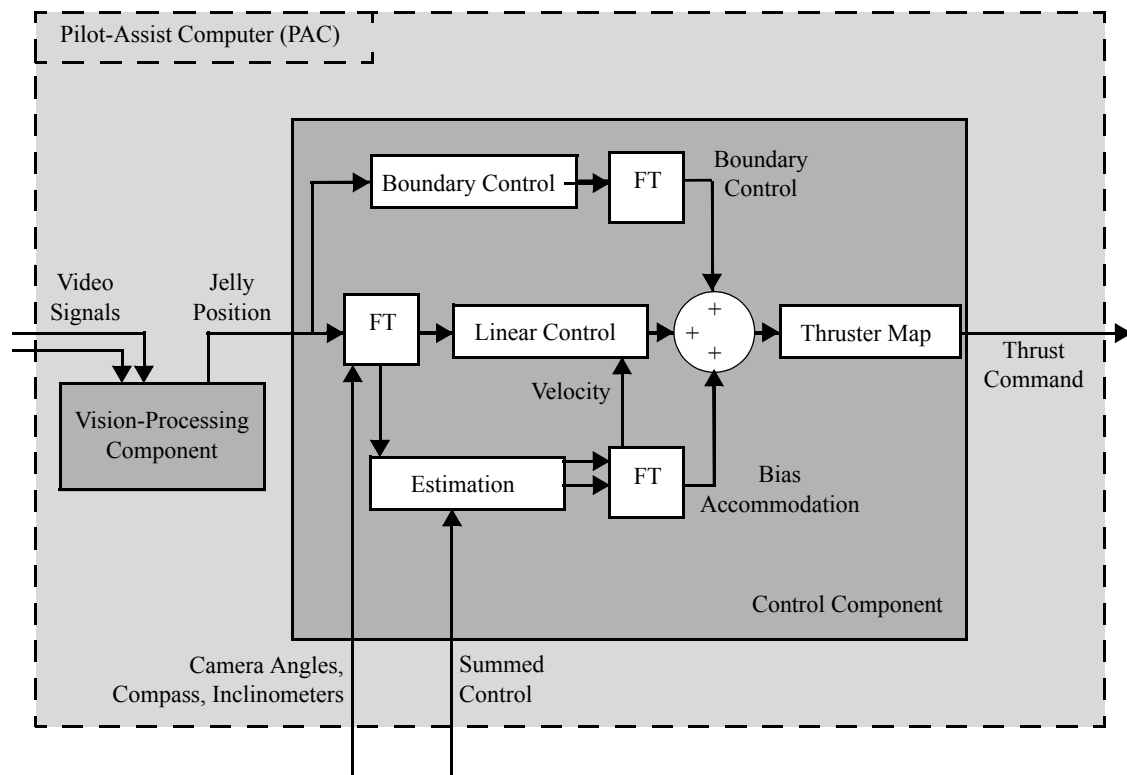


**Figure 3.6 Control Component**

*The block diagram illustrates the pilot-assist computer and the details of the control component. The abbreviation FT denotes a frame transformation block. See also the corresponding diagram, Figure 3.3, which shows the detailed blocks within the vision-processing component.*

The first issue affects the linear control block illustrated in Figure 3.6. With its pitch and roll motion regulated by a passive stability moment, the ROV plant exhibits motion in its four remaining DoFs. The visual sensor, however, detects only its three DoF translation relative to the target. The three DoF relative position signal contains, in fact, sufficient information to close the jelly-tracking loop. In designing the control system, a challenge resides in decomposing the dynamic system to a form compatible with this lower dimensional control objective. As described in Chapter 5.2, a modified cylindrical transformation is employed to decompose the ROV dynamics into a range space associated with the control objective and into an orthogonal null space.

The second issue, that of null space design, involves the thruster map block of Figure 3.6. The thruster map transforms the control input from control-objective form into a form consistent with the requirements of the *Ventana* Control Computer. The thruster map also augments the dimension of the control-objective command from three DoF to four DoF. Thus, the design of the thruster map introduces the challenge of choosing a thrust command in the control-objective null space. Chapter 5.3 considers two means of exploiting the null space to accomplish secondary system objectives: (1) to minimize total thruster forces and thereby reduce the chances of disturbing

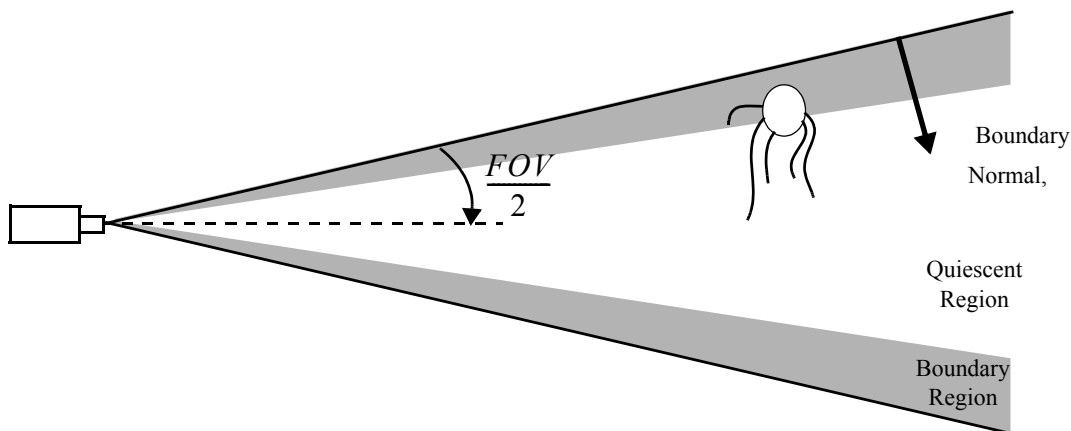


**Figure 3.7 Viewing Cone Boundaries and Nonlinear Boundary Control**

*Cameras used for visual servoing have a limited viewing cone, defined by the field-of-view angle (FOV). If a strong disturbance on the ROV pushes the target animal into the shaded boundary region, the nonlinear boundary control term provides aggressive control to return the target to the quiescent central region. Boundary control action reduces the risk that an out-of-frame event interrupts the vision positioning signal.*

the behaviors of the target animal or (2) to permit non-interfering shared control between the human pilot and the automated controller.

The third issue, that of rejecting large disturbances before the target animal leaves the camera image, involves the boundary control and estimation blocks of Figure 3.6. The basic linear controller is designed to track changes in the motion behavior of the target animal. Linear control gains are designed low to reject repeated periodic animal motions and sensor noise with the goal of minimizing hydrodynamic motions which might disturb animal behavior. Consequently, the linear control block does not act aggressively enough to counter large disturbance forces on the ROV which might displace the target outside the sensing volume, called the camera viewing cone (illustrated in Figure 3.7). Chapter 5.4 augments the baseline linear controller with two additional control terms, a boundary-control term, that activates at the edges of the viewing cone, and a disturbance-accommodation term, that uses an estimator to measure quasi-steady bias forces on the ROV. These terms help manage low and high-frequency disturbance forces, respectively.

---

## 3.9 Summary

This chapter described the system used for automated jelly-tracking experiments. The unmanned submersible, ROV *Ventana*, serves as the primary system component. MBARI owns and operates both this robotic vehicle and its support ship, the R/V Point Lobos. A pilot-assist computer, located in the control room of the support ship, accomplishes all processing required for jelly tracking. Control commands issued via a serial link by the pilot-assist computer interface with the main *Ventana* control computer. This computer sums automated controller commands with joystick commands from the human pilot before sending them through the umbilical to the submerged ROV. A stereo camera pair, mounted on the ROV, provides target position data to enable station keeping relative to the animal. Additional sensors, including camera angle sensors, a compass, and inclinometers, are used to define a jelly-fixed frame. Jelly tracking software for vision-processing and control acts to interpret these sensor data to produce thruster commands.





*We should be spending more time looking at patch dynamics and less time, on average, worrying about averages.*

- W.M. Hamner, 1988 [43]

---

This chapter presents a vision algorithm that enables reliable automated jellyfish tracking using the experimental system introduced in the previous chapter. Discussion focuses on algorithm design.

Introduction of a novel performance assessment tool, called segmentation efficiency, aids in matching potential vision algorithms to the jelly-tracking task. This tool uses a model of segmentation to assess quantitatively the image statistics employed by various processing methods. In comparison with other evaluation techniques, this technique offers two advantages. First, the method simplifies analysis by assuming a decoupling of tracking into an application-specific segmentation subcomponent and into a more general-purpose recognition subcomponent. Second, the method evaluates a single, general model, rather than a multitude of specific segmentation algorithms, in order to reduce the implementation effort required of the design engineer.

In the context of jelly-tracking, this tool is applied to the segmentation of transparent animals under uneven illumination in particle-filled scenes. The result is the selection of a fixed-gradient, threshold-based vision algorithm that requires no in-the-field parameter tuning. Additional analysis assesses the sensitivity of the reliable-recognition assumption and defines an effective operational envelope for field jelly tracking. Field experiments further validate the capability of this algorithm to track successfully a wide variety of animal subjects viewed under unstructured lighting conditions.

---

## 4.1 Introduction

Human ROV pilots easily identify and track gelatinous animals displayed on a video monitor. In principle, a simple software algorithm should enable automation of this visual jelly-tracking activ-

ity. In practice, the robustness requirements for field operations make construction of an appropriate software algorithm a challenge. The vision software must track a deformable, transparent target against an uneven, cluttered background. The software must reliably detect a wide range of different animal species under different lighting conditions. Furthermore, to enable reliable long-duration tracking, the software must consistently identify the target in each successive frame. Synthesizing an algorithm with all these characteristics and validating the algorithm's reliability are goals of this research.

### 4.1.1 Background

A very large number of existing algorithms, drawn from the vision literature, provides a basis for the construction of a jelly-tracking vision system. Unfortunately, no mechanisms exist to predict the performance of a particular vision method in processing a video clip for a particular application. This chapter attempts to fill this gap by introducing the segmentation efficiency method, a new approach for the design of vision-tracking algorithms for natural-environment applications.

The primary concept of the new design approach involves the decomposition of the tracking process into two subcomponents: segmentation and recognition (see Figure 4.1). The segmentation component analyzes each new video image to detect regions, or segments, of related pixels. The recognition component performs an operation to identify the segment that best matches the tracked target. This output establishes a two-dimensional target position (which can be upgraded to a three-dimensional vector through a ranging technique like stereo, as described in Chapter 3.6.2). The segmentation-efficiency design procedure assumes that the information required to cluster groups of pixels into segments is application-specific, but that the information required to perform recognition consists of general-purpose statistics, evaluated over each segment. In effect, this assumption assumes recognition reliability and places the burden of robust tracking on the segmentation component.

This emphasis on the application-specific nature of segmentation processing earns the new design procedure its name: segmentation efficiency. A segmentation efficiency metric assesses the ratio (efficiency) of correct pixel classification, in a segment-area weighted sense, across a ground-truthed image. The metric is evaluated for various image processing filters (color, gradient, optical flow, etc.) over various topologies (large areas and narrow edges) that model broad

classes of segmentation processing. Segmentation strategies belonging to classes with high efficiency offer the strongest potential for robust segmentation.

The assumption of general-purpose recognition processing and its decomposition from application-specific segmentation well suits the jelly-tracking design problem. Under typical conditions, the application-specific demands of jelly-tracking arise primarily from segmentation processing. The segmentation algorithm must reliably identify pixels associated with the target animal in successive image frames regardless of uneven lighting, background clutter, target transparency, deformations or rotations. The stress on the recognition component is low by compari-

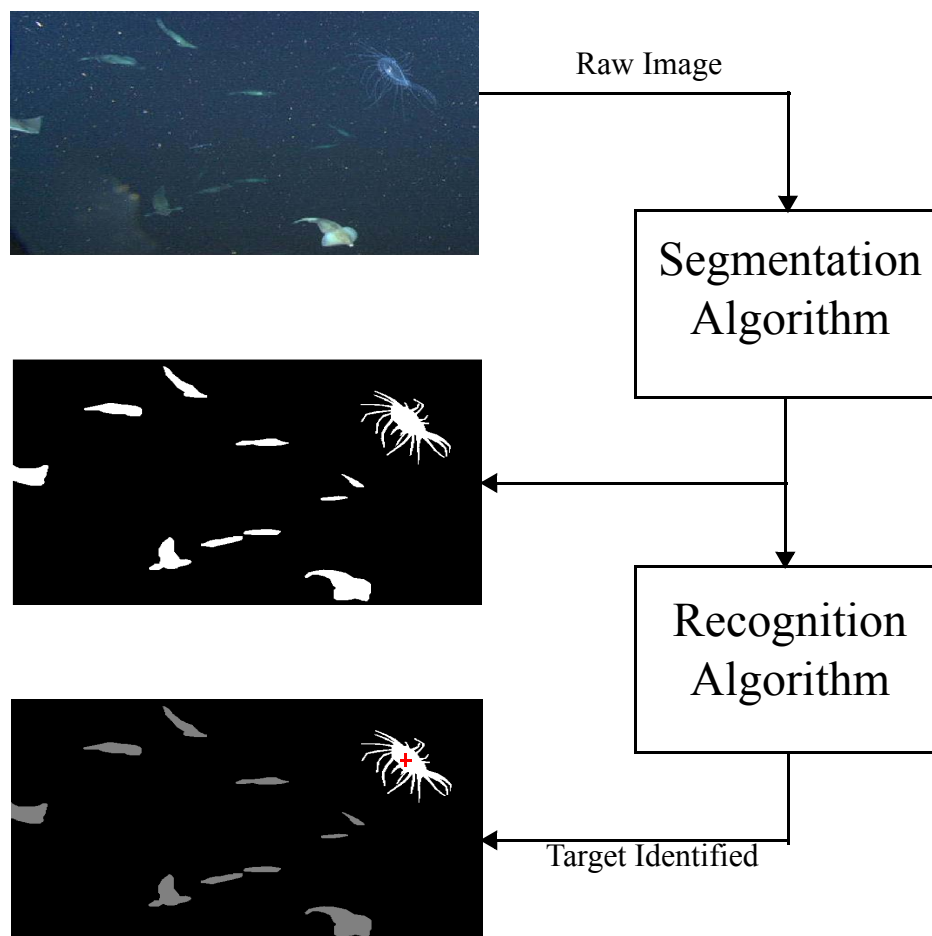


**Figure 4.1 The Two Subcomponents of Visual Tracking: Recognition and Segmentation**

*In general, visual tracking algorithms perform both segmentation and recognition operations, either sequentially or iteratively. Segmentation is the process of clustering pixels to identify possible target regions (or segments). Recognition evaluates those candidates to identify the most likely target segment (marked with a crosshair).*

son, as midwater jellies are generally encountered as individuals, distant from other members of the same species (Chapter 2). Given the sparseness of similar animals encountered under normal operating conditions and the relatively short sample period (0.1 s), in comparison to the time scale of jelly motion, simple statistics, like last-reported position, provide strong information on which to base the recognition subcomponent of the jelly-tracking algorithm.

Since few segmentation methods perform consistently for different jelly specimens and different lighting conditions, the segmentation efficiency technique offers a means of assessing a large number of processing strategies for a minimal designer workload.

### 4.1.2 Related Work

This section provides an overview of the two major topics relevant as background to the chapter: (1) related work in experimental visual servoing and (2) related work in performance evaluation of vision algorithms.

#### **Related Work in Visual Servoing**

The visual jelly-tracking application falls within the broad research area known as position-based visual servoing. The term *visual servoing* implies the use of video as a sensor for automatic control. In many cases, including the jelly-tracking application, visual servoing requires the use of a *visual tracking* algorithm. Visual tracking algorithms are designed to follow projected objects through a 2D video sequence, without any implication of closed-loop motion control of the imaging platform. Visual tracking algorithms implicitly or explicitly address two related imaging problems: segmentation and recognition. The segmentation process clusters pixels into regions that may correspond to the tracked object, while the recognition process distinguishes among these regions to identify the best match to a target profile.

The field of visual servoing has spawned numerous applications. Recent publications that capture the breadth and history of the visual servoing field are [101,133]. Although these reviews of visual servoing make little mention of underwater applications, the ocean community has made substantial progress in the visual navigation of submersible vehicles relative to the ocean floor [106,108,110,111,115,116,117,120,121,124,127,131].

Almost every visual servoing solution uses a different visual tracking strategy tailored to the nature of the application. The tracking design problem is most straightforward when the target can

be modified by the addition of visual markers. For example, Leahy *et al.* enabled visual servoing for aircraft refueling by placing easily identified white markers near the fuel port [114]. Amidi *et al.* report helicopter experiments that identified a ground target using color segmentation or template-based detection [95]. In many applications, the design problem cannot be streamlined by adding markers to the tracking target. For these cases, the designer must identify characteristics of the target that enable reliable segmentation and recognition. Batavia *et al.* detected overtaking vehicles in a car's blind spot by propagating an edge map of the background scene and comparing this prediction to the current measurement [96]. Minami *et al.* used a triangular template strategy to track a fish in a tank using a robotic manipulator [119].

The rich variety of visual tracking methods employed by each of these cases implies that the selection of a reliable visual tracking algorithm for a new application is nontrivial. In fact, for most visual servoing applications, several tracking algorithms produce viable solutions (of varying quality). This freedom in algorithm choice introduces an important design question, central to this chapter. The designer of a visual servoing system must somehow assess the match between tracking algorithms and the visual environment characteristic to an application.

This chapter discusses a method for synthesizing a robust and efficient vision strategy for endurance tracking of a single gelatinous animal. Prior to this work, no attempt has been made to implement such an experimental visual servoing system, despite the opportunity such a platform offers to extend the science of marine ecology. The lack of published data regarding visual tracking of gelatinous animals, along with the differences between the imaging environments for this application and for other terrestrial, aerial, and marine visual servoing applications, motivates a thorough characterization of the deep-ocean imaging environment. Midwater images depict natural, unprepared scenes. Such scenes do not contain man-made features, like corners or straight lines, nor can an observer artificially augment the scene without disturbing the animal behaviors under study.

These issues somewhat resemble problems encountered by Tang, Fan, Kocak and others in their pursuit of automated systems for the visual detection and classification of marine plankton [105,112,125,128,129,130,134]. Nonetheless, the jelly-tracking problem possesses additional characteristics that distinguish it. In particular, light source geometry for remotely operated vehicles (ROVs) changes dramatically from dive to dive. On any given dive, spatial lighting gradients are visible, in addition to temporal derivatives resulting from pan/tilt motion, light source oscilla-

tions, and variations in concentration of suspended organic matter, known as marine snow. The automated jelly-tracking system must function despite these noise sources.

The vision algorithm must also rise to meet the two key challenges for field operation: tracking reliability (for ROVs and AUVs) and energy efficiency (for AUVs). To meet the reliability requirement, mean-time-to-failure for the vision system must match the application duration, measured in hours for ROV deployments and in days for AUV deployments. Also, the system must display low sensitivity to prior selection of algorithm parameters. The segmentation efficiency tool addresses these issues by assessing the reliability and parameter sensitivity of various vision-processing strategies.

Although this chapter focuses primarily on the reliability challenge for ROV deployment, the segmentation efficiency approach does permit a degree of flexibility to address the energy efficiency challenge (for AUV deployment). Specifically, choosing a processing algorithm with a low operations count can enable the use of a low-power DSP chip rather than a higher power, higher speed processor. In this sense, computational efficiency equates with energy efficiency.

In the context of the robustness challenge and, to a lesser degree, the AUV energy efficiency challenge, this chapter develops an algorithm for jelly tracking using the new segmentation efficiency tool. The tool identifies a category of existing vision algorithms (region-based algorithms with morphological-gradient filtering) that achieves reliability without requiring parameter tuning in the field. Within this category, a threshold-type vision algorithm was selected for its adequate noise properties and its excellent computational efficiency.

### **Related Work in Performance Assessment of Vision Algorithms**

Several recent investigations have addressed the topic of performance evaluation of vision algorithms with respect to particular data sets [97,98,102,104,132,135]. From a system-design viewpoint, these methods can aid in evaluating candidate tracking algorithms to enable long-duration, reliable tracking for a new application. These methods, however, require implementation of all algorithms to be evaluated, a characteristic that limits the size of the practical search space and greatly increases the design workload. To provide true utility as a design tool, an evaluation method must characterize reliability without demanding high implementation overhead on the part of the user. This chapter introduces a new characterization approach that reduces implementation overhead by focusing on the input, rather than the output, of visual tracking algorithms.

From a designer's point of view, implementing existing assessment techniques requires substantial effort. First, to evaluate a number of tracking algorithms, the designer must implement all of the possibilities, often a time-consuming procedure. Second, the designer must modify the algorithm to accept a wide range of possible image filters that may enhance signal-to-noise ratio for the application specific visual environment. Third, the designer must ground truth image sequences in order to apply the metric. The resulting design procedure is combinatorially large. For the case of  $P$  alternate prefilters,  $Q$  vision algorithms, and  $M$  image sequences, each sequence containing  $N$  frames, the procedure requires that the designer implement a total of  $P \cdot Q$  algorithms and ground truth a total of  $M \cdot N$  frames. The assessment procedure must then analyze  $M \cdot N \cdot P \cdot Q$  image frames. The resulting combinatorial explosion is depicted by Figure 4.2a.

The new segmentation efficiency design approach focuses not on the specific *output* of individual tracking algorithms but on the image-statistics describing the *input* to related sets of tracking algorithms. The input-focused approach greatly reduces implementation overhead, because the designer need not implement code for the  $P \cdot Q$  algorithms under consideration. The segmentation efficiency approach enables further reduction in the overhead for tracking-system performance evaluation by focusing specifically on the segmentation component of the tracking algorithm and by suppressing analysis of the recognition component. This reduces the number of ground truth images required from  $M \cdot N$  to  $M$  (one for each video clip) and the number of frames analyzed to  $M \cdot P$ . These improvements are summarized by Figure 4.2b.

Certain characteristics of the jelly-tracking application permit the analysis of the recognition subcomponent to be decoupled and suppressed in the overall system reliability assessment. These characteristics are embodied by a pair of assumptions which generally describe the ROV-based jelly-tracking activity.

**Assumption 4.1.** Short Sample-Period Assumption: The sample period is shorter than the time scale of animal motion (typically on the order of seconds for gelatinous animals). Thus image statistics for the target segment change little between successive frames. Specifically, target position, size, shape and brightness over the target segment remain quasi-invariant from one frame to the next.

The short sample-period assumption states that target segment properties *do* change over time, but that the individual changes are small from one time step to the next. Because accumulated

changes over time may be substantial, an accurate segmentation is required at each successive time step, so that the target statistical profile can be accurately updated through time.

The amount by which generic target segment statistics may change between frames depends on the density of similar targets observed in the tracking environment. For the jelly-tracking activity, animal targets are infrequently seen together in the same video image.

**Assumption 4.2.** Target Species Sparsity Assumption: Animals of similar visual characteristics are infrequently observed together in an image. Thus the slowly varying, generic statistics available through the short sample period assumption permit reliable correspondence of the target across subsequent image frames.

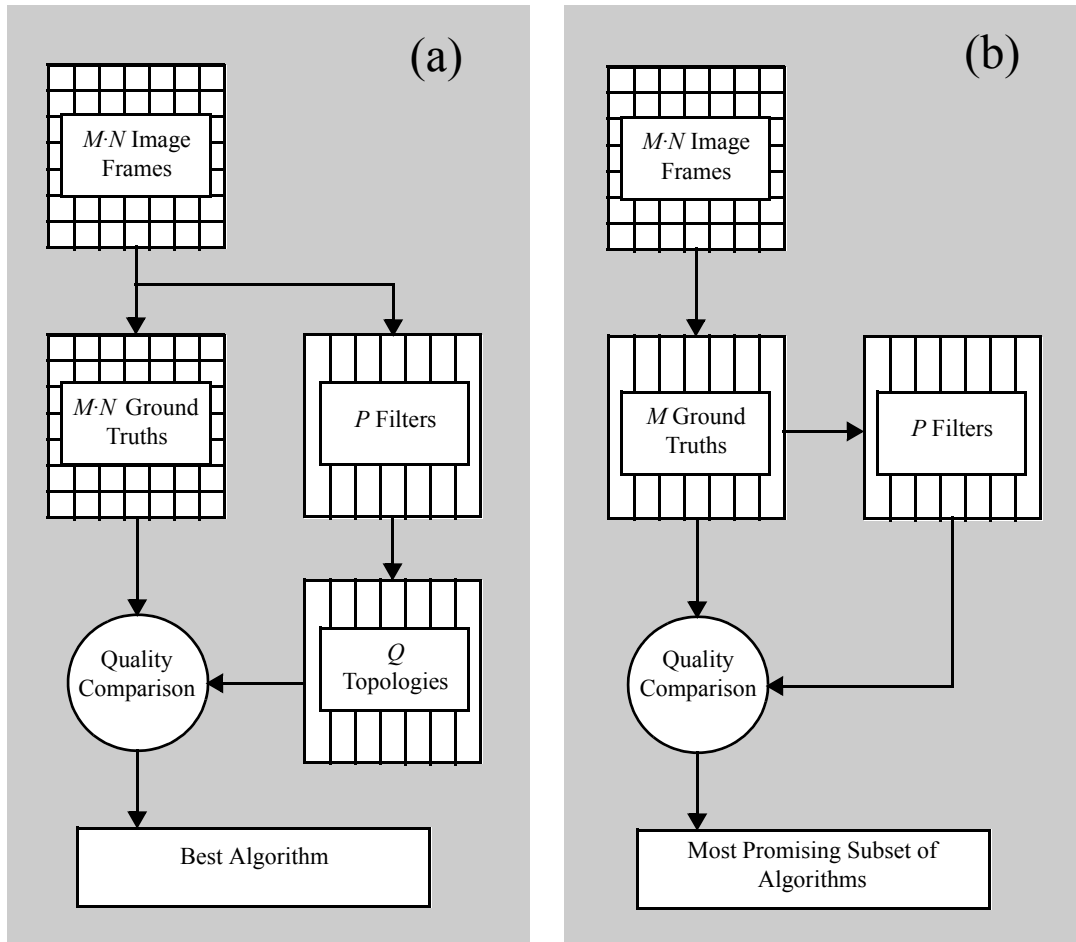


**Figure 4.2** Comparison of Performance Assessment Methods for Visual Tracking

*Comparison of processing and preparation requirements for (a) existing assessment techniques and (b) a new input-focused technique. Analysis considers application of  $P$  prefilters and  $Q$  tracking algorithms to a database consisting of  $M$  image sequences, each with  $N$  frames.*



These two assumptions regarding short sample period and the sparsity of the animal population together imply that generic segment statistics provide sufficient information to reliably perform interframe recognition. Thus these assumptions imply that recognition reliability is high, as long as a consistent, reliable segmentation processing technique is employed to keeps the recognition profile up-to-date and to prevent error accumulation in the recognition profile over time.

Given the two above assumptions, the major challenge in visual tracking, then, involves the design of a robust segmentation process that reliably distinguishes target pixels from background pixels. The segmentation technique must operate for any of a variety of animal species subject to nonuniform lighting conditions and to marine-snow noise.

The following section, Section 4.2, develops segmentation efficiency as a technique for design of a reliable segmentation subcomponent. Segmentation reliability results in reliable vision-tracking in the context of the above assumptions, which imply high reliability for the recognition component. Section 4.3 describes the application of the segmentation efficiency analysis to design a specific vision-processing method tailored to the jelly-tracking application. This algorithm was deployed as a critical component of the experimental ROV-based tracking system. Subsequently, Section 4.4 discusses the limitations of the experimentally tested tracking algorithm for very long duration AUV applications. Recognition system analysis becomes significant for this task, as the sample rate assumption (Assumption 4.1) may not hold for long-duration AUV deployment. Finally, Section 4.5 summarizes the salient results discussed in this chapter.

---

## 4.2 Segmentation Efficiency

The new input-focused design strategy, called segmentation efficiency analysis, focuses on performance assessment of the segmentation subcomponent of vision-tracking algorithms. Implementing this design approach requires a metric to assess segmentation input data. To assess input data, this section first proposes a model of the segmentation process, consisting of a topological processing strategy and a filtering strategy. From this model follows a metric that tallies the total number of correctly identified pixels, weighted by region area, over the target and background segments defined by a choice of topological processing and filtering strategies. Results for individual images may be grouped for a large image database to compute an ensemble-averaged segmentation efficiency metric. The ensemble-averaged metric thus indicates the best combinations of filtering and topology processing strategies to provide reliable segmentation for a reference database.

### 4.2.1 Modeling Segmentation Algorithms

Evaluating the image data on which segmentation algorithms operate requires a generalized model that describes the processing structure of diverse segmentation algorithms. For the purpose of analyzing segmentation input, all segmentation algorithms may be described as methods that combine two types of processing: filtering and topological clustering. Segmentation algorithms use filters to extract information about individual pixels or local pixel groups. (Sample filters include luminance, color, texture, gradients, and optical flow.) Segmentation algorithms use topological clustering to group pixels together in specific patterns. (Two primary topologies are considered here: regional topologies, consisting of all the pixels in a closed set, and edge topologies, consisting of the boundary pixels of the target region.)

The following two subsections describe methods that quantitatively describe the filtering and topological clustering operations. The segmentation efficiency metric, defined subsequently, evaluates the ability of various filters and topologies to distinguish between target and background pixels.

#### Filtering for Segmentation

Segmentation algorithms use pixel level filtering to extract or emphasize particular components of the video stream. This section describes fifteen filters chosen to form a partial basis for the space of pixel-level information. Table 4.1 lists the fifteen filters and their formulae. Since these filters are commonly described in introductory imaging texts such as [109], this section offers only a cursory outline of the notation used in Table 4.1.

The expression  $f^k(x,y)$  denotes the value of a filtered image at pixel location  $(x,y)$  for the  $k^{\text{th}}$  frame of a video sequence. Base images are defined as 24-bit color frames consisting of three color components,  $c_r$ ,  $c_g$ , and  $c_b$  (each defined, for the jelly-tracking application, on the domain  $D_f$  of  $320 \times 240$  images). As most filters are defined at a single time step, the  $k$ -superscript is generally suppressed, except for the few filters (like optical flow) which operate on changes between successive images.

The notion of Table 4.1 includes the  $\Delta f / \Delta x$  and  $\Delta f / \Delta y$  operators, which denote the spatial central difference for approximation of the first derivative. The  $**$  operator indicates a two-dimensional image convolution. For smoothing operations, the convolution kernel,  $h$ , was chosen to be the  $3 \times 3$  uniform kernel. The size of this and other kernels were chosen to produce good

results. In general, kernel size could be consider an additional parameter in defining the filter space.

The morphological operators for erosion ( $\ominus$ ) and dilation ( $\oplus$ ) are defined as follows:

$$\begin{aligned}(f \oplus q)(x, y) &= \max \{f(x + m, y + n) \mid (x + m, y + n) \in D_f \text{ and } (m, n) \in D_q\} \\ (f \ominus q)(x, y) &= \min \{f(x + m, y + n) \mid (x + m, y + n) \in D_f \text{ and } (m, n) \in D_q\}\end{aligned}\quad (4.1)$$

Symbol	Filter	Equation
$c_r$	Red	
$c_g$	Green	
$c_b$	Blue	
$l$	Luminance	$l = [0.30 \ 0.59 \ 0.11] [c_r \ c_g \ c_b]^T$
$\ \nabla l\ _2$	Euclidian Gradient	$\ \nabla l\ _2 = \sqrt{\left(\frac{\Delta l}{\Delta x}\right)^2 + \left(\frac{\Delta l}{\Delta y}\right)^2}$
$\ \nabla l\ _{2,s}$	Smoothed Euclidian Gradient	$\ \nabla l\ _{2,s} = \ \nabla l\ _2 ** h$
$\ \nabla l\ _M$	Morphological Gradient	$\ \nabla l\ _M = (l \oplus q) - (l \ominus q)$
$\ \nabla l\ _{M,s}$	Smoothed Morphological Grad.	$\ \nabla l\ _{M,s} = \ \nabla l\ _M ** h$
$\ \nabla l_{oc}\ _M$	Snowless Morphological Grad.	$\ \nabla l_{oc}\ _M = (l_{oc} \oplus q) - (l_{oc} \ominus q)$
$\nabla^2 l$	Laplacian	$\nabla^2 l = l ** \begin{bmatrix} 0 & 1 & 0 \\ 1 & -4 & 1 \\ 0 & 1 & 0 \end{bmatrix}$
$\nabla^2 l_s$	Smoothed Laplacian	$\nabla^2 l_s = \nabla^2 l ** h$
$d_t$	Time Difference	$d_t = l^k - l^{k-1}$
$d_b$	Background Difference	$d_b = l - \hat{l}_b$
$\ p\ $	Optical Speed	$\ p\  = \sqrt{u^2 + v^2}$
$\angle p$	Optical Flow Direction	$\angle p = \text{atan2}(u, v)$

TABLE 4.1. Types of Filtering

Effectively the dilation operator enlarges bright regions of a grayscale image, while the erosion operator shrinks them. These morphological filters require a structuring element,  $q$ , with domain  $D_q$ . For this work, structuring elements were chosen with a domain of 3 x 3 pixels. Erosion and dilation operations are used to compute the morphological gradient and to create the snowless luminance image. The snowless image results from the application of a successive morphological operations called *opening* and *closing*, operations which together remove small speckles, like marine snow, from an image. The opening operation ( $\circ$ ), which removes small islands and peninsulas of image brightness, and the closing operation ( $\bullet$ ), which fills in small dark holes surrounded by bright pixels, are defined as:

$$\begin{aligned} f \circ q &= (f \ominus q) \oplus q \\ f \bullet q &= (f \oplus q) \ominus q \end{aligned} \quad (4.2)$$

Given these definitions, the snowless image,  $l_{oc}$ , is described by the following equation:

$$l_{oc} = (l \circ q) \bullet q \quad (4.3)$$

The local pixel velocities,  $u$  and  $v$ , were computed using the optical-flow conservation equation for local luminance, along with a least squares constraint. The technique solved the following equation in a least squares sense over a 5x5 support region.

$$\begin{bmatrix} \left( \frac{\Delta f}{\Delta x} ** h \right) & \left( \frac{\Delta f}{\Delta y} ** h \right) \end{bmatrix} \begin{bmatrix} u \\ v \end{bmatrix} = -d_t \quad (4.4)$$

The **arctan2** operation, which extracts the direction of the optical flow vector, is the arctangent operator defined with the full four quadrant range,  $-\pi$  to  $\pi$ .

The background difference filter,  $d_b$ , is the difference between an image and a model of the background-lighting field. Generating the background-lighting image requires that an external agent first describe a bounding box around the target, so that the target may be excluded from the background image. Pixels in the box-shaped hole are then interpolated to form the estimate of the background image,  $\hat{l}_b$ . Although cubic spline interpolation is often implemented for hole filling, this work instead interpolated using the solution of the heat equation over the hole,  $\Omega$ , given the Dirichelet boundary condition of the original image pixel values (“temperatures”) around the hole.

$$\begin{aligned}\nabla^2 \hat{l}_b(x, y) &= 0 \text{ in } \Omega \\ \hat{l}_b &= l \text{ on } \partial\Omega\end{aligned}\tag{4.5}$$

The solution of the heat equation resulted in smooth, diffusion of the boundary pixel values into the hole interior. The heat equation was solved using a standard separation of variables technique which resulted in an orthogonal basis for the heat equation [99]. Interpolation results comparable with those of a cubic-spline fit were obtained using an approximate solution based on the first two harmonics of the heat-equation superposed with a bilinear function. The resulting technique requires solving for only 12 coefficients (compared with 16 for the cubic spline method) and, because of the orthogonality of its terms, avoided the need to compute a matrix pseudoinverse.

### Topological Clustering

Segmentation algorithms use topological clustering to group filtered pixels into sets. Most often, segmentation methods are named for their topological processing subcomponent; however, the complete segmentation algorithm consists of both local filtering and topology processing.

Typically, topological clustering methods identify either edges or regions. Edge-based methods distinguish between nonboundary pixels and pixels along the target boundary. Region-based methods classify pixels as members of either the closed set of target pixels or as members of the complementary background pixel set. A few hybrid methods combine both region and edge topologies. Table 4.2 lists selected topological clustering algorithms in three categories, as edge-based, region-based, and hybrid methods.

Region-based topological clustering methods include well known techniques like (1) the expectation maximization technique, which clusters pixels under an arbitrary number of parameterized ellipses; (2) the template masking technique, which scales and aligns a template to maximize pixel contrast interior and exterior to the template; (3) threshold techniques, which cluster neighboring pixels above or below a selected threshold; and (4) the correlation technique, which assesses correspondence between a reference image and the current video frame.

Edge-based topological clustering methods listed in Table 4.2 include (1) active contour techniques, which solve a dynamic equation for the target boundary based on a forcing function derived from an edge image; (2) convex edge-merging methods, which group edges based on the

assumption of a convex target; and (3) Hough transform methods, which extract boundaries from an image given a parameterized contour shape.

Finally, Table 4.2 lists two hybrid segmentation methods, which combine both edge-based and region-based decision criteria. These hybrid techniques include (1) region-merging methods, which join neighboring pixels of similar value, and (2) watershed methods, which filter out internal edges by joining neighboring pixels sharing a common level-set boundary.

In order to model the effects of topology on segmentation performance, these three classes of topology processing must be quantitatively linked to pixel geometry. Each topology processing strategy is defined by a combination of two pixel sets, which can be described generically as  $g_A$  and  $g_B$ . To describe a region-based topology, for instance, requires the definition of the two pixel sets  $g_t$ , the set of pixels over the entire target segment, and  $g_b$ , the complementary set of image pixels which describe the background around the target. To describe edge-based topologies requires the definition of  $\partial g_t$ , the set of exterior-boundary target pixels, and  $\partial g_b$ , the set of interior-boundary background pixels. Small operator error in the ground truthing process may introduce

Topology	Processing Method	Pixel-Level Distinction	Shape Assumptions
Region	Expectation Maximization (EM) over elliptical regions	Ellipse interior vs. exterior	Union of ellipses describes target
	Template Masking	Mask interior vs. exterior	Target shape known
	Threshold	Blob interior vs. exterior	No shape assumptions
	Adaptive Threshold	Blob interior vs. exterior	No shape assumptions
	Correlation	Under reference image vs. outside it	Target shape described by reference image
Edge	Active Contours (Snakes)	Edge vs. non-edge pixels	Target contour connects edges with minimum length and curvature
	Convex Edge Merging	Edge vs. non-edge pixels	Target contour connects convex region
Hybrid	Hough Transform	Edge vs. non-edge pixels	Target shape known
	Region Merging	(1) Initial seed: pixels interior vs. exterior to an amorphous region; (2) Termination Criterion: edge vs. non-edge pixels	Target shape arbitrary, but characterized by well defined edges at regional boundaries
	Level-Set / Watershed	As above	As above

TABLE 4.2. Topology Processing Algorithms

noise in this definition of the target boundary. Also, some filters cause migration of edge information. To make edge-topology assessment more robust to these effects, comparisons of the interior target or background regions to their boundaries,  $g_t^\circ$  to  $\partial g_t$  or  $g_b^\circ$  to  $\partial g_b$ , are also used to assess edge-based topological clustering methods.

For the purposes of analysis, an external agent must supply a segmentation ground truth from which to construct these topological pixels sets. The external agent, which may be a reference segmentation algorithm or a human operator, need only distinguish between the set of pixels that belong to a target,  $g_t$ , to the background,  $g_b$ , or to a region excluded from analysis,  $g_x$ . From this ground truth, the target boundary,  $\partial g_t$ , can be automatically determined as the set of pixels interior to  $g_t$  that intersect with the dilation of  $g_b$ :  $g_t \cap (g_b \oplus q)$ . Applying a set difference between the target region and the target boundary defines the target interior,  $g_t^\circ = g_t \setminus \partial g_t$ . The background boundary,  $\partial g_b$ , and the background interior,  $g_b^\circ$ , can be automatically determined through an analogous procedure.

### 4.2.2 Segmentation Efficiency Defined

If segmentation algorithms are modeled as the synthesis of a filtering strategy and a topology-processing strategy, then a performance assessment technique can be defined to evaluate the ability of any given filter to distinguish between pixels grouped according to any topology. This section defines such an evaluation method, called segmentation efficiency, that calculates the pixel fractions correctly identified by any combination of filtering strategy,  $f$ , with a topology processing strategy based on a region pairing,  $g_A$  and  $g_B$ . The resulting metric has a value, between zero and one in magnitude, that assesses the quality of a combination of a processing strategies for a given reference image.

#### Histograms as a Tool for Analysis of Midwater Scenes

In effect, segmentation efficiency plays a similar role to the image histogram, one of the primary tools used for segmentation analysis. Classically, researchers have used bimodal histograms to establish thresholds between cleanly separated peaks associated with a pair of image regions. As early as 1972, Chow and Kaneko derived the optimal segmentation threshold given a bimodal histogram and the assumption of equal weight for misclassification of pixels from either region [100]. The importance of pixels in the two segments is not always equal. A two-objective optimization

surface called the receiver operating characteristic (ROC) curve is often employed to express the trade-offs involved with differentially weighted misclassifications [98,102,103].

Despite its long history as a performance assessment tool, a histogram analysis based on a search for bimodal peaks is not an effective method for analysis of midwater scenes. Figure 4.3 depicts a jellyfish image, selected because the brightness of the animal target clearly exceeds that of the background scene. The classifier that best distinguishes between the ground-truthed target and background regions does not align with a valley between the two dominant histogram peaks.

Two principal effects mask the target peak in this histogram. The first effect involves the multitude of histogram extrema that result from correlations among neighboring pixel values. Integration can smooth these local extrema, which appear as noise in the global histogram. The

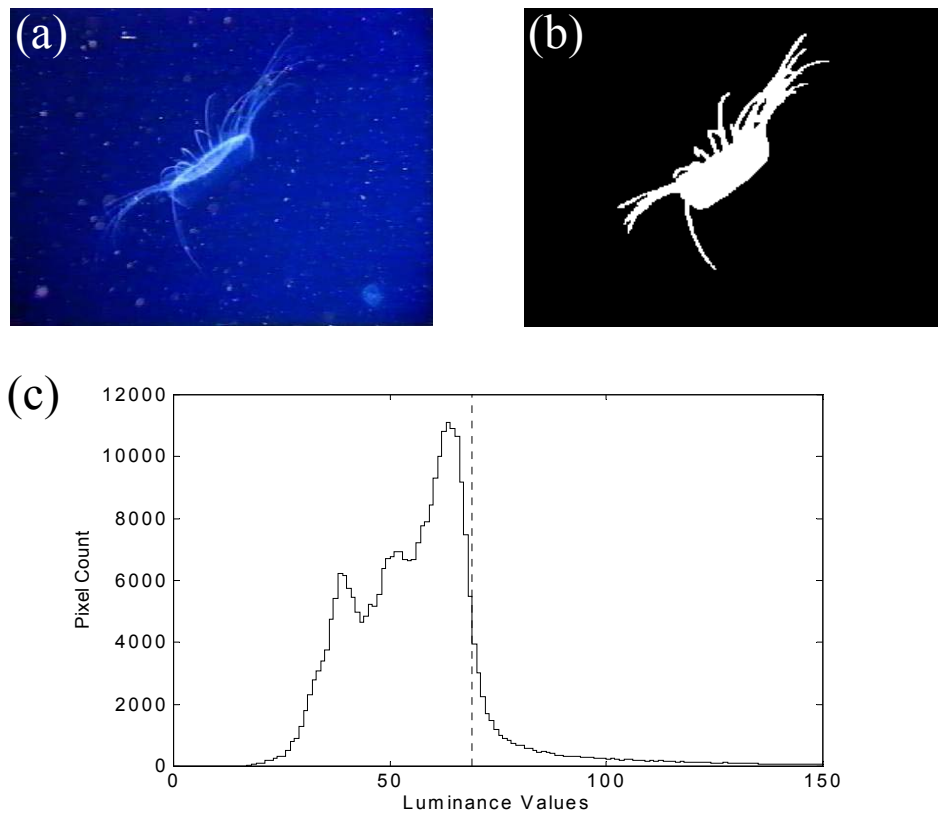


**Figure 4.3 A Luminance Histogram for a Jellyfish Image**

*Global histograms of midwater scenes provide little information to aid in evaluating the effectiveness of a filtering strategy. (a) An image of a Solmissus jellyfish was analyzed by a human operator to produce (b) a ground truth segmentation. (c) The luminance histogram of the Solmissus image counts the pixels at each gray level across the entire image. On the histogram, the vertical dashed line represents the luminance classifier that best distinguishes between pixels in the target and background regions of the ground truth image. This line does not align with any clear histogram feature.*



second effect that masks the target histogram peak involves the small pixel area of the target region relative to the background region. Global histograms do not account for the relative size of a target region. A target region containing few pixels appears as a small bump on a global histogram, indistinguishable from local extrema.

#### **Segmentation Efficiency: The $\infty$ -Norm of a Difference of Cumulative Distribution Functions**

Given the model developed in the previous section to describe segmentation processing, a metric can be defined to account for both these issues. This metric, called the segmentation efficiency metric, employs a pair of cumulative distribution functions (CDFs) defined separately, using ground truth, over both the pixel sets,  $g_A$  and  $g_B$ , that define a particular topological processing strategy. These CDFs describe the distribution of pixel values produced by a particular filter,  $f$ , over the region pair. The segmentation efficiency metric is the maximum value ( $\infty$ -Norm) of the difference of these two CDFs.

The use of CDFs, rather than histograms, addresses both the area-weighting and local noise problems. CDFs are constructed from probability distribution functions (PDFs), which are image histograms normalized by the total number of samples. Thus each PDF has an integrated value of unity. Since, in the segmentation efficiency approach, PDFs are calculated separately for the two regions to be evaluated,  $g_A$  and  $g_B$ , the process of histogram-normalization in constructing each PDF automatically solves the area-weighting problem associated with global histogram analysis. CDFs are constructed by integrating each PDF. This process smooths local extrema, solving the second issue associated with global histogram analysis.

The following equation summarizes this process of constructing each CDFs from the original image:

$$\chi(m; f, g) = \left\{ \sum_{n \leq m} \frac{H(n; f, g)}{N_g} \mid m, n \in D_H \right\} \quad (4.6)$$

Here the original histograms,  $H$ , are calculated for a filtered image,  $f$ , over each pixel set,  $g_A$  or  $g_B$ .  $N_g$  refers to the number of pixels in the pixel set.  $D_H$  refers to the set of histogram bins.

For each value of classifier,  $\delta$ , in the domain of the filter,  $D_f$ , the CDF,  $\chi$ , indicates the weighted fraction of pixels below that classifier. The difference of the CDFs for the two pixels sets that define the topology ( $g_A$  and  $g_B$ ) indicates, therefore, the total area-weighted fraction of

pixels correctly identified by that classifier. Because CDFs always have a value between 0 and 1, the magnitude of the difference of the two CDFs also has a value between 0 and 1. In this sense, the difference of the two CDFs may be considered an efficiency describing the ratio of correctly identified pixels (in an area-weighted sense) to the total number of image pixels. Hence the difference of the two CDFs is labeled the segmentation efficiency distribution,  $\eta(\delta)$ .

$$\eta(\delta; f, g_A, g_B) = \chi(\delta; f, g_B) - \chi(\delta; f, g_A) \quad (4.7)$$

The segmentation efficiency *metric* is defined as the infinity norm of this distribution,  $\|\eta(\delta)\|_\infty$ . This metric describes the best segmentation result achievable given a particular filter,  $f$ , and a particular topology, defined by the pair  $g_A$  and  $g_B$ . The property of the segmentation efficiency distribution to evaluate filter and topology information derives from the properties of the individual CDFs. Each value of the CDFs represents the fraction of pixels in a segment correctly identified by a point classifier,  $\delta = m$ . Applying this classifier globally to the filtered image,  $f$ , divides its pixels into two estimated segments,  $\hat{g}_A$  and  $\hat{g}_B$ .

$$\begin{aligned} \{\hat{g}_A &= (x, y) \mid f(x, y) \leq \delta, (x, y) \in D_f\} \\ \{\hat{g}_B &= (x, y) \mid f(x, y) > \delta, (x, y) \in D_f\} \end{aligned} \quad (4.8)$$

In terms of these estimated segments, generically referred to as  $g_j$ , the fraction of pixels correctly identified in each region is

$$\Theta(\delta; g_j) = \frac{\text{area}(\hat{g}_j \cap g_j)}{\text{area}(g_j)} \quad (4.9)$$

The correctly identified pixel fractions,  $\Theta$ , over each region may thus be written in terms of the CDF over that region.

$$\begin{aligned} \Theta(\delta; f, g_A) &= 1 - \chi(\delta; f, g_A) \\ \Theta(\delta; f, g_B) &= \chi(\delta; f, g_B) \end{aligned} \quad (4.10)$$

The total fraction of correctly classified pixels, in the area-weighted sense, is  $\eta(\delta; f, g_A, g_B)$ .

$$\begin{aligned}
\eta(\delta; f, g_A, g_B) &= \Theta(\delta; f, g_B) + \Theta(\delta; f, g_A) - 1 \\
&= \chi(\delta; f, g_B) - \chi(\delta; f, g_A)
\end{aligned}
\tag{4.11}$$

Thus the  $\eta(\delta)$  distribution describes the total fraction of pixels, weighted by region size, that are correctly identified by a given classifier  $\delta$ . A classifier that achieves unity segmentation efficiency perfectly distinguishes between two pixel sets. Zero efficiency means that a classifier makes no distinction between the two sets. The sign of  $\eta(\delta)$  distinguishes the region for which the classifier is an upper bound and is otherwise arbitrary; that is:

$$\eta(\delta; f, g_A, g_B) = -\eta(\delta; f, g_B, g_A) \tag{4.12}$$

The calculation of segmentation efficiency distributions for a sample pair of images demonstrates the difficulty in empirically selecting a segmentation strategy for jelly tracking. Figure 4.4 and Figure 4.5 depict a *Solmissus* medusa and a ctenophore specimen, respectively. Both figures include plots of segmentation efficiency distribution and the associated CDFs using the luminance filter and region-based topology clustering. Whereas the filter+topology processing combination clearly distinguishes the *Solmissus*, the same combination performs poorly for the ctenophore image.

### 4.2.3 Ensemble Averaged Segmentation Efficiency

Given a large number of video clips imaged under application-specific environmental conditions, segmentation efficiency can identify the most useful filters and topologies for target extraction. Whereas, the previous section defined the segmentation efficiency distribution for an individual image, this section considers the application of the concept to a multiple-image database. In its most general form, the process of clustering entries from a large database of segmentation efficiency distributions (catalogued for each database image, each possible filter, and each topology) is a complex pattern recognition problem. If all the records in the image database are considered as a single cluster, however, the pattern recognition problem can be simplified substantially. This section considers such a single-cluster problem, the problem of identifying the best individual filter and topology for extracting all targets in the target-image database.

A metric that describes the ability of a single filter+topology combination to extract targets across an image database is the ensemble-averaged segmentation efficiency metric. This metric is

computed as the infinity-norm (maximum magnitude) of the distribution formed by ensemble averaging segmentation efficiency distributions for all images in the database.

$$\langle \eta \rangle_{\infty}(f, g_B, g_A) = \max_{\delta} \left( \frac{1}{M} \left| \sum_{i=1}^M \eta(\delta; f, g_B, g_A) \right| \right) \quad (4.13)$$

Here the average applies to a database of  $M$  images. Each choice of filter,  $f$ , and topology, defined by the pair  $g_A$  and  $g_B$ , results in a distinct value of the metric  $\langle \eta \rangle_{\infty}$ . High values of  $\langle \eta \rangle_{\infty}$  indi-

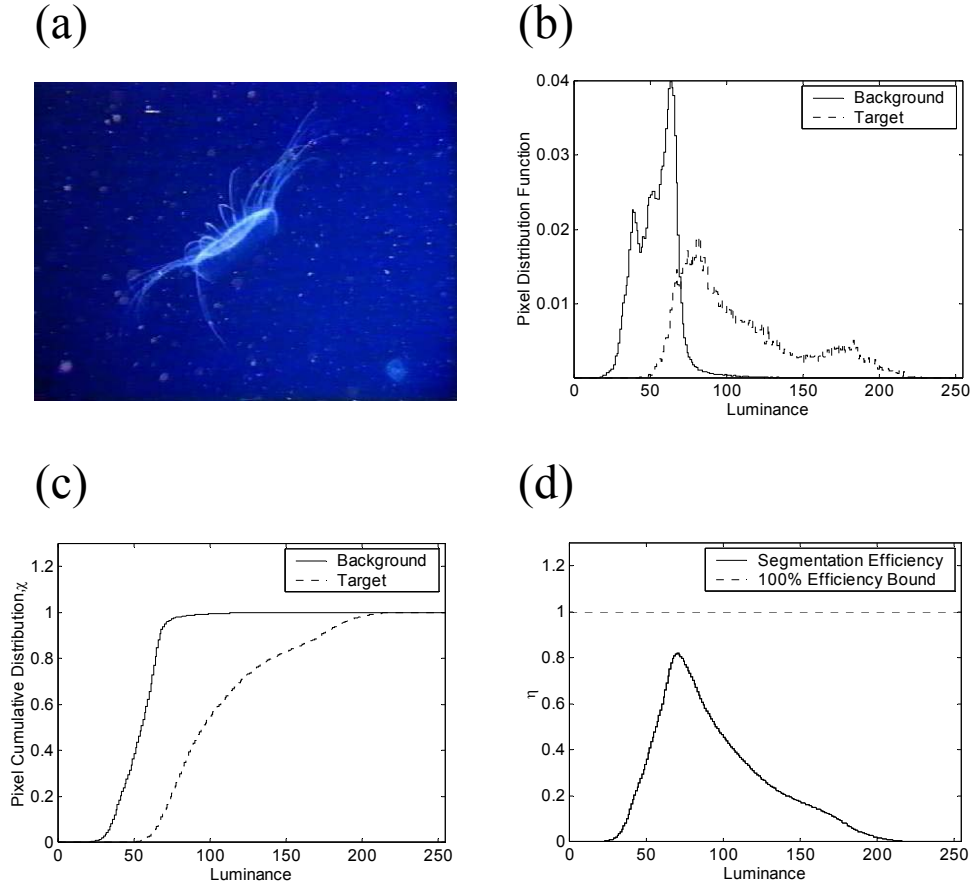


**Figure 4.4 Segmentation Efficiency for a Jellyfish Image**

(a) This image was chosen for its strong brightness distinction between background and target pixels. Integrating the (b) pixel distribution functions (PDFs) for each ground truthed target region gives (c) two cumulative distribution functions (CDFs). (d) The segmentation efficiency distribution is the difference of these two CDFs. The strong peak of the segmentation efficiency, near its maximum value of unity, confirms that a luminance filter applied to regional topological processing effectively distinguishes background and target pixels.

cate filter-topology combinations with high likelihood of extracting any target from the image database. The classifier argument that maximizes  $\langle \eta \rangle_\infty$  is labeled  $\delta_{\max}$ . The confidence limits of  $\eta(\delta_{\max})$  for the sample population of  $M$  images also serves as a useful supplementary statistic for assessing filter+topology combinations. Whereas the  $\langle \eta \rangle_\infty$  metric is a measure of quality, the confidence limits of  $\eta(\delta_{\max})$  are a measure of consistency. Both quality and consistency of a classifier affect the reliability of a visual servoing system.

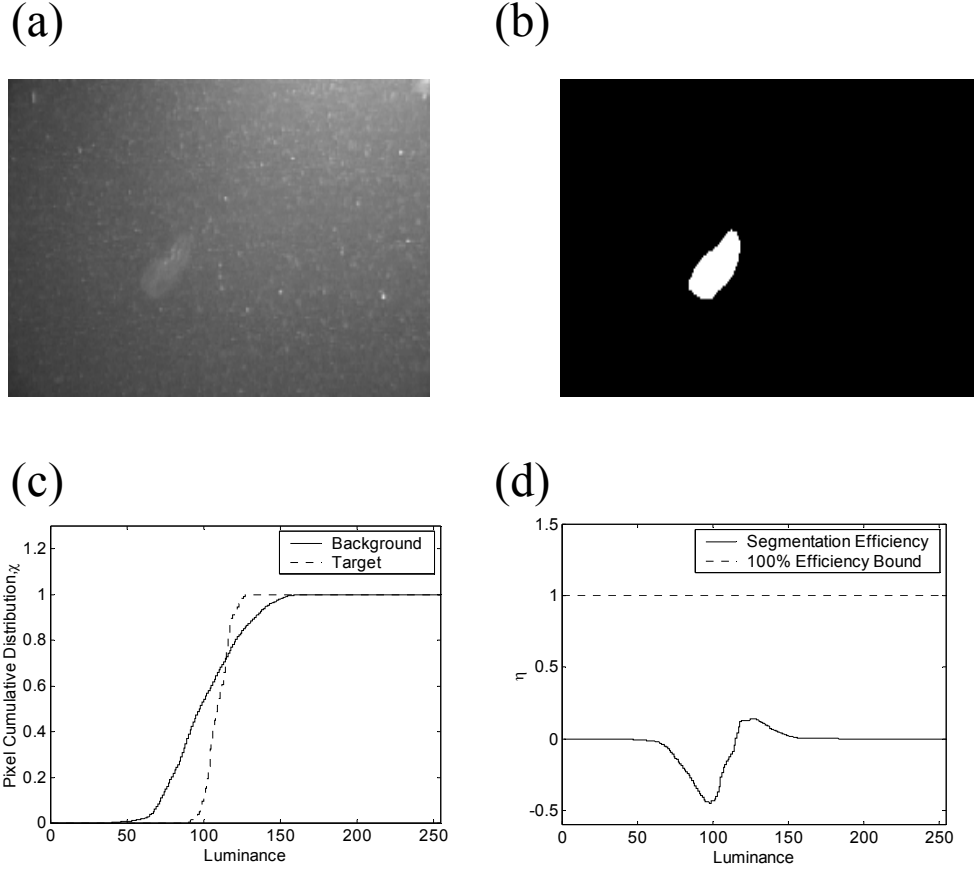


**Figure 4.5 Segmentation Efficiency for a Ctenophore Image**

With respect to the luminance filter evaluated over a regional topology, the statistics for (a) this ctenophore image differ strongly from those of the preceding Solmissus image, depicted in Figure 4.4. Given (b) a ground truth segmentation, (c) cumulative distribution functions (CDFs) and (d) segmentation efficiency are illustrated for the ctenophore image. The strong negative values of the segmentation efficiency distribution indicate the background is generally brighter than the target, in contrast with the results of Figure 4.4. The infinity-norm of the distribution indicates a 55% misclassification error when using a global luminance classifier to distinguish between pixels in the target and background regions.

### 4.3 A Segmentation Method for Jelly Tracking

This section describes the development of the vision-processing component that enabled jellyfish tracking during field demonstrations. The segmentation subcomponent, designed using the segmentation efficiency approach, relies on the application of global thresholding (a regional topological processing method) to gradient-filtered images. The recognition subcomponent uses a simple feature vector based on slowly-varying segment statistics.

#### 4.3.1 Application of Segmentation Efficiency to Jelly Tracking

A number of processing challenges make determination of a segmentation method by empirical means difficult in the case of midwater gelatinous animal images. The shape and appearance of gelatinous animals, for instance, varies substantially from species to species. The unstructured lighting environment, furthermore, results in an unpredictable background scene; in many cases, a mild lighting gradient of less than one gray level per pixel creates significant differences in luminance across the background image, as great as 40 gray levels or more. Specks of floating organic matter called marine snow act as small point scatterers that add additional noise to midwater images. These characteristics cause common segmentation algorithms, including luminance thresholding, gradient-based active contour methods, and level-set methods, to fail when applied naively to gelatinous animal images.

The application of the segmentation efficiency metric to a marine life database aids in designing a robust jelly-tracking system. Segmentation efficiency analysis identifies the most useful filtering and topological processing strategies for extracting gelatinous targets from noisy video sequences filmed in the midwater.

To characterize the jelly-tracking application, a marine life database was constructed of 182 short (half-second) clips of animals filmed *in situ* by ROV *Ventana*. Video clips depicted a wide range of gelatinous animal species filmed under a variety of unstructured lighting conditions. Lighting variations result from a variety of lamp configuration, camera zoom settings, camera gain settings, and marine snow backscatter conditions. Animals were imaged at ranges from 0.2 to 3 meters at 320 x 240 pixel resolution for field of view angles between 10° and 60°. For each clip in the database, a human operator provided ground truth by defining the target region,  $g_t$ , with a spline fit to the target interior edge. The background region,  $g_b$ , was defined as the image comple-

ment to the target animal region(s) and to the excluded region,  $g_x$ , consisting of small snow particles:

$$g_b = (g_x \cup g_t)^C \quad (4.14)$$

Here snow pixels were identified automatically, without human input, according to the relation:

$$g_x = \{(x, y) | \Phi(x, y) \geq \delta_{snow} \text{ and } (x, y) \in D_q\} \quad (4.15)$$

$$\Phi(x, y) = \frac{\sum_{m, n \in D_q} l(x - m, y - n) > l(x, y)}{\sum_{m, n \in D_q} 1} \quad (4.16)$$

In effect, this operator recognizes marine snow by identifying small pixel regions with high contrast to their neighbors. For this work the structuring element,  $q$ , was chosen on a 5x5 square grid, with the domain,  $D_q$ , comprised of the grid's 16 border elements.  $\delta_{snow}$  was set equal 0.75.

Table 4.3 shows the peak magnitude of ensemble averaged segmentation efficiency,  $\langle \eta \rangle_\infty$ , computed across all images in the marine life database. Peak height is listed for the fifteen filters and four topologies described in Section 4.2.1. The first column of Table 4.3 describes region-based topologies with  $\langle \eta \rangle_\infty(f, g_b, g_t)$  (where  $f$  indicates a generic filter and  $g_b$  and  $g_t$  indicate the specific pixel sets associated with region-based topologies). The background difference filter, the gradient filters, and the monochrome luminance filter have the highest peak values for distinguishing regions of target and background pixels. That gradient values are high over the entire target region is surprising; in most vision applications, high gradients are expected at edges between regions but not in region interiors. In contrast, most jellies display sufficient internal structure that gradient filters reliably distinguish between interior pixels in both the target and background regions.

The second, third, and fourth columns of Table 3 assess edge-based topologies. In these columns, the strongest responses were observed for  $\langle \eta \rangle_\infty(d_b, \partial g_b, \partial g_t)$ , the strict-edge comparison using the background difference filter, and for  $\langle \eta \rangle_\infty(\|\nabla l_{oc}\|_M, g_b^\circ, \partial g_b)$ , the background edge-to-interior comparison using the snowless gradient filter.

Of all the entries in Table 4.3, the highest peak value of segmentation efficiency corresponds to the background-difference filter applied regionally,  $\langle \eta \rangle_{\infty}(d_b, g_b, g_t)$ . This peak value indicates the high quality of the background-difference signal for region-based segmentation. The restriction that an external agent initialize the filter (see Section 4.2.1) limits its use in real-time tracking applications, however.

In contrast, the gradient filters achieve high regional segmentation efficiency without any need for special initialization. Segmentation efficiency analysis indicates, in fact, that a fixed-level gradient classifier consistently describes the target region associated with gelatinous animals, even under the wide range of lighting conditions encountered in the marine life database.

	Region-Based	Edge-Based		
Symbol	$\langle \eta \rangle_{\infty}(f, g_b, g_t)$	$\langle \eta \rangle_{\infty}(f, \partial g_b, \partial g_t)$	$\langle \eta \rangle_{\infty}(f, \partial g_t, g_t^{\circ})$	$\langle \eta \rangle_{\infty}(f, g_b^{\circ}, \partial g_b)$
$c_r$	0.2353	0.2139	0.0909	0.0312
$c_g$	0.0709	0.0763	0.0300	0.0284
$c_b$	0.1888	0.1720	0.0697	0.0330
$l$	0.4755	0.3253	0.1390	0.1626
$\ \nabla l\ _2$	0.5398	0.3344	0.1304	0.3052
$\ \nabla l\ _{2,s}$	0.6688	0.2989	0.1427	0.5102
$\ \nabla l\ _M$	0.6668	0.3571	0.1555	0.4512
$\ \nabla l\ _{M,s}$	<b>0.7212</b>	0.2819	0.1453	0.5886
$\ \nabla l_{oc}\ _M$	0.5904	0.1291	0.2343	<b>0.6296</b>
$\nabla^2 l$	0.2280	0.2553	0.1150	0.1848
$\nabla^2 l_s$	0.3647	0.4392	0.1316	0.3871
$d_t$	0.1876	0.1590	0.0572	0.1043
$d_b$	<b>0.8678</b>	<b>0.6068</b>	0.2199	0.2680
$\ p\ $	0.1011	0.0206	0.0328	0.0746
$\angle p$	0.0228	0.0060	0.0164	0.0228

**TABLE 4.3. Segmentation Efficiency for Jellyfish Database**

*The table presents the ensemble-averaged segmentation efficiency metric computed for a database of gelatinous animal images.*



Although the gradient filter performs almost as well for boundary comparisons as for regional ones, segmentation efficiency is slightly higher for regional comparisons. Consequently, the subset of segmentation algorithms identified as most promising according to the  $\langle \eta \rangle_\infty$  metric are those methods employing gradient filtering over a region-based topology.

The tight confidence limits of  $\langle \eta \rangle_\infty$  for regional gradient processing further support the utility of this class of segmentation algorithm. Confidence limits for the gradient filter are significantly tighter than those for competing filters such as the luminance filter. Figure 4.6 depicts the mean distribution and 90% confidence interval for segmentation efficiency as a function of classifier,  $\delta$ , for both the luminance and morphological gradient filters. Confidence limits are significantly tighter for morphological gradient than those for the luminance distribution. Significantly, the peak value of segmentation efficiency always occurs in approximately the same location,  $\delta_{\max}$ ,

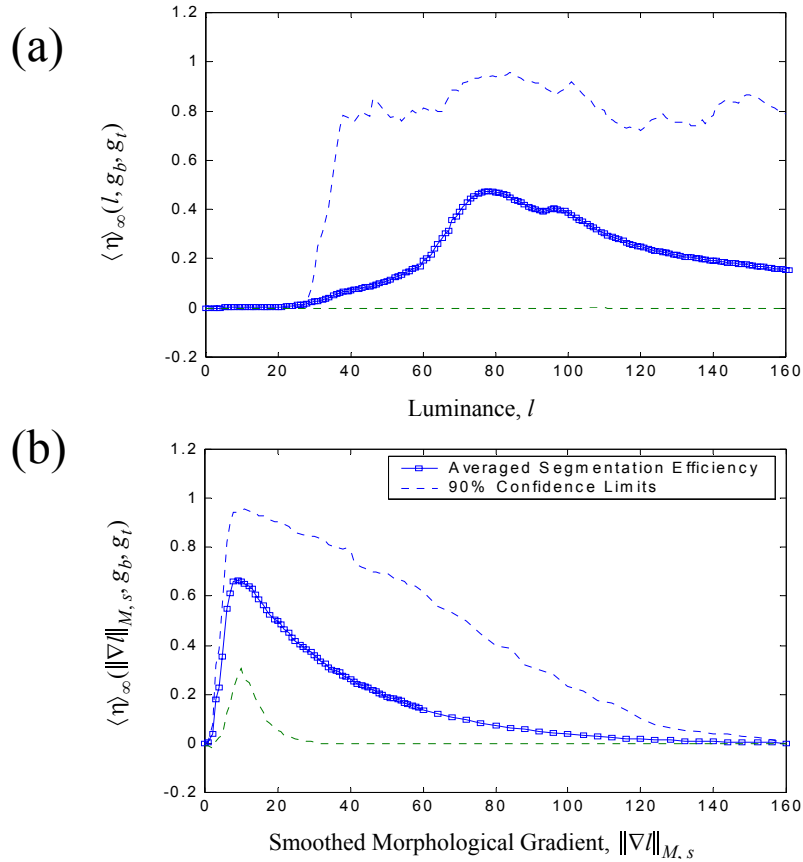


**Figure 4.6 Ensemble-Averaged Segmentation Efficiency Confidence Limits**

*Ensemble-averaged segmentation efficiency distribution and confidence limits are plotted for all transparent animal samples in the marine life video database. Distributions were calculated using a region-based topology with (a) luminance filtering and (b) smoothed morphological-gradient filtering.*

for morphological gradient distributions across the database. At 320x240 resolution, the gradient classifier,  $\delta_{\max}$ , (equal 10 gray levels per pixel) yields an efficiency of at least 0.30 for 95% of transparent animal samples drawn from the marine life database. By comparison, the lower confidence bound for the luminance distribution is nearly flat at zero efficiency. As a consequence, a regional gradient segmentation method has a very high probability of providing the consistency required to implement recognition.

Inconsistent peak height for luminance information results from scene-to-scene luminance variations and from mild image gradients (smaller than one gray level per pixel) across typical ROV-imaged scenes. A global luminance classifier that distinguishes target pixels from background pixels does not always exist given uneven lighting. Figure 4.7 illustrates this phenomenon by displaying a luminance contour that envelops both a target ctenophore and a section of the background image. By contrast, gradient and background difference filters cleanly distinguish the target in this case.

A method exploiting luminance information would thus need to adapt spatially and temporally to compensate for poor consistency of luminance classifiers; adaptation introduces concerns of convergence and processing requirements for real-time, power-constrained applications. By comparison, a gradient algorithm can use a fixed-level classifier to identify gelatinous targets consistently. This characteristic of gradient information enables the implementation of a non-iterative, bounded-time segmentation component in a visual tracking algorithm.

The high  $\langle \eta \rangle_{\infty}$  score for gradient and background-difference filters applied to regional topologies stands in contrast with previous biology-inspired vision-processing studies. Other studies have successfully employed, for example, region-based optical flow methods for fish tracking [105], edge-based gradient methods for the study of bioluminescence [112], and region-based luminance methods for classification of plankton [119,129,130]. Differences among applications motivate the choice of these particular filtering and tracking strategies. These differences emphasize the importance of a design tool, such as segmentation efficiency, which aids in the synthesis of a vision tracking algorithm by assessing filtering and topological processing strategies that best identify the target for a new application.

### 4.3.2 Constraining Algorithm Choice Based on System Requirements

Segmentation efficiency, alone, determines only the general class of segmentation algorithm suited to a particular application. An understanding of application constraints completes the design process, enabling the selection of a specific vision algorithm from the subset flagged by segmentation efficiency analysis.

For jelly tracking, the first priority of the vision system is robustness to variable lighting conditions and target species. Considering the discussion of the prior section, gradient-based regional segmentation methods have a strong advantage in terms of signal quality, as predicted by peak segmentation efficiency height, and in terms of consistency, as predicted by tight confidence limits. Likewise, the high efficiency peak for the background difference filter suggests that this information could enable accurate jelly segmentation, given automation of the filter's external agent

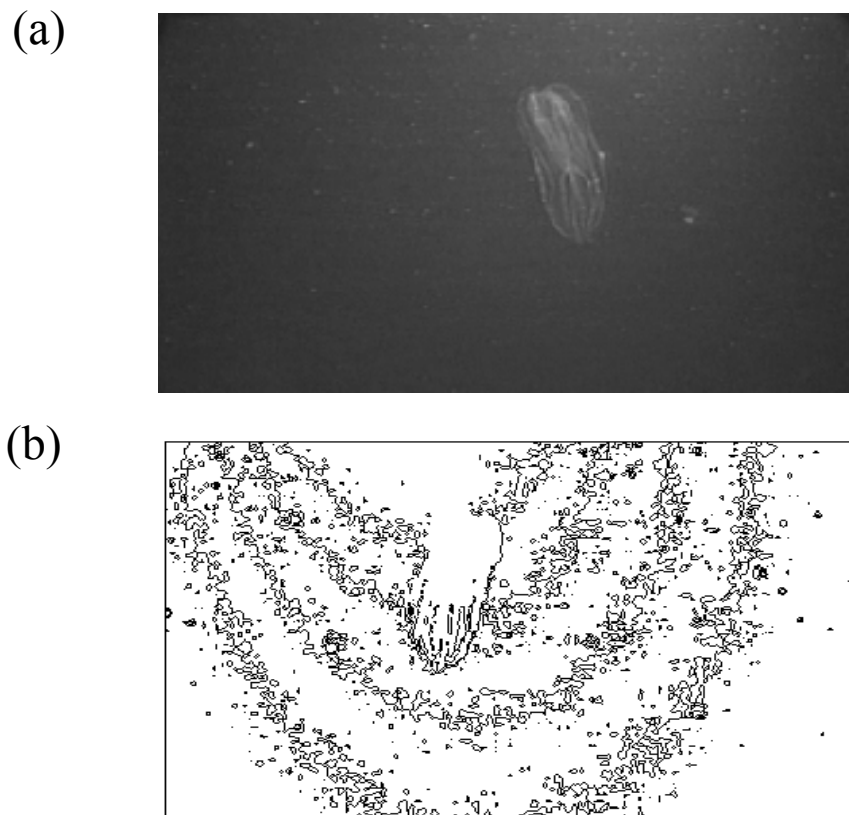


**Figure 4.7 Luminance Contours under Nonuniform Illumination**

*No unique luminance threshold separates this ctenophore target from the background. Given the nonuniform illumination across this (a) ctenophore image, the luminance values of the target and background overlap. This fact is evident in (b) the luminance contour plot of the image, with contours spaced at intervals of 8 gray levels.*

requirement. These results narrow the search for a jelly-tracking algorithm to the class of region-based topological processing methods applied to images filtered with a gradient operator, or possibly with the background difference operator.

Within this region-based class, topological clustering methods may be distinguished primarily by two characteristics: (1) incorporation of shape knowledge and (2) parameter adaptation. As summarized in Table 4.2, certain methods incorporate a definite notion of target shape (the template masking technique) or target pixel pattern (the correlation technique). Other region-based methods possess some ability to handle varying image conditions through adaptation (the adaptive threshold and expectation maximization techniques). For the jelly-tracking application, the target's flexible, three-dimensional structure makes explicit incorporation of shape knowledge difficult. Parameter adaptation, on the other hand, is unnecessary, as a fixed-parameter, non-adaptive technique can robustly segment targets over a wide range of lighting conditions. Both adaptation and shape-constraints add complexity to a segmentation algorithm. As neither characteristic clearly benefits the jelly-tracking application, an appropriate selection criterion among region-based topological processing methods is simplicity. Of the region-based methods, fixed-parameter global thresholding, which incorporates neither adaptation nor shape specification, is the least complex.

A fixed-gradient global thresholding method thus fits the requirements for both ROV and AUV operations. The application of a global threshold to an image, along with assignment of neighboring pixels to amorphous segments, results in an easily implemented, robust segmentation strategy with excellent computational efficiency. Because the method does not require parameter tuning, it behaves reliably and repeatably upon activation. This insensitivity to initialization means the method is well suited to tracking across a range of sample rates, as high as 30 Hz for an ROV pilot assist and as low as a fraction of a Hertz for a strobed AUV application.

### 4.3.3 Segmentation Method for Field Experiments

Based on a segmentation efficiency analysis in the context of application constraints, a gradient-based global threshold method was implemented, along with a pattern-vector recognition routine, as the visual tracking algorithm for field operations. The global-threshold segmentation method relies on smoothed morphological gradient information, extracted by the  $\|\nabla I\|_{M,S}$  filter. This filter was selected among the gradient filters of Table 4.1 because it produced the highest peak value

of  $\langle \eta \rangle_\infty$ . For this filter, the fixed gradient threshold is chosen to be  $\delta_{\max}$ : 10 gray levels per pixel (for 320x240 resolution). The complete segmentation algorithm is summarized as follows:

1. Apply a 3x3 uniform filter to the monochrome luminance image
2. Calculate morphological gradient for the smoothed luminance image
3. Apply a global threshold to identify potential target regions
4. Calculate size of connected regions and filter out small segments (snow)

The algorithm has low computational complexity. For an image containing  $P$  pixels, the uniform smoothing filter, which is separable, requires  $4P$  addition operations. Morphological erosion and dilation operators, used to calculate morphological gradient, are also separable when a square, in this case 3 x 3, structuring element is applied. It follows that the operations count to compute morphological gradient involves  $8P$  comparisons and  $P$  subtractions. Application of a global threshold requires  $P$  pixel comparisons. The total algebraic operations count for the method is thus  $5P$  additions and no multiplications. No iteration is required. Because the computational burden of the method is low, the algorithm is well suited for a real-time, processor-constrained application.

Although gradient filters consistently recognize jelly targets, they also amplify snow particles. Step 4 of the segmentation algorithm, above, addresses this issue and removes snow particles by filtering potential target segments based on pixel count. A size filter of 25-30 total pixels

Target Size Classification	Count
$10^0$ - $10^1$ Pixels	0
$10^1$ - $10^2$ Pixels	18
$10^2$ - $10^3$ Pixels	149
$10^3$ - $10^4$ Pixels	77
$10^4$ - $10^5$ Pixels	19
<b>Snow Size Classification</b>	
$10^0$ - $10^1$ Pixels	156487
$10^1$ - $10^2$ Pixels	23950
$> 10^2$ Pixels	0

TABLE 4.4. Target Size Distribution

(given 320x240 resolution and typical zoom and marine lighting configurations) removes the majority of marine snow pixels from consideration. Table 4.4 emphasizes the small size of the majority of snow particles and validates the use of a snow filter based on size information. Removing snow particles prior to recognition reduces computational requirements for the recognition step.

An additional theoretical concern associated with gradient-based segmentation addresses extreme camera resolution and lighting settings. At some limit of high zoom or low lighting, gradients over the target inevitably fall below camera sensitivity. In practice however, gradient threshold segmentation works very well at a range of zoom settings, target ranges, and target sizes. Table 4.4 describes these variations across the reference database in terms of target size in pixels.

#### 4.3.4 Recognition Method for Field Experiments

For ROV applications, a simple recognition scheme complements gradient based segmentation to form a complete tracking solution. The experimental vision-tracking algorithm acts on two video sequences filmed simultaneously by a camera pair in a precalibrated stereo-triangulation configuration. The segmentation algorithm operates on images from each video stream separately. The recognition algorithm identifies the target in each image as the best match to a reference profile (as illustrated in Figure 4.1). The centroids of the best-match segments for each of the two stereo cameras are used in triangulating target position.

The recognition subcomponent used in experiments employed a feature vector of simple statistics to construct a target profile (Assumption 4.1). The components of the feature vector included the average segment luminance, its pixel area, its aspect ratio and its centroid position. Features that simultaneously incorporate information from both cameras, such as measurements of physical target size (in centimeters) or a penalty function based on epipolar geometry, were not used in the experimental system.

Figure 4.8 summarizes the recognition subcomponent of the visual tracking system. The recognition algorithm computes a feature vector for each candidate segment. The segment with the feature vector closest to the target profile (compared using a weighted 2-norm) is identified as the target. At each time step, the target profile is updated using a low-pass filter to incorporate the statistics for the best-match segment. Before updating the profile, however, the recognition algorithm applies a false-positive test. In cases for which the best-match feature vector differs from the pro-

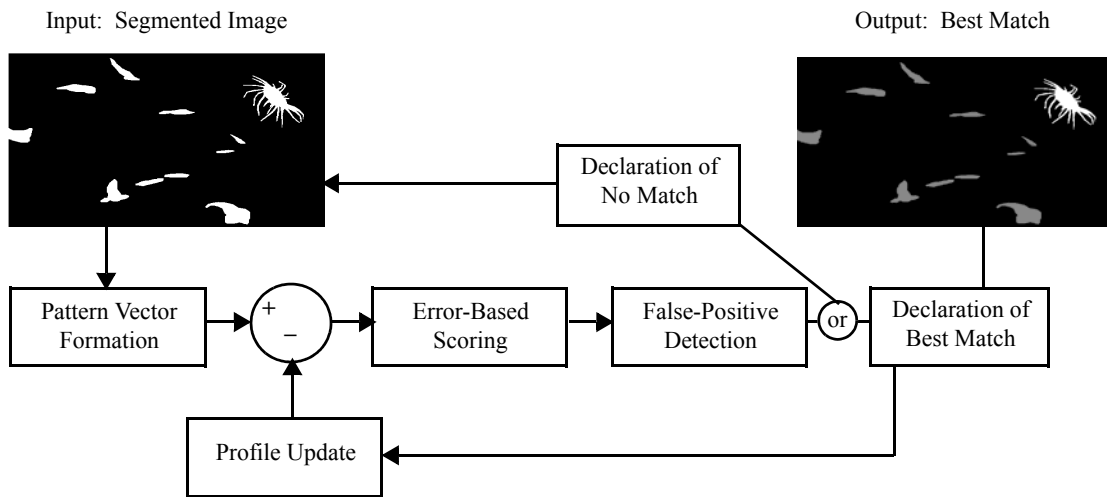


**Figure 4.8 Block Diagram for Recognition Component**

file by more than a preset threshold the test declares an invalid match. If the best match is declared an invalid false-positive, the recognition algorithm neither updates the target profile nor the reported target position.

The recognition subcomponent employed in field trials relies on the human pilot for initialization. The recognition algorithm constructs a target profile during a brief, 1-2 second training period. The pilot activates the training sequence with a button click. During this time, the recognition algorithm uses a profile that assumes a nominal target pixel area and a target location at the image center. If the pilot maintains the target near the image center throughout the training period, the automated tracking system acquires the correct target. At this moment, the automated pilot assist begins to issue control commands and the human pilot may ease off the control stick.

The complete vision system, consisting of this recognition algorithm and the segmentation algorithm from the previous section was implemented to enable successful long-duration tracking experiments. During field trials, the vision processing system ran at an update rate of 10 Hz.

## 4.4 Reliability of the Recognition Subcomponent for Very Long-Duration Jellyfish Tracking

The previous section described a vision processing algorithm that enabled jellyfish-tracking experiments (see Chapter 6) which held station on gelatinous animals *in situ* for durations as long as 89

minutes. For these experiments, the primary reliability challenge for the vision-processing system involved segmentation. The recognition subcomponent of the tracking system was assumed to perform reliably given consistent segmentation (Assumption 4.1 & Assumption 4.2). Although these assumptions generally apply for ROV-based jellyfish tracking, they do not necessarily hold for extended-duration AUV-based jellyfish tracking. Over long durations (many hours) and for sample periods greater than 0.1 s, the reliability of the recognition subcomponent does, in fact, become an important issue in defining overall system reliability. Improved vision-processing methods are required to enable reliable AUV-based jellyfish tracking, which may endure for periods as long as 24 hours and which may employ low sample rate tracking to reduce power consumption (see Chapter 7).

Section 4.4.1 examines the issue of recognition algorithm reliability in more detail, both to justify Assumptions 4.1 and 4.2 and to illustrate the limitations of these assumptions in describing operational tracking. Improved recognition techniques are not considered in this dissertation; nonetheless, a more accurate segmentation can enable the extraction of recognition features with less variance over time. To this end, Section 4.4.2 introduces an alternate segmentation algorithm for jellyfish tracking that provides more accuracy, at a higher processing cost, in comparison with the experimentally validated jellyfish tracking algorithm. The refined segmentation component will serve, in the future, as an important element of an improved system for very long-duration AUV-based jellyfish tracking.

#### 4.4.1 Recognition Number

This section considers the conditions under which the reliability of the recognition algorithm plays an important role in determining the reliability of the overall system. These conditions include jellyfish tracking for durations of many hours, tracking at low sample rate, and tracking in a high density of nearby animal specimens.

The standard features used for recognition in the experimental ROV-based system, such as target position, aspect ratio, and mean luminance, are all weakly time-variant. Thus, although these features are readily available, their uncertainty may grow quickly if Assumptions 4.1 and 4.2 are not valid. The limited precision of these features may also cause problems after a very large number of recognition steps (i.e. after many hours of tracking).



The sample period assumption, Assumption 4.1, plays a particularly important role in the performance of weakly time-variant features. The degradation of performance with decreasing sample rate depends on the drift rate of features from the estimated target profile. Because the drift rate is application dependent, a useful generalization of the sample period may be obtained by normalizing sample period by the time scale for profile drift. This section introduces the term *recognition number* ( $\mathcal{R}$ ) to refer to this nondimensional sample period.

$$\mathcal{R} = \frac{\text{Sample Period}}{\text{Time Scale of Profile Drift}} \quad (4.17)$$

The recognition number concept enables analysis of recognition system reliability for various sample intervals independent of the time scale of target motion.

For position-based features, the time scale for profile drift is approximately equal to the width of the animal divided by the square root of its velocity variance,  $E(v^2)$  (the deviation of the target's velocity from its predicted value). This time scale is based on the notion that an accelerating or decelerating jelly will not, generally, move more than one body length in a second. Based on this time scale, the recognition number for drift of position-based features is

$$\mathcal{R} = \frac{\Delta t}{d} \sqrt{E(v^2)} = \frac{\text{Sample Period}}{\text{Time Scale of Target Motion}}. \quad (4.18)$$

The velocity variance is assumed isotropic in space, such that the animal may change velocity in any direction with equal probability.

This section uses the recognition number concept to derive an expression for the reliability of a recognition processing method that relies on position-based statistics (like the recognition system used for the experimental system). In this reliability analysis for the recognition component, two mechanisms may lead to possible system failures: drift events and occlusion events. In a drift failure, the target moves away from the reference profile, and the recognition algorithm incorrectly identifies a second object as the target. In an occlusion failure, the target moves briefly behind a secondary object, and the recognition algorithm fails to identify the target when it reemerges into view. The probability of failures caused by either mechanism define an overall failure probability,  $P_{\text{fail}}$ . After some number of events,  $N$ , the overall probability that the tracking system continues to operate successfully, assuming independence of each event, is:

$$P_{\text{success}} = (1 - P_{\text{fail}})^N \quad (4.19)$$

The probability of failure due to an event is related to the likelihood of the event,  $P_q$ , and the probability that the algorithm gracefully recovers following the event,  $P_{\text{recovery}|q}$ .

$$P_{\text{fail}, q} = P_q(1 - P_{\text{recovery}|q}) \quad (4.20)$$

The probability of recovery is algorithm dependent; better recognition algorithms recover from recognition events more reliably.

The probability that an event occurs,  $P_q$ , depends on the density of targets,  $\rho$ , in a space defined as the event volume,  $V$ . For occlusion events, the event volume is the section of the viewing cone that lies in front of the target. For drift events, the event volume is a ball in feature-space centered on the target profile, with radius defined by the drift of the target's feature vector away from the profile. For this analysis, only image-plane position features are considered. Thus the drift event volume, like the occlusion event volume, is defined as a portion of the camera viewing cone. Figure 4.9 illustrates the viewing geometry.

Within the event volume, the expected number of events over an interval of time is

$$E(N_q) = E(V\rho). \quad (4.21)$$

When the likelihood of an event occurrence is much less than one,  $E(N_q)$  serves as an approximation of the probability that an event occurs.

$$P_q \approx E(V_q \rho) \quad (4.22)$$

For both drift and occlusion events, the event volume is a length of cone with a volume proportional to the solid angle subtended by the cone. Occlusion events are defined to occur when a secondary object center enters the cone subtended by the target, assumed to have a characteristic width,  $d$ .

$$V_{\text{occlusion}} \propto \pi \left(\frac{d}{2}\right)^2 \quad (4.23)$$

#### 4.4 RELIABILITY OF THE RECOGNITION SUBCOMPONENT FOR VERY LONG-DURATION JELLY-

Drift events are defined to occur when secondary objects enter into the cone defined by the drift of the target away from a predicted location. The drift distance is the product of a drift velocity,  $v$ , and the sample interval for recognition,  $\Delta t$ .

$$V_{\text{drift}} \propto \pi(v\Delta t)^2 \quad (4.24)$$

If an encounter density per a solid angle of  $\pi(d/2)^2$  is defined as  $\tilde{\rho}$ , and if this density is assumed uniform in space, then the probability of an event occurrence is expressed by (4.25).

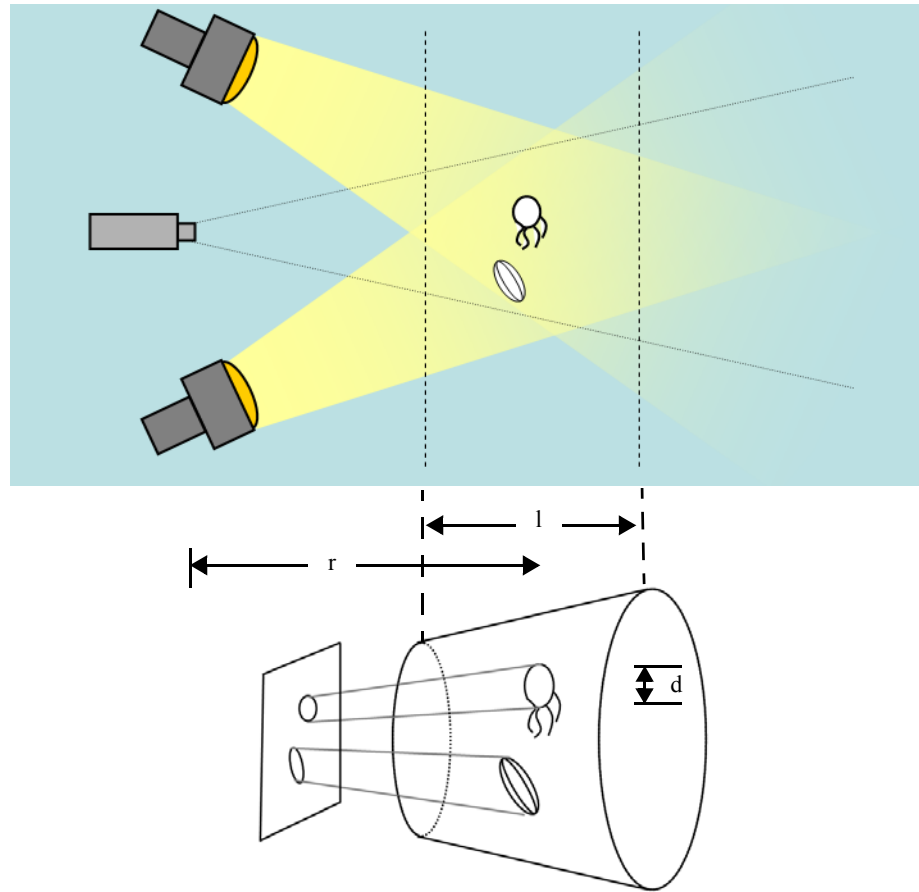


**Figure 4.9 Model of Image Plane Projection**

*When two animals swim near each other, an occlusion or a recognition failure may occur. The lighted volume occupies a length,  $l$ , along rays extending from the camera's focal center. The target, of a characteristic width,  $d$ , stands at a range,  $r$ , away from the camera.*

$$\begin{aligned}
P_{\text{occlusion}} &\approx 0.5 \cdot E(\rho) = 0.5 \cdot \rho \\
P_{\text{drift}} &\approx E\left(4\left(\frac{v\Delta t}{d}\right)^2 \tilde{\rho}\right) = 4\mathcal{R}^2 \tilde{\rho}
\end{aligned} \tag{4.25}$$

In the equation for  $P_{\text{occlusion}}$ , an extra factor of one-half has been introduced under the assumption that the target sits roughly halfway through the lighted volume and that occlusions only occur when the secondary object passes in front of the target. A representative value for secondary object density, under experimental conditions, is  $\tilde{\rho} = 3.5 \times 10^{-4}$  animals per a solid angle of  $\pi(d/2)^2$ . This density corresponds to the appearance, somewhere in the ROV camera viewing cone, of one animal every five minutes for a five second duration.

According to (4.20), the probability of failure following an event is a function of the event probabilities, given by (4.25), and of the recovery probabilities. Nominal values for the recovery probabilities, based on the performance of the algorithms used in the experimental system are:

$$\begin{aligned}
P_{\text{recovery}|\text{occlusion}} &= 0.85 \\
P_{\text{recovery}|\text{drift}} &= 0.2
\end{aligned} \tag{4.26}$$

Based on these representative values, the overall probability of successful recognition over an extended tracking period can be calculated using (4.19). The number of possible drift events,  $N_{\text{drift}}$ , is one per sampling interval,  $\Delta t$ . Over a run of total duration,  $T$ , the number of drift events is:

$$N_{\text{drift}} = \frac{T}{\Delta t} \tag{4.27}$$

Occlusion events only occur when the recognition system tries to distinguish the target from the occluding object after some interval of occlusion. A characteristic occlusion interval,  $\tau_{\text{occlusion}}$ , is approximately 1 second. Given this interval, the number of occlusion events is:

$$N_{\text{occlusion}} = \frac{T}{\tau_{\text{occlusion}}} \tag{4.28}$$

At any occlusion interval, either an occlusion event or a recognition event could cause system failure. Given the form of (4.22), the total probability of failure is proportional to the total event vol-

ume for both the drift and occlusion failure modes. The two event volumes always overlap, so the combined failure probability is less than the sum of the failure probabilities. The sum of the probabilities may be used, however, as a conservative upper bound on the total failure probability at the end of an occlusion interval.

The probability for successful tracking over a duration  $T$  is thus given as follows.

$$\begin{aligned}
 P_{\text{success}} &= (1 - P_{\text{fail,combined}})^{N_{\text{occlusion}}} (1 - P_{\text{fail,drift}})^{N_2} \\
 P_{\text{fail,drift}} &= 4\mathcal{R}^2 \tilde{\rho} \cdot (1 - P_{\text{recovery|drift}}) \\
 P_{\text{fail,combined}} &= P_{\text{fail,drift}} + 0.5 \cdot \tilde{\rho} \cdot (1 - P_{\text{recovery|occlusion}}) \\
 N_2 &= \begin{cases} N_{\text{drift}} - N_{\text{occlusion}}, & \tau_{\text{occlusion}} > \Delta t \\ 0, & \tau_{\text{occlusion}} \leq \Delta t \end{cases}
 \end{aligned} \tag{4.29}$$

Figure 4.10 plots  $P_{\text{success}}$  subject to variations in recognition number, tracking duration and animal density. Increases in all three of these parameters can significantly degrade the probability of

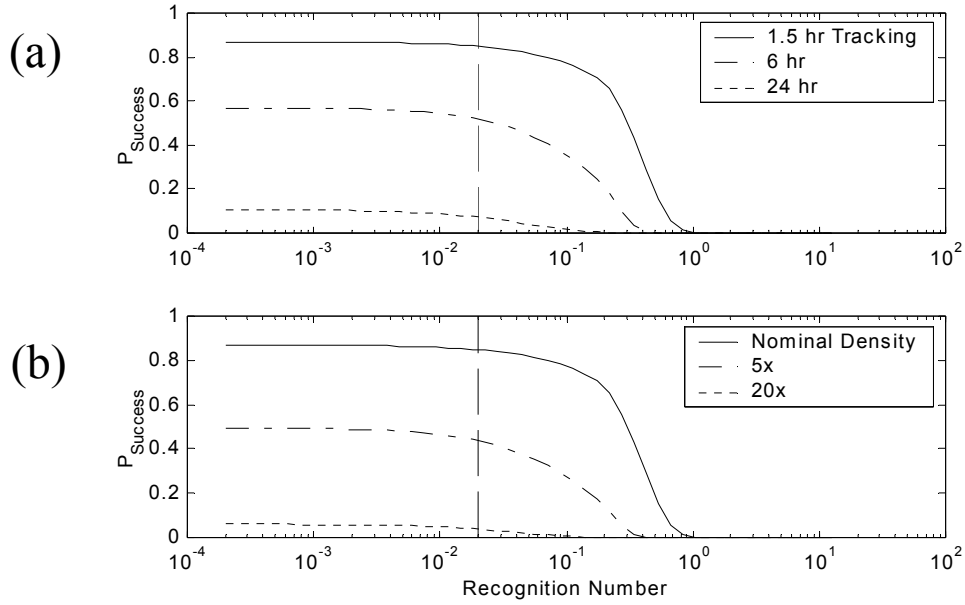


**Figure 4.10 Probability of Recognition Success**

*These plots illustrate the probability of mission success, as a function of recognition number, for (a) extended mission length and (b) higher animal density. All other parameters equal, increases in mission duration, in animal density, or in recognition number severely degrade the probability of completing a successful mission.*

successfully completing a tracking run. Plotted against recognition number,  $P_{\text{success}}$  transitions between a short sample rate behavior, dominated by occlusion errors, and a long sample rate behavior, dominated by recognition errors. On these plots, the recognition number for experiments is plotted as a dashed line at  $\mathcal{R} = 0.02$  (assuming  $\sqrt{E(v^2)} = 0.02$  m/s,  $d = 0.1$  m, and  $\Delta t = 0.1$  s).

Figure 4.10(a) indicates that AUV-based tracking places much greater demands on the recognition system than ROV-based tracking. AUV-based tracking will enable very long-duration tracking (e.g. as long as 24 hours). Meeting power restrictions for extended operations may require substantial reductions in the sample rate for the visual tracking system (see Chapter 7). If the experimental system's sample interval were lengthened by a factor of 10, to a one-second sample period, Figure 4.10(a) indicates that the probability of successfully tracking a target for 24 hours is less than 1%. The success probability depicted in Figure 4.10 is somewhat conservative, as the drift reliability analysis considered only position-based statistics, and not other image-derived statistics, and because the expression for  $P_{\text{fail,combined}}$  is conservative. Nonetheless, the low success probabilities illustrated in Figure 4.10(a) indicate that improved recognition capabili-

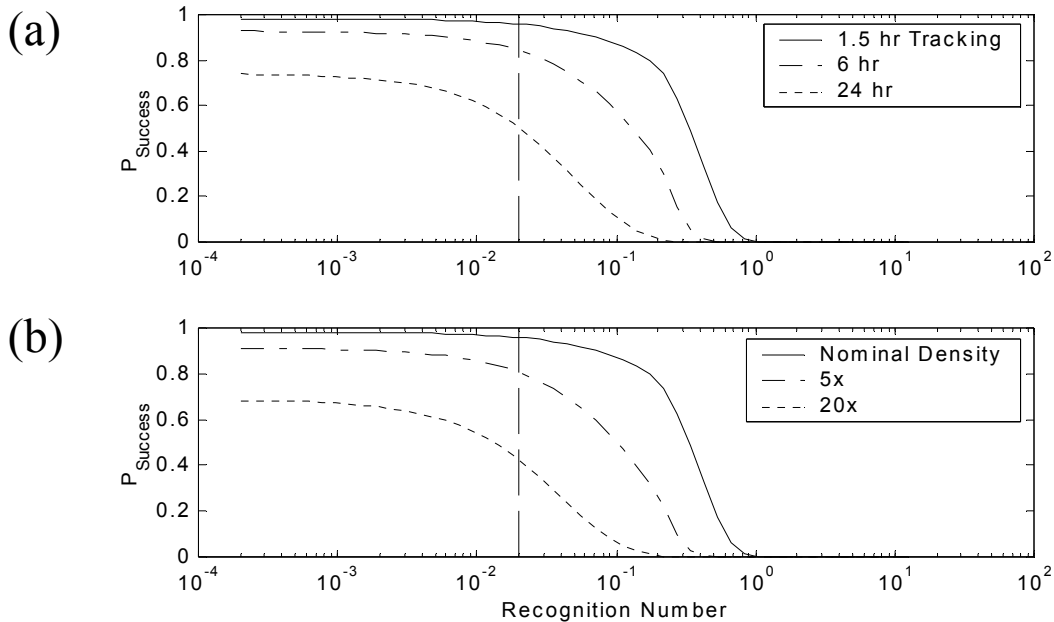


**Figure 4.11 Success Probability with Improved Occlusion Handling**

*These plots replicate Figure 4.10, but with the probability of recovery after an occlusion improved from (a) 85%, or about 1 failure in 7, to (b) 98%, or 1 failure in 50.*

ties are required to achieve long duration, long sample-period tracking. Improved recognition reliability is also important for tracking in areas of high animal density, as illustrated by Figure 4.10(b).

Improving the quality of the segmentation subcomponent of the tracking algorithm can have a positive effect to increase the probability of mission success. A higher quality segmentation algorithm can enable the extraction of segment statistics with lower variance,  $\sqrt{E(v^2)}$ . Lowering variance for a fixed sample rate effectively decreases recognition number and increases reliability. The extraction of features with less temporal drift can also enable better occlusion handling algorithms with better recovery probability,  $P_{\text{recovery}|\text{occlusion}}$ . Figure 4.11 shows the dramatic impacts of increasing the frequency of occlusion recovery.

#### 4.4.2 Improving Target Segmentation with the Background Difference Filter

This section leverages the segmentation efficiency analysis, discussed in Section 4.3, to develop a higher accuracy segmentation subcomponent. This component could be incorporated with improved recognition techniques to improve recognition reliability (by decreasing  $\sqrt{E(v^2)}$  and increasing  $P_{\text{recovery}|\text{occlusion}}$ ).

Segmentation efficiency analysis indicated that background difference filter,  $d_b$ , offers potential for very high quality segmentation. The background difference filter cannot, however, be applied to an image without external input. A successive filter approach can automate generation of this external input. First, a gradient based method akin to the technique described in Section 4.3.3 produces a rough segmentation. The snowless gradient filter, which reliably captures target edge information while automatically eliminating small snow particles, works well for this first step. Bounding boxes are calculated around high gradient regions and passed to the background difference filter as external inputs. Within each bounding box, a second step calculates background difference and applies a  $d_b$  threshold. The result is a more accurate segmentation for which recognition statistics may be calculated with greater accuracy. Figure 4.12 shows typical segmentation results using gradient information only and using the augmented background difference method.

The refined algorithm involves the following steps:

1. Apply the snowless filter (open and then close the monochrome luminance image)

2. Calculate morphological gradient for the snowless image,  $\|\nabla l_{oc}\|_M$
3. Apply a global threshold to identify potential target regions
4. Calculate bounding boxes for each segmented region
5. Synthesize a background image for each bounding box
6. Calculate the background difference image,  $d_b$ , in each bounding box
7. Apply a background difference threshold within the bounding box

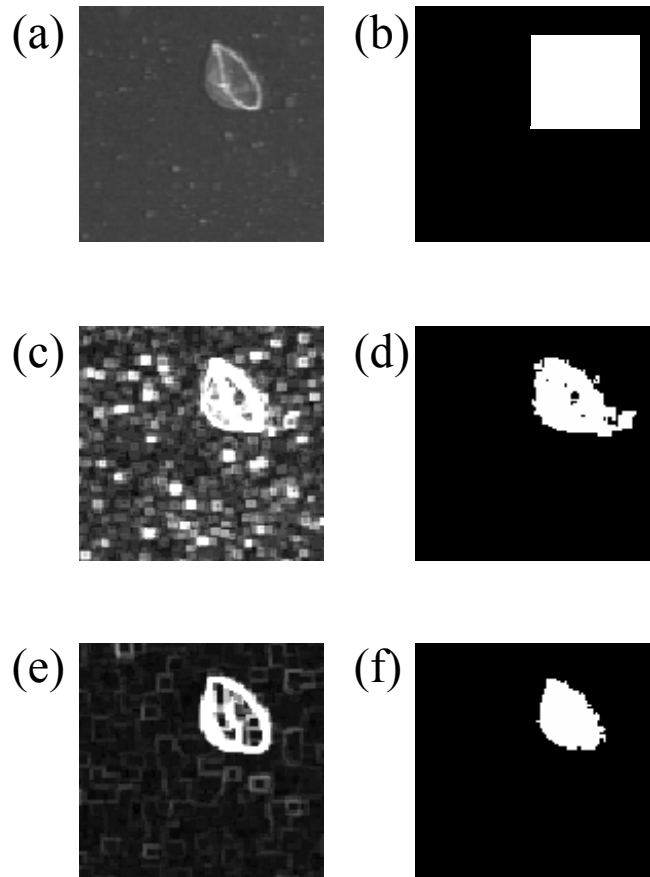


**Figure 4.12 A Two-Step Segmentation Strategy for Long-Sample Interval Jelly Tracking**

*The refined segmentation method performs segmentation by interpolating the background of (a) the luminance image within (b) an externally defined bounding box. The refined segmentation method involves two steps. First, a threshold algorithm is applied to the (c) smoothed gradient image to obtain (d) an initial segmentation. This initial segmentation step defines the dimensions of the bounding box, within which an interpolation estimates the background image with the animal absent. Subtracting the estimated background image from the original luminance image gives (e) the background difference image. Thresholding the background difference image produces (f) a refined segmentation.*



This augmented algorithm requires more computational effort than the simple gradient-threshold algorithm from Section 4.3.3. In exchange for this higher level of complexity, the algorithm produces a higher quality segmentation. For an image containing  $P$  pixels, the opening and closing operations, based on  $3 \times 3$  square structuring elements, require  $16P$  comparisons. The operations count to compute morphological gradient requires  $8P$  comparisons and  $P$  subtractions. Application of a global threshold requires  $P$  pixel comparisons. Each bounding box encloses  $Q$  pixels,  $Q < P$ . Synthesizing the background image requires  $11Q$  multiplications and additions and  $8Q$  table lookups. Calculating the background difference image requires  $Q$  subtractions. The final threshold step requires an additional  $Q$  comparisons. The final algebraic operations count is  $12Q + P$  additions and  $11Q$  multiplications. No iteration is required. Thus, if  $Q$  approaches  $P$ , the algorithm's computational cost greatly exceeds the  $5P$  additions required for the basic gradient threshold method.

Neither the background difference segmentation algorithm, nor a refined recognition method, has yet been implemented for ocean testing.

---

## 4.5 Summary

This chapter introduced a design tool, called segmentation efficiency, that streamlines synthesis of visual-tracking algorithms for new applications. The tool restricts the subset of vision algorithms that a designer need consider and, thus, decreases development time required for coding, for establishing ground truth, and for performing empirical experiments. The method reduces overhead by (1) assuming reliable performance of a general-purpose recognition strategy and (2) by quantifying application-specific segmentation reliability using a general model. In this context, the streamlined design approach relies on a metric, called the segmentation efficiency metric, which evaluates the area-weighted fraction of correctly identified pixels in an image given a particular choice of the model parameters for filtering and topological processing strategies. Combinations of strategies that result in high segmentation efficiency identify those classes of algorithm with highest potential for robust segmentation performance.

Applied to the jelly-tracking task, the segmentation efficiency approach identified morphological gradient and background difference filtering, over regional topologies, as the best strategies for reliable segmentation. This analysis resulted in the implementation of a computational simple but highly robust segmentation strategy based on a global threshold of morphological gradient. A

visual tracking system was implemented based on this segmentation subcomponent and a recognition subcomponent relying on a simple feature vector. In field experiments, this algorithm played a significant role in enabling long duration jelly tracking with an ROV-based pilot assist.

To predict the reliability of the vision system for very long AUV-based deployments, this chapter introduced the concept of the recognition number (a nondimensional sample period) to enable a new analysis of recognition system reliability. This analysis indicated a need for improved recognition reliability to permit AUV-based jelly tracking with a long sample period ( $\Delta t \approx 1$  s). Although this chapter does not search for improved recognition features directly, it does present an alternate segmentation strategy, based on the segmentation efficiency analysis, that improves the reliability of the existing feature set. The refined algorithm, which provides greater segmentation consistency at a slightly higher computation cost, will play a role in future testing of a low sample rate jelly-tracking system for energy-constrained AUV applications.

*Given conservatively estimated swimming speeds of most zooplankton during a vertical diurnal migration, it is clear that considerable horizontal distances can be traversed with ease in several hours. Furthermore, many species at specific developmental stages or even throughout their entire life cycle do not migrate vertically, and one sometimes wonders how these animals really do spend their time.*

- W.M. Hamner, S.W. Strand, G.I. Matsumoto and P.P. Hamner, 1987 [42]

---

As a component of the jelly-tracking system, the control law maps the visually derived position signal into a thrust command. Thrust commands actuate the tracking vehicle to center the animal in the camera viewing cone. The constraints of the vision sensor, used simultaneously to collect science data and, as described in the previous chapter, to detect target position, strongly influence the control design process. At its heart, the jelly-tracking law is a classical linear controller. The nature of the system hardware, however, motivates several enhancements to the control design. Specifically, this chapter discusses a strategy to harness redundant degrees of freedom in the jelly-tracking system to minimize thruster forces that might disturb the tracked target. Also the chapter describes the use of a nonlinear boundary control term and an estimator-based bias accommodation term to counter large external disturbances (transient or steady) in order to permit the use of a low-gain control law tuned to the bandwidth of jelly motion. This complete control system takes into account sensor and thruster geometry, the limited viewing field of the camera sensor, and the incorporation of a human pilot in a shared-control pilot-assist configuration.

Symbols in this and subsequent chapters are defined in the Nomenclature, pp. xix-xx.

---

## 5.1 Introduction

For low speed operations, ROV dynamics reduce, essentially, to those of a damped second order inertia. This form lends itself to a classical control design approach. Indeed, the core of the control law for the experimental system uses proportional-derivative (PD) control. This law alone, however, does not address all of the requirements for reliable jelly-tracking in the field. Additional considerations are required to account for system-level complexity, embodied by three

major issues: (1) identifying the subset of vehicle dynamics required to complete the control objective, (2) defining control commands in the redundant vehicle degree of freedom (DoF) to optimize secondary system goals, and (3) accounting for large disturbances given vision-system constraints. This chapter addresses these major issues in order to develop the control law used for field experiments. The chapter is organized as follows.

The remainder of Section 5.1 discusses related work and introduces a generic baseline linear control law, illustrated by Figure 5.1. The baseline law issues control in four DoFs, three translational and one yaw rotational. This classical control law provides a starting point for jelly-tracking and assists in pinpointing application-specific issues.

Section 5.2 considers the implications of jelly-tracking using a camera rather than a generic sensor. The camera sensor measures three DoF motion relative to the jelly. Accordingly, only three of the vehicle's four DoFs need be actuated to accomplish the control objective. Section 5.2 defines a subset of the plant dynamic equations required for tracking ( ${}^{\odot j}V'$  in Figure 5.2a). The control input to the plant,  ${}^{\odot j}u$ , is a three dimensional, based on a three-dimensional tracking error vector,  ${}^{\odot j}q_v$ . (In this chapter the letters  $q$  and  $p$  refer to the dimension of a position vector and the letters  $u$  and  $\tau$  refer to the dimension of a control input vector:  $q, u \in \mathbb{R}^3$  and  $p, \tau \in \mathbb{R}^4$ ). A cylindrical transformation is employed to decouple the DoFs required to complete the control objective (the range space) from those redundant for jelly tracking (the null space). The control reference must also be redefined to maintain consistency with the control objective.

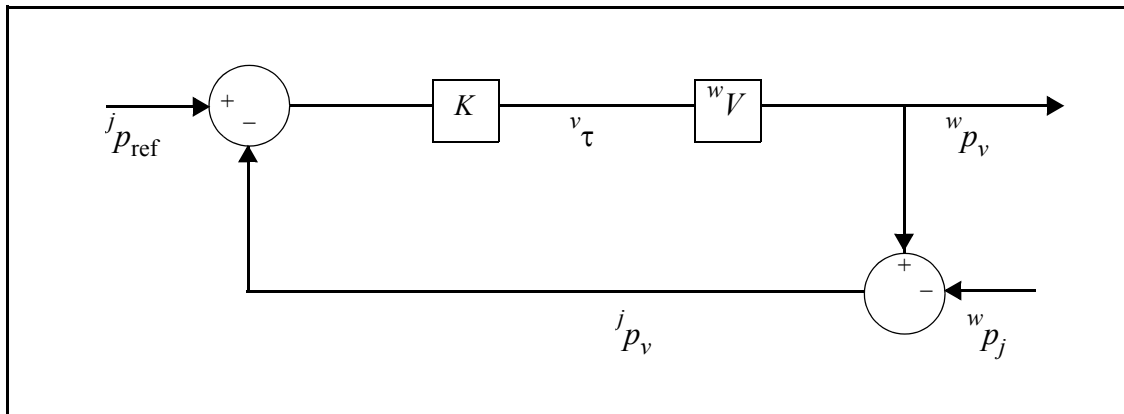


**Figure 5.1 Baseline Control Law**

*The baseline control law actuates the tracking vehicle ( ${}^wV$ ) in four degrees of freedom. The control input,  ${}^v\tau$ , is synthesized from a linear gain matrix ( $K$ ) and the error in the vehicle's position relative to a control reference expressed in the frame of the target jelly.*

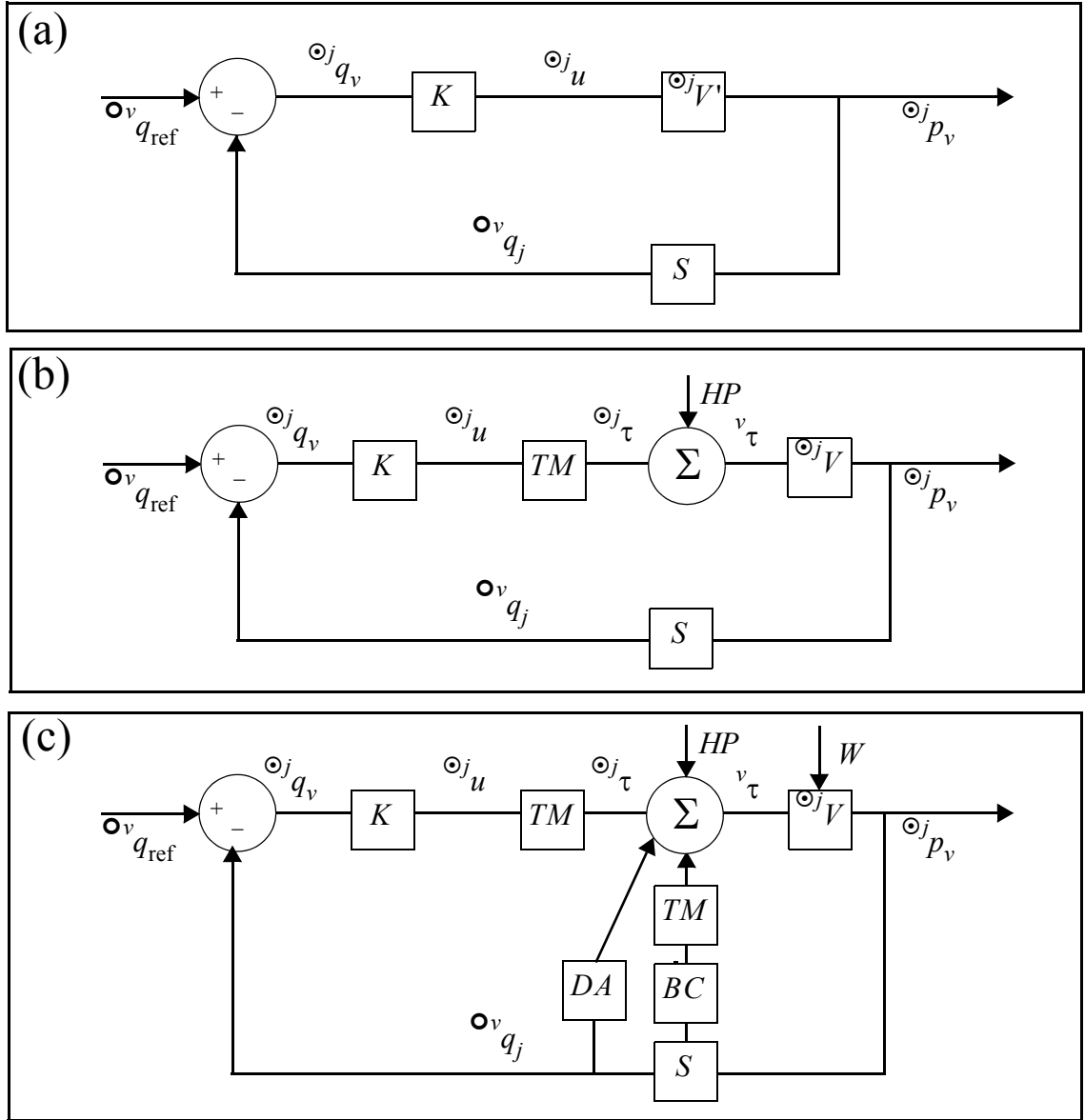


**Figure 5.2 Extensions to the Baseline Control Law**

Block diagrams explain modifications to a baseline control law developed in the following three sections. Frame transformations are implicit in each block. (a) Section 5.2 modifies the baseline control law to account for the use of a camera sensor. Because the camera sensor ( $S$ ) produces a three-coordinate position measurement relative to the target, only a tracking-objective subset of vehicle dynamics,  $\odot_j V$ , need be controlled. (b) Section 5.3 further modifies the baseline control law to account for the actual vehicle thruster arrangement. A thruster map ( $TM$ ) rotates and augments the dimension of the error signal into the four degree-of-freedom (DoF) form used for vehicle input. Flexibility in the redundant vehicle DoF permits system optimization and enhancement of control sharing with the human pilot ( $HP$ ). (c) Given the limited viewing cone of a real camera, Section 5.4 considers issues associated with large environmental disturbance forces ( $W$ ). Two additional control terms, a disturbance accommodation term ( $DA$ ) and a nonlinear boundary control term ( $BC$ ), help to prevent target loss.

Section 5.3 addresses a second issue for jelly tracking: mapping the control command into the form used by the vehicle thrusters. As illustrated by Figure 5.2b, the thruster map ( $TM$ ) to rotate and augment the dimension of the control input. Flexibility in design of the thrust command for the null space direction (orthogonal to the control objective space) permits an opportunity to optimize system design. The thruster map may be defined, for instance, to minimize hydrodynamic forces produced by the vehicle thrusters which might disturb the tracked animal. Alternatively, the redundant degree of freedom may be exploited to enhance shared control between the human pilot and the automated controller.

Section 5.4 addresses a third issue for jelly tracking: enforcing the boundaries of the camera image in the face of large disturbance forces on the tracking vehicle. As illustrated by Figure 5.2c, the section examines plant disturbance forces ( $W$ ) and divides them into two categories, quasi-steady disturbances and rapid transient disturbances. An estimator-based disturbance accommodation term ( $DA$ ) is employed to remedy offsets caused by quasi-steady bias forces. A nonlinear boundary control term ( $NL$ ) is employed to counter rapid transient disturbances which threaten to carry the target outside the boundaries of the camera image.

Finally, Section 5.5 summarizes the complete control law used for field jelly-tracking experiments.

### 5.1.1 Related Work

A significant body of prior work describes the control of underwater robotic vehicles. Fossen provides a good overview of the control challenges and the dynamics associated with hovering underwater robots [147]. Traditional techniques, including linear classical control [153] and feedback linearization [136], perform well in many situations. Given uncertainty in plant parameters, an issue of particular interest for ROV operations, many authors have also studied robust and adaptive control techniques. Some of these methods include linear  $H_\infty$  control [139,140], sliding mode control [143,144,151,163], and adaptive feedback linearization [137,150,159,165]. A large number of these studies share a common set of assumptions, namely the pitch-roll stabilization assumption, the axis-independence assumption, and the uniform current assumption. These three assumptions, described in more detail in the next section, are applied to the development of the control law for the jelly-tracking application.

### **Related Work in Experimental Tracking and Control**

The requirements of jelly tracking differ somewhat from those of previous submersible control applications and also from tracking applications in non-submerged environments. Most other underwater applications (employing torpedo-style vehicles), terrestrial tracking applications (employing wheeled vehicles), and aerial tracking applications (employing fixed-wing and rotor aircraft) have dynamic constraints and actuator constraints different from those for a fully-actuated, hovering submersible. In many ways, the closest prior analog to tracking a gelatinous animal is ocean-floor (benthic) station keeping, also using a hovering submersible. Vision-based benthic station keeping experiments face many of the same environmental challenges faced by the jelly-tracking application [106,108,110-111,115-118,120-121,124,127,131]. The primary differences between these station-keeping applications and jelly tracking involve the requirement to minimize disturbances to the tracked target and to respect the limits of the viewing cone. (The plane of the ocean floor, in benthic station keeping, rarely leaves the camera image except when holding position near a cliff. By comparison, a jellyfish is difficult to relocate if it leaves the camera image.)

Two prior experiments have reported the use of a submersible to track artificial targets in confined test tanks [118,126]. These experiments neither faced harsh ocean conditions, nor explicitly addressed constraints associated with tracking living targets or with tracking under constraints associated with a camera sensor.

### **Related Work in Null Space Decomposition for Underwater Robots**

A conventional ROV is overactuated with respect to the jelly-tracking task. The redundant DoFs, also called a null space, provide an opportunity to optimize the control law for the particulars of an application. In one underwater robot application, for instance, Sarkar investigated the use of the null space of a thruster map to compensate for thruster failure and saturation [158]. In a separate study, Rives decomposed the workspace for a pipe-following submersible robot into two modes, with separate controllers for translational motion, along the pipe, and tracking motions, perpendicular to the pipe [157]. This chapter combines the thruster map selection and workspace decomposition concepts in the context of jelly tracking.

### **Related Studies of the Disturbance Environment for Underwater Robots**

Large disturbances on the jelly-tracking vehicle may cause loss of the target animal outside the camera field of view. This chapter divides these disturbances into two groups: (1) rapid transient

disturbances and (2) low-frequency disturbances that remain approximately constant through time. Previous studies have analyzed disturbances which fall into both these categories.

An important source of rapid-transient disturbances involves the vehicle thrusters. Thrusters are assumed to perform with a high bandwidth, significantly higher than that for the closed-loop vehicle dynamics. This assumption is, in general, justified by existing models of thruster dynamics [138,152,161,162,164]. These models indicate, however, that nonlinearity in the thruster equations produces variable thruster bandwidth, which drops toward zero with the rotor angular velocity. Infrequent aggressive control is required to compensate for slow thruster dynamics in these instances.

The dominant source of large quasi-steady disturbances, for ROV applications, is the vehicle tether. A study by McLain measured internal tension in the tether for the ROV *Ventana* [154]. These data demonstrate the need for the control law to offset significant low-frequency, high-magnitude tether traction, even in the case of a neutrally-buoyant tether.

This chapter recommends the use of a low-gain cylindrical PD control law, supplemented by two additional control terms: an estimator-based disturbance accommodation term and a nonlinear boundary control term. The low gain control law tracks motion of the animal target without requiring significant thruster action which might influence animal behavior. The disturbance accommodation term counters quasi-steady biases associated, for instance, with strong tether traction. The boundary control term provides aggressive control when the animal approaches the edges of the camera image in order to counter transient disturbances, such as unmodelled dynamics of the nonlinear vehicle thrusters. Neither the low-frequency disturbance accommodation concept [148,166] nor the boundary control concept, based loosely on sliding mode control [146], is fundamentally new. The synthesis of the complete jelly-tracking control system and its experimental validation, however, represent a significant contribution to the underwater robotics field.

### 5.1.2 A Baseline Control Law

This section develops the plant model and a baseline control for jelly-tracking, as shown by Figure 5.1. Standard assumptions for a hovering submersible robot are applied to simplify the plant model to a four DoF, independent-axis representation. This form lends itself to classical control design techniques. The baseline control does not, however, address the specific hardware and constraints for the jelly-tracking application. A description of these deficiencies motivates further



extensions to the control law, which are developed in detail in the subsequent sections of this chapter.

### Plant Model in Cartesian Coordinates

The six-DoF equation of motion for the hovering submersible is:

$$\mathcal{M} {}^w\ddot{\mathbf{p}}_v = {}^wT - {}^wD + {}^w\boldsymbol{\tau} \quad (5.1)$$

Tether forces and the buoyancy-gravity difference are lumped into the term  ${}^wT$ . Hydrodynamic forces are split into the drag force,  ${}^wD$ , and the unsteady added-mass reaction, which is lumped into  $\mathcal{M}$ , the vehicle's inertia matrix. The  ${}^w\boldsymbol{\tau}$  term captures thruster forces. All variables are vectors in  $\mathbb{R}^6$ , except for the mass term,  $\mathcal{M}$ , which is a square matrix. The leading  $w$ -superscript indicates the water fixed frame. If ocean currents are uniform and irrotational, then the water frame is an inertial frame.

**Assumption 5.1. Uniform Current Assumption:** The length and time scales for gradients in the hydrodynamic flow field are assumed significantly longer than the vehicle size or time constant. Consequently local flow is considered to be a parallel current with constant, uniform velocity (relative to the ocean floor).

A further assumption reduces the number of controlled DoFs from six to four. This assumption involves pitch and roll motions, which are negligible for the jelly-tracking vehicle.

**Assumption 5.2. Pitch-Roll Deviations Assumed Small:** Pitch and roll axes are assumed regulated by a passive-buoyancy moment or by active control. Pitch and roll angle deviations from the equilibrium trim angle are thus small.

Indeed, pitch and roll motions are small for ROV-type vehicles, which generally have a strong buoyancy moment produced by a vertical separation of dense components below flotation. For the experimental vehicle, ROV *Ventana*, this form of passive stabilization generally holds pitch and roll deviations within fewer than  $5^\circ$  from neutral. Assumption 5.2 is also generally valid for low-speed, hovering vehicles that actively stabilize pitch and roll motion. (e.g. This is the case for Stanford's OTTER [137] and the University of Hawaii's ODIN [160].)

A final assumption maintains that the four remaining vehicle axes have independent dynamics.

**Assumption 5.3. 4-Axis Independence Assumption:** At low speeds, hydrodynamic coupling and inertia coupling affects are neglected for the hovering submersible. Moment terms resulting from axial tether, drag and thruster forces are also neglected. The vehicle is assumed to be independently actuated in the three translational and in the yaw rotational DoF.

For axis-independence, both off-diagonal inertia matrix terms and cross-coupling hydrodynamic drag terms must be small, and the dimension of the actuator input must match the dimension of the vehicle state space. Also, the centers for axial thrust, hydrodynamic drag and the tether force must approximately align with the vertical line through the center of mass, such that these forces exert no significant moments in the yaw direction. With pitch and roll angles assumed small, axis coupling effects can be neglected, even for ROV platforms subject to large lateral tether forces applied vertically above the vehicle's mass center.

These assumptions are reasonable for a large ROV like the experimental vehicle, *Ventana*. For other platforms, if the assumptions are not valid, a feedback linearization law is necessary to recover axis independence [137,144]. Thus the jelly-tracking vehicle is presumed to deliver independent four-axis dynamics. The dynamics for the four DoF system still follow the form of (5.1), which represents a damped second-order inertia subject to tether, buoyancy and thruster forces.

### Coordinate Frames

To describe the jelly-tracking control system requires the definition of four reference frames. These frames are fixed to the vehicle ( $v$ ), to the primary camera sensor ( $s$ ), to the jellyfish ( $j$ ), and to the water ( $w$ ). The axes of the vehicle frame are assigned according to the standards of the Society of Naval Architects and Marine Engineers (SNAME). The vehicle  $x_v$ -axis corresponds to the surge (fore-aft) direction; the  $y_v$ -axis, to the sway (lateral) direction; and the  $z_v$ -axis to the heave (vertical) direction. The camera axes are assigned to align with the vehicle axes when the camera points straight downward. For this reason, the camera optical axis aligns with the  $z_s$ -axis. The water-frame axes align with world coordinates; the  $z_w$ -axis always points along the gravitational direction, downward. In the case of a constant, uniform current, the water frame may be treated as an inertial frame. Finally, the jelly-frame is defined with its origin on the centroid of the gelatinous animal target. Because the vision sensor does not detect the orientation of the animal relative to the camera, the axes of the jelly frame are assigned to align with the water frame axes at all times. Hence the jelly frame translates, but does not rotate, with the animal subject.

ROV sensors provide full observability of motion of the vehicle frame ( $v$ ) relative to the jelly frame ( $j$ ). The stereo-camera pair measures the position vector,  ${}^s q_j$ . Given knowledge of the camera-vehicle offset vector,  ${}^v q_s$ , which is calibrated in advance, and knowledge of the camera angles, the vector between the jelly and the vehicle,  ${}^j q_v$ , may be inferred in real time. The compass measures the relative angles between the  $j$  and  $v$  frames. Thus the four DoF state vector  ${}^j p_v$  is fully specified for the purposes of control.

Although water-relative measurements are not required for control, they are relevant for scientific study. The optional addition of a DVL instrument, which measures the water-relative velocity,  ${}^w \dot{q}_v$ , can provide observability of vehicle motion relative to the water column.

### A Baseline Control Law

This section outlines a classical control law for a second-order plant with four independent axes. This law provides a baseline for the development of an extended control law specifically tailored

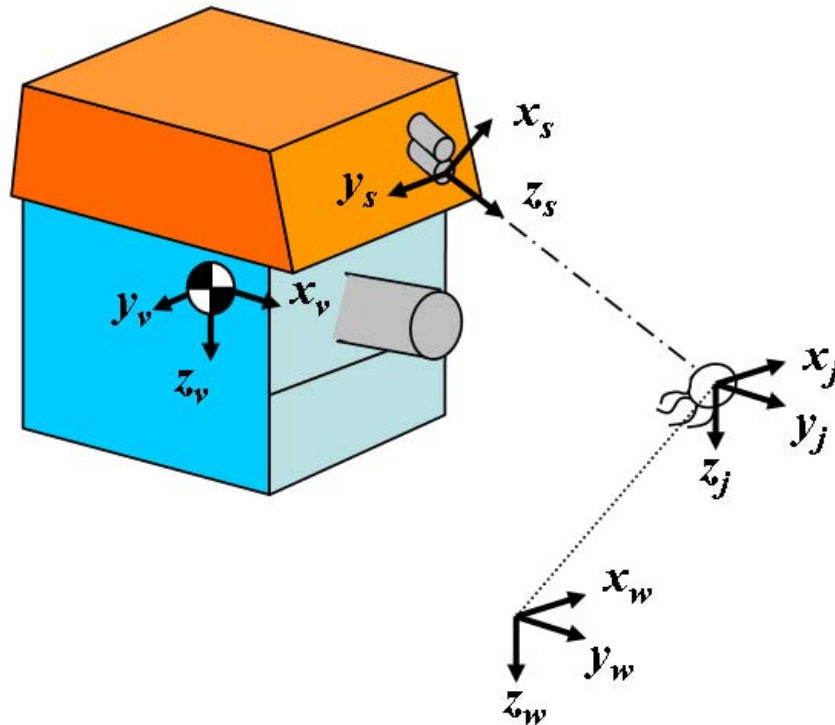


**Figure 5.3** Coordinate Frames

*The jelly tracking system uses four coordinate frames: an inertial frame attached to the water,  $w$ , a non-rotating frame attached to the jelly centroid,  $j$ , a frame attached to the camera sensor,  $s$ , and a frame attached to the vehicle's mass center,  $v$ .*

to details associated with the sensors, the thruster configuration and the animal target associated with the jelly-tracking application.

The baseline control operates on the state vector  ${}^w p_v$ , which relates the vehicle ( $v$ ) to the water frame ( $w$ ) and consists of three translational coordinates,  $x$ ,  $y$ , and  $z$ , and by one yaw coordinate,  $\psi$ .

$${}^w p_v = \begin{bmatrix} {}^w x_v & {}^w y_v & {}^w z_v & {}^w \psi_v \end{bmatrix}^T \quad (5.2)$$

For the case of no jellyfish motion relative to the water column, the water-fixed frame ( $w$ ) and the jelly-fixed frame ( $j$ ) are identical. Given the plant can be represented approximately as an independent-axis inertial mass, a classical proportional-derivative law can be specified as:

$${}^w \tau = \begin{bmatrix} K_p & K_d \end{bmatrix} \begin{bmatrix} {}^w p_v \\ {}^w \dot{p}_v \end{bmatrix} \quad (5.3)$$

Here the gain matrices  $K_p$  and  $K_d$  are diagonal matrices in  $\Re^4$ . Nominal gains are based on a simple estimate of the vehicle inertia. In the field, the nominal gains may be adjusted to compensate for variation of model parameters and for the effects of sensor noise

Control law (5.3) is, in fact, the law employed by prior researchers to demonstrate artificial-target tracking in confined tanks [118,126]. A similar control law has also been used for benthic station-keeping with an ROV in the deep ocean [153].

### Motivation for an Extended Control Law

Issues specific to the biology application or to the system hardware are not explicitly addressed by the baseline control law. The subsequent three sections of this chapter address these limitations.

A first concern involves the discrepancy in the dimension of the camera measurement (3 component position) and of the vehicle dynamic equation (4 DoF). The control goal requires only that the target remain centered in the camera; hence, a set of control objective equations can be developed for the vehicle that decouple the redundant DoF.

Second, the baseline control makes no attempt to minimize water motions which might impact animal behavior. The redundant DoF can be exploited to optimize thruster output to reduce

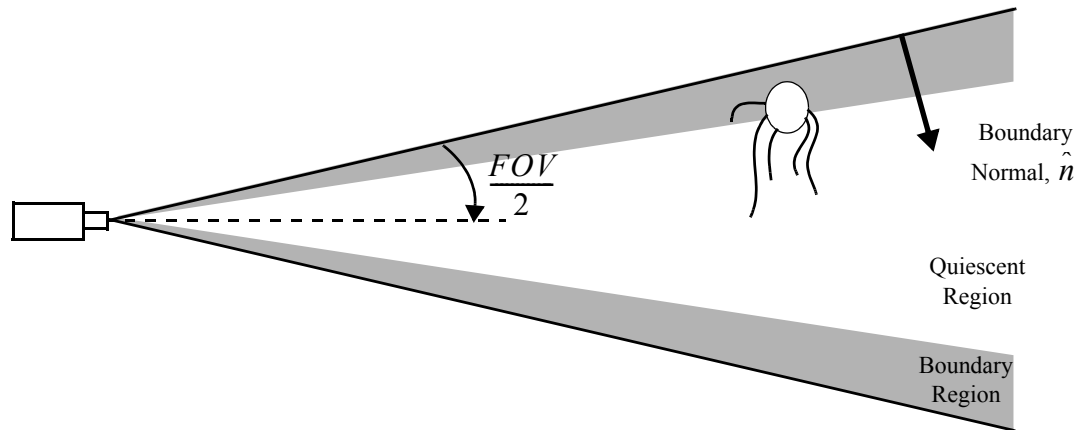


**Figure 5.4 Camera Viewing Cone**

*The figure illustrates the limited volume within which the camera can detect the jelly target.*

the momentum ejected by vehicle thrusters. The redundant DoF also provides an opportunity to construct a shared control in which the human and computer pilots cooperate to issue simultaneous, noninterfering commands.

Finally, the baseline control law does not specifically account for large disturbances on the tracking vehicle, nor does it recognize the limits of the viewing cone for the camera sensor (illustrated by Figure 5.4). Given the desire to keep control gains low to minimize momentum output by the thrusters, low and high frequency disturbance forces may introduce large deviations in the error state. These deviations may in turn result in loss of the target outside the camera viewing cone. This circumstance is to be avoided as it interrupts the sensor signal used for control and the data stream for science. The addition of disturbance-accommodation and boundary-enforcing control terms helps prevent target loss while permitting thrust to remain low during normal operation.

## 5.2 Defining the Control Objective

The baseline system of Figure 5.1 assumes generic sensor capabilities. The choice of specific sensor hardware, including the primary (camera) sensor and the secondary (compass, camera angle) sensors, motivates a careful definition of the control objective. The use of physical sensor hardware also involves additional frame transformations and consistent specification of the reference

state. This section details these modifications to the baseline control law, as illustrated by Figure 5.2a. First, Section 5.2.1 describes a cylindrical transformation of the vehicle dynamics to decompose the plant into a set of control-objective equations required for the jelly-tracking task, and into an orthogonal equation, that defines the tracking-law null space. Subsequently, Section 5.2.2 describes the frame transformations and the control reference specifications required to map the camera position signal into the control-objective space.

### 5.2.1 Decomposition of Vehicle Equations

This section discusses transformation first of the vehicle kinematic states and second of the vehicle dynamic equations into control-objective coordinates. The control-objective coordinates, consisting of the target-relative range, depth and yaw bearing, embody the requirements of effective tracking. The decomposition of vehicle DoFs into control objective form specifically distinguishes between the control range space and the orthogonal null space, which consists of DoFs not required to accomplish the jelly tracking objective. The key to this decomposition is a transformation of the vehicle kinematics from cartesian coordinates into cylindrical coordinates.

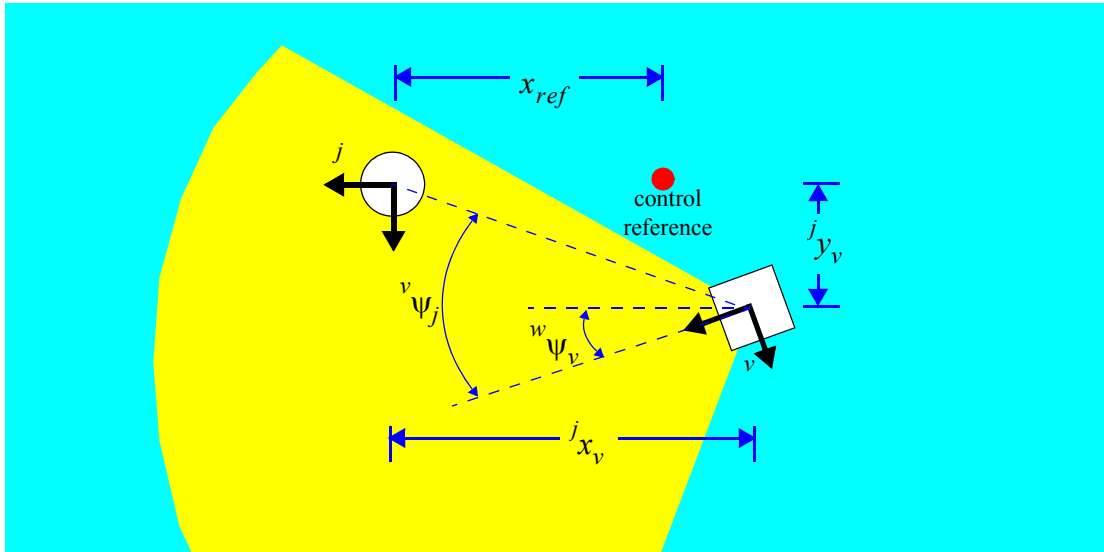


**Figure 5.5 The Viewing Cone and ROV Overactuation**

*The figure depicts the coupling between the ROV's three planar degrees of freedom. The ROV (square) needs to control only two planar states to keep the jelly (circle) in the highlighted viewing cone.*

### Decomposition of Kinematic States

Because sensors do not observe water-relative motion, vehicle position is specified in jelly-relative coordinates:

$${}^j p_v = \begin{bmatrix} {}^j x_v & {}^j y_v & {}^j z_v & {}^w \psi_v \end{bmatrix}^T \quad (5.4)$$

The jelly-fixed frame is defined treating the jelly as an irrotational point; thus the jelly frame translates but does not rotate relative to the inertial frame ( $w$ ). In this section, the camera sensor is assumed to be attached rigidly to the vehicle, so that the sensor frame ( $s$ ) and the vehicle frame are equivalent. This assumption will be relaxed in Section 5.2.

The jelly-tracking objective requires that the target remain at a fixed position relative to the camera sensor. The horizontal pixel location of the target in the video image depends on the relative bearing between the target and vehicle,  ${}^v \psi_j$ . The relative bearing in turn depends on the vehicle yaw heading,  ${}^w \psi_v$ , and vehicle translation in the horizontal plane. Setting aside the vertical degree of freedom (under the axis-independence assumption), the vehicle retains three in-plane actuated DoFs, but requires only 2 in-plane actuated DoFs to perform the tracking task. This fact is illustrated by Figure 5.5. In the figure, the x-axis of the jelly frame can be defined, without loss of generality, to pass through the control reference position, offset from the jelly by a distance  $-x_{ref}$ . The relative bearing angle is a nonlinear combination of yaw heading and the vehicle's position in the horizontal plane.

$${}^v \psi_j = {}^w \psi_v + \tan\left(\frac{{}^j y_v}{{}^j x_v}\right) \quad (5.5)$$

Chapter 2 recommends a minimum standoff distance for biological observation of approximately  $x_{ref} \approx 1$  m. Equation (5.5) simplifies for the case of small errors relative to the standoff distance,  $x_{err} \ll x_{ref}$ . Here, the error vector is the location of the tracking vehicle relative to the control reference.

$$(x_{err}, y_{err}) = ({}^j x_v - x_{ref}, {}^j y_v) \quad (5.6)$$

For the case of small errors,  ${}^v x_j$  can be suppressed in (5.5), with  ${}^v x_j \approx x_{ref}$ . Also, a small angle approximation for the tangent function in (5.5) may be applied since  $y_{err} \ll x_{ref}$ . The resulting small error approximation is (5.7).

$${}^v \psi_j \approx {}^w \psi_v + \frac{{}^j y_v}{x_{ref}} \quad (5.7)$$

Thus for small errors, the relative bearing angle is a linear combination of yaw heading and lateral position errors. Thus, the control objective may be implemented using yaw actuation alone, lateral actuation alone, or actuation in both directions simultaneously.

The linear baseline control, (5.3), encounters problems for large errors, at which the assumptions underlying the relationship (5.7) break down. To maintain this two-coordinate, linear relation at large angles requires a transformation of the state vector, (5.4), from Cartesian coordinates to cylindrical coordinates.

The cylindrical coordinate system, like the Cartesian, is centered on the jellyfish and translates, but does not rotate, with respect to the inertial frame. The cylindrical coordinate system, illustrated in Figure 5.6, is described by the following state vector.

$$\mathbf{o}^j p_v = \begin{bmatrix} {}^j r_v & {}^j \gamma_v & {}^j z_v & {}^w \psi_v \end{bmatrix}^T \quad (5.8)$$

In this expression, the coordinate  ${}^j r_v$  denotes a range from the animal to the tracking vehicle,  ${}^j \gamma_v$  denotes the vehicle's circumferential location,  ${}^j z_v$  denotes the depth differential, and  ${}^w \psi_v$  denotes the vehicle heading.

The cylindrical coordinate system inherently decouples two coordinate axes critical for the jelly-tracking task: the relative range and the relative depth. The third coordinate axis required to stabilize the position of the viewing cone around the target animal is the yaw bearing angle. In cylindrical coordinates, the yaw bearing is an affine combination of the components of (5.8).

$${}^v \psi_j + \pi = {}^w \psi_v - {}^j \gamma_v \quad (5.9)$$



This equation has the same form as (5.7), but does not rely on a small-error approximation. The affine offset of  $\pi$  in (5.9) may be removed through a redefinition of the relative bearing angle,  ${}^v\psi_j$ , to incorporate the offset.

Thus the set of kinematic states required to accomplish the jelly-tracking control objective may be captured by a linear projection matrix,  $\sigma_r$ .

$$\sigma_r = \begin{bmatrix} 1 & 0 & 0 & 0 \\ 0 & -1 & 0 & 1 \\ 0 & 0 & 1 & 0 \end{bmatrix} \quad (5.10)$$

The corresponding null space projection,  $\sigma_n$ , describes the DoF that does not impact the jelly-tracking objective.

$$\sigma_n = \begin{bmatrix} 0 & 1 & 0 & 1 \end{bmatrix} \quad (5.11)$$

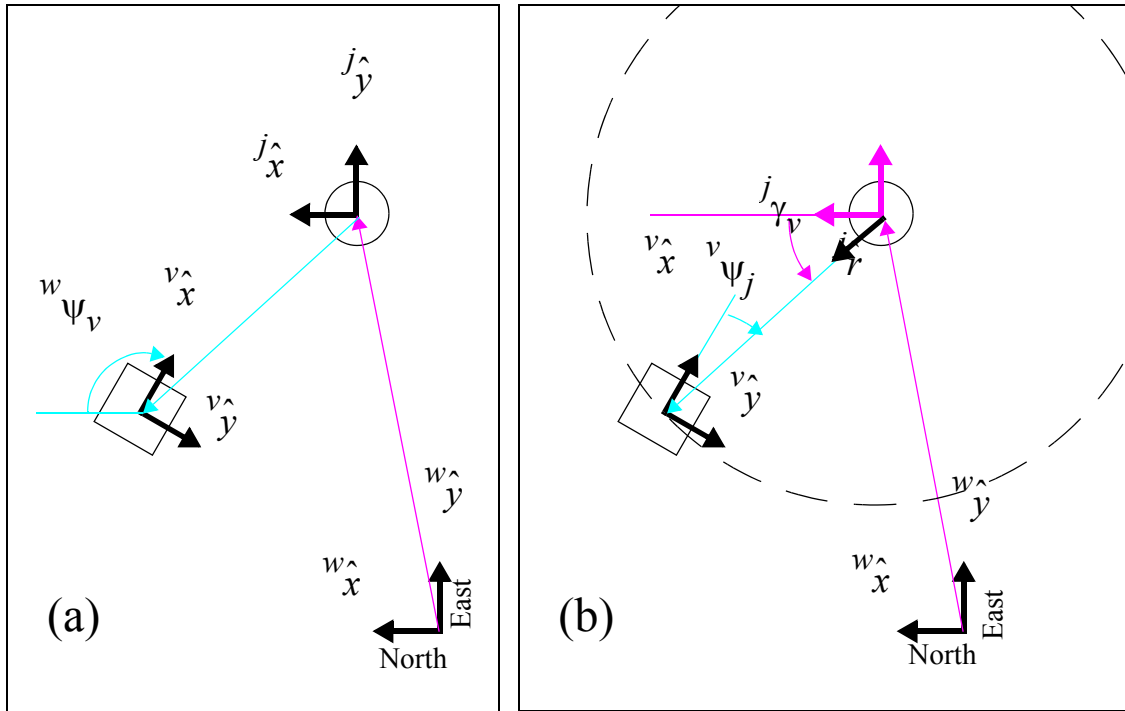


**Figure 5.6 Jelly-Tracking Coordinate Systems**

Two coordinate systems are compared: (a) Cartesian and (b) Cylindrical. In both diagrams, the circle indicates the jelly target. The square indicates the ROV

The full rank matrix,  $\sigma$ , combines the range and null space projections.

$$\sigma = \begin{bmatrix} \sigma_r \\ \sigma_n \end{bmatrix} \quad (5.12)$$

In effect transformation by  $\sigma$  decomposes the cylindrical kinematic states according to the requirements of the jelly-tracking control objective.

$$\odot_j p_v = \sigma \bullet_j p_v \quad (5.13)$$

$$\odot_j p_v = \begin{bmatrix} {}^j r_v & {}^v \psi_j & {}^j z_v & {}^j n \end{bmatrix}^T \quad (5.14)$$

The new control-objective vector incorporates the three tracking coordinates (relative range, bearing to the target, and relative depth) as well as the null space coordinate,  ${}^j n$ .

### Decomposition of Dynamic Equations

The decomposition operator,  $\sigma$ , can further be applied to decompose the vehicle dynamic equations. This section first develops the vehicle dynamic equations in cylindrical coordinates and then decomposes them into the range and null spaces for the tracking objective.

As an intermediate step in deriving the cylindrical motion equations, it is useful to first transform the inertial dynamics of (5.1) into the cartesian jelly-fixed frame. This transformation between the water-fixed frame,  $w$ , and the jelly-fixed frame,  $j$ , generates an acceleration pseudo-force,  ${}^w A_j$ .

$${}^w A_j = -\mathcal{M} {}^w \ddot{p}_j \quad (5.15)$$

Because the jelly-fixed frame is defined to translate with the target jelly, but not to rotate with respect to the inertial frame, the yaw component of  ${}^w A_j$  is zero. Incorporating this pseudoforce term, the jelly-frame dynamics for the tracking vehicle are as follows.

$$\mathcal{M} {}^j \ddot{p}_v = {}^j T - {}^j D({}^w \dot{p}_j, {}^j \dot{p}_v) + {}^j \tau + {}^w A_j \quad (5.16)$$

As expressed by (5.16), the drag force in the jelly-fixed frame is a function of both this unobserved jellyfish velocity,  ${}^w\dot{p}_j$ , and the observed jelly-relative velocity,  ${}^j\dot{p}_v$ .

A second transformation takes the dynamics of the vehicle in the jelly-fixed frame from Cartesian coordinates, as expressed by (5.16), into cylindrical coordinates. New inertial terms, associated with the Coriolis and centrifugal pseudoforces, appear in this transformation:

$${}^vA_{\mathbf{O}j} = M \begin{bmatrix} {}^j r_v ({}^j\dot{\gamma}_v)^2 & -2 \frac{{}^j\dot{\gamma}_v {}^j\dot{r}_v}{{}^j r_v} & 0 & 0 \end{bmatrix}^T. \quad (5.17)$$

Incorporating the pseudoforce vector,  ${}^vA_{\mathbf{O}j}$ , the vehicle equations in cylindrical, jelly-fixed coordinates are

$${}^{\mathbf{O}j}\ddot{p}_v = \mathcal{M}^{-1} ({}^jS_{\mathbf{O}j} ({}^jT - {}^jD - {}^wA_j + {}^j\tau) + {}^vA_{\mathbf{O}j}). \quad (5.18)$$

The drag, tether, and thruster forces ( ${}^jD$ ,  ${}^jT$ , and  ${}^j\tau$ ), along with the inertial acceleration term associated with jelly swimming,  ${}^wA_j$ , must all be rotated through the transformation matrix,  ${}^jS_{\mathbf{O}j}$ , which relates Cartesian and cylindrical coordinates:

$${}^jS_{\mathbf{O}j} = \begin{bmatrix} \cos({}^j\dot{\gamma}_v) & \sin({}^j\dot{\gamma}_v) & 0 & 0 \\ -\sin({}^j\dot{\gamma}_v) & \cos({}^j\dot{\gamma}_v) & 0 & 0 \\ {}^j\dot{r}_v & {}^j\dot{r}_v & 0 & 0 \\ 0 & 0 & 1 & 0 \\ 0 & 0 & 0 & 1 \end{bmatrix}. \quad (5.19)$$

The cylindrical dynamic equation (5.18) isolates acceleration for two of the three coordinates required to accomplish the jelly-tracking control objective: range and depth. The acceleration for the third objective coordinate, relative bearing, is a linear combination of yaw and circumferential acceleration.

$${}^v\ddot{\Psi}_j = {}^w\ddot{\Psi}_v - \dot{{}^j\gamma}_v \quad (5.20)$$

Based on this linear relationship, the decomposition of the dynamic equations requires, simply, a multiplication of (5.18) by the decomposition matrix,  $\sigma$ . The resulting dynamic equation, decomposed in terms of the jelly-tracking objective and its null space, is

$${}^{\odot j}\ddot{p}_v = \sigma \mathcal{M}^{-1} ({}^jS_{\mathbf{O}_j}({}^jT - {}^jD - {}^wA_j + {}^j\tau) + {}^vA_{\mathbf{O}_j}) \quad (5.21)$$

The acceleration vector,  ${}^{\odot j}\ddot{p}_v$ , is the second derivative of the position vector expressed in control-objective coordinates, (5.14). For control purposes, it is useful to rewrite the dynamic equation (5.21) to separate the control term and convert it, also, to tracking-objective coordinates. The following equation, (5.22), shifts the control term to the left side of the equality; the remaining forces, treated as disturbances, remain on the right side of the equality.

$${}^{\odot j}\ddot{p}_v - {}^{\odot j}\tilde{\tau} = \sigma \mathcal{M}^{-1} ({}^jS_{\mathbf{O}_j}({}^jT - {}^jD - {}^wA_j) + {}^vA_{\mathbf{O}_j}) \quad (5.22)$$

The tilde in the term  ${}^{\odot j}\tilde{\tau}$  represents normalization by the inertia matrix,  $\mathcal{M}$ . In effect, (5.22) describes the revised plant dynamics block,  ${}^{\odot j}V$ , illustrated in Figure 5.2a.

### 5.2.2 Specifying a Consistent Control Reference and Error State

The previous section did not distinguish between the vehicle frame ( $v$ ) and the sensor frame ( $s$ ). This section discusses the frame transformations necessary to align the control error measurement with the vehicle dynamic equations, (5.22). These transformations are embedded in the  $S$  block in Figure 5.2. The frame transformation also affects the definition of the reference state.

The experimental system defines the reference state using a position-based visual servoing strategy to avoid discrepancies associated with uncertainties in frame transformations. This section describes both position-based visual servoing (PVS) and the alternative approach commonly employed in the vision literature, image-based visual servoing (IVS). A comparison of the techniques establishes the advantages of the PVS approach for the jelly-tracking application. Whereas the PVS framework controls vehicle position, the IVS framework controls camera position. As such, PVS forms an error vector that incorporates the camera-vehicle offset. Formed directly in the camera frame, the IVS error state need not include the camera-vehicle offset. With IVS, however, the dynamic equations must be transformed into the camera frame (through the offset rota-

tion and translation) to design a control law that stabilizes camera position. Figure 5.7 illustrates the error states defined for each of these two approaches.

Offset uncertainty, in the form of an unknown bias, occurs commonly in field operations. It is assumed that measurements of the angle and translation offsets between the camera focal point and the vehicle mass center contain bias errors. Measurements by the camera angle sensors, in particular, contain biases that result from frequent vehicle reconfiguration, from shifts caused by rough seas, and from sensor drift. These errors, in turn, bias transformation of vectors between the sensor frame ( $s$ ) and the vehicle frame ( $v$ ). Because PVS and IVS incorporate the camera-vehicle offset differently, unknown biases affect each of these methods in a different manner.

For the PVS approach, used in the experimental platform, the Cartesian position measurement of the jelly in the sensor frame,  ${}^s q_j$ , was transformed into a cylindrical position in the vehicle frame,  ${}^v q_j$ . Here the vector is labeled  $q$  instead of  $p$  to reflect the reduced dimension ( $q \in \mathbb{R}^3, p \in \mathbb{R}^4$ ). Biases in the camera-vehicle offset measurement would result in steady state errors if the control reference were specified in the jelly frame. To subtract out the effects of uncertainty in the camera-vehicle offset, the control reference must be defined in the camera frame

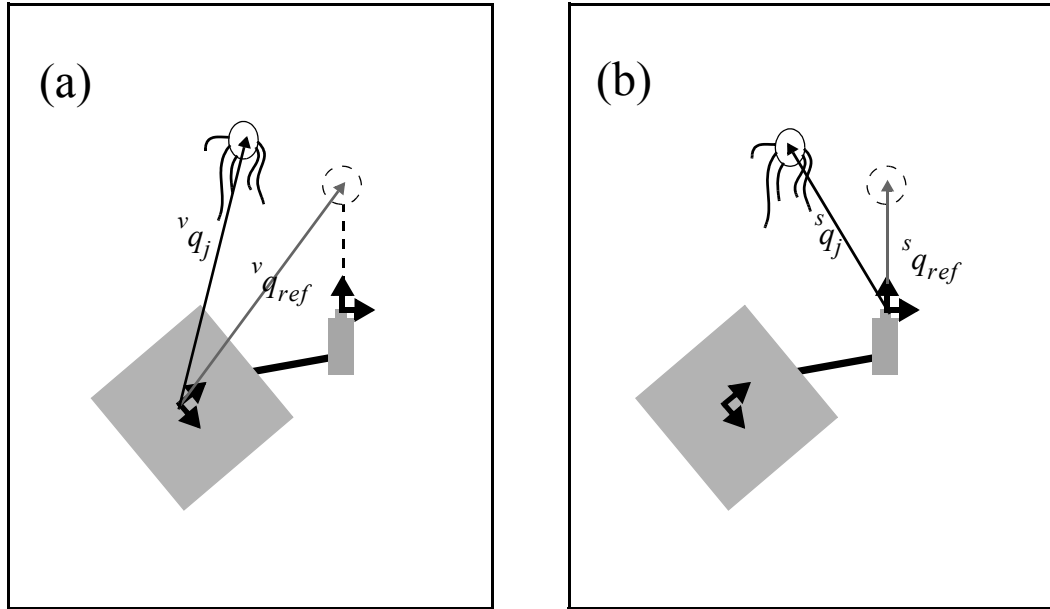


**Figure 5.7 Defining the Error State**

Two error state formulations are compared: (a) Position-Based Visual Servoing (PVS) and (b) Image-Based Visual Servoing (IVS)

and must undergo the same transformation as the target position measurement. Thus the control reference is defined in the sensor frame at a scalar distance along the optical axis,  ${}^s z_{ref}$ .

$${}^s q_{ref} = \begin{bmatrix} 0 & 0 & {}^s z_{ref} & 0 \end{bmatrix}^T \quad (5.23)$$

In PVS, a first step in transforming both the control reference and the sensor measurement involves the operator  ${}^s \bar{S}_v({}^s q)$ , which converts vectors from the sensor frame,  $s$ , into the vehicle frame,  $v$ .

$${}^v q = {}^s \bar{S}_v({}^s q) = {}^s R_v {}^s q + {}^v q_s \quad (5.24)$$

Here the rotational offset between the sensor and the vehicle is captured by the rotation matrix,  ${}^s R_v$ . The translational offset is captured by the vector  ${}^v q_s$ . Following this transformation, a second transformation takes the control reference and sensor measurement vectors from Cartesian to cylindrical coordinates. This is a nonlinear operation,  ${}^v \bar{S}_{\mathbf{O}_v}({}^v q)$ .

$$\mathbf{O}_v {}^v q = {}^v \bar{S}_{\mathbf{O}_v}({}^v q) = \begin{bmatrix} {}^v r \\ {}^v \psi \\ {}^v z \end{bmatrix} = \begin{bmatrix} \sqrt{{}^v x^2 + {}^v y^2} \\ \text{acos}\left(\frac{{}^v x}{\sqrt{{}^v x^2 + {}^v y^2}}\right) \text{sgn}({}^v y) \\ {}^v z \end{bmatrix} \quad (5.25)$$

The PVS error vector is based on a difference of transformations reference vector,  ${}^s q_{ref}$ , and the transformed target position vector,  ${}^s q_j$ :

$$\mathbf{O}_v q_{pvs} = {}^v \bar{S}_{\mathbf{O}_v}({}^s \bar{S}_v({}^s q_j)) - {}^v \bar{S}_{\mathbf{O}_v}({}^s \bar{S}_v({}^s q_{ref})) \quad (5.26)$$

By subtracting two vectors transformed by the same process, the PVS error formulation yields a zero value when the reference and target positions align, even when subject to an unknown bias in the camera-vehicle offset. The error vector in tracking-objective coordinates,  ${}^{\odot j} q_v$ , is simply the negative of (5.26).

$${}^{\odot j}q_v = -{}^{\bullet v}q_{pvs} \quad (5.27)$$

A feedback control law based on this term defines a range-space thruster input,  ${}^{\odot j\sim}u \in \mathfrak{R}^3$ , that, supplemented by a null space control component,  $\mathfrak{v}$ , defines the full four-DoF input,  ${}^{\odot j\sim}\tau \in \mathfrak{R}^4$ .

$${}^{\odot j\sim}\tau = \begin{bmatrix} {}^{\odot j\sim}u \\ \mathfrak{v} \end{bmatrix} \quad (5.28)$$

The full four-DoF thrust serves as the input to the objective-space plant model, given by (5.22).

By contrast, the IVS error vector would be formed by converting the reference and target position vectors into cylindrical coordinates in the camera frame and subtracting.

$${}^{\bullet s}q_{ivs} = {}^s\bar{S}_{\bullet s}({}^s q_j) - {}^s\bar{S}_{\bullet s}({}^s q_{ref}) \quad (5.29)$$

Here the transformation into cylindrical coordinates,  ${}^s\bar{S}_{\bullet s}({}^s q)$ , has a form analogous to (5.25). The error vector can be expressed in a set of tracking-objective coordinates centered on the sensor-frame,  ${}^{\odot s}q_v$ .

$${}^{\odot j}q_s = -{}^{\bullet s}q_{ivs} \quad (5.30)$$

To stabilize the camera using this error vector requires that the vehicle dynamic equation, (5.22), be transformed into the cylindrical coordinate system centered on the camera sensor. Based on the kinematic relationship between the camera and sensor frames, defined by (5.24), the 4-DoF sensor-frame equations in control-objective form are as follows.

$${}^{\odot j}\ddot{p}_s = \sigma \mathcal{M}^{-1}({}^j S_{\bullet j}(\Lambda({}^j T - {}^j D + {}^j \tau - {}^w A_j) + {}^v A_{\bullet j}) + {}^s A_{\bullet j}) \quad (5.31)$$

The dynamic equations are those for a two-link serial dynamic chain, with the first link from the jelly target to the vehicle mass center and the second link from the vehicle's mass center to the sensor focal point. The acceleration forces associated with the first link,  ${}^s A_{\bullet j}$ , are identical to those described by (5.17). The acceleration forces associated with the second (vehicle-to-sensor) link are  ${}^s A_{\bullet j}$ .

$${}^s A_{\mathbf{O}_j} = -\mathcal{M}^s R_j \begin{bmatrix} j \ddot{\psi}_v \times {}^v R_j {}^v q_s + j \dot{\psi}_v^2 ({}^v R_j {}^v q_s) \\ 0 \end{bmatrix} \quad (5.32)$$

This pseudoforce vector consists of a tangential and a centripetal acceleration term, but no Coriolis term. Also, the moments on the camera sensor are transformed by the  $\Lambda$  matrix which depends on the forces on the vehicle and the moment arm to the sensor.

$$\Lambda = \begin{bmatrix} 1 & 0 & 0 & 0 \\ 0 & 1 & 0 & 0 \\ 0 & 0 & 1 & 0 \\ -{}^v R_j {}^v q_s \cdot \hat{y}_j & -{}^v R_j {}^v q_s \cdot \hat{x}_j & 0 & 1 \end{bmatrix} \quad (5.33)$$

The nonlinear term (5.32) is not negligible and must be considered in formulating an IVS control law that stabilizes camera location, rather than vehicle location. Moreover, because the bias uncertainty in the measurement of the vehicle-camera offset does not subtract out of the IVS dynamic equation (5.31), an adaptive capability may be required to estimate this bias on-the-fly. Because of these complexities, the position-based visual servoing approach was selected over the image-based visual servoing approach in designing the control law for the experimentally fielded system.

---

### 5.3 Null Space Applications

The baseline system of Figure 5.1 assumes generic actuation capabilities. Accounting for the specific actuator configuration of the experimental platform motivates additional changes to the generic baseline control law. Figure 5.2b illustrates these refinements related to the thruster arrangement of the experimental ROV. A new thruster map block ( $TM$ ) rotates and augments the dimension of the three-DoF control-objective signal to generate a control input that takes advantage of the vehicles full four-DoF actuation capabilities. The specification of the null space thrust command,  $\mathbf{u}$ , permits a degree of design freedom. The null space thrust can be selected arbitrarily to optimize jelly-tracking goals secondary to the primary tracking activity. This section focuses on two implications associated with the choice of a the null space thruster command: (1) minimizing



the effect of water motions on tracked animal behavior and (2) reducing the interaction between the human pilot and the automated controller during shared control. This section also considers a minor modification to the plant dynamic equations, (5.22), to account for the thruster transducer coefficients associated with the experimental vehicle.

### 5.3.1 Applying the Null Space to Minimize Thrust

This section considers means of exploiting the vehicle null space control command,  $\mathbf{v}$ , to accomplish other task goals in addition to the primary tracking task. A first significant goal involves the use of the null space dimension to minimize total vehicle thrust output. (Simply setting  $\mathbf{v}$  to zero does not minimize the summed thruster force.) Reducing vehicle thrust, in turn, reduces the chances of triggering target behavior through a hydrodynamic stimulus.

#### Thruster Map

In terms of the control software, control commands for the experimental system are always issued in the vehicle frame. With regard to the system block diagram, this fact requires the addition of a new thruster map block (*TM*). Figure 5.2b illustrates this change. As indicated by the figure, the three-DoF control command in objective coordinates,  ${}^{\odot j} \tilde{\mathbf{u}}$  must be translated into the vehicle frame and augmented in dimension. The output of the thruster map is the four-DoF thrust command in vehicle coordinates,  ${}^v \tilde{\boldsymbol{\tau}}$ .

$${}^v \tilde{\boldsymbol{\tau}} = (\sigma^j S_{\odot j}^v S_j)^{-1} \begin{bmatrix} {}^{\odot j} \tilde{\mathbf{u}} \\ \mathbf{v} \end{bmatrix} \quad (5.34)$$

Here the decomposition matrix,  $\sigma$ , is the same matrix used to decompose both the vehicle kinematic states and dynamic equations into a three-coordinate range space and a one-coordinate null space (see Section 5.2.1).

#### Designing the Null Space Control Input to Minimize Vehicle Thrust Force

The null space thrust  $\mathbf{v}$  can be chosen arbitrarily without affecting the tracking control law. The null space command may be chosen, for instance, to minimize the overall thrust output of the vehicle. This reduces the impact of the thrusters in stirring the hydrodynamic environment around the vehicle, an effect which reduces thruster impact on the animal's habitat and behavior. Thrust

forces are minimized for a specific choice of  $\mathbf{v}$  not equal zero. This choice of  $\mathbf{v}$  may be determined by examining the relationship between the control command and the thruster output:

$$\tilde{\boldsymbol{\tau}} = \mathcal{M}^{-1} \boldsymbol{\lambda} \mathbf{v}_{\mathcal{F}}. \quad (5.35)$$

The thruster force output,  $\mathbf{v}_{\mathcal{F}}$ , consists of a three component force vector and a yaw force couple, all expressed in cartesian coordinates centered on the vehicle. Thus  $\mathbf{v}_{\mathcal{F}}$  has pure force units, as compared with  $\tilde{\boldsymbol{\tau}}$ , which mixes force and torque units (normalized by vehicle mass). The moment-arm conversion matrix,  $\boldsymbol{\lambda}$ , enables this transformation.

$$\boldsymbol{\lambda} = \begin{bmatrix} I_3 & 0 \\ 0 & l \end{bmatrix} \quad (5.36)$$

By combining the three previous equations, a relationship is established between  $\mathbf{v}$  and the resulting thruster force output.

$$\mathbf{v}_{\mathcal{F}} = \boldsymbol{\lambda}^{-1} \mathcal{M} (\boldsymbol{\sigma}^j S_{\mathbf{o}_j} \mathbf{v}_{S_j})^{-1} \begin{bmatrix} \odot_j^j u \\ \mathbf{v} \end{bmatrix} \quad (5.37)$$

The goal is to choose  $\mathbf{v}$  to minimize the total thruster force (or one-norm),  $\|\mathbf{v}_{\mathcal{F}}\|_1$ . A brief analysis shows the optimization of the thrust-force norm calls for zero lateral thrust or zero yaw thrust, depending on the parameters of the experimental vehicle.

In assessing the norm of (5.37), it is convenient to remove two unitary rotation matrices, which do not affect the norm magnitude. The cylindrical transformation matrix,  ${}^j S_{\mathbf{o}_j}$ , is the product of a scaling matrix,  ${}^j S_{\mathbf{o}_j, sc}$ , and a rotation matrix,  ${}^j S_{\mathbf{o}_j, rot}$ .

$${}^j S_{\mathbf{o}_j} = {}^j S_{\mathbf{o}_j, sc} {}^j S_{\mathbf{o}_j, rot} = \begin{bmatrix} 1 & 0 & 0 & 0 \\ 0 & {}^j r_v^{-1} & 0 & 0 \\ 0 & 0 & 1 & 0 \\ 0 & 0 & 0 & 1 \end{bmatrix} \begin{bmatrix} \cos({}^j \gamma_v) & \sin({}^j \gamma_v) & 0 & 0 \\ -\sin({}^j \gamma_v) & \cos({}^j \gamma_v) & 0 & 0 \\ 0 & 0 & 1 & 0 \\ 0 & 0 & 0 & 1 \end{bmatrix} \quad (5.38)$$

The matrix  ${}^vS_j$  is also a rotation matrix (through the compass heading,  ${}^j\psi_v$ ). These rotation matrices commute with the  $\lambda^{-1}\mathcal{M}$  matrix because of their particular structure. The  $\lambda^{-1}\mathcal{M}$  matrix has the following form:

$$\lambda^{-1}\mathcal{M} = m \begin{bmatrix} I_3 & 0 \\ 0 & \kappa^2/l \end{bmatrix} \quad (5.39)$$

The  $\lambda^{-1}\mathcal{M}$  matrix incorporates the moment arm,  $l$ , the vehicle scalar mass,  $m$ , and the vehicle inertia expressed in terms of the radius of gyration,  $\kappa$ . Matrix commutation is allowed because the rotation matrices have only scalar diagonal entries in their fourth row/column and because the  $\lambda^{-1}\mathcal{M}$  matrix is structured as an identity block with only a scalar diagonal entry in the fourth row/column.

Commuting the rotation matrices results in (5.40).

$${}^vF = {}^vS_j^{-1} {}^jS_{\bullet j, rot}^{-1} (\lambda^{-1}\mathcal{M}) {}^jS_{\bullet j, sc}^{-1} \sigma^{-1} \begin{bmatrix} \odot^j u \\ v \end{bmatrix} \quad (5.40)$$

In this form, it is clear that the rotation matrices have no effect on the thrust vector magnitude. A rotated thruster force vector,  $\bullet^jF$ , may be defined based on (5.40).

$$\bullet^jF = {}^jS_{\bullet j, rot} {}^vS_j {}^vF \quad (5.41)$$

The rotated thruster vector has the same magnitude as the original thruster vector, because the rotation matrices are unitary.

$$\|\bullet^jF\|_1 = \|{}^vF\|_1 \quad (5.42)$$

The expression for the magnitude of the thruster vector is thus

$$\|{}^vF\|_1 = \left\| \lambda^{-1}\mathcal{M} {}^jS_{\bullet j, sc}^{-1} \sigma^{-1} \begin{bmatrix} \odot^j u \\ v \end{bmatrix} \right\|_1. \quad (5.43)$$

The leading matrix terms on the right hand side form the following product:

$$\lambda^{-1} \mathcal{M}^j S_{\mathbf{O}_{j,sc}}^{-1} \sigma^{-1} = m \begin{bmatrix} 1 & 0 & 0 & 0 \\ 0 & -j r_v / 2 & 0 & j r_v / 2 \\ 0 & 0 & 1 & 0 \\ 0 & \kappa^2 / (2l) & 0 & \kappa^2 / (2l) \end{bmatrix}. \quad (5.44)$$

Thus, the thrust vector magnitude is

$$\| \mathbf{v}_F \|_1 = m (| \odot^j u_1 | + | \odot^j u_3 |) + m^j r_v (| \odot^j u_2 - v | + \xi | \odot^j u_2 + v |) \quad (5.45)$$

where

$$\xi = \frac{\kappa^2}{l^j r_v}. \quad (5.46)$$

The slope of the total thrust vector with respect to the null space thrust,  $\partial \| \mathbf{v}_F \|_1 / \partial v$ , is never zero if  $\xi \neq 1$ . Rather, the minimum thrust occurs at the discontinuities, where  $v = \pm \odot^j u_2$ . The geometric parameter  $\xi$  determines at which of the discontinuities this minimum lies.

$$v_{\min} = \begin{cases} + \odot^j u_2, & \xi < 1 \\ - \odot^j u_2, & \xi > 1 \end{cases} \quad (5.47)$$

According to the definition of the null space in (5.12), the former case ( $\xi < 1$ ), results in zero net thrust in the circumferential direction about the jelly. The latter case ( $\xi > 1$ ), results in zero net thrust in the yaw direction.

Thus, in effect, the parameter  $\xi$  represents the effectiveness ratio of circumferential to yaw thruster forces in commanding relative yaw bearing. Given the geometry ( $\kappa=0.98$ ,  $l=0.64$ ) of the experimental platform, ROV *Ventana*, yaw thrust will outperform circumferential thrust when the range to target,  $j r_v$ , exceeds 1.3 meters. For experimental operations,  $j r_v$  generally exceeds 2.4 m (since the camera stands approximately 1.4 m from the vehicle mass center and since the biological standoff distance adds an additional 1 m). Consequently,  $\xi$  is always less than unity, for the

experimental platform, and yaw thrust always outperforms circumferential thrust. This performance advantage could be further amplified in a dedicated jelly tracking AUV by increasing the thruster separation,  $l$ , while maintaining a small radius of gyration,  $\kappa$  (see Figure 5.8).

In the context of (5.47), the thruster map (TM) block of Figure 5.2b may be expressed as the following linear matrix:

$$TM = (\sigma^j S_{\mathbf{O}_j}^v S_j)^{-1} \begin{bmatrix} I_3 \\ [0 \ 1 \ 0] \end{bmatrix} \quad (5.48)$$

where

$$\tilde{\tau}^v = (TM)^{\odot j} \tilde{u}. \quad (5.49)$$

In effect, this thruster map sets the vehicle's circumferential thrust component to zero.

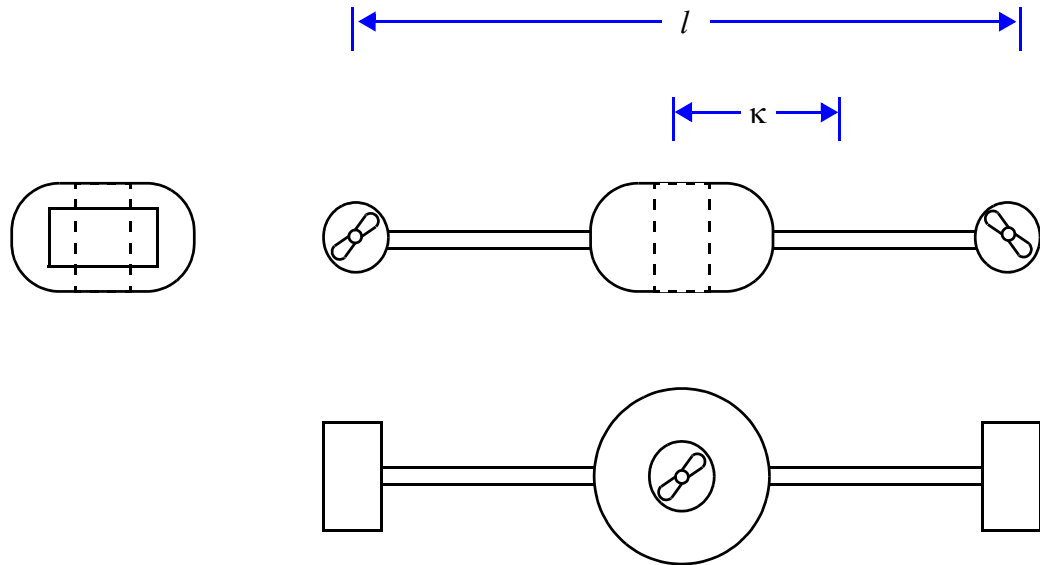


**Figure 5.8 Geometry for a Dedicated Jelly Tracking AUV**

*This figure shows three orthographic views of a concept AUV dedicated to jelly tracking. The AUV design uses a large interthruster distance,  $l$ , and a small radius of gyration,  $k$ , to maximize yaw performance.*

### 5.3.2 Applying the Null Space to Noninterfering Shared Control

In addition to offering an opportunity for optimization of the thruster output magnitude, the control null space also provides a convenient method for control sharing between the automated controller and a human pilot. The total control command to the tracking vehicle is the sum of a pilot control command, issued through a joystick, and the automatic control command. The block diagram of Figure 5.2b illustrates this superposition of control commands, where the human pilot input is denoted as *HP*. The pilot need only issue commands during the initialization phase of a jelly-tracking experiment; however, the pilot maintains the option to issue supplementary control commands at any time to modify the appearance of science video.

In ROV-based jelly tracking, the pilot plays an important role in determining viewing orientation relative to the target. Vision-processing algorithms used for experiments (described in Chapter 4) do not sense the relative orientation of the target to the tracking vehicle. Consequently, the automated control laws presented in this chapter do not stabilize perceived target orientation. In contrast, a human pilot viewing video transmitted from the tracking vehicle can quickly infer the orientation of gelatinous target. Acting on this knowledge, the human pilot can control the viewing direction toward the target, within the actuation capabilities of the tracking ROV. This capability permits a scientist to request a human pilot to circle around the target animal to obtain a preferred viewing orientation. For instance, the scientist might request the pilot to slide around a medusa to view its subumbrellar surface and the contents of the animal's stomach.

The human pilot can issue such a command without affecting automated tracking by using the control law null space. To accomplish this action, the pilot must simultaneously issue circumferential and yaw commands that keep the target animal centered in the camera image while sliding the tracking vehicle circumferentially around its target. Using the independent-axis dynamic assumptions of Section 5.1, these combined actions can be trivially reduced to a single pilot command. In practice, limited coupling between circumferential motion and the tether yaw bias complicate the relationship. Experiments in null-space control sharing are described in Chapter 6.3.

### 5.3.3 Thrust Signal Pathway

This section considers details specific to the experimental platform (inside the  ${}^{\odot j}V$  block of Figure 5.2b) that affect the implementation of the control law. A first detail involves the units of the control signal sent to the ROV *Ventana*. A second detail involves the commutivity of the linear

control gain block ( $K$ ) and the thruster map block ( $TM$ ) for the experimental platform. This commutativity allows the thruster transducer coefficients to be wrapped into the control gain expression; the result simplifies control system implementation without otherwise affecting the feedback loops illustrated by Figure 5.2.

### Thruster Transducer Coefficient

Control commands are issued to the *Ventana* Control Computer (see Chapter 3) as proportional-thrust commands. These commands are unitless, and are scaled by the system pathway (through the *Ventana* Control Computer, through the ROV's hydraulic power distribution system and through the ROV's thrusters) to have force or moment units. A set of transducer coefficients,  $\tilde{f}$ , defines the relationship between each unitless thrust command and the physical output produced by each thruster channel. These transducer coefficients thus represent a scaling factor between the desired mass-normalized thrust command ( $\tilde{v}_\tau$ ) and the actual signal issued by the Pilot-Assist Computer to the *Ventana* Control Computer. Approximate values for *Ventana*'s thruster transducer coefficients are listed in the Appendix to this dissertation.

Thrust commands are issued in an open-loop fashion. The *Ventana* system does not employ load cells, encoder wheels, or other sensors to detect actual thrust output or actual rotor velocity. Thrust commands are simply accepted by the *Ventana* Control Computer, mapped to invert system nonlinearities, and output to the thrusters. Thruster dynamics are assumed to be of a higher bandwidth than closed-loop vehicle dynamics and thus to quickly achieve their steady-state thrust values.

In terms of the block diagram of Figure 5.2b, the thruster transducer coefficients are internal to the plant model block,  ${}^{\odot j}V$ . Figure 5.9 shows the internal structure of the plant block, which was suppressed in the earlier block diagram. This internal structure represents the pathway of the control signal from the pilot-assist computer through the vehicle thrusters. First, the requested thrust vector is modulated in the Pilot-Assist Computer by a factor of  $1/\tilde{f}$  to account for the thruster transducer coefficient. The resulting nondimensional signal is sent to the *Ventana* Control Computer which maps the signal through a nonlinear block,  $NL^{-1}$ , that inverts the steady-state performance curve of the ROV's hydraulic system. These signals travel to the ROV via a tether. The hydraulic system of the ROV,  $NL$ . The hydraulic system commands the thrusters which, in

effect, scale the thrust command by the transducer coefficient,  $\tilde{f}$ . These forces and force-couples drive the plant dynamics,  $V$ .

### Control Gain Commutivity

Because the inverse-transducer coefficients,  $1/\tilde{f}$ , are implemented by the Pilot-Assist computer, they may be folded into the control gains. To lump the control gains and inverse-transducer coefficients, however, requires that both the  $\tilde{K}$  and the  $1/\tilde{f}$  blocks be expressed in a common frame. Frame alignment was accomplished for the experimental system by taking advantage of the special-case commutivity of the thruster mapping ( $TM$ ) and the linear control ( $\tilde{K}$ ) blocks.

The  $TM$  and  $K$  blocks are not, in general, commutative. Given the special structure of the control objective function and the null space design choice that sets the circumferential control command to zero (Section 5.3.1), the blocks are commutative for the experimental system. In essence, the three control gains in the control-objective coordinate system map directly into the control gains in the vehicle-fixed coordinate system. The vertical axes are the same for both coordinate systems. Relative-bearing commands in control-objective coordinates map directly into the vehicle-frame yaw command, since the circumferential control component is set to zero. Finally, range commands in control-objective coordinates map into both the vehicle fore-aft and lateral

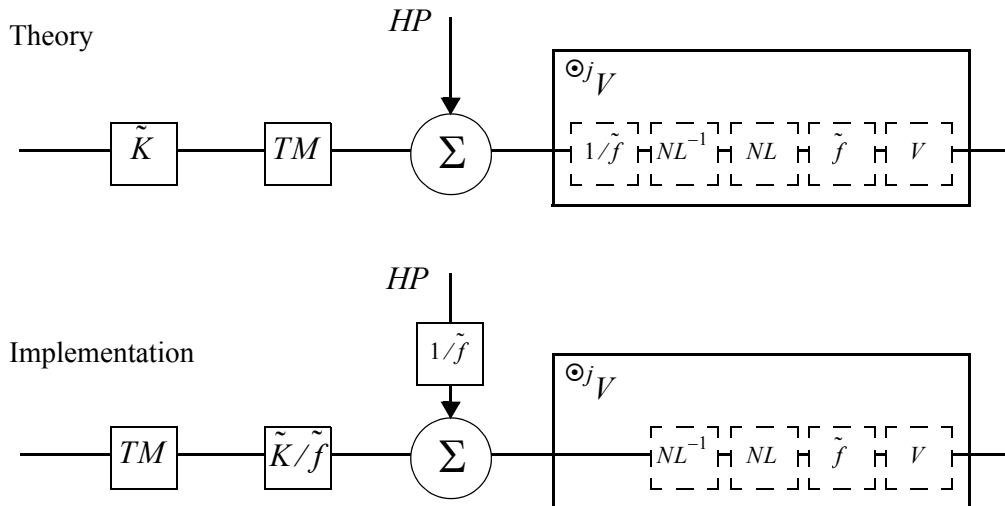


**Figure 5.9 Block Diagram Algebra: Control Block for Experimental System**

*The implemented experimental system manipulates slightly the block diagram of Figure 5.2b-c, but is functionally equivalent. In effect, the implemented system takes advantage of the zero-value circumferential control command to commute the  $K$  and  $TM$  blocks; under these conditions, the thruster transducer coefficient may be folded into the control gain block.*



directions, depending on relative bearing to the target. By setting the control gains equal for both axes (again, because the circumferential control component is always zero), a uniform range gain is effected, regardless of vehicle orientation.

Thus for the experimental system, the control gain block and the inverse-transducer coefficient block are merged into a common  $\tilde{K}/\tilde{f}$  block. The result simplifies implementation without affecting the function of the feedback loops illustrated in Figure 5.2. In this context, control gains were set as follows:

$$\begin{aligned}\frac{\tilde{K}_p}{\tilde{f}} &= \begin{bmatrix} 20 & 20 & 10 & 20 \end{bmatrix} \\ \frac{\tilde{K}_d}{\tilde{f}} &= \begin{bmatrix} 10 & 10 & 5 & 10 \end{bmatrix}\end{aligned}\tag{5.50}$$

These control gain values were chosen based on ocean-floor station-keeping tests and on their properties to reject animal acceleration, as discussed in the following section.

---

## 5.4 Countering Large Disturbance Forces

The previous sections discussed aspects of control law implementation associated with system sensor hardware and with system actuators, respectively. This section introduces an additional aspect of implementing a control system for field experiments: knowledge of the disturbance environment. In the context of a visual sensing system with a limited effective viewing cone, large disturbances may carry the target outside the sensing volume. Such events are highly undesirable, as they interrupt both the control signal and the collection of scientific data.

This section overviews the major disturbances on the jelly-tracking system (illustrated as  $W$  in the block diagram of Figure 5.2c). The linear control block,  $\tilde{K}$ , counteracts disturbances caused by jellyfish swimming. Control gains are set only high enough to track animal acceleration; low-gains limit sensitivity to sensor noise and reduce jittering vehicle motions which might disturb the target animal. With low gains, however, the linear control law cannot prevent target loss from the viewing cone under large plant disturbances. This section augments the classical controller with two additional control terms that offset large disturbances: a disturbance-accommodation term that counteracts low-frequency bias forces and a boundary control term that acts aggressively in

cases of high-frequency disturbances. Figure 5.2c illustrates these additional control terms as the  $DA$  and  $BC$  blocks, respectively.

### 5.4.1 Acceleration of the Animal Target

Motion of the jelly-target generates an inertial pseudoforce term,  ${}^wA_j$ , in the dynamic equations that describe relative motion between the tracking vehicle and the animal subject. Rejecting these disturbances is the major function of the linear tracking control law. To enable successful closed-loop tracking, the bandwidth of the tracking law must match the bandwidth associated with target motion. The dynamic equation for the target animal is a first-order differential equation for animal acceleration, relative to the water.

$$(m + m_a) {}^w\ddot{p}_j + D({}^w\dot{p}_j) = \tau \quad (5.51)$$

Sample values for the drag function,  $D({}^w\dot{p}_j)$ , and the thrust production term,  $\tau$ , are described for medusae in Chapter 2, with equations (2.3) and (2.4). For a given animal, the drag function, thrust production, and the added mass coefficient,  $m_a$ , vary throughout the swimming cycle. Thus, it is useful to introduce a period averaged dynamic equation.

$$(m + m_a) \overline{{}^w\ddot{p}_j} + D(\overline{{}^w\dot{p}_j}) = \bar{\tau} \quad (5.52)$$

As bandwidth is only defined, in a strict sense, for a linear transfer function, the drag term is here approximated with a representative linear coefficient,  $D({}^w\dot{p}_j) \approx b_{jelly} {}^w\dot{p}_j$ .

For a linear first-order differential equation, the transfer function's crossover frequency approximates its bandwidth. The crossover frequency,  $\omega_c$ , is related to the 90% rise time,  $t_{90}$ , by the following relationship:

$$\omega_c = \frac{-\ln(0.1)}{t_{90}} \quad (5.53)$$

For bell-swimmers, the rise time for the period-averaged velocity occurs over approximately 4-5 pulsing periods [29]. Although the pulsation period may be slightly reduced during acceleration from rest to escape or cruise velocities, a reasonable approximation for rise time is given by (5.54).

$$t_{90} = \frac{4}{f_{pulse}} \quad (5.54)$$

Here the pulsation duration is described as the inverse of the pulsation frequency,  $f_{pulse}$ , measured in Hz. Values of  $f_{pulse}$  for a wide variety of animals are described in Chapter 2 (Table 2.3, Table 2.4, and Figure 2.5). For large animals, pulsation frequencies may be as low as 0.1 Hz. For small animals, pulsation frequency may be as high as 3 Hz. Thus the approximate bandwidth of the target animal's motion falls between 0.06 rad/s and 1.7 rad/s, depending on animal size and species.

Whether or not a tracking vehicle can effectively pursue an animal depends primarily on its bandwidth (and to a lesser extent, on its maximum velocity and the size of the viewing cone). For the ROV *Ventana*, used in experimental trials, the closed-loop bandwidth which resulted from the gain choice of Section 5.3.3 was approximately 0.7 rad/s (see Appendix). Thus the experimental system was capable of tracking most jellyfish targets during an acceleration from rest to active swimming. Animals that accelerate unusually fast, like free-swimming larvaceans, some siphonophores, and medusae of the Family Rhopalonematidae, however, do exceed the bandwidth capabilities of the experimental pilot-assist system.

The tracking controller also responds, in some degree, to instantaneous velocity oscillations of pulsing jellies. The relationship between the pulsation frequency and the period-averaged crossover frequency is obtained by combining (5.53) and (5.54).

$$\omega_c = \frac{-\ln(0.1)}{8\pi} \omega_{pulse} = 0.09 \cdot \omega_{pulse} \quad (5.55)$$

Approximately one order of magnitude separates the period-averaged cross-over frequency from the pulsation frequency. Because the experimental jelly-tracking system was designed with fixed gains, tailored for response to faster moving animal targets, the jelly-tracking system effectively tracks the instantaneous velocity of large animals with low pulsation frequency. The experimental system will, however, filter out some of the oscillations in instantaneous swimming velocity for animals whose period-averaged bandwidth falls near the ROV's closed-loop bandwidth ( $\sim 0.7$  rad/s).

### 5.4.2 Other Disturbance Forces

Jellyfish acceleration represents a relatively small plant-model error. Other larger forces on the tracking submersible, however, may lead to substantial excursions in the relative error state. This section examines these unmeasured disturbance forces and their impact on jelly-tracking.

The primary system disturbances are described by the right hand side of (5.22), which is repeated here.

$${}^{\odot j}\ddot{\mathbf{p}}_v - {}^{\odot j}\tilde{\boldsymbol{\tau}} = \boldsymbol{\sigma}\mathcal{M}^{-1}({}^jS_{\mathbf{O}_j}({}^jT - {}^jD - {}^wA_j) + {}^jA_{\mathbf{O}_j}) \quad (5.22)$$

In addition to inertial pseudoforce associated with jellyfish acceleration,  ${}^wA_j$ , these disturbance forces include the tether and buoyancy forces, grouped in  ${}^jT$ ; the vehicle drag,  ${}^jD({}^w\dot{\mathbf{p}}_j, {}^j\dot{\mathbf{p}}_v)$ ; and the nonlinear Coriolis and centrifugal acceleration terms,  ${}^jA_{\mathbf{O}_j}$ , which result from circumferential motion about the target. An additional modelling disturbance may result from a discrepancy between the desired control force,  ${}^{\odot j}\tilde{\boldsymbol{\tau}}_{des}$ , and the actual force delivered by the thrusters,  ${}^{\odot j}\tilde{\boldsymbol{\tau}}$ . This section considers each of these disturbance forces in greater detail.

#### Buoyancy-Gravity Differential

Most underwater vehicles are trimmed to achieve a slight positive buoyancy, with average vehicle density just less than that of seawater. Trimming the vehicle near neutral buoyancy reduces the thrust requirement to maintain vehicle depth. The slight offset towards positive buoyancy offers two practical operational advantages. First, in the event of a vehicle shutdown, positive buoyancy ensures that the vehicle eventually returns, albeit slowly, to the ocean surface. Second, positive buoyancy slightly reduces the need for downward thrust and helps to control the sediment clouds which may result from downward thrust during operations above the ocean floor. Thus, for most operational configurations, the buoyancy-gravity differential introduces a small force bias in the vertical direction.

#### Tether Forces

For ROV-based jelly-tracking operations, the vehicle tether exerts significant forces on the tracking vehicle. In experiments with the ROV *Ventana*, the vehicle tether was maintained at neutral buoyancy by attaching football-shaped floats along the tether length. This neutral-buoyancy compensation technique mitigated the high-loads otherwise associated with taught, negatively buoyant

tethers, including snap loads resulting from sudden surface waves [145]. Compensating for tether weight also removes the restoring force associated with the tether's natural preference to hang vertically, as described in the tether model used by Corradini [143]. Even without the affects of gravity loading along the tether, significant tether tension forces have been measured in *Ventana*'s neutrally buoyant tether. Figure 5.10 plots measurements of tether tension for the *Ventana* vehicle, as reported by McLain [154]. As the figure illustrates, a low frequency component dominates the energy spectrum of the tether tension signal. Because tether tension measurements are not currently available in real time, this traction may be modeled approximately as a strong low-frequency bias force,  ${}^j\bar{T}$ , plus a random higher-frequency component of smaller magnitude,  ${}^jT'$ .

$${}^jT = {}^j\bar{T} + {}^jT' \quad (5.56)$$

The direction of tether traction is expected to remain approximately constant in the jelly frame over time. Because the gravity-buoyancy differential also remains fixed in the jelly-frame, the tether and buoyancy terms are lumped together in the expression  ${}^j\bar{T}$ .

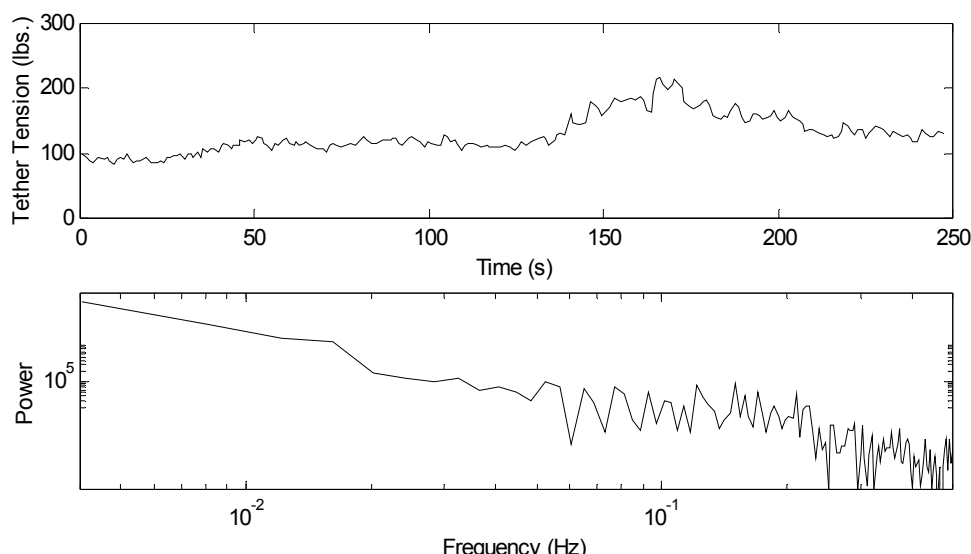


**Figure 5.10 Tether Tension Measurements**

*ROV Ventana tether tension measurements from September 10, 1991, as reported by McLain [154]. Tether tension can be quite high. During this station-keeping run, loads reached as high as 220 lbs; during another run, tension loads briefly reached a peak of 600 lbs. The majority of the signal power, as seen in the frequency domain plot, resides at low frequencies. The power at frequencies below 0.02 Hz is more than four orders of magnitude greater than the power at 0.5 Hz.*

### Hydrodynamic Forces

Hydrodynamic forces resist vehicle motion. An added mass term, associated with the acceleration of ocean water as the submersible robot accelerates, is incorporated in the inertia matrix,  $\mathcal{M}$ . Friction forces, that depend on the vehicle velocity relative to the water,  ${}^w\dot{p}_v$ , are incorporated into the drag term,  ${}^jD$ . The water-relative velocity is not observable using the jelly-tracking vision sensor, which detects only the component of vehicle velocity relative to the target animal,  ${}^j\dot{p}_v$ . The vehicle velocity vector, relative to the water, consists of an additional, unobserved component: the velocity of the jelly,  ${}^w\dot{p}_j$ .

$${}^w\dot{p}_v = {}^j\dot{p}_v + {}^w\dot{p}_j \quad (5.57)$$

In this equation, the transformation between velocities in the jelly-frame and the water frame,  ${}^jS_w$ , is an identity matrix.

The magnitude of the target velocity,  $\|{}^w\dot{p}_j\|$ , depends on animal behavior. Typical behaviors, as described in Chapter 2, consist of ambush predation, filter feeding and slow-trawl foraging. Animals which hunt by ambush or filter-feeding remain motionless for long periods of time, with  ${}^w\dot{p}_j \approx 0$ . Ambush hunters may, however, move quickly over short time periods to flee a predator or to seek new hunting grounds. This assumption for ambush hunters, a group consisting of many species of siphonophore and prolate medusa, also applies to stationary filter feeders, like larvaceans. These behaviors contrast with the motion behavior of slow-trawl foragers, a class which includes ctenophores, oblate medusae and large siphonophores. Foragers move slowly, nearly continuously through the water column. The magnitude and direction of period-averaged velocity,  $\overline{{}^w\dot{p}_j}$ , are approximately constant in the water-fixed frame.

Because period-averaged animal velocity changes infrequently for both ambush hunters and foragers, this unmeasured water-relative velocity also introduces a small, low-frequency bias force offset through the drag term,  ${}^jD(\overline{{}^w\dot{p}_j})$ . In concept, this swimming-drag term could be estimated through DVL measurements or even through visual-processing techniques [122]. For the purposes of the experimental tracking system, however, the steady drag term acts similarly to the tether force. Thus a new low-frequency force term,  $\overline{{}^jF}$ , can be introduced to capture the quasi-steady contributions of the buoyancy, tether and drag forces.

$$\overline{{}^jF} = \overline{{}^jT} - {}^jD(\overline{{}^w\dot{p}_j}) \quad (5.58)$$

The nonlinearity of the total drag force,  ${}^jD(\dot{p}_v + {}^w\dot{p}_j)$ , makes it difficult to fully decouple the contributions of drag due to the motion of the jellyfish and due to the relative motion of the vehicle.

$${}^jD(\dot{p}_v; \overline{{}^w\dot{p}_j}) = {}^jD - {}^jD(\overline{{}^w\dot{p}_j}) \quad (5.59)$$

Because the total drag function,  ${}^jD$ , is monotonic and dissipative, however, it can be stated that the remaining drag component due to the relative vehicle motion,  ${}^jD(\dot{p}_v; \overline{{}^w\dot{p}_j})$ , is always dissipative. Thus, even though the remaining component of drag cannot be modeled explicitly, for lack of knowledge of  $\overline{{}^w\dot{p}_j}$ , it can be stated that this term has a stabilizing effect on the control law, as it always acts to remove energy from the system.

### Cylindrical Acceleration

The transformation of the vehicle dynamic equations into a cylindrical coordinate system introduces the curvilinear pseudoforce vector,  ${}^jA_{Oj}$ . This pseudoforce vector contains a centripetal term,  $A_{cen} = m {}^j\dot{r}_v ({}^j\dot{\gamma}_v)$ , and a Coriolis term,  $A_{cor} = -2m {}^j\dot{\gamma}_v {}^j\dot{r}_v$ . Since both terms have strong dependence on circumferential angular velocity,  ${}^j\dot{\gamma}_v$ , it is possible to neglect these terms when  ${}^j\dot{\gamma}_v$  is small. Figure 5.11 plots the magnitude of the centripetal and Coriolis forces as a function of circumferential velocity for jelly-tracking with the experimental platform, ROV *Ventana*. The figure assumes a typical reference radius,  ${}^j\dot{r}_v$ , of about 2.5 m (see Section 5.3) and the nominal vehicle dynamic parameters described in the Appendix. For clarity, the figure expresses pseudoforce terms as normalized by *Ventana*'s maximum lateral thruster output; also, circumferential velocity is normalized by the vehicle's terminal velocity (its velocity at maximum thrust, balanced by the drag force):  $v_{norm} = ({}^j\dot{r}_v {}^j\dot{\gamma}_v) / v_{term}$ . For the Coriolis force term, the radial velocity,  ${}^j\dot{r}_v$ , is assumed to have a worst case value of 20% of terminal velocity.

Under this assumption, the figure shows that centripetal and Coriolis pseudoforces grow to a significant fraction of vehicle thrust only when the circumferential velocity grows very large. When the vehicle travels at circumferential velocities below one-third of its terminal velocity, the magnitude of both pseudoforces remains smaller than 10% of maximum vehicle thrust. In this context, it is possible to neglect the coriolis and Centripetal forces for typical operations with ROV *Ventana*. Sudden brief burst of lateral speed may result in large transient pseudoforce, however.

### Thruster Forces

The vehicle plant equations, (5.22), were developed without considering thruster dynamics. In general, it is valid to neglect thruster dynamics for the experimental ROV, since thruster bandwidth, in a linearized sense, is approximately 10-15 rad/s, an order of magnitude greater than vehicle maximum closed-loop bandwidth, approximately 0.7 rad/s. Nonetheless, this assumption does not hold true under all conditions. As discussed by Yoerger [164], nonlinearity in the thruster dynamic equation makes open-loop thruster bandwidth a function of the angular velocity of the thruster rotor. Yoerger proposes the following one-state thruster model.

$$\dot{\omega}_t = \alpha_1({}^v\tau_{des} - \alpha_2\omega_t^2) \quad (5.60)$$

$${}^v\tau = \alpha_2\omega_t^2 \quad (5.61)$$

In the preceding equations, the rotational velocity of the thruster is  $\omega_t$ . The term  ${}^v\tau_{des}$  refers to the desired thrust command while  ${}^v\tau$  refers to the generated thrust. The  $\alpha_i$  are constant thruster parameters. If the two preceding equations are combined to eliminate  $\omega_t$ , the following equation results.

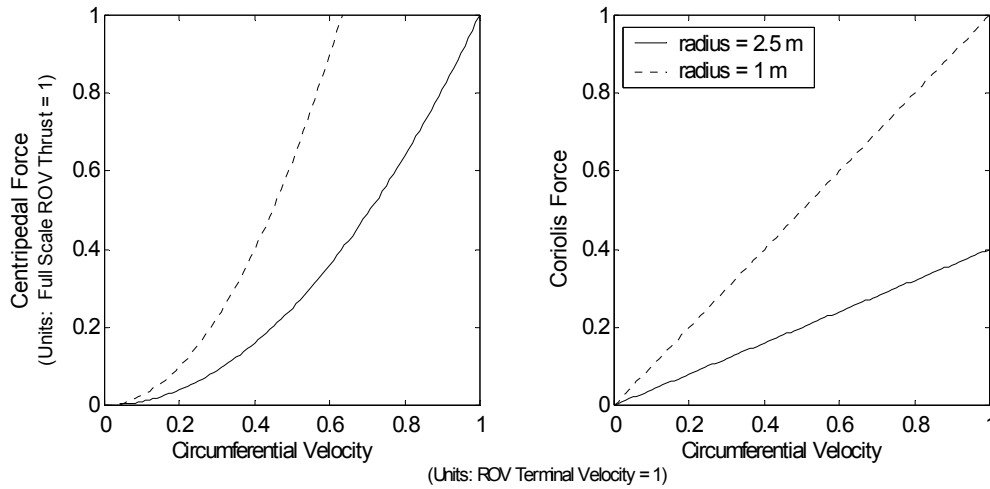


**Figure 5.11 The Magnitude of Curvilinear Disturbance Forces for the Experimental System**

*These plots describe the relative magnitude of the centripetal and Coriolis pseudoforces, normalized by the full-scale vehicle thrust, given the vehicle parameters for the ROV Ventana (see Appendix). Plot (a) describes the centrifugal force as a function of vehicle velocity in the circumferential direction (normalized by the terminal velocity for maximum thrust). Plot (b) describes the coriolis force as a function of normalized circumferential velocity, assuming a radial velocity of 0.1 m/s.*



$$\dot{\tau} = \alpha \sqrt{\tau} (\tau_{des} - \tau) \quad (5.62)$$

From this equation, it can be seen that the thruster time-constant,  $\alpha \sqrt{\tau}$ , is dependent on the current thrust level. The thruster time constant becomes very long (and the bandwidth becomes very low) when the generated thrust approaches zero.

The thruster modeling error introduces occasional high-frequency disturbances to the plant model. To avoid problems associated nonlinear thruster bandwidth, Yoerger recommends the use of a sliding mode controller [164]. The jelly-tracking controller uses an alternate control technique that maintains generally low control gains but that provides aggressive control near the boundaries of the camera viewing cone.

### 5.4.3 Augmenting the Baseline Control to Counter Large Disturbances

In the context of the previous section, large disturbances on the tracking vehicle may be divided between low-frequency bias forces (buoyancy, tether, swimming-drag) and occasional high-frequency disturbances (curvilinear pseudoforces, thruster nonlinearity). This section proposes two additional control terms that address high and low-frequency disturbances to reduce the risk of target loss outside of the camera image.

Figure 5.2c shows these two additional control terms, the disturbance-accommodation (*DA*) term and the boundary-control (*BC*) term, which complement the linear controller (*K*). These three control terms sum before entering the plant block,  ${}^{\odot j}V$ .

$${}^{\odot j}\tilde{\tau} = {}^{\odot j}\tilde{\tau}_K + {}^{\odot j}\tilde{\tau}_{BC} + {}^{\odot j}\tilde{\tau}_{DA} \quad (5.63)$$

Because the dynamic equations in control-objective form, (5.22), decouple each of the DoFs required for tracking (range, depth differential, and relative bearing) the control terms may be designed independently along each axis.

The boundary control term,  ${}^{\odot j}\tilde{\tau}_{BC}$ , acts aggressively against high-frequency disturbances when they push the target toward the edge of the camera viewing cone. Whereas the linear term was designed to minimized thrust exerted on the surrounding medium during standard operations (Section 5.4.1), the nonlinear  ${}^{\odot j}\tilde{\tau}_{BC}$  term is designed to produce aggressive control in the critical situation where the sensor may lose the target animal. In particular, the boundary control term

plays a significant role when the thruster state passes through its low-bandwidth zone, as described by (5.62).

The disturbance-accommodation control term,  $\tilde{\tau}_{DA}$ , counteracts the low-frequency bias force,  $\overline{F^j}$ , as described by (5.58). In the absence of a low-frequency control term, these disturbances result in steady-state error, with the target shifted away from its reference location. If disturbances are sufficiently large, the steady-state error may push the target outside the sensor viewing cone. The disturbance-accommodation term is designed in such a way to counteract these disturbances, but to ignore bias control commands issued by the human pilot.

### Boundary Control Term

The tracking system risks permanent target loss if the tracked animal drifts outside the sensor viewing cone. A boundary control term,  $\tau_{BC}$ , is introduced to reduce the risk of an out-of-frame event for the case of large transient disturbances that the linear control term,  $\tau_K$ , cannot reject.

In a broader context, the management of viewing cone restrictions is an obstacle avoidance problem. Potential fields have proved useful for a range of boundary avoidance tasks, from other applications with viewing-cone constraint, like visual manipulation of a robot arm [142,155], to other classes of boundary-avoidance problem, like automobile lane-keeping [149]. Thus, the jelly-tracking boundary-control strategy incorporates the notion of a potential field; because the jelly-tracking application requires a sudden switch between low-gain control and aggressive boundary control, however, the jelly-tracking strategy also incorporates the notion of variable-structure control (aka sliding mode control).

In effect, the potential field associated with the boundary makes a step change between a central quiescent region, in which only the linear control operates, and the boundary region, in which the boundary-control term becomes active. Figure 5.12 depicts this potential function. The resulting control law is a form of variable-structure control, similar in implementation to sliding-mode control using a large boundary layer.

The performance of the boundary-control term is most easily analyzed in one dimension. In 1-D, the potential function for the boundary term, combined with that for the linear control law, defines the following decrescent, positive definite Lyapunov function.

$$V = \begin{cases} \frac{1}{2}k_p x^2 + \frac{1}{2}\dot{x}^2, & |x| \leq x_q \\ \frac{1}{2}k_p x^2 + \frac{1}{2}\delta|x| + \frac{1}{2}\dot{x}^2, & |x| > x_q \end{cases} \quad (5.64)$$

Here the one-dimensional coordinate is  $x$  and the boundary of the quiescent central region is  $x_q$ . The control parameters,  $k_p$  and  $\delta$  are defined by the following dynamic system and control law.

$$\ddot{x} = \tau_x = \tau_{K,x} + \tau_{BC,x} \quad (5.65)$$

$$\tau_{K,x} = -k_p x - k_d \dot{x} \quad (5.66)$$

$$\tau_{BC,x} = \begin{cases} 0, & |x| \leq x_q \\ -\delta \operatorname{sign}(x), & |x| > x_q \end{cases} \quad (5.67)$$

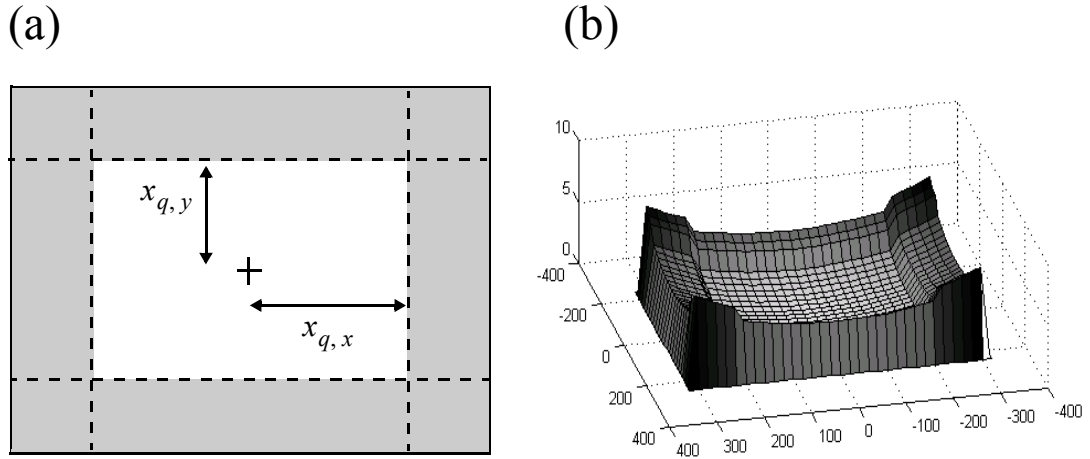


**Figure 5.12 Zone of Influence for Boundary Control**

Two views depict the zone of influence for the boundary control term, which acts aggressively to keep the jelly target away from the edges of the camera viewing cone. (a) The domain of the quiescent zone, light, and the boundary zone, shaded, in the image plane. (b) The Lyapunov function for the combined linear and boundary controllers in the image plane, with velocity error assumed zero.

The time-derivative of the Lyapunov function, (5.64), is continuous and negative semidefinite for all  $x, \dot{x}$ .

$$\frac{\partial V}{\partial t} = -k_d \dot{x}^2, \quad \forall x \quad (5.68)$$

Thus the function  $V$  is stable in the sense of Lyapunov. LaSalle's principle may further be invoked to establish global asymptotic stability. (For the set,  $S$ , of states with  $\dot{V} = 0$ , the state  $\dot{x}$  is everywhere zero but the state  $x$  is not necessarily zero. On  $S$ , the derivative of  $\dot{x}$  is given by (5.65). This equation establishes that all trajectories on  $S$  will leave the set unless  $x = 0$ . Thus by LaSalle, the system has global asymptotic stability.)

The stability proof differs somewhat from that of standard sliding-mode control in that the boundary controller does not obey the projection constraint on the design of a sliding surface [146]. (For the dynamic equation (5.65), an allowable sliding surface must be a linear combination of the position and velocity states,  $s = m_1 x + m_2 \dot{x}$ , and not just of the position state, as is the case for the boundary-control term.)

Despite their minor differences, both the boundary-control term and standard sliding-mode control possess the capability to reject large disturbances. When a large disturbance force, up to the magnitude  $\delta$ , carries the target beyond  $x_q$ , the nonlinear boundary control term immediately counteracts the disturbance force. For the experimental system:

$$\tilde{\delta} = 3\tilde{f}. \quad (5.69)$$

This value implies that the boundary-control term immediately counters large target excursions with an additional 60% of maximum thrust ( $5\tilde{f}$ ).

Also like sliding-mode control, the boundary-control term may result in a form of chatter. Boundary chatter results in the presence of a low-frequency bias force which repeatedly returns the error state to the boundary at which the  $BC$  control term activates. The low-frequency  $DA$  control term helps prevent such instances of chatter.

In its three-dimensional implementation, the  $BC$  term issues commands in the image plane and subsequently rotates them into the control-objective frame. The fundamental principles underlying 3-D boundary control term are otherwise identical to that of the 1-D case (5.67). The equation for the 3-D  $BC$  term is given as follows:

$$\tilde{\tau}_{BC}^s = \sum_{i=1}^4 \tilde{\tau}_{BC,i}^s \quad (5.70)$$

$$\tilde{\tau}_{BC,i}^s = \begin{cases} 0, & |x_{pix}| \leq x_{q,i} \\ \delta \hat{n}_i, & |x_{pix}| > x_{q,i} \end{cases} \quad (5.71)$$

The boundary control term is the sum of four components, one associated with each boundary of the camera field of view. The unit-normals of the camera boundaries,  $\hat{n}_i$ , are defined as the inward pointing normals, as illustrated by Figure 5.4. In (5.71), the expression  $x_{pix}$  refers to the position of the target animal relative to the image center, in pixels. The boundary of the quiescent region,  $x_{pix,q}$ , is also expressed in image pixels; for the experimental system,  $x_{pix,q}$  was set to one-quarter of the full image width in pixels. The rotation that takes the boundary control term into objective coordinates is as follows.

$$\odot_{j\sim} \tilde{\tau}_{BC} = {}^v S_{\mathbf{O}_{v,rot}} {}^s S_v \tilde{\tau}_{BC} \quad (5.72)$$

The initial rotation,  ${}^s S_v$ , takes the boundary control term into the vehicle coordinate frame. The subsequent rotation,  ${}^v S_{\mathbf{O}_{v,rot}}$ , takes the control term into the frame whose axes align with the radial vector (from the vehicle to the target), the vertical depth direction, and the normal to these two directions (aligned with yaw bearing). The thruster mapping block,  $TM$ , governs what combination of circumferential thrust and yaw thrust are employed to reject yaw-bearing errors. In its final form, the experimental system thruster map,  $TM$ , used only the yaw thrusters for boundary control, leaving the circumferential thrust term equal zero.

#### **Disturbance-Accommodation Control**

Low-frequency disturbances introduce an offset in the error vector relative to the desired reference location. In extreme cases, this quasi-steady offset may push the target animal outside the viewing cone.

A disturbance-accommodation control,  $\odot_{j\sim} \tilde{\tau}_{DA}$ , was employed to counter low-frequency disturbances. The  $DA$  control acts in a manner similar to integral control for the case of shared control. The  $DA$  control uses an estimator to combine control commands from all sources (human

pilot, linear controller, boundary controller, saturation block) to provide a continuous estimate of the low-frequency disturbance force regardless of the source of the control input. As such, the *DA* controller does not inadvertently cancel desired control commands, only disturbance forces,  $W$ , that act directly on the ROV platform. Figure 5.13 compares block diagrams for the integral and estimator-based approaches.

Thus the *DA* control term simply acts to offset the estimated low-frequency bias force,  $j_{\hat{F}}$ .

$$\ominus j_{\tau_{DA}}^{\sim} = -\sigma \mathcal{M}^{-1} j_{S_{\mathbf{O}_j}} \left( j_{\hat{F}} \right) \quad (5.73)$$

In the experimental implementation, the *DA* control term was not projected through the thruster map,  $TM$ , because the estimated bias disturbance acts along all four system degrees of freedom. The observed disturbance,  $j_{\hat{F}}$ , is measured by an estimator formulated in the jelly-fixed frame. As such the estimator need not incorporate nonlinear curvilinear dynamics. In fact, the estimator uses a fully linear, axis-decoupled plant model. To achieve linearity, vehicle drag is modeled as approximately linear over the range of speeds encountered during jelly tracking; the drag coefficient matrix,  $\delta$ , is taken to be diagonal and rotationally symmetric in the horizontal plane. Under this assumption, the vehicle position and velocity states may be estimated in the jelly-fixed coordinate system using the estimator state vector,  $w$ .

$$\hat{w} = \begin{bmatrix} j_{\hat{p}_v} & j_{\dot{\hat{p}}_v} & j_{\hat{F}} \end{bmatrix}^T \quad (5.74)$$

The estimator equation is given by (5.75), where the estimator gain,  $\mathcal{L}$ , is designed as a steady-state Kalman Filter:

$$\begin{aligned} \dot{\hat{w}} &= \mathcal{A} \hat{w} + \mathcal{B} j_{\tau}^{\sim} + \mathcal{L}(y - C \hat{w}) \\ j_{p_v} &= C w \end{aligned} \quad (5.75)$$

$$\mathcal{A} = \begin{bmatrix} 0 & I & 0 \\ 0 & -\mathcal{M}^{-1} \delta & \mathcal{M}^{-1} \\ 0 & 0 & 0 \end{bmatrix} \quad \mathcal{B} = \begin{bmatrix} 0 \\ \mathcal{M}^{-1} \\ 0 \end{bmatrix} \quad C = \begin{bmatrix} I & 0 & 0 \end{bmatrix}. \quad (5.76)$$

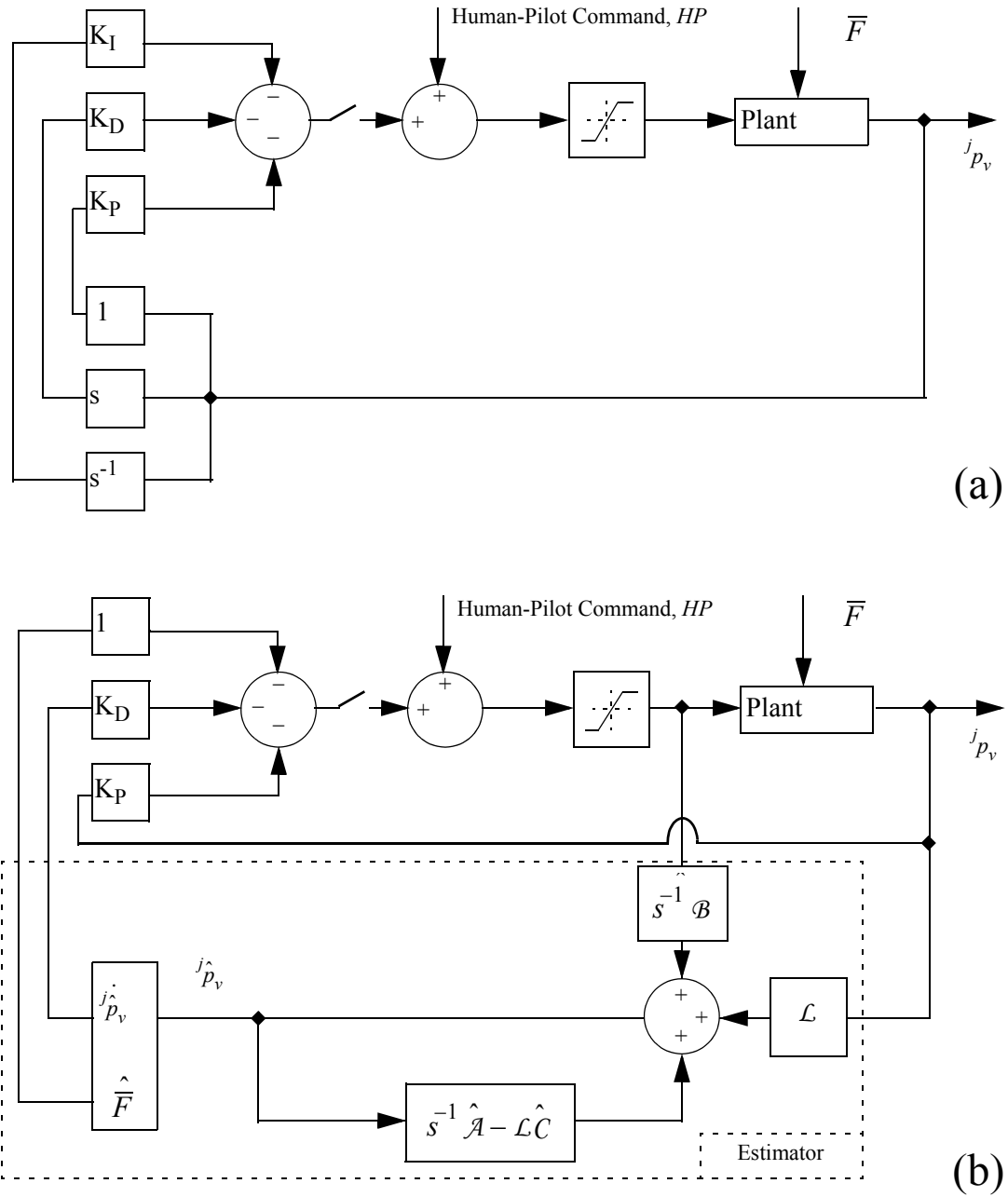


**Figure 5.13** System block diagram (individual axis).

An integral control technique (a) is compared to a disturbance accommodation technique (b).  $T$  estimator loop (a) continues to run even when the control signal is switched off (i.e. the line labeled  $u_a$  is broken). If at a later time the control signal is switched on, the low-frequency control term can be applied immediately, by using this bias-disturbance state estimate.

### Circumferential Stabilization by a Large Quasi-Steady Disturbance

Most dive experiments were run in the absence of DA control. In the absence of any other control in the circumferential direction, the low-frequency bias disturbance actually acts as a circumferential restoring force. In effect, the bias force sweeps the tracking vehicle in a circle about the tracked target, much in the manner that gravity sweeps a pendulum about its attachment point. Under a strong quasi-steady disturbance, the circumferential equation of motion has two equilibrium points. These equilibrium points may be found by taking the dynamic equation (5.16) to steady state. The resulting equation is

$$\mathbf{o}^j \ddot{\mathbf{p}}_v = 0 = {}^j S_{\mathbf{o}_j} ({}^j \overline{\mathbf{F}} + {}^j \boldsymbol{\tau}) \quad (5.77)$$

Equation (5.77) can be rewritten in terms of the components of the disturbance force and the angle,  ${}^j \psi_F$ , which describes the yaw angle of the disturbance force projected into the yaw plane.

$$0 = \begin{bmatrix} ({}^j F_x^2 + {}^j F_y^2)^{1/2} \cos({}^j \gamma_v - {}^j \psi_F) \\ \frac{({}^j F_x^2 + {}^j F_y^2)^{1/2}}{{}^c r_v} \sin({}^j \gamma_v - {}^j \psi_F) \\ {}^j F_z \\ {}^j F_\psi \end{bmatrix} + \begin{bmatrix} \tau_{c,x} \\ 0 \\ \tau_{c,z} \\ \tau_{c,\psi} \end{bmatrix} \quad (5.78)$$

Two equilibrium circumferential positions exist, at  ${}^j \gamma_v = \{{}^j \psi_F, {}^j \psi_F + \pi\}$ . These are the two points along the line, through the origin of the polar coordinate system, parallel to the direction of the disturbance force vector. Only the first of the two equilibrium points is stable.

---

## 5.5 Summary

This section summarizes the control law used in the field for deep ocean experiments.

The control input was designed to stabilize the tracking vehicle's yaw bearing, depth differential and range relative to the jelly target. In order to accomplish this control objective, the feed-



back control loop was transformed into the a control-objective form, as depicted by Figure 5.2a. The control-objective transformation took the vehicle dynamic equations into a modified set of cylindrical coordinates that decoupled the control range space, required to accomplish the tracking objective, from the control null space, a coordinate with no impact on the tracking objective. This process, which accounted for the position signal produced by the actual camera sensor used in the experimental system, also affected the definition of the reference target position, which was specified using a position-based visual servoing approach.

A second set of modifications to the baseline control law, summarized by Figure 5.2b, accounted for the thruster configuration of the experimental vehicle. In accounting for the four-DoF output of the vehicle thrusters, a thruster map ( $TM$ ) was defined to augment the three-DoF control output based on the control-objective range space. The thruster map augmentation exploited the null space thrust command to produce a minimum total-thrust output to reduce the risk of disturbing the tracked animal during jelly-tracking. A means of using the null space to implement noninterfering shared control between a human pilot and the automated tracking law was also considered. This control-sharing technique took advantage of the pilot's ability to issue circumferential commands which determined the orientation of the camera relative to the scientific target; these circumferential commands may be issued independently from automated controller commands, which have a zero value in the circumferential direction.

A third set of modifications to the baseline control law, summarized by Figure 5.2c, introduced two additional control terms to account for high and low-frequency disturbances which might otherwise carry the target animal outside the limits of the camera viewing cone. The total control command issued by the pilot assist computer is thus the sum of a linear PD control command ( $K$ ) that tracks jellyfish acceleration, a boundary-control command ( $BC$ ) that handles high-frequency disturbances, and a disturbance-accommodation control command ( $DA$ ) that handles low-frequency bias forces.

$$\odot_{\tau}^{j\sim} = \odot_{\tau_K}^{j\sim} + \odot_{\tau_{BC}}^{j\sim} + \odot_{\tau_{DA}}^{j\sim} \quad (5.63)$$

The three control terms are defined as follows.

$$\begin{aligned}
\odot_{\tau_K}^{j\sim} &= \begin{bmatrix} K_p & K_d \end{bmatrix} \begin{bmatrix} \odot_{p_v}^j \\ \odot_{\dot{p}_v}^j \end{bmatrix} \\
\odot_{\tau_{BC}}^{j\sim} &= {}^vS_{\odot_{v,rot}} {}^sS_v \sum_{i=1}^4 \begin{cases} 0, & |x_{pix}| \leq x_{pix,q} \\ \delta \hat{n}_i, & |x_{pix}| > x_{pix,q} \end{cases} \quad (5.79) \\
\odot_{\tau_{DA}}^{j\sim} &= -\sigma \mathcal{M}^{-1} {}^jS_{\odot_j} \left( {}^j\hat{\overline{F}} \right)
\end{aligned}$$

The next chapter describes experiments that demonstrate automated robotic tracking of jellyfish in the deep ocean. The control law developed in this chapter, along with the vision-processing system described by Chapter 4, were together instrumental to the success of repeated field tracking experiments.

*Behavioral observations are always subject to biases caused by the presence of the observer, and while animal behavior patterns are one of the most exciting new areas of submersible-based research, we must be cautious to acknowledge the inherent biases.*

- B.H. Robison, 1992 [7]

---

This chapter describes experiments that demonstrate, for the first time, automated robotic tracking of a deep-ocean animal in its native habitat. Experiments played an integral role in both the development and the validation of the ROV-based jelly-tracking system. Field testing took place through a series of twelve experimental dives performed in the deep ocean with ROV *Ventana*, an unmanned submersible operated by MBARI. These dives comprised three experimental phases: a first phase investigating visual methods for sensing gelatinous animals, a second phase evaluating control techniques for ROV-based jelly tracking, and a final phase validating the utility of the integrated system as a tool for biological science. The first set of visual sensing experiments collected data for off-line analysis and tested the resulting vision processing techniques during human-piloted tracking runs. The second set of control experiments employed the visual sensor in a closed-loop configuration to evaluate the control requirements for jelly tracking. The third set of experiments tested the capability of the vision and control software, integrated with the experimental hardware, to accomplish long-duration reliable tracking, a system requirement to enable new *in situ* biology experiments. Compared with a baseline system, which tracked only a small subset of animal targets encountered and those only for minutes at a time, the refined system, described in this dissertation, enabled very long tracking periods, as long as 89 minutes following a *Ptychogena* specimen.

---

## 6.1 Introduction

This section provides an overview of the techniques employed for jelly-tracking experiments with the science robot ROV *Ventana*. Deep-ocean experiments played an indispensable role in defining

and addressing the key research problems associated with the jelly-tracking task. Experimental trials face major operational challenges that abstracted lab experiments and simulation ignore. Critical issues became immediately apparent during field testing and motivated the research presented in this dissertation. In particular, early experiments identified the need for vision-processing methods to handle the complex midwater imaging environment and the need for a specialized control law to reduce the likelihood of artificially disturbing target behavior. Continuing experiments validated refined vision and control techniques under real, often unfavorable field conditions over extended tracking durations.

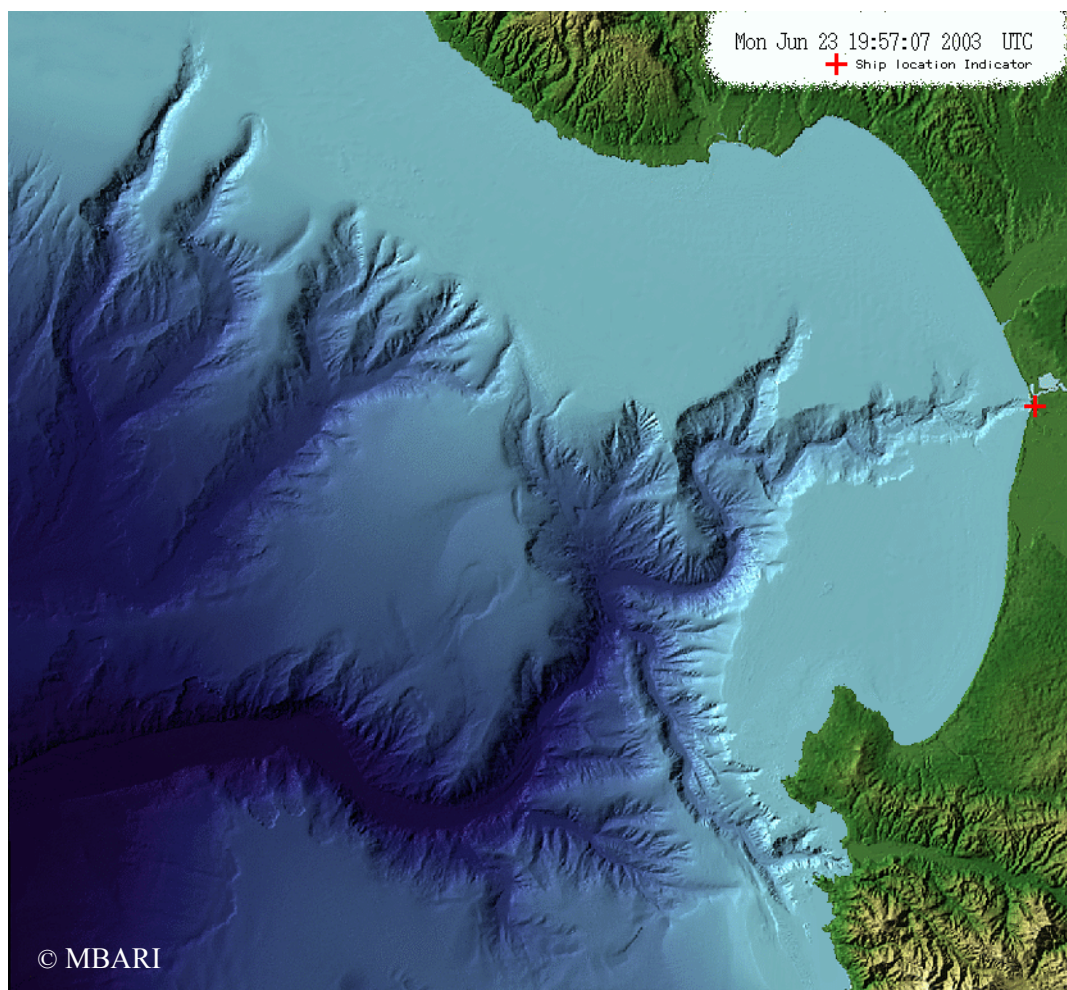


**Figure 6.1 Monterey Canyon**

*Monterey Bay bathymetry map, courtesy of MBARI, 2003.*

### 6.1.1 Dive Sites and Timeline

This chapter considers twelve *Ventana* dives between Summer 2000 and Autumn 2002, and it focuses in particular on the final five dives of the series. Dives explored the waters of Monterey Canyon, at sites within 10 nautical miles of the MBARI headquarters in Moss Landing, California. Figure 6.1 illustrates the bathymetry of the Monterey Canyon. In the figure, Moss Landing is indicated by a cross. The dramatic submarine canyon that extends from Moss Landing makes Monterey Bay one of the world's foremost locales for the study of deep-ocean phenomena in a near-shore setting. The United States government has further enhanced the significance of this sight for biology research by declaring it a national marine sanctuary, with severe restrictions on commercial fishing.

Table 6.1 lists, in chronological order, the twelve dives that led up to and through the demonstration of successful, long-duration jellyfish tracking. Dives occurred under an ongoing Stanford-MBARI collaboration to explore precision control technologies for underwater robots. Each dive devoted approximately two hours to jelly-tracking research; continuing refinement of automated ocean-floor (benthic) station-keeping capabilities consumed the remainder of each dive. Dives were spread uniformly through the two major ecological seasons in the Monterey Bay: the

Date	Vision Status	Control Status	Applications
August 02, 2000	Development	Development	
December 01, 2000	Development		
March 07, 2001	Development		
April 13, 2001	Development		
July 23, 2001	Development	Development	
September 27, 2001	Development	Development (Param ID)	
October 23, 2001	Final Vision Processing	Development	
March 13, 2002		Development (Param ID)	
May 09, 2002		Development	
June 26, 2002	Parallel Stereo Added	Final Control System	
September 24, 2002			Biology Applications
October 11, 2002			Biology Applications

TABLE 6.1. Dive Timeline

upwelling and non-upwelling seasons (Chapter 2.4). Table 6.1 indicates that the dive schedule spread experiments over nine of the twelve months of the year.

With two exceptions, all experiments placed the ROV in depths between 200 and 700 m. The first exception occurred during the earliest jelly-tracking dive, on August 2, 2000, during which the ROV briefly tracked a *Phacellophora camtschatica* specimen at approximately 100 m in depth. This shallow dive contrasts with an especially deep dive on April 13, 2001, which explored depths of nearly 1000 m. This deep dive, performed as a “piggyback” experiment to test the vision system during a mission devoted primarily to filming jellyfish for a Monterey Bay Aquarium exhibit, encountered a high incidence of deep red medusae, including the recently discovered species *Tiburonia granrojo*.

### 6.1.2 Experimental Equipment

The experimental system employed the unmanned submersible, ROV *Ventana*. Chapter 3 described this robotic vehicle in detail, along with its sensors, its support ship, and the computing system used to run automated jelly-tracking software. In contrast with the system hardware, the system software evolved substantially over the course of the experimental dive sequence. Early experiments tested a baseline configuration (Chapter 5.1.2). Subsequent experiments led to the development of refined vision and control components (Chapter 4.3 and Chapter 5.5, respectively). The vision processing algorithm stabilized to its final form by the 10/23/01 dive. The control algorithm stabilized later, along with the stereo camera configuration, on the 6/26/02 dive.

### 6.1.3 Experimental Procedures

All jelly-tracking experiments followed a common procedure. This procedure included both a pre-dive component, designed to detect and prevent major system faults, and a dive-day component, designed to simplify operations under the stresses associated with ocean experimentation.

The predive procedure tested the automated pilot-assist software with the physical hardware setup aboard the support ship R/V *Point Lobos*. These tests occurred in the week preceding the experimental dive, during a maintenance or mobilization day with the support ship docked. Because *Point Lobos* and *Ventana* comprise an operational scientific system, communication pathways and sensors are frequently reconfigured to meet the needs of various science experiments.

The prediver test procedure sought to identify configuration changes which interfered with autopilot function. This procedure consisted of the following steps:

- Install latest software version on the pilot-assist computer (PAC).
- Test communications to ensure all serial connections and video pathways are intact.
- Check sensor inputs to the PAC to verify units, sign, and nominal zero.
- Recalibrate the stereo geometry, if cameras were adjusted during vehicle maintenance.

Whereas the prediver procedure focused primarily on system implementation, the dive-day procedure focused on system operation. The dive-day procedure consisted of the following steps:

- Transit to the dive site, selected for both benthic and midwater experimentation.
- Adjust ROV light sources manually, while vehicle on deck.
- Trim ROV buoyancy within 25 pounds of neutral, erring to positive buoyancy.
- Descend to depth and perform Benthic experiments to validate control performance.
- Ascend and locate animal target; engage tracking software.
- Evaluate visual tracking and target ranging with human pilot in control.
- Begin closed-loop automated tracking, with human control active during initialization.
- Continue tracking with no pilot intervention until the occurrence of manual termination or of a tracking failure.

---

## 6.2 Vision-Only Experiments

A first set of experiments (8/2/00 - 10/23/01) investigated the requirements for visual jellyfish sensing. These vision experiments began with the evaluation of a baseline vision-processing system. After demonstrating the fundamental problems with the baseline system, further vision experiments collected data for off-line analysis and performed field evaluation of the new tracking method based on that analysis. These image-processing methods detect target bearing, only.

Thus, in addition to supporting the study of image-processing methods, vision experiments also evaluated methods for generating a target range signal. The final visual sensor employed gradient-based vision processing (Chapter 4.3) with parallel stereo ranging (Chapter 3.6.2).

The initial experimental dive (8/2/00) assessed baseline vision-processing and control laws to establish if this “off-the-shelf” system could accomplish effective jellyfish tracking. These tests indicated clearly that the baseline system, which relied on luminance-threshold segmentation, failed to segment hydrozoan medusae encountered throughout the day. The baseline system effectively detected and tracked only one medusa specimen, a large specimen of the scyphozoan species *Phacellophora camtschatica*. From a vision-processing point of view, the baseline system suffered from high sensitivity to the luminance threshold level, which varied with different animal specimens, with their position in the lighting field, and with the angle of the camera relative to the lighting field. Transparency and nonuniform lighting also contributed to vision-processing difficulties; these factors resulted, in some instances, in cases for which no luminance threshold successfully distinguished between target and background pixels.

The baseline experiment motivated the vision-system analysis described in Chapter 4. To support this analysis, the following series of dives (12/1/00 - 10/23/01) achieved two goals. These dives both collected sample video, including footage of more than 30 animal specimens (medusae, comb jellies, larvaceans), and evaluated the performance of a refined vision-processing technique under field conditions. Although an early hypothesis suggested the use of multiple simultaneous vision filters (color, gradient, luminance) to improve the identification of different animals under different lighting conditions [123], subsequent off-line and in situ testing showed that a single filter (smoothed morphological gradient) with a fixed threshold performed reliably and efficiently enough to enable tracking of a broad range of animals under a diversity of lighting conditions (Section 4.3.3).

In parallel with the development of the image-processing system, vision experiments also assessed methods for target ranging. Single camera images, in the absence of additional information, provide measurements of target bearing, only. Fully automated jelly tracking, however, requires both a bearing and a range signal. To this end, early experiments attempted to use target pixel-area as a relative ranging signal. Though easily implemented, this method proved noisy and only moderately reliable; problems occurred whenever the target’s shape deformed or it rotated out of the image plane. Subsequent experiments shifted to converging stereo ranging (Section 3.6.2)



to avoid these problems with area-based ranging. The converging stereo technique, first implemented for the 7/23/01 dive, enabled the first-ever demonstration of fully automated jelly tracking, a demonstration which lasted for approximately 2.5 minutes.

The converging stereo setup used two cameras, the main vehicle science camera and an upper pilot camera, to produce a stereo baseline of 1 meter. This large baseline configuration required little calibration; however, human pilots found initialization of the converging stereo system difficult, because initialization required alignment of the jelly target in two cameras separated by an arbitrary rotation angle. A number of tracking runs aborted immediately because the target did not remain in both camera viewing cones throughout the initialization phase.

To overcome the initialization problems associated with converging stereo, a parallel stereo configuration was introduced for the 6/26/02 dive. Using two cameras mounted together on the same pan/tilt unit, the parallel stereo baseline was reduced to 10 cm. The reduced-baseline, parallel-stereo configuration required a more precise calibration than the larger-baseline, converging-stereo configuration. Nonetheless, the parallel-stereo configuration greatly relieved the initialization requirement. With parallel-stereo, the pilots needed to align the target in only one camera, rather than two, because of the significant overlap between the viewing cones of the parallel stereo cameras. Before introduction of parallel stereo, on the 10/23/01 dive date, converging-stereo issues caused 7.5% of test runs to abort immediately and an additional 10% of test runs to end when the automated controller lost the target from the upper of the two converging-stereo cameras. After introduction of the parallel stereo configuration, on 6/26/02, the rate of failures caused by stereo-related problems dropped significantly, with 0% of runs ending through either of these failure mechanisms.

The parallel stereo configuration also offered a second practical advantage for scientific application of the ROV-based pilot aid. Because the parallel-stereo configuration did not employ the ROV's main science camera, this camera remained free for use in science experiments. As a consequence the science camera could be zoomed, focused, panned and tilted without affecting automated target tracking. As a demonstration of this advantage, the science camera was employed to snap several high resolution images during automated jelly-tracking. A sample high resolution image of a *Ptychogena* specimen is illustrated in Figure 6.2, below.



**Figure 6.2 Ptychogena Specimen**

*Tracked autonomously on 9/24/02.*

---

## 6.3 Tracking Experiments

A second set of experiments (7/23/01 - 6/26/02) applied the visual sensor to enable closed-loop ROV tracking. These experiments both motivated and field tested the control design for the tracking system. This section details experiments evaluating the control performance of the jelly-tracking system. Time-series data illustrate the significance of the boundary control term, as well as the implications of the low-frequency control term and of the control-law null space (Chapter 5).

In enabling extended tracking runs, the most important control modification was the boundary control term. The occurrence of extended duration tracking runs increased dramatically with the introduction of this term. The disturbance-accommodation control term complements the boundary-control term by smoothing boundary chatter. In theory, the disturbance-accommodation control term should also aid in transition from human control to computer control in the presence of large tether forces. A fundamental human-computer interaction issue uncovered during ocean trials, however, prevented the use of the low-frequency control term for this purpose.

Experiments also demonstrated the system's null space design characteristics. According to the design of the thruster map (Chapter 5.3), the linear controller issued no commands in the circumferential direction. As discussed in Chapter 5.4.3, the circumferential coordinate was instead

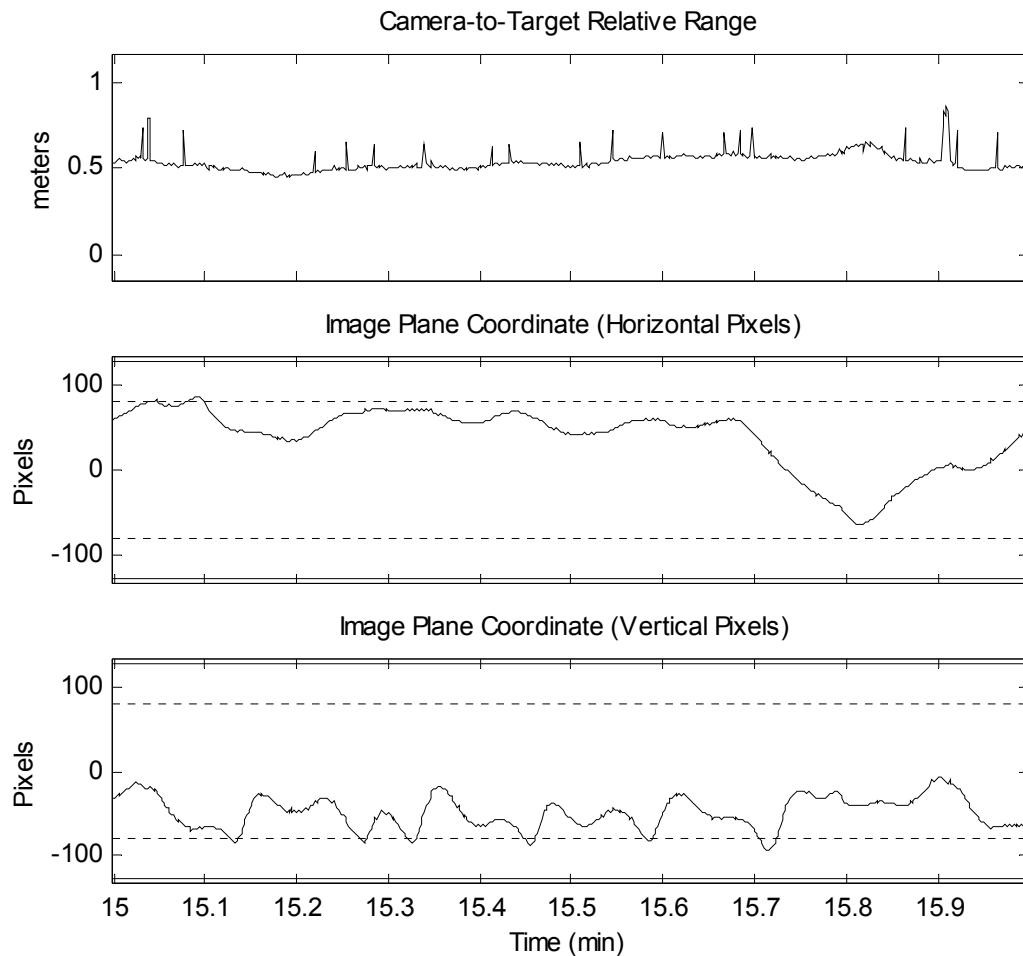
stabilized by a strong tether bias. During extended tracking runs, infrequent changes in the bias force resulted in significant shifts in the equilibrium circumferential position. Allowing circumferential position to drift effectively reduced the need for circumferential control and reduced excess thrust in the circumferential direction. In an independent test, the null space was exploited to demonstrate effective control sharing between the automated controller and a human pilot (Chapter 5.3.2). In these tests, the pilot issued only lateral (circumferential) thruster commands and successfully modified the viewing angle to a sinking larvacean house without affecting the performance of the automated tracking law.

An extended-duration tracking experiment, which pursued a *Ptychogena* for 89 minutes, provided strong evidence for the utility of the jelly-tracking control system. Although the disturbance-accommodation term was disabled for this run, this experiment otherwise demonstrates the complete control system described in Chapter 5, including the linear control term, the boundary control term, and the action of the tether bias to stabilize the control-objective null space.

### 6.3.1 Boundary Control

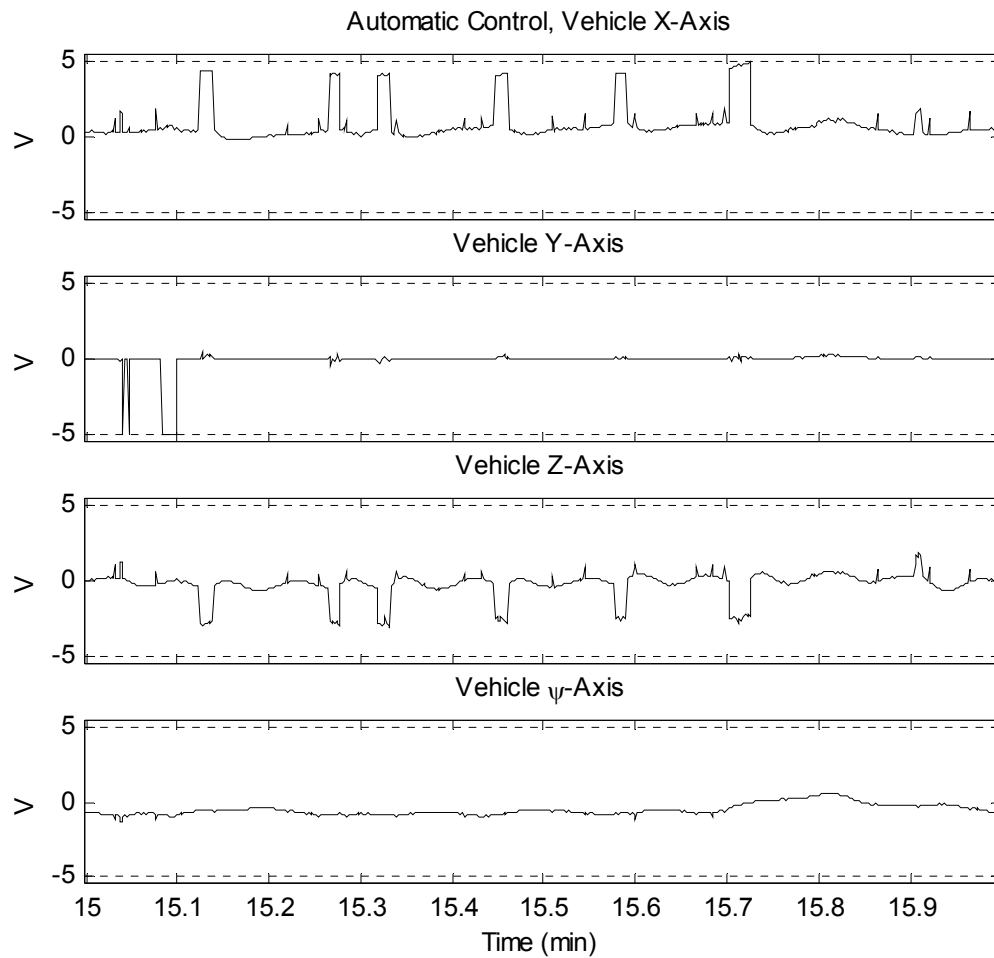
The boundary control term serves a critical role in enforcing the viewing cone limits during extended tracking runs. The boundary control term was active for all jelly-tracking runs subsequent to and including the 6/26/02 dive. To illustrate the significance of the boundary control term, this section examines time traces from a portion of a 19-minute run which tracked the medusa *Benthocodon* (Data Log 37 on 6/26/02). The following plots are representative of the function and performance of the boundary control term on 6/26/02 and during subsequent dives.

Figure 6.3 shows the raw measurements of target location during minute 15 of the data log. The measurements include a target range signal, derived from parallel stereo, and two image plane measurements, for the main stereo camera (an Insite model Orion). Spikes in the range measurement result from brief dropouts in the tracking signal that result, in turn, from the lower-quality video produced by the auxiliary camera (an MSC 2000). The figure shows the limits of the viewing cone occur at  $\pm 128$  pixels from the image center. Interior to these limits are two dashed lines, which indicate the limits of the quiescent zone (see Figure 5.12). The boundary control term becomes active if the target's image plane coordinates pass outside the quiescent zone. The effectiveness of the boundary control signal is apparent from the small magnitude of target excursions outside the quiescent zone.



**Figure 6.3 Benthocodon 1: Raw Measurements, Boundary Control**

*One Minute of the Benthocodon Run (6/26/02 DL37). This plot shows the raw measurements from the parallel stereo (short baseline) camera configuration. In the range signal (top), occasional spikes are clearly visible. These spikes result from noisy segmentation or from a brief loss of visual lock in the upper (auxiliary) stereo camera. The bottom two plots show the target image plane location in pixels in the lower (main) stereo camera. The image boundaries are at  $\pm 128$  pixels. The boundary for the boundary control term is shown as a dashed horizontal line. The boundary control keeps the target inside these boundaries while preserving less aggressive control in the quiescent inner region of the vision cone. For these experiments the boundary control term was linked to the main camera, only, and not to the auxiliary camera.*



**Figure 6.4 Benthocodon 2: Vehicle Control Input**

*One Minute of the Benthocodon Run (6/26/02 DL37). This run uses the parallel stereo configuration, with the cameras pointed downward  $60^\circ$  from vertical. Because of the camera tilt, the vertical image-plane direction maps into both the vehicle x and z -axes. Consequently, boundary control spikes occur simultaneously in both the x and z-axis plots. Boundary control spikes for the y-axis correspond, instead, with the target's horizontal location in the image plane.*

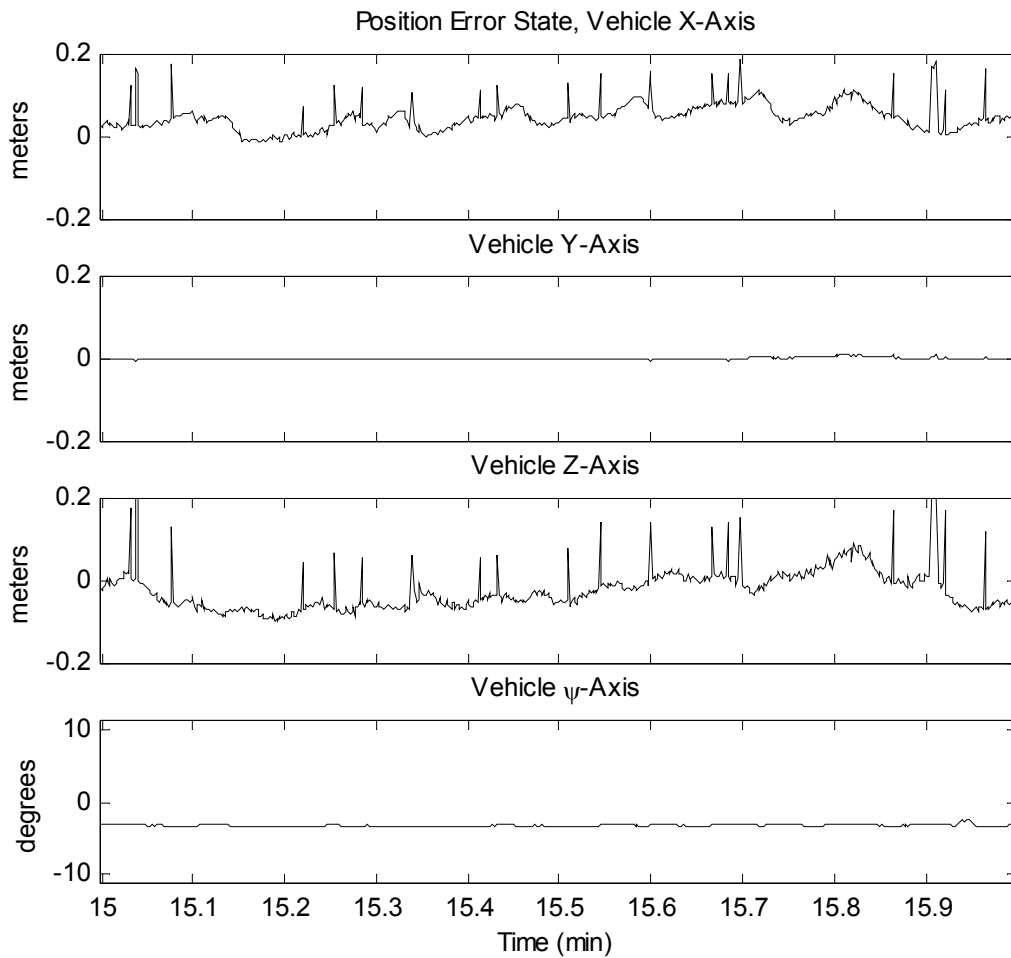


**Figure 6.5 Benthocodon 3: Position Error State**

*One Minute of the Benthocodon Run (6/26/02 DL37). This plot shows the position error state on which the control in Figure 6.4 is acting. Notice the significant vertical spikes in the x and z-axis directions. These result from noise in the parallel stereo measurement. Each spike lasts approximately 1/10th of a second (the sample frequency for the control application).*

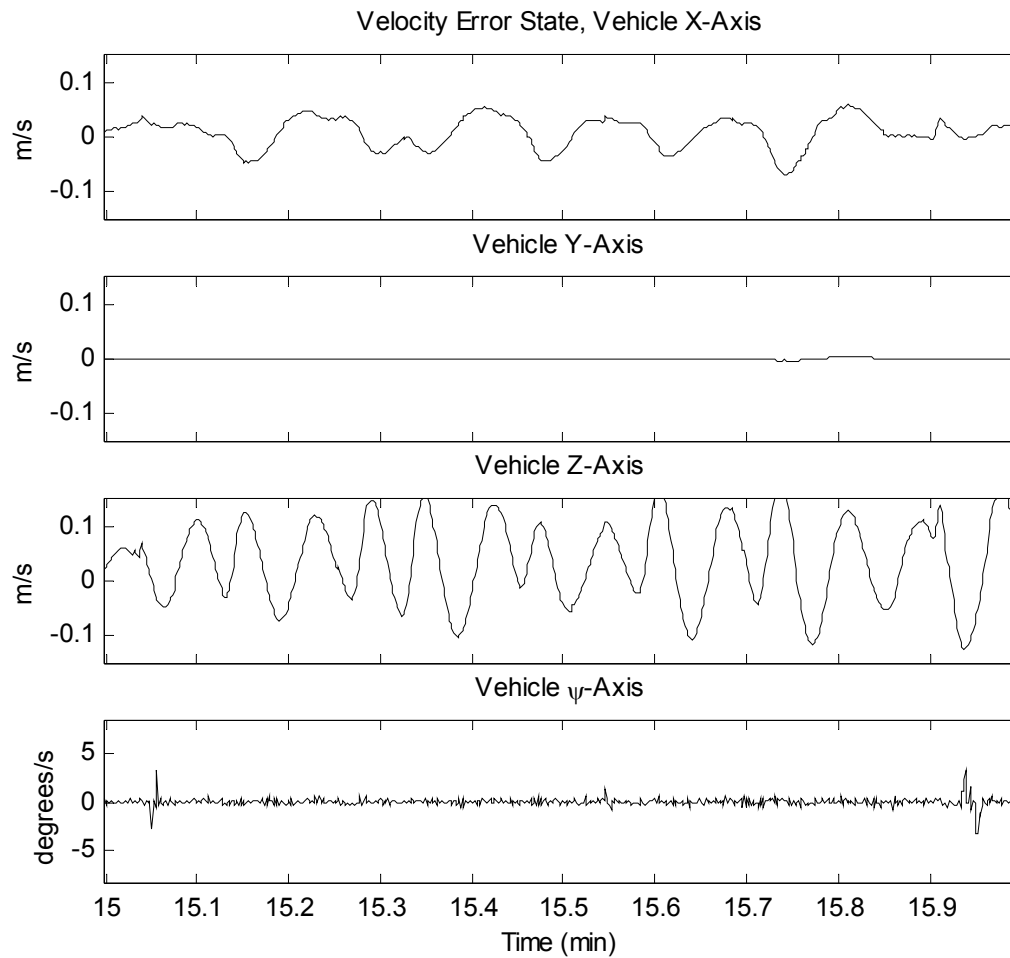


**Figure 6.6 Benthocodon 4: Velocity Error State, Chatter and Limit Cycles**

*One Minute of the Benthocodon Run (6/26/02 DL37). This plot shows the velocity error state on which the control in Figure 6.4 is acting. The velocity is calculated through an estimator (Section 5.4.3). Velocity oscillations are apparent in the x and z-axis directions. With the disturbance-accommodation term inactive, the boundary control term appears to result in chatter (Figure 6.3), which drives the fore-aft oscillations and excites, in part, the vertical oscillations. The z-axis oscillations, unlike the x-axis oscillations, do not correspond to the chatter frequency. These z-axis oscillations may result from a thruster limit cycle.*

The boundary control term acts rapidly to keep the target's image plane coordinates inside the dashed boundaries of the quiescent zone. Figure 6.4 shows the control input in the vehicle frame. Brief, approximately one-second plateaux of elevated control indicate periods during which the boundary control term was active. Throughout this tracking run, the stereo camera pair points  $60^\circ$  downward from the horizontal; as a consequence, the image frame coordinates (Figure 6.3) and the vehicle frame coordinates (Figure 6.4) do not align. Excursions in the vertical image plane direction thus invoke a boundary control term that acts simultaneously in both the ROV's fore-aft (x-axis) and vertical (z-axis) directions. By contrast, horizontal excursions of the target beyond the image plane's quiescent zone limits invoke boundary control action in the vehicle's lateral (y-axis) direction. On subsequent dives, these boundary actions were mapped instead into the vehicle's yaw ( $\psi$ -axis) direction to maintain consistency of the thruster map's null space augmentation (see Figure 5.2c).

The spikiness of the range signal, as seen in Figure 6.3, has a small effect on the control signals along the vehicle's x-axis and z-axis. The projection of these range errors into vehicle coordinates is evident in the position error plots of Figure 6.5. Spikes are seen in the error signal for the vehicle's fore-aft and vertical axes, only, because the camera frame is tilted but not panned relative to the vehicle axes. These error spikes cause small spikes in the x-axis and z-axis control signals, as seen in Figure 6.4.

Figure 6.6 shows oscillations along both the vehicle's fore-aft and vertical axes. Periodic behavior in the fore-aft axis appears to correspond with the vertical image-plane boundary control action (as seen by the comparison of Figure 6.6 and Figure 6.3). Thus fore-aft oscillations may reflect chattering action at the edge of the boundary controller's quiescent region. For the data log plotted, the estimated force bias on the vehicle was 0.94 V (on a scale where 5 V represents maximum thrust) rearward along the vehicle's x-axis. Because the disturbance-accommodation control term was inactive for this experimental run, the boundary control term was left to repeatedly counter the steady bias force whenever it pushed the animal outside the image plane's quiescent region.

In contrast with the fore-aft axis oscillations, the vertical (z-axis) oscillations do not directly correlate with boundary control action. Vertical oscillations do occur, however, at about twice the boundary-control chatter frequency. A possible mechanism to explain these vertical oscillations involves nonlinear thruster dynamics. In the absence of a bias force (the vertical direction bias



estimate is 0.0 V for this run), the work of Yoerger *et al.* predicts that an ROV will limit cycle on account of nonlinear thruster dynamics [164].

In summary, as of 6/26/02, the boundary control terms were consistently active during all jelly-tracking runs. Boundary chatter observed under a steady bias disturbance suggests the utility of the disturbance-accommodation term to smooth control input. A small limit cycle did occur along the vehicle's vertical axis, but it did not appear to affect tracking duration.

### 6.3.2 Low-Frequency Disturbance Accommodation

Quasi-steady forces dominate the disturbance profile for ROV-based jelly tracking. Figure 6.7 describes disturbance forces over the five jelly-tracking dives between 10/11/01 and 10/23/02. The figure compiles bias force statistics, measured by the disturbance-accommodation estimator (Chapter 5.4.3). Statistics are applied to the bias forces values time-averaged for each datalog. Figure 6.7 plots the median datalog-averaged bias force on each day with an "x." The boxes surrounding each "x" contain the interquartile range on each side of the median (that is, they contain one quarter of the samples on either side of the median). Error bars indicate the extreme values of bias force computed on each day. The horizontal dotted lines, at  $\pm 5$  V, indicate the saturation levels for vehicle thrusters.

Significant bias forces were observed on all dates except 10/23/01. Tether traction is believed to be the dominant component of these bias forces. The largest biases generally occurred in the vertical direction; however significant biases were also observed in the horizontal plane and in the yaw direction. These twisting yaw-biases were not predicted, but were significant (approximately 40% of thrust on average) on the two dates with the longest tracking runs, 6/26/02 and 9/24/02. In general, pilots initiated tracking runs with the bias force pulling the ROV away from the target. This choice reduces the magnitude of the thruster jets directed toward the animal target.

By estimating the bias force during the initial period of human pilot control, a low-frequency accommodation controller can, in principal, enable smooth transition from human pilot to automated control in the presence of a bias disturbance. (i.e. In Figure 5.13, the estimator loop is closed even if the feedback-control loop is open.) The smooth transition problem, however, proves more complicated for the jelly-tracking application than for many other instances of control transfer. In the jelly-tracking application, the human pilot remains in the control loop after the transition to automatic control. In fact, the pilot can remain in the control loop as long as desired

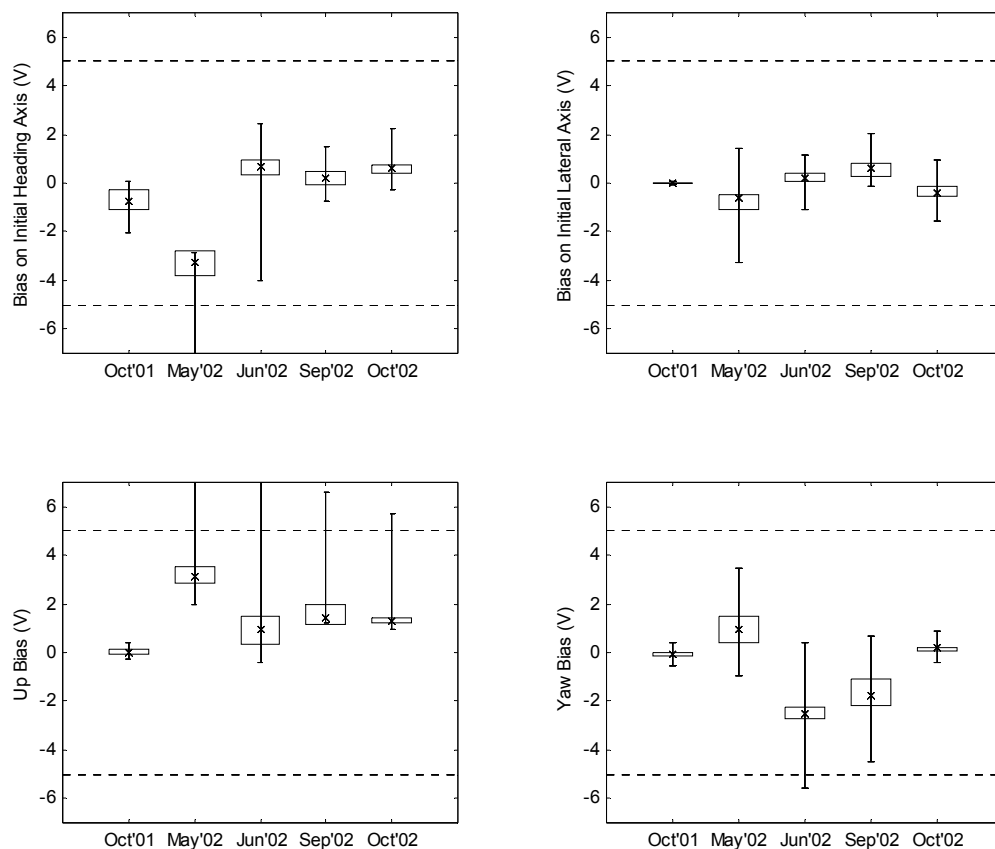


**Figure 6.7 Biases through Time 1**

*This set of box plots shows the estimated bias for each of five successive dive dates in each of the four actuated vehicle axes. On the 5/9/02 dive, biases were significantly higher than usual, particularly in the fore-aft and vertical directions. Bias values shown in the figure are mean values over each datalog. For each day, the median datalog-averaged bias value is marked with an x. The surrounding box bounds the middle two quartiles of bias measurements for that day. The error bars indicate the extreme values of datalog-averaged bias for each day.*

and re-enter the control loop at any time after activation of the automatic controller. Implementing bumpless transfer for this class of supervisory control system demands that the human and computer controllers interact to transfer the bias control component.

Preliminary transfer tests were attempted on 5/9/02, the dive date with the highest levels of bias force in the vertical direction and in the horizontal plane, as described by Figure 6.7. In these tests, the low-frequency disturbance response term was ramped in gradually, over a fixed period of time. The approach assumed that the human pilot would notice a gradual shift in the target position and, in response, ease off control. This approach proved problematic in practice, as demonstrated by Figure 6.8.

Figure 6.8 depicts two successive attempts at initializing a jelly-tracking control run. The top plot shows motion of the target in the image-plane, in the vertical direction. Motion of the target away from the zero-pixel location, in this plot, indicates initialization of the pilot-assist system. During the initialization period, the pilot assist runs in open-loop mode and estimates the bias force on the vehicle. The second plot of Figure 6.8 depicts the bias forces computed by the disturbance-accommodation estimator. The gray, shaded regions on these plots indicate the time during which the low-frequency control signal was phased in. The boundary control term was not enabled for these tests; however, the linear control term became active at the start of the gray, shaded region. The third and fourth plots depict control signals issued by the human and computer controllers. The third plot shows the sum of the two control commands, issued to the ROV thrusters. The fourth plot shows the human and computer control commands individually.

During the first transition attempt, the low-frequency bias component was ramped in over 10 seconds. The pilot control commands indicate that the pilot did not become aware of the bias force until after the ramp was completed. Effectively, the double-integrator relationship between bias force and target position meant that the pilot, observing only the target's position in the video stream, reacted to the bias force change only when the bias force built up to a significant level. During this transition, the pilot indicated a lack of perception of the ramp, as if the transition happened all at once.

For comparison, a very rapid (1-second) transition was attempted, to reduce confusion about when the automated bias force would become active. Even with this additional external queue, telling the pilot when the transfer would occur, the bias transfer still caught the pilot off guard. In the second case, like the first, the low-frequency control ramped up blindly. The summed control

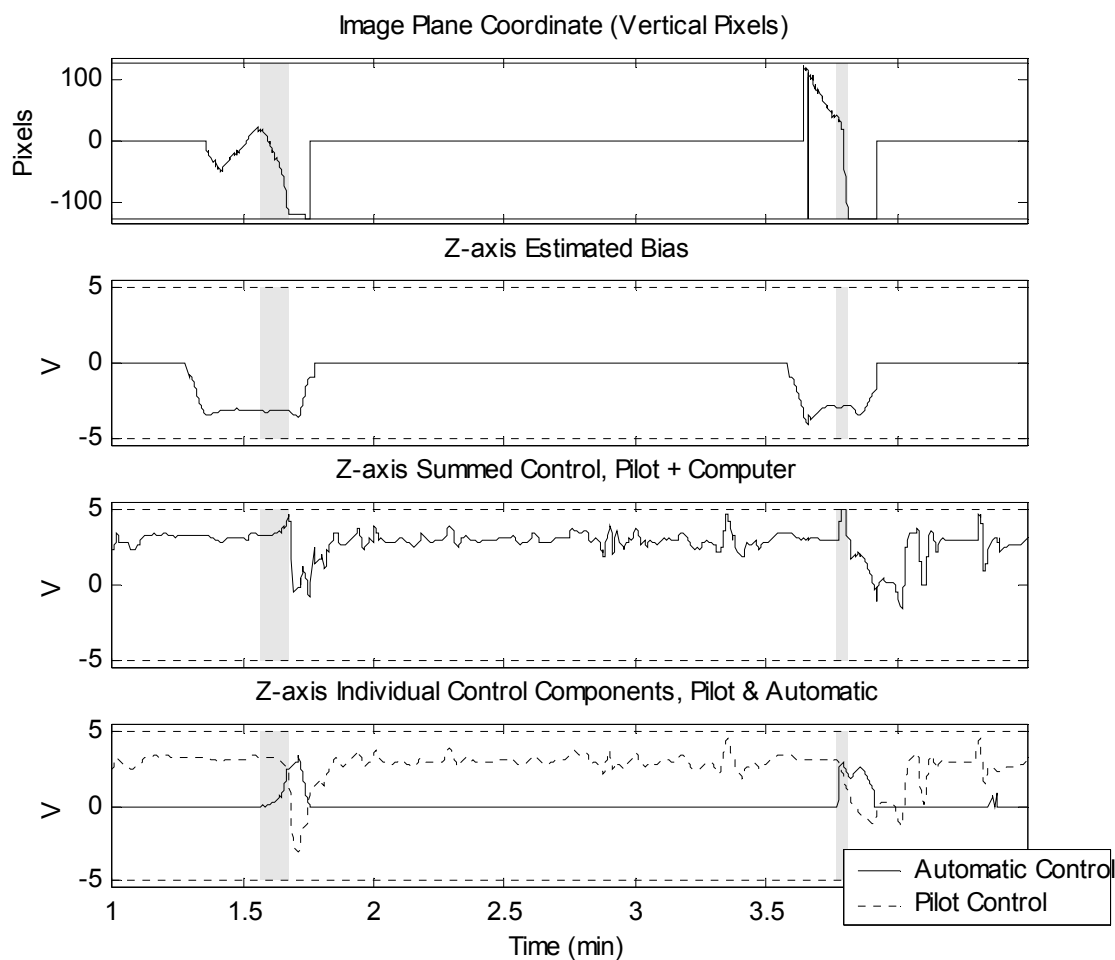


**Figure 6.8 Double Bias Compensation**

*These data describe two aborted initializations (5/9/02 DL20). These runs occurred on a day with an unusually strong tether pull. This bias, experienced by computer and human pilot alike, may have been caused by strong surface winds and a large gradient in current velocity between the surface and the operational depth. To compensate for the tether bias, the disturbance-accommodation control term was used. The disturbance-accommodation estimator was first allowed to converge while the human pilot flew. Then the linear controller was switched on. From the time of the switch, the disturbance-accommodation control term was ramped in slowly (first over 10 seconds, then over 1 second). For each ramp period (gray shaded regions, above), both the pilot and the automatic control simultaneously attempted to compensate for the tether bias. The double compensation caused the target to shoot outside the vision cone boundaries in the direction opposite the tether force.*

term effectively double-counted the bias force, with offsets provided by both the human and computer pilots. In response, the target quickly shot off the top of the viewing screen, in the direction opposite the tether force.

These tests indicate a need for future investigations into human-computer interaction in the case of transfer between overlapping, non-communicating controllers. To avoid problems during subsequent jelly-tracking runs, the low-frequency control term was generally deactivated for control experiments between 6/26/02 and 10/11/02. In a few cases, the low-frequency control term was activated, but only after the human pilot ceased issuing control signals. An example is presented in the following section, which describes a shared control experiment.

In the absence of a technique for rapidly offsetting bias forces, strong initial transients frequently marked the initiation of automated jelly-tracking. Figure 6.9 depicts an initial transient in the range direction, given a horizontal component of the bias force of approximately 1 V (20% of thruster). In this case, the range reference was set to 90% of the range measurement on autopilot initialization. When automatic control switched on, as shown by the upper plot of Figure 6.9, the range increased from its initial value of 0.71 m to a value of approximately 0.8 m, under the rearward pull of the tether bias. Subsequently, control action countered the bias and returned range toward the reference, at 0.63 m, overshooting slightly. Finally, the range value settled at 0.68 m, with the steady-state error caused by the quasi-steady bias disturbance.

### 6.3.3 Shared Control Using the Control-Objective Null Space

The experimental run of 10/11/02, data log 34, evaluated the concept of human pilot control in the tracking law's null space. Human-pilot commands were issued in the circumferential direction, for which thrust was set to zero by the null space thruster map (Chapter 5.3.2). In contrast with other extended length tracking experiments, which operated under full automatic control with no pilot input after initialization, the shared control experiment combined simultaneous human pilot and computer control. These simultaneous commands did not interfere with each other, as the human pilot commands acted orthogonal to those issued by the linear tracking and nonlinear boundary control laws.

During the shared control test, the human pilot was asked to circle the ROV around the gelatinous target, a sinking larvacean house. The test simulated the control action necessary to respond to a scientist's request to circle around an animal subject to acquire a different point of view. The

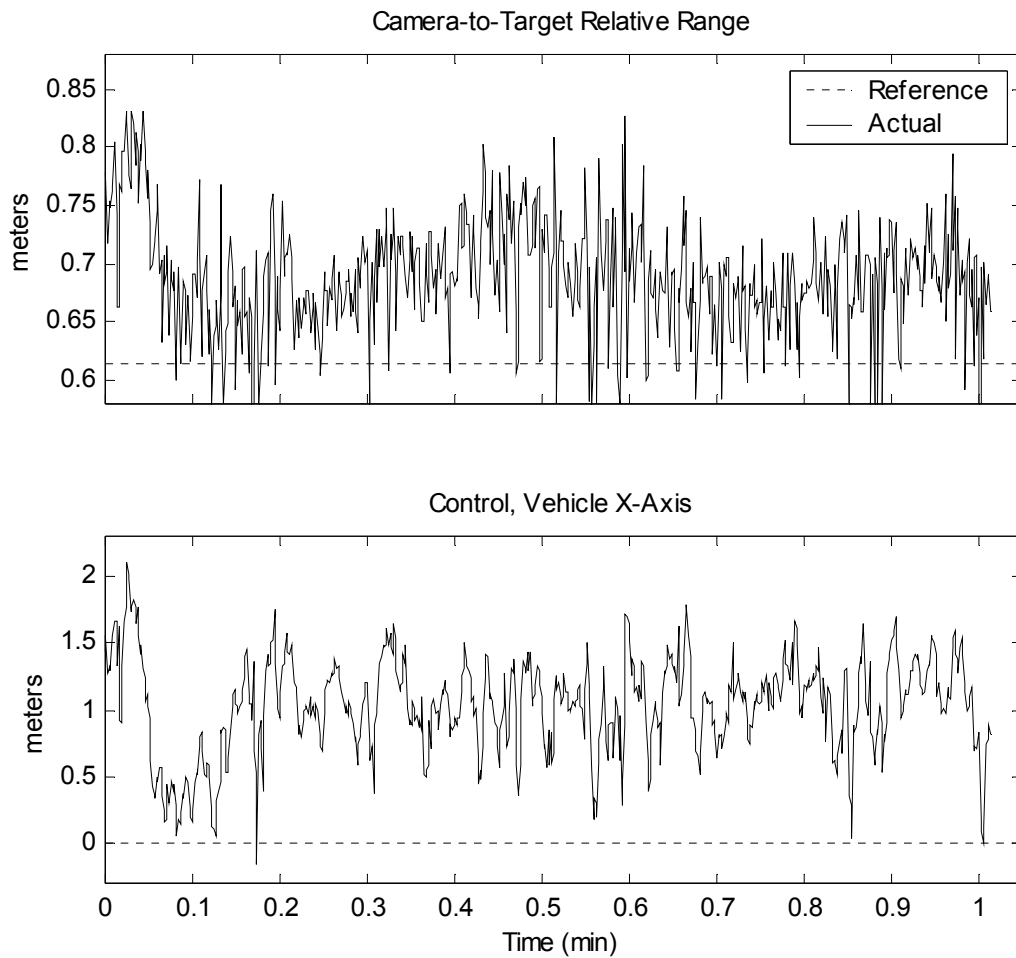


**Figure 6.9 Initial Range Response**

*Ptychogena* run (10/11/02 DL24). This plot shows range measurements and control at the initiation of a typical run. The range reference is set to 90% of the initial range. In these plots, the range is seen to increase immediately, because of a tether force. (The disturbance-accommodation control term is not active in this run.) The controller attempts to counteract this tether bias, and pulls the animal closer to the range reference, overshooting slightly. Because no integral or disturbance accommodation terms are active, the steady state error is non-zero (approximately 5 cm).

success of the test, which ended when the release of ink by a nearby squid completely obscured the viewing area, validates null-space control sharing for the jelly-tracking application and establishes the system capability as a useful feature for science applications.

In addition to demonstrating the feasibility of control sharing, the experiment also illustrates the full control law described in Chapter 5. For the shared control experiment, all three control terms were active: linear tracking, nonlinear boundary control, and disturbance-accommodation (DA) control. The computer issued no commands in the circumferential coordinate about the target animal, except for a low-frequency DA command. This circumferential control was designed to offset the circumferential restoring force that results from a bias in the horizontal plane (Chapter 5.4.3). In theory, this design achieves neutral stability in the circumferential direction, allowing the pilot to place the vehicle at any circumferential coordinate with minimal continuous control action required.

Figure 6.10 illustrates the vehicle's yaw heading and the lateral pilot and computer control inputs during the shared control experiment. Because the yaw bearing error remains small (less than  $5^\circ$  through the experiment), the yaw heading angle is approximately equal to the circumferential ROV position, offset by  $180^\circ$  (according to Equation 5.9). The heading plot shows that the ROV makes one complete turn to port, between minutes 5 and 9, and then reverses the turn direction to starboard for a second complete turn, between minutes 10 and 13. A third turn was commenced, to port, starting at minute 16, but this turn was not completed.

Accompanying the yaw heading plot on Figure 6.10, the lateral control plots describe the circumferential control action during the shared control experiment. As the vehicle continually turned to point at the target, the vehicle's lateral coordinate was always aligned, within  $5^\circ$ , to the jelly-frame circumferential direction. The computer command in the lateral direction is shown in the bottom plot of Figure 6.10. This command is approximately zero through the beginning of the first turn, because the vehicle is aligned, initially, such that the tether bias force pulls radially away from the target, orthogonal to the circumferential axis (see the bias estimate plots, Figure 6.11). During the turns, the lateral DA control takes a sinusoidal form, as the tether bias force, approximately fixed in direction in the world frame, rotates in the vehicle frame. This sinusoidal form is particularly apparent during the first turn, minutes 5-9. The sinusoidal variations in bias are offset from zero, however, because the lateral controller also attempts to counter circumferential drag, which was inaccurately modeled by the estimator predictor. Drag accommodation acts in a single

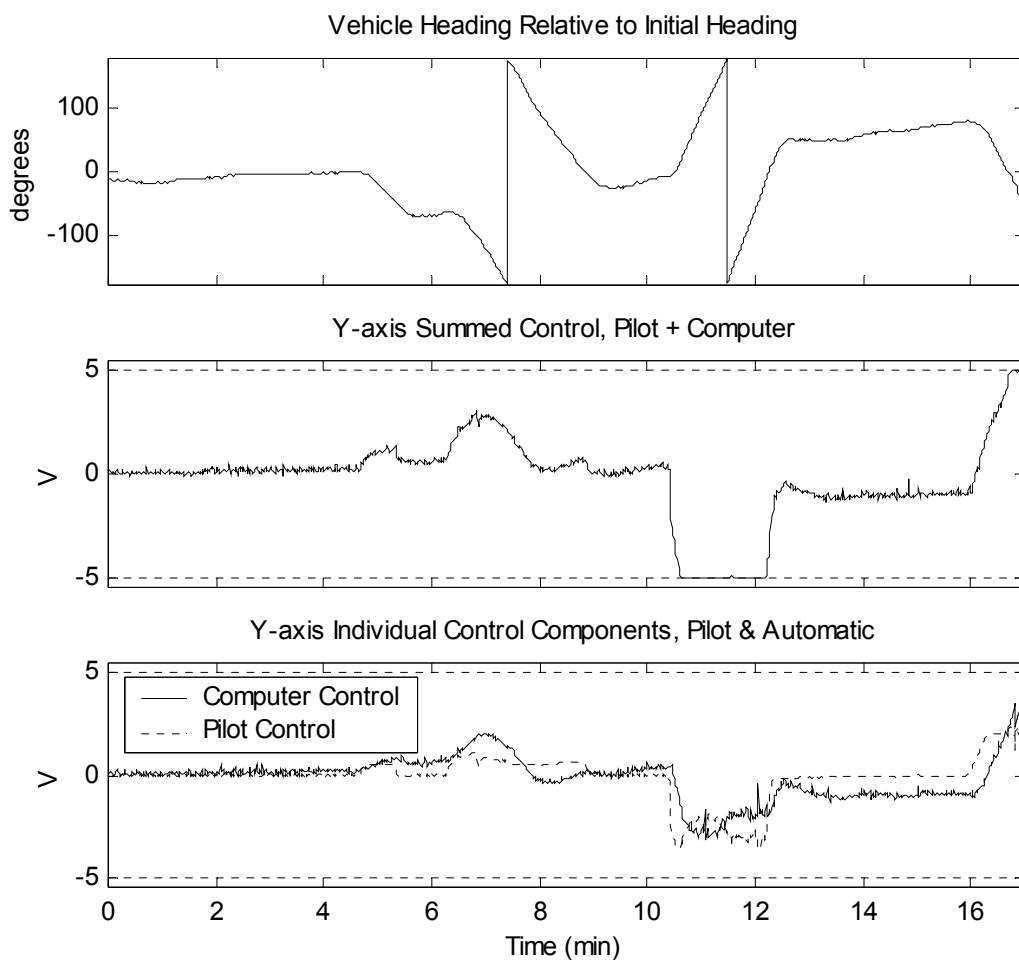


**Figure 6.10 Shared Control 1: Circumferential Control Signals**

Data describes a shared-control experiment (10/11/02 DL34). The pilot turns the vehicle first to port (Minutes 5-9) and then to starboard (Minutes 10-13). The vehicle heading plot (top) shows the yaw angle change over time. The summed control plot (middle) shows the total control issued in the lateral direction by both the human pilot and the automated controller. The computer and manual control commands are also plotted individually (bottom). Automated control in the lateral direction is the result of the DA control term. A portion of the bias is fixed in the world frame (the bias force caused by the vehicle tether) and does not rotate with the vehicle. A portion of the bias is fixed in the vehicle frame (drag force bias due to limitations in the vehicle model) and rotates with the vehicle. As a result, the automated control during each rotation event appears sinusoidal (world-fixed tether component) and offset from the zero axis (vehicle-fixed drag component).



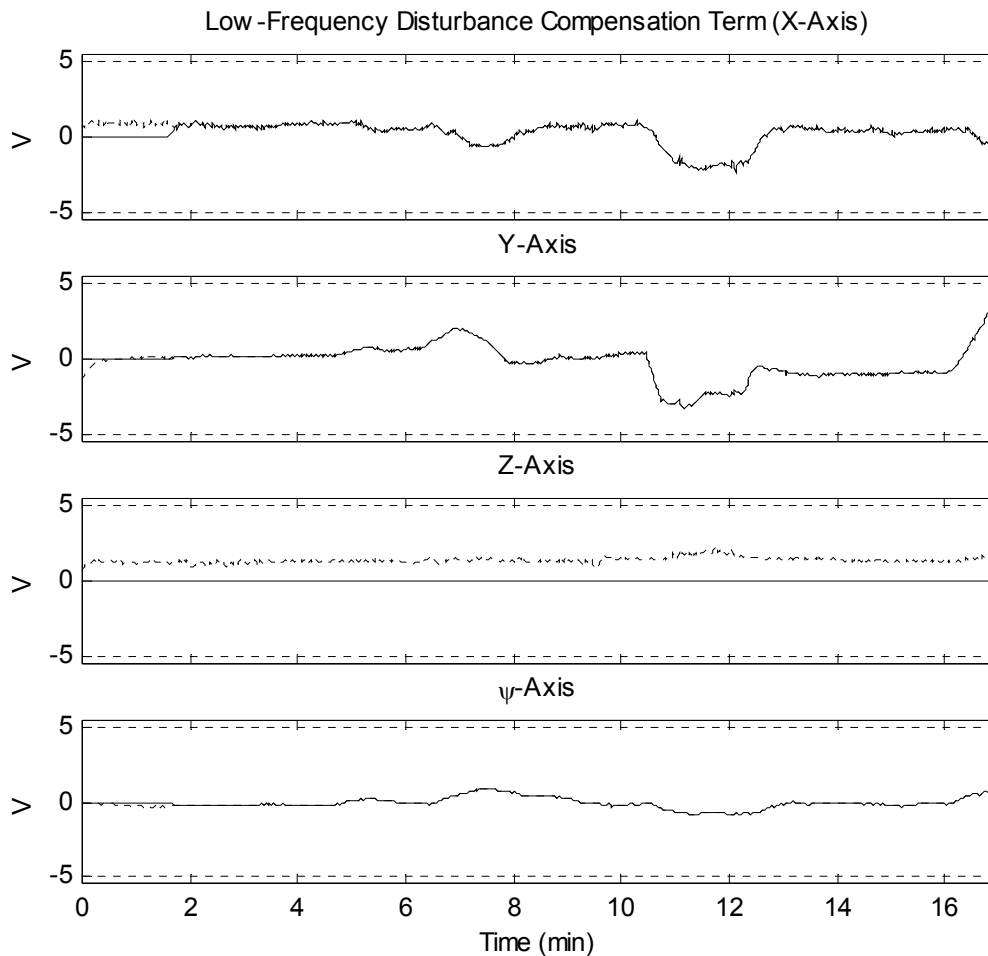


**Figure 6.11 Shared Control 2: Disturbance-Accommodation (DA) Control**

Data describes a shared-control experiment (10/11/02 DL34). The DA control term was activated at minute 2, rather than initially, to avoid double bias compensation. DA control ramped in over 15 seconds. The top plot shows DA control in the vehicle x-axis (range). During the first turn (Minutes 5-9) the bias changes from +1 to -1 and back, compensating for the tether direction (approximately fixed in the world frame). During the second turn, the range-axis bias changes from +1 to -2 and back. The asymmetry likely resulted from thruster saturation during the turn. The z-axis DA control was set to zero, because the pilot's vertical control slider does not automatically zero itself when the pilot ceases manual control (this feature lets the pilot trim the ROV for buoyancy). The yaw bias was not predicted. Because the yaw bias appears only during the turns, and because its sign switches with the sense of the turn, it is possible that the bias results from the vehicle lateral drag center being located in front of its center of mass.

direction, circumferentially and offsets the sinusoidal tether accommodation by approximately 1 V away from zero (during minutes 5-9). This cycling of the tether force is also apparent in the range direction (the vehicle frame x-direction in Figure 6.11). The range direction variations in tether bias are cosinusoidal, out of phase with the circumferential DA term by  $90^\circ$ . The drag offset does not affect the bias estimate along the vehicle's x-axis.

The sinusoidal variation in the vehicle-frame representation of the tether bias is less apparent during the second turn (minutes 10-13). Saturation of the vehicle's lateral thruster action (Figure 6.10, middle plot) affects estimator performance during the second turn. During saturation, the hydraulic system on the ROV cannot deliver the desired rate of flow of hydraulic fluid to the individual actuators. As such, delivered thrust drops below requested thrust. The estimator used for DA control does not take into account this effect. Consequently, the apparent magnitude of bias disturbances are magnified during saturation conditions (this occurs in both the vehicle x-axis and y-axis, as shown by Figure 6.11).

During minutes 13 to 16, the DA control achieves its stated purpose and makes the vehicle approximately neutrally stable in the circumferential coordinate. While the pilot's lateral command is zero, the automatic controller holds a non-zero quasi-steady bias (Figure 6.10, bottom plot). During this time, the circumferential angle drifts only slowly (Figure 6.10, top plot).

During both turns, a small bias force was measured in the yaw ( $\psi$ -axis) direction. The sign of the yaw bias remained constant during each turn, but changed sign when the direction of the turn shifted from port to starboard. The yaw bias returned to zero between turns. Based on this evidence, the tether was not likely to be the cause of the yaw bias. A bias caused by tether twisting would not have returned to zero between turns, when the tether was twisted by  $360^\circ$ . Likewise, a moment caused by an offset of the tether attachment point from a vertical line through the ROV mass center would have changed sign halfway through a complete revolution. Because the sign of the yaw bias remained constant throughout each turn, but changed sign for turns of opposite direction, a likely cause for the yaw bias involves drag-moment coupling. If the lateral drag center were positioned forward of the mass center, lateral drag would act to turn the ROV to port during a starboard motion, and vice versa, as observed. In any case, this phenomenon has the surprising effect of stabilizing relative yaw bearing during the turn. For the shared control experiment, the controller was not reconfigured to issue a yaw command to counteract the pilot's circumferential control command (Chapter 5.3.2). Nonetheless, the system appears to regulate yaw-bearing error within

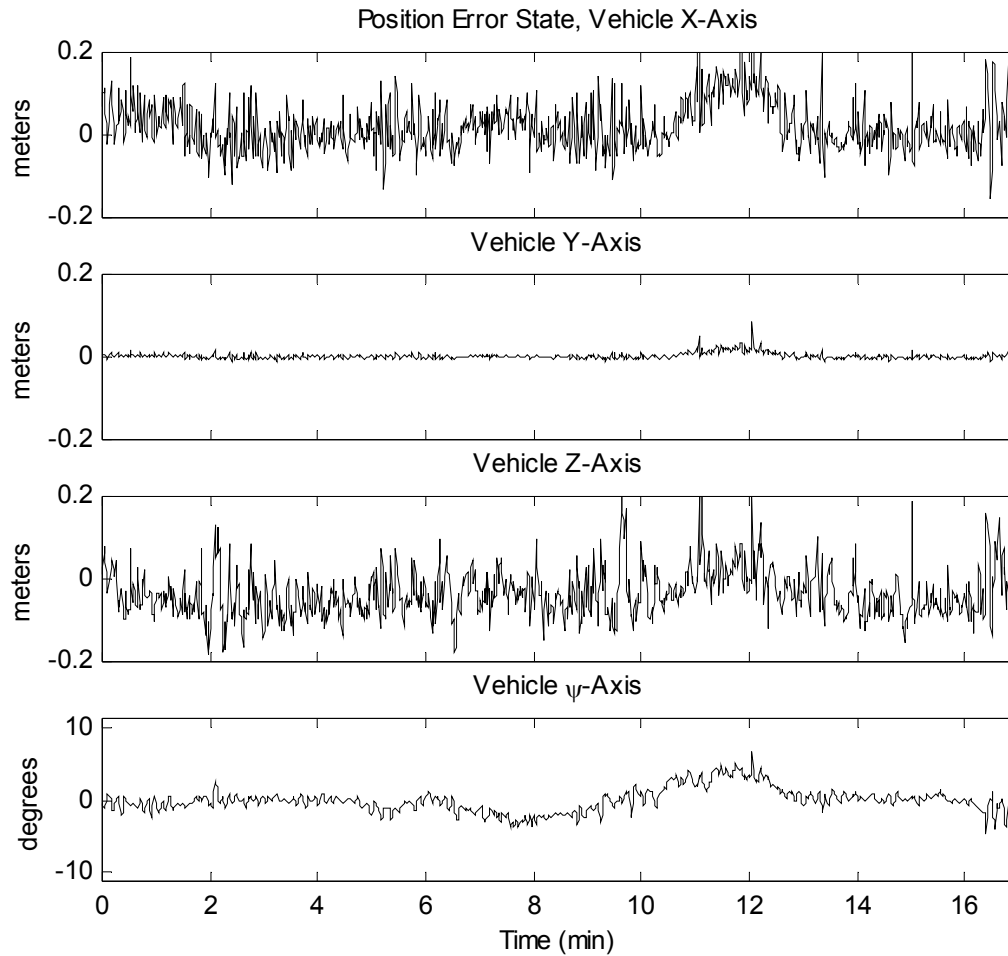


**Figure 6.12 Shared Control 3: Position Error**

*Data describes a shared-control experiment (10/11/02 DL34). These plots of position error show that the dominant noise source resides in the range measurement. Because the camera is tilted 41 degrees from vertical and 8 degrees to starboard, the range signal effects the vehicle x, y and z-axis errors, (although the effect on the y-axis is minimal). Errors are largest during the second turn (to starboard, minutes 10-13). During this time control saturates. The estimator does not account for the drop in flow rate of hydraulic fluid to the thrusters under high thrust conditions. This phenomenon appears to result in lower-than-commanded thrust during thruster saturation.*

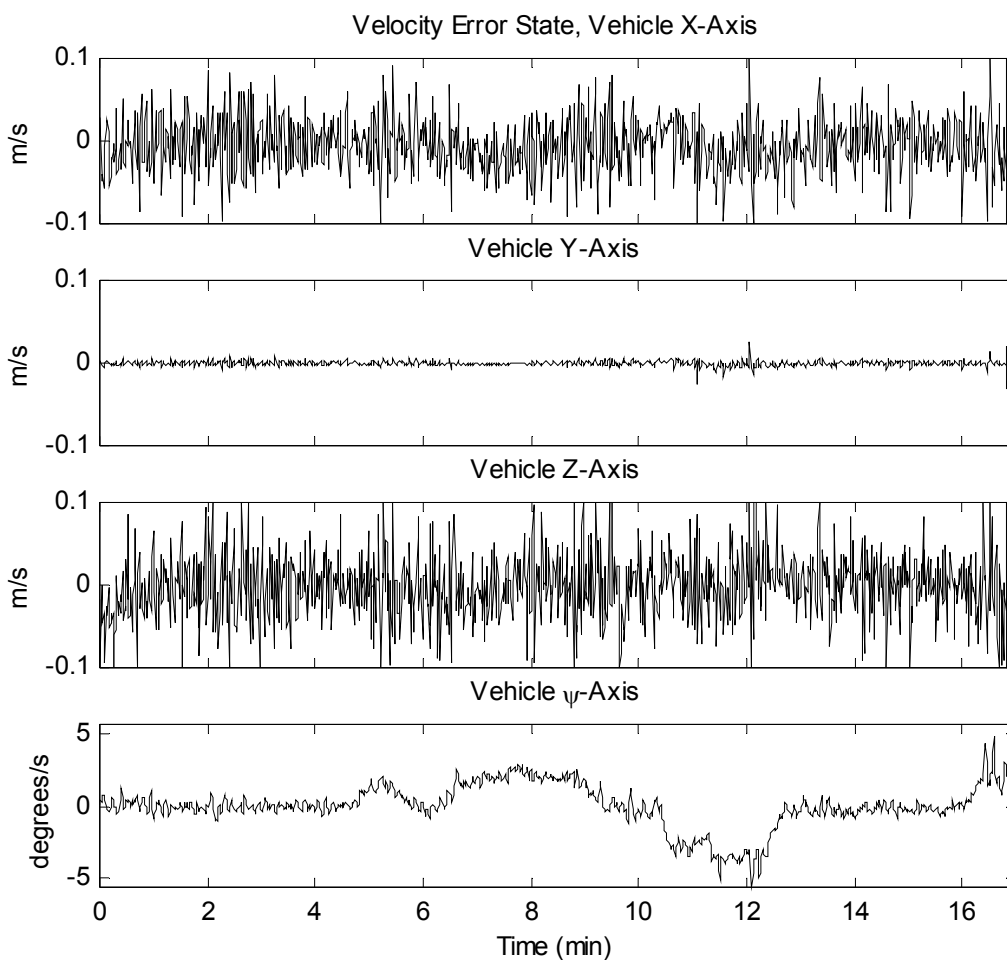


**Figure 6.13 Shared Control 4: Velocity Error**

*Data describes a shared-control experiment (10/11/02 DL34). These plots show the velocity error states used for control. Noise in the range signal creates significant noise in the velocity signals in the x and z-axes. (The values shown are, in fact, filtered by the state estimator, Section ). For this data log, the angular velocity error was based on yaw heading, rather than on relative yaw bearing.*

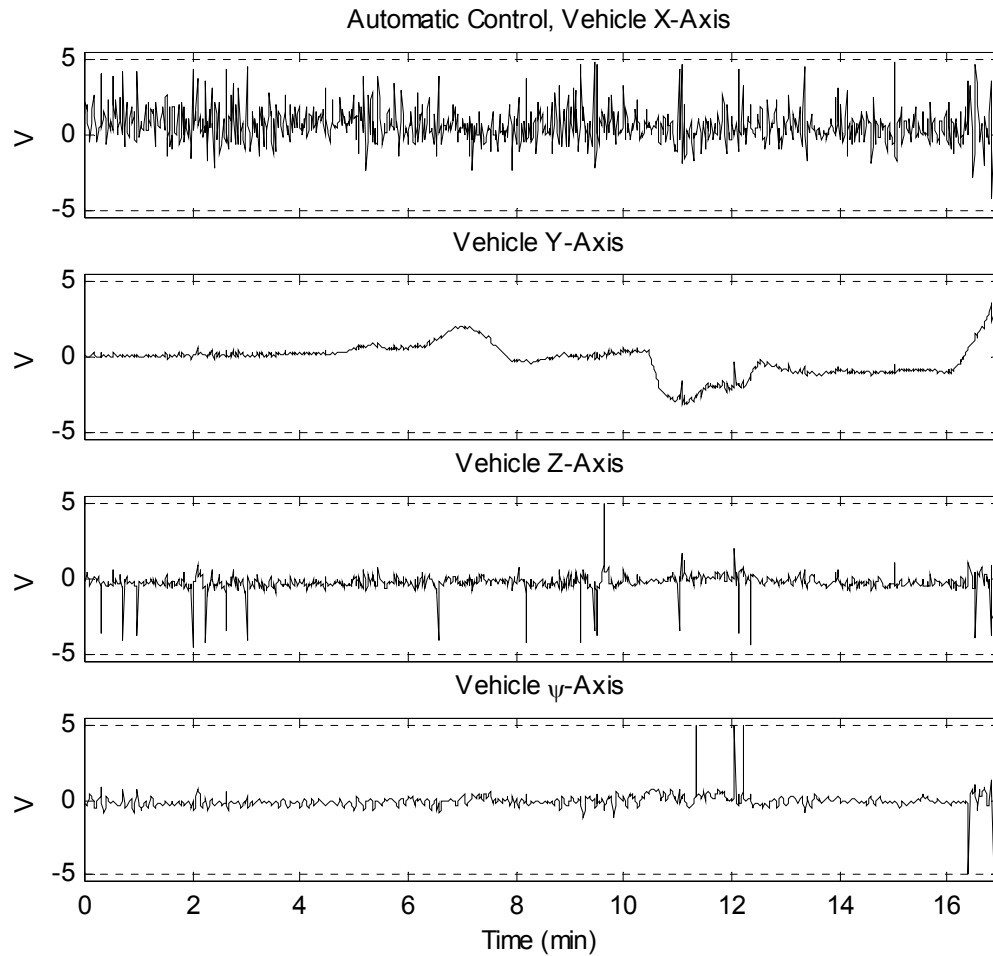


**Figure 6.14 Shared Control 5: 4-Axis Automatic Control**

*Data describes a shared-control experiment (10/11/02 DL34). During the shared-control run, the automated system tracks a sinking larvacean house in 3 DOF: relative range, bearing, and depth. The DA and boundary control terms were both active during this run. For this run, the boundary control is coupled in the vehicle x and z directions, because the parallel stereo cameras are pointed downward  $41^\circ$  from vertical. The horizontal image boundary control activates the yaw thrusters. Thus, spikes in the x, y, and  $\psi$  axes result from boundary control action.*

5° of zero (Figure 6.12, bottom) during both 360° turns with essentially zero mean control action (Figure 6.14).

Range measurements appear particularly noisy during the shared control run. Because the parallel stereo pair points downward at 41° from the horizontal, the range estimate affects the noise levels for the position (Figure 6.12) and velocity errors (Figure 6.13) along both the vehicle's x-axis and z-axis. Because the linear control gains were four times higher for the x-axis than the z-axis, this noise appears as a more significant part of the x-axis control signal than the z-axis control signal, as seen in Figure 6.14. Range measurement noise resulted from inconsistent segmentation of the thin target. Because of the target's thin shape, small variation in segmentation resulted in large changes in the measured bearing to the target centroid. These variations, in turn, resulted in significant noise in the triangulated range.

The nonlinear boundary control term played an important role in preserving the shared-control run from an out-of-frame target loss. Figure 6.15 details the action of the boundary controller during the shared control experiment. The figure shows both the vertical and horizontal pixel location of the target, as seen from the main camera (first and fourth plots). Whenever the image plane position strays outside the boundaries of the quiescent region, indicated by the dashed lines, boundary control triggered (second and fifth plots). The trigger activated an impulsive control term in the appropriate direction. An excursion of the target along the vertical image coordinate activated boundary control in the x-direction and z-direction (third plot shows the z-axis). An excursion of the target along the horizontal image coordinate activated boundary control in the  $\psi$ -axis direction (final plot). For these tests, boundary control action was applied in the yaw coordinate, rather than the lateral coordinate, to minimize interaction with the human pilot commands issued in the circumferential direction.

A final plot illustrates the three-dimension position of the ROV, relative to the target jelly (Figure 6.16). This plot summarizes the principal goal of the shared control experiment: the human pilot successfully used the null space to issue commands that did not interfere with automated jellyfish tracking. The human commands shifted the ROV in a circle and back around the target animal, allowing it to be viewed from a variety of angles.

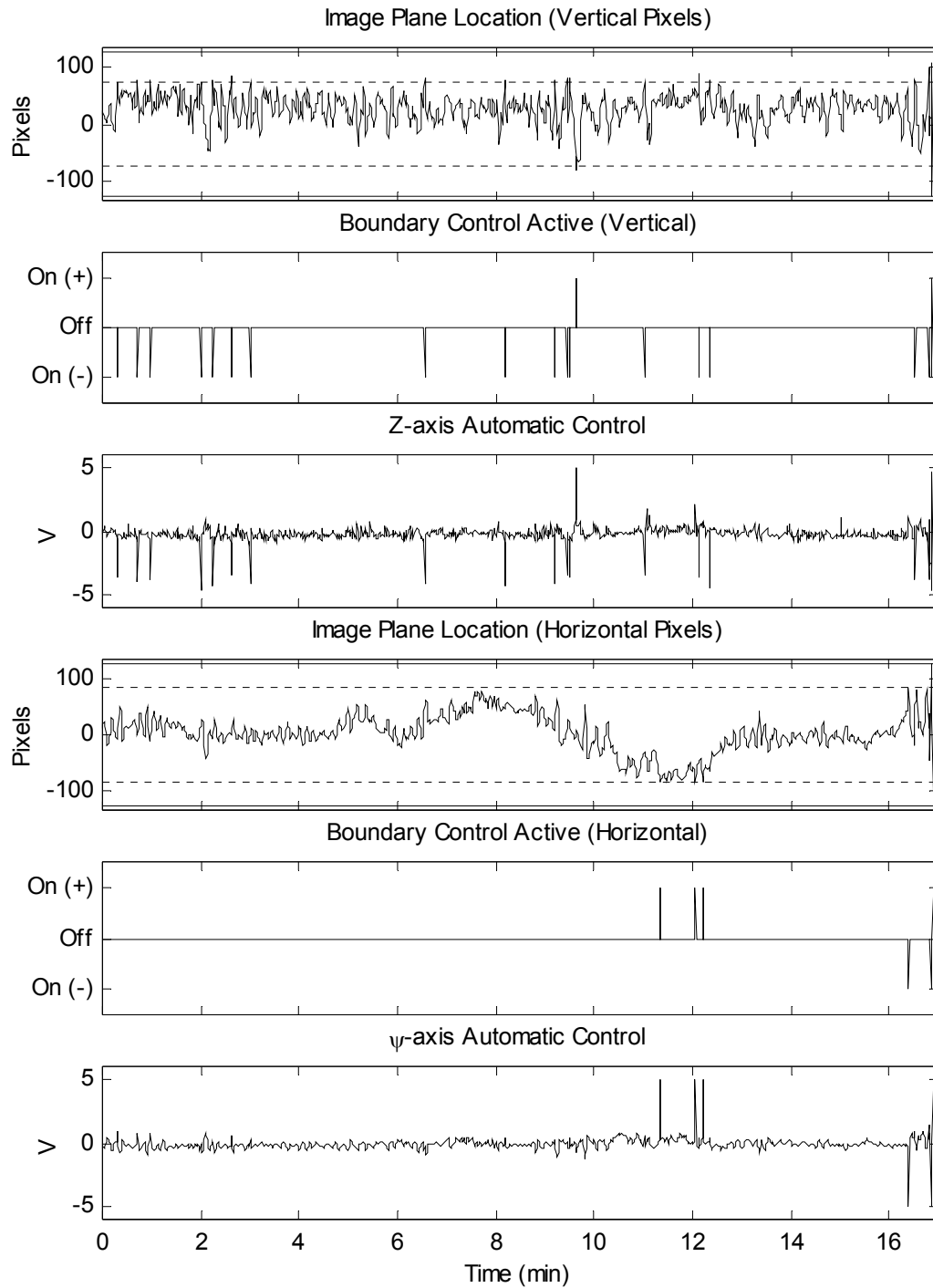


**Figure 6.15 Shared Control 6: Boundary Control**

*Data describes a shared-control experiment (10/11/02 DL34). These plots show the role of the boundary control term in keeping the animal away from the edges of the main camera image.*

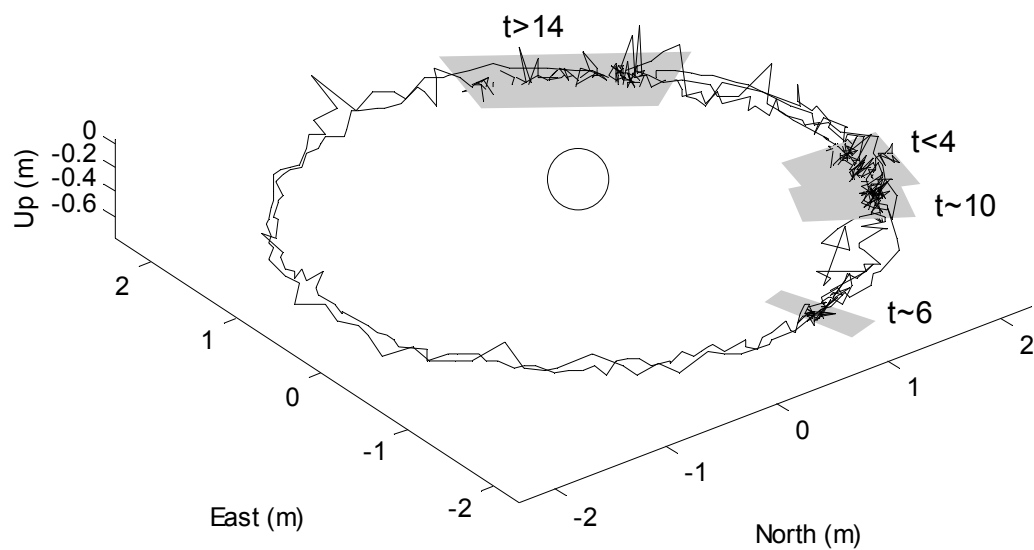


**Figure 6.16 Shared Control 7: Three-Dimensional Position, Relative to the Target**

*Data describes a shared-control experiment (10/11/02 DL34). This plot shows the ROV's position over time relative to the target jelly (depicted as a small circle at the origin). Positions at various points in the run are indicated with gray shaded boxes. The run ended just short of 17 minutes when a cloud of squid ink obscured the target animal.*



#### 6.3.4 The Long Duration *Ptychogena* Run

Extended duration tracking runs bring together the major features of jelly-tracking control already discussed in this chapter: the importance of the boundary control term, of bias disturbances, and of the null-space thruster map. An 89-minute run tracking the medusa *Ptychogena* serves as a useful illustration of system performance over an extended time period. The *Ptychogena* run occurred as data log 31 on the 9/24/02 dive.

In the *Ptychogena* experiment, as in previous runs, the linear tracking law provides continuous regulation of vehicle position relative to the animal subject. This tracking proved sufficient to keep the camera centered on the jellyfish throughout much of the run, including the first 33 minutes of the run during which the animal swam continuously. The boundary control term activated only occasionally during the first forty minutes of the dive. Despite a mild bias disturbance ( $< 1$  V in control units or  $< 15$  lbs. in force units) pulling the ROV radially away from the target, the boundary control remained relatively inactive. In fact, the term triggered only seven times due to horizontal image-plane excursions and only three times due to vertical excursions (Figure 6.20). By only occasionally applying aggressive control when needed, the system maintained generally low levels of control and thereby reduced hydrodynamic disturbances on the environment caused by excessive actuation.

Environmental forcing on the ROV became more severe after minute 40 of the experiment. Both transient and quasi-steady disturbance forces grew in magnitude at this point. The increased intensity of transient disturbances is evident from more frequent triggering of the boundary control term. The increase in environmental disturbances may have resulted from the entry of the ROV into the turbulent ocean-floor boundary layer. The vehicle approached within 15 meters of the ocean floor at minute 40 of the run, and it remained there until minute 50 of the run. Increased transient disturbances may also have resulted from tether snap loads.

Quasi-steady disturbances, most likely the influence of tether traction, also increased significantly after minute 43 of the run and remained elevated until run termination. Increased control input (Figure 6.20) and steady-state error (Figure 6.17) both result from higher bias disturbances levels. Ultimately, near run termination, the bias disturbances grew so strong that they overpowered the vehicle actuators (operating in the boundary control chatter mode) and pulled the ROV away from the target. Following this event, the human pilot resumed control in an attempt to reacquire the target. The human pilots merely confirmed, however, that the tether disturbance had

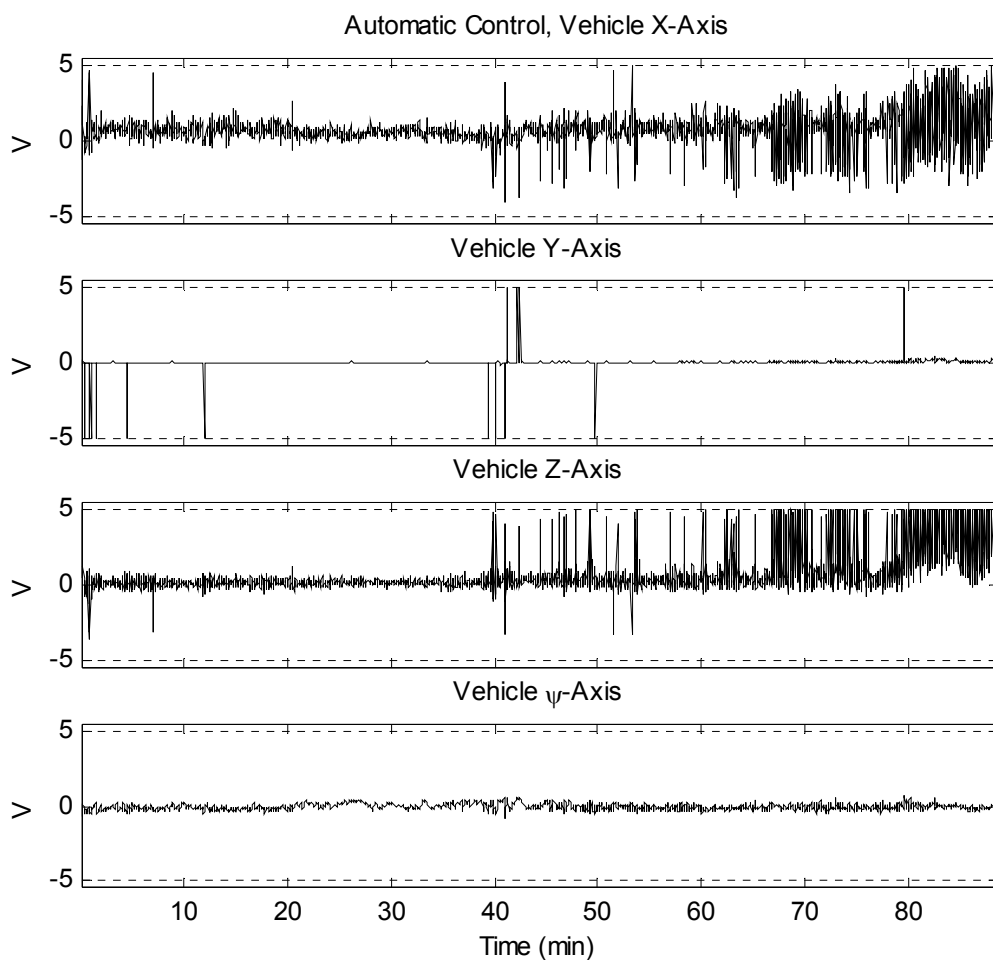


**Figure 6.17 Ptychogena Run 1: Automated Control over Entire 89 Minute Duration**

*Data describe an 89-minute experiment tracking the medusa Ptychogena (9/24/02 DL31). This figure shows the control inputs to the ROV through the entire 89 minute tracking period. Spikes indicate action by the boundary control law. At the end of the run, a strong tether force biases the control input in the x and z directions. After this time, the control signal is dominated by chatter - a rapid succession of boundary term spikes. At the 89 minutes mark, the heavy tether pull overcame the thruster output of the ROV, and the target drifted out of the viewing cone.*

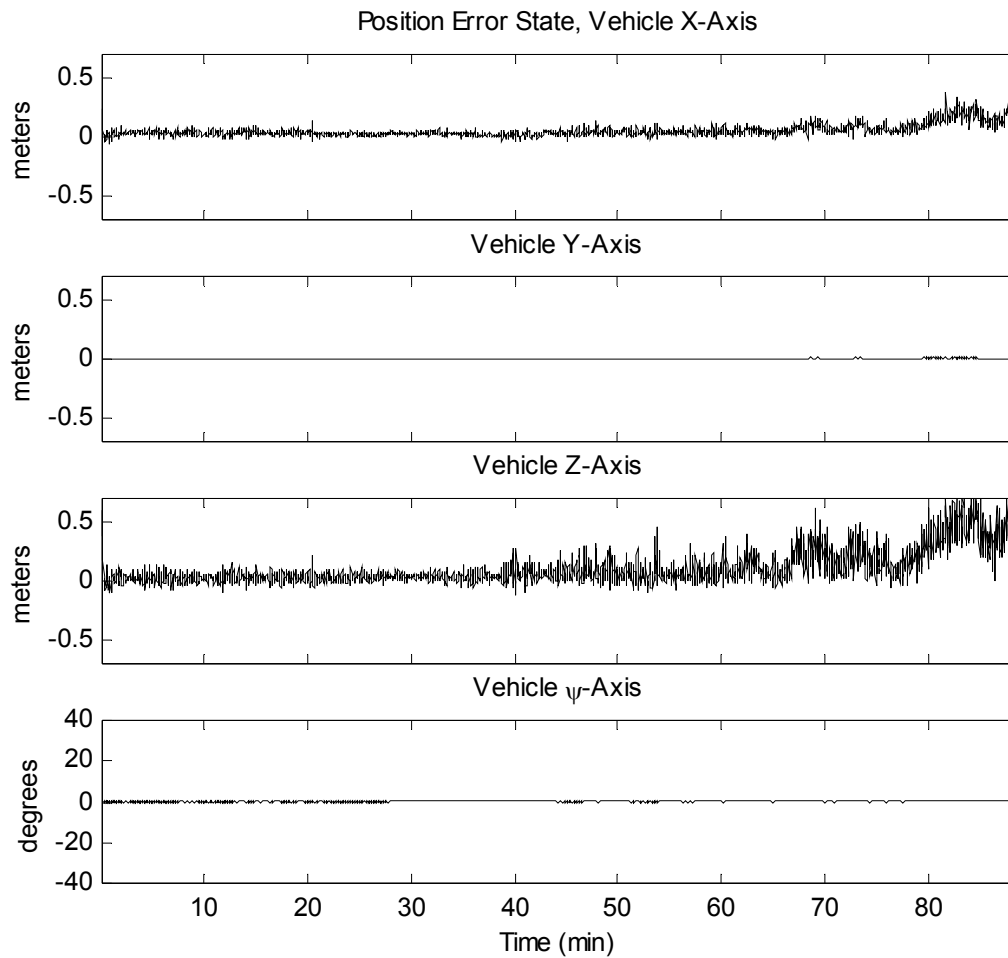


**Figure 6.18 Ptychogena Run 2: Position Error Signal over 89 Minute Run**

Data describe an 89-minute experiment tracking the medusa Ptychogena (9/24/02 DL31). This figure shows the position error from which the control signal was derived. The position error in relative yaw bearing is very small compared with the other controlled axes (x and z axes), in part because of circumferential stabilization by the tether (Section 5.4.3). Increases in tether tension after the 80 minute mark caused the increase in the position error signal seen in the x and z directions.

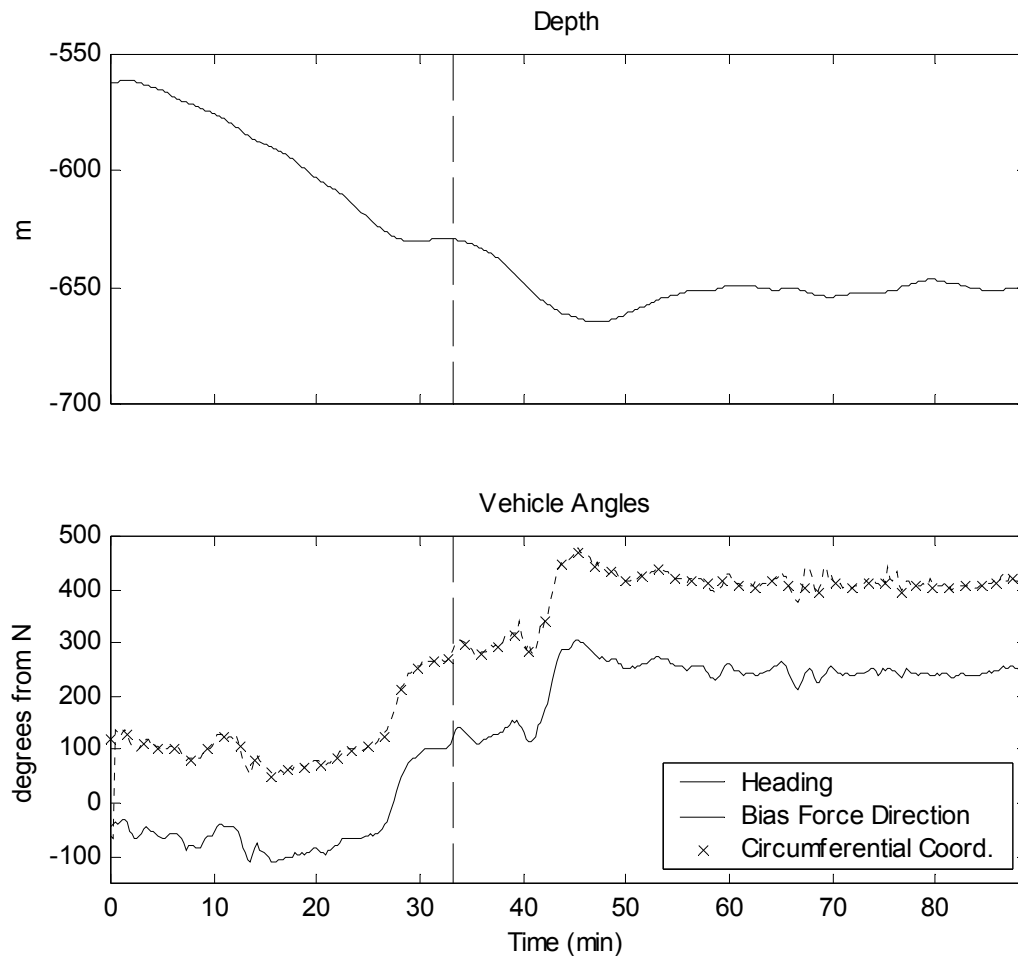


**Figure 6.19 Ptychogena Run 3: Jelly Swimming and Tether Traction**

Data describe an 89-minute experiment tracking the medusa *Ptychogena* (9/24/02 DL31). These plots show motion of the ROV relative to the environment during the extended tracking run. The plot of pressure depth (top) indicates the distance covered by the swimming *Ptychogena* specimen. The dashed vertical line indicates the time at which the *Ptychogena* subject switched from a swimming behavior to a resting behavior. Depth changes after this point were the result of currents near the ocean floor. The plot of compass heading (bottom) indicates that the ROV shifted its circumferential position relative to the jelly twice during the tracking run. The ROV completed one full revolution in the process. As no circumferential control commands were issued, these shifts were most likely caused by changes in the direction of the low-frequency tether bias.

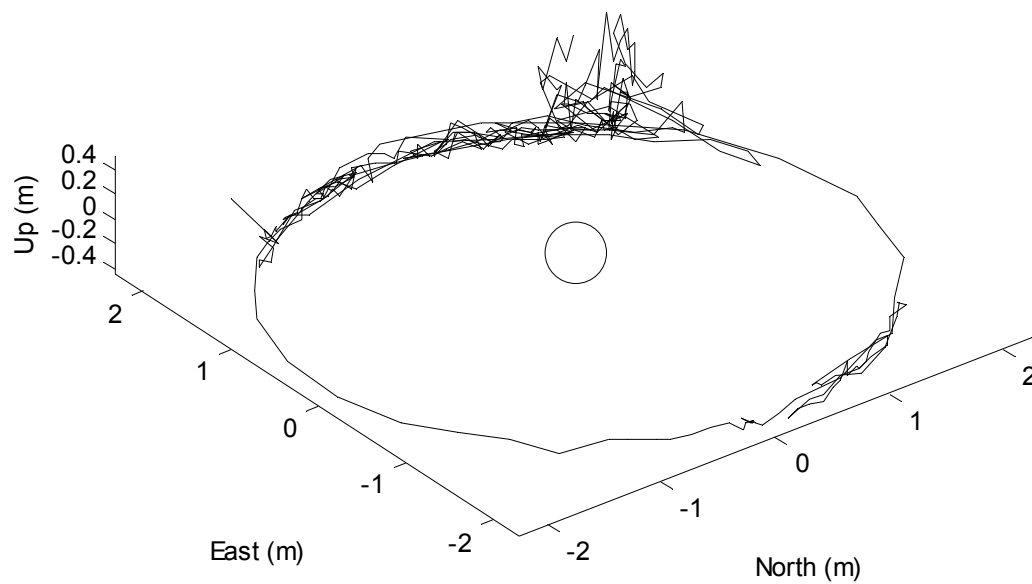


**Figure 6.20 Ptychogena Run 4:**

*Data describe an 89-minute experiment tracking the medusa Ptychogena (9/24/02 DL31). This plot shows the position of the ROV, in three dimensions, during the entire 89 minute run. Coordinates are plotted relative to the jellyfish, which is depicted as a small circle at the origin. From this plot it is clear that the ROV made one complete turn during the tracking run (a half turn during the time of bottom lock, and a second half turn at a later time).*

indeed grown too powerful for the ROV thrusters to overcome, and the *Ptychogena* specimen drifted slowly away.

The tether forces that terminated the *Ptychogena* run represent a fundamental limitation of the ROV platform. Some ocean conditions, such as high current conditions, may restrict the motion of the surface vessel and its ability to relieve tether tension for the submerged ROV. Thus, even given an “ideal” software package for tracking, tether restrictions may make ROV tracking impractical for very long-duration tracking.

In the face of these significant bias disturbances, encountered after minute 43, the null space control design also played a role in preserving the tracking run. During the *Ptychogena* run, no control commands were issued, by either the human pilot or the automatic controller, in the circumferential direction. The bias disturbance was allowed to stabilize the circumferential coordinate of the ROV about the jellyfish subject (Chapter 5.4.3). Changes in the bias force twice altered the vehicle’s circumferential coordinate, at minute 43 and at minute 28 (Figure 6.19). Each of the two major changes in the bias force direction rotated the vehicle approximately one half turn. Figure 6.20, which plots the three dimensional position of the ROV about the target jelly, illustrates that the ROV turned a complete circle during the 89 minute run. Freedom of motion in the circumferential direction accomplished two purposes. First, the elimination of circumferential control commands reduced the magnitude of the total thruster force output (Chapter 5.2). Second, circumferential rotations altered the vehicle position so that the bias force always pulled away from the target animal; actuator commands to counteract the bias force thus propelled water away from the jellyfish rather than towards it (Figure 6.19). Both of these effects reduced hydrodynamic stimuli to which the jelly target might react.

---

## 6.4 Biology Applications

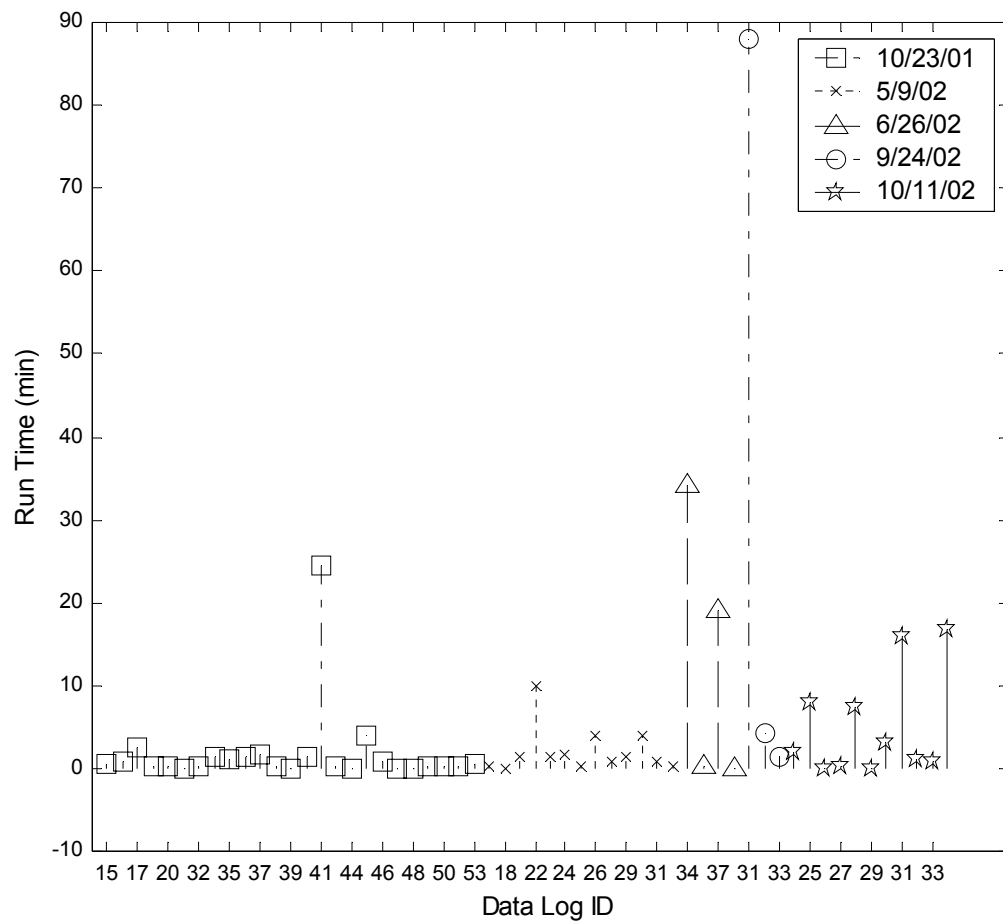
A final set of experiments (10/23/01 - 10/11/02) applied the combined control and vision software to demonstrate the potential of automated jelly-tracking technologies to enable new science experiments. The utility of jelly tracking as a capability for acquiring marine biology data depends strongly on the reliability of the overall tracking system. Statistics gathered during the final dive sequence demonstrate system reliability; in particular, these experiments establish both the automated system’s ability to track jellies repeatably for long durations and the mechanisms for system failure, when failure occurs. Furthermore, extended-length dives validate the ability of the auto-

mated jelly-tracking system to collect data relevant for biology applications. The two longest runs, one tracking a sinking larvacean house for 34 minutes and a second tracking the hydromedusa *Ptychogena* for 89 minutes, illustrate the potential of the automated tracking system to collect large quantities of motion and behavior data concerning individual gelatinous specimens.

### 6.4.1 System Reliability Statistics

This section discusses system-level statistics that demonstrate dramatic improvements in the reliability of closed-loop tracking during the final five-dive sequence. Discussion focuses on two reliability measures: (1) the maximum achieved tracking duration and (2) the frequency of run terminations caused by specific failure mechanisms. The tracking duration metric indicates how well the system can perform and what classes of biology experiment the system can support. Run termination statistics, on the other hand, pinpoint the reasons for system failure and the bottlenecks that restrict the achievable tracking duration.

Figure 6.21 plots the tracking duration achieved in each data log during the final five test dives. Prior to this dive sequence, the maximum achieved tracking duration was 2.5 minutes, as recorded during the 7/23/01 dive. The achieved tracking duration increased dramatically during the 10/23/01 dive, to a duration of 24 minutes (data log 41). This run distinguished itself from other runs on the same dive date, which suffered from initialization problems that limited most tracking times to only one or two minutes, as shown by Figure 6.21. This one highly successful run handled initial transients, which otherwise resulted in rapid control or vision failures, and tracked a swimming *Solmissus* specimen until a second gelatinous animal partially occluded the *Solmissus* and corrupted the recognition profile. Initialization problems continued to plague jelly-tracking tests until the 6/26/02 dive, during which the introduction of parallel-stereo ranging and of the boundary-control term largely eliminated the problems associated with system initialization. During this June 2002 dive, the ROV-based tracking system followed a sinking larvacean house for 34 minutes, a new tracking duration record (data log 34). This run was terminated manually when the larvacean house reached the ocean floor. On the same day, an extended run tracked the hydromedusa *Benthocodon* for 19 minutes, until the run was terminated manually to meet dive time restrictions. The final increase in achieved tracking duration occurred during the 9/24/02 dive, when an experimental run demonstrated fully autonomous jelly-tracking for an 89 minute duration (data log 31). Unencumbered by concerns about the proximity of the ocean floor or by





dive-time restrictions, this run continued until ROV tether traction grew stronger than the maximum thruster output of the tracking ROV. That the ROV tether caused termination of this long run suggests that consistently achieving longer tracking periods may require the use of an untethered AUV platform.

Thus, after all experiments, the maximum dive duration metric achieved a value of 89 minutes. This 89-minute run, and the three other longest tracking runs, are summarized in Table 6.2.

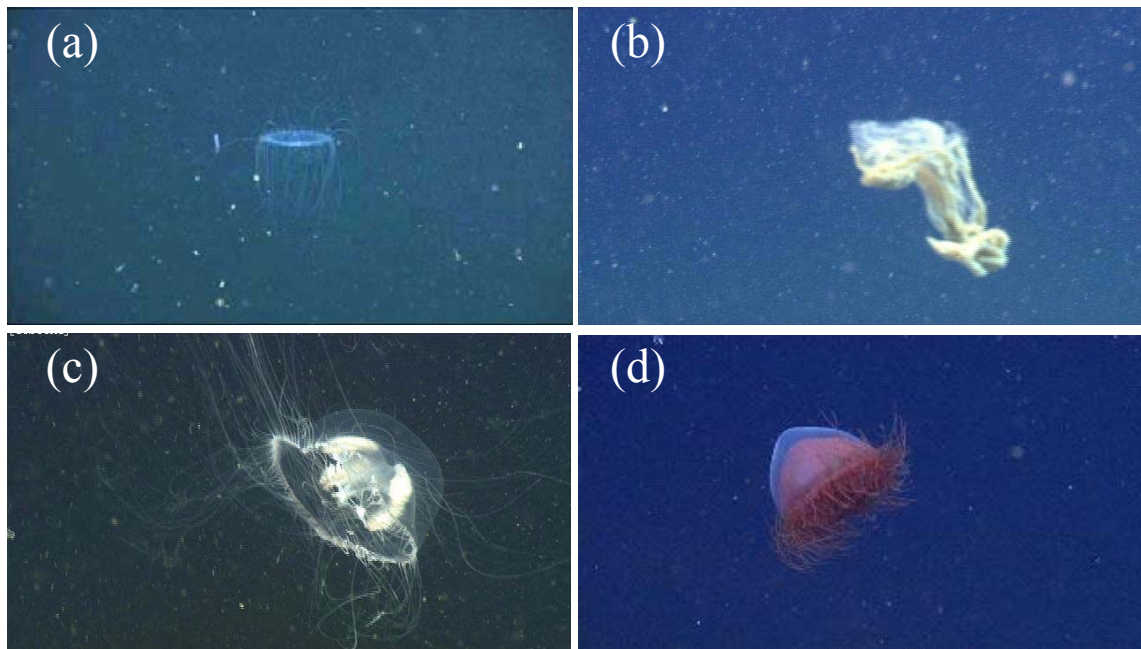


**Figure 6.22 Four Specimens Tracked in the Deep Ocean by Ventana**

Four specimens tracked for an extended duration: (a) *Solmissus*, (b) Larvacean house, (c) *Benthocodon*, (d) *Ptychogena*.

Animal Tracked	Length	Run Termination
<i>Solmissus</i>	24.5	Loss of vision lock: recognition failure
Larvacean House	34.2	Larvacean house reaches ocean floor
<i>Benthocodon</i>	19.4	End of dive: support ship recalls ROV
<i>Ptychogena</i>	89.1	Tether reaches maximum length and overpowers thrusters

**TABLE 6.2. Summary for Four Extended Tracking Experiments**

Experiments were conducted in the open-ocean deploying the ROV Ventana under full autonomous control, with no control commands issued by a human pilot after initialization.

The table also lists the reasons for termination of these four longest runs. The gelatinous specimens tracked during each of the four runs are illustrated in Figure 6.22.

During the final dive sequence, many shorter tracking runs were also recorded, each run terminating for one of a variety of reasons. The causes for termination fall into four broad categories: (1) vision failures, in which the vision system lost the target while it remained inside the viewing cone; (2) control failures, in which the control system allowed the target to wander outside the limits of the camera viewing cone; (3) immediate abort failures, in which the target was lost within fewer than ten seconds after the start of autonomous control; and (4) other termination modes, not related to the reliability of the control or vision software routines. Table 6.3 specifically details the cause of termination for each time the tracking system was activated during the final five-dive sequence. The table summarizes termination statistics in terms of the four broad categories, already introduced, and also in terms of several subcategories, described in detail by the following list.

#### **Vision System Failures:**

- **Bad Segmentation:** In this failure mode, the segmentation system (described in Chapter 4.3.3) failed to extract a set of pixels associated with the target animal. Although this failure mode dominated early vision system experiments (8/2/00 - 4/13/01), only one segmentation failure occurred during the final five-dive sequence, when the segmentation algorithm failed to detect a target faintly illuminated by a challenging lighting configuration (with no forward pointing light sources).
- **Bad Recognition:** Recognition failures occur when the target profile best matches an object other than the target animal, a phenomenon which can cause the tracking system to acquire the new object as its tracking target, inadvertently. These failures were not, in early experiments, a significant factor limiting tracking duration. As discussed in Chapter 4.4.1, however, recognition system limitations become more significant when tracking for increased durations or through high-density animal populations. At the end of the experimental dive sequence, the single most significant culprit contributing to premature run termination was the recognition subcomponent. Recognition failures were particularly problematic during the 10/11/02 dive, which operated in a dense population of squid which were attracted to the ROV lights (i.e. Assumption 4.2 was invalid).

Reason for Failure	Oct. 23, 2001	May 9, 2002	June 26, 2002	Sep. 24, 2002	Oct 11, 2002
<i>Summary</i>					
<b>Vision</b>	9	1	0	2	6
<b>Control</b>	23	18	0	0	0
<b>Immediate Abort</b>	7	5	1	0	2
<b>Other</b>	1	0	2	1	4
<i>Detail</i>					
<b>Vision</b>					
Bad Segmentation	1	0	0	0	0
Bad Recognition	0	1	0	0	4
Bad False Positive	4	0	0	2	2
Degraded Profile	4	0	0	0	0
<b>Control</b>					
Target Loss - Range	4	6	0	0	0
Target Loss - Bearing	19	12	0	0	0
<b>Immediate Abort</b>					
Target Too Small	1	0	0	0	0
Bad Vision Profile	2	2	1	0	2
Bad Control	1	3	0	0	0
Converging Stereo Alignment	3	0	0	0	0
<b>Other</b>					
Manual Termination	1	0	2	0	0
Tether Management	0	0	0	1	0
Occlusion by Squid Ink	0	0	0	0	3
Target Disintegration	0	0	0	0	1

TABLE 6.3. Run Termination Statistics

- **Bad False Positive:** This variant of the recognition failure occurs when no segmented region closely matches the target profile. In these cases, the vision system assumes the target has left the viewing cone, and attempts to command the vehicle to move in the direction in which the target was last seen. Normally, this behavior helps the system to recover a target following an out-of-frame event. If a false positive is triggered while the target is still in the viewing cone, however, a tracking run may end abruptly. These bad false-positive failures cause spontaneous loss of the animal target even in the absence of any other animal in the viewing field. Bad false-positives, along with other recognition failures, only emerged as an important contributor to premature run termination when other vision and control problems had been eliminated.
- **Degraded Profile:** In this failure mode, the control system allows the target to wander partially out of the viewing cone. During the target's time on the edge of the viewing boundary, its profile statistics reflect only the visible portion of its body. These statistics degrade the recognition profile and increase the likelihood of a recognition failure when the target returns into the center of the viewing cone. This failure mode, involving the interaction of the control and vision systems, has not occurred since the introduction of the boundary-control term.

**Control:**

- **Target Loss - Range:** In this failure mode, the control system fails to regulate the target's range relative to the camera sensor. Subsequently, the target becomes too small for the vision system to identify or exits altogether from the viewing cone of one of the two stereo cameras. This problem did not occur after the parallel stereo configuration replaced the large-baseline, converging stereo configuration.
- **Target Loss - Bearing:** These control failures result in the loss of the target outside the boundaries of the camera viewing cone. Historically, bearing control failures were a major problem and caused a majority of failures through the 5/9/02 dive. The subsequent introduction of the boundary control term appeared to remedy this failure mode.

**Immediate Abort:**

- **Target Too Small:** This failure mode occurs when the target is too small for the vision system to identify. During initialization, the human pilot can perceive and track targets smaller than the detection threshold for the vision system. In fact, because of the increased sensitivity of visual positioning at high zoom or at short range, human pilots prefer not to enlarge the target's size in the control camera. Thus, the human pilot may choose operate at ranges greater than the capability of the automated vision system, while the automated vision system operates preferentially at ranges shorter than comfortable for a human pilot. For small sized animals the band of overlap between the ranges preferred by the human pilot and the computer controller may be small. Consequently, a human operator may attempt to initiate a tracking run without realizing that a target is too far away for visual acquisition. To reduce the likelihood of this occurrence, the reference range for tracking runs was reduced to 90% of the range measured during human-piloted tracking (see Figure 6.9).
- **Bad Vision Profile:** Bad profile failures occur when the vision system locks on to the wrong tracking target from the start of the tracking run. The initial recognition profile assumes a target of a particular size located near the center of the camera image. In some cases, glare on the camera dome or image noise may better approximate the initial profile than the intended tracking target. Consequently, the vision system immediately acquires the wrong target.
- **Bad Control:** This failure mode occurs when the control routine fails to stabilize target position at run initialization. As a result, the target moves rapidly out of the viewing cone. This class of immediate-abort failure did not occur after the introduction of the boundary-control strategy.
- **Converging Stereo Alignment:** These failures occurred when the target exited the viewing cone of a converging stereo camera shortly after the initialization of a tracking run. This problem resulted from the poor human-factors design of the converging-stereo configuration, which required that the human pilot initialize the tracking system by aligning the target simultaneously in video sequences produced by two cameras rotated by an arbitrary angle. In practice, the human pilot focused on only one video stream at a time. As a result, the target frequently exited the second camera's viewing cone while the pilot concentrated

on the first camera. Shifting to a parallel stereo configuration, in which the two cameras provide nearly the same view, appeared to solve this immediate abort problem.

#### **Other Reasons for Run Termination:**

- **Manual Termination:** In several cases the run was terminated by choice. Reasons for manual intervention included the decision to start a dissimilar experiment, the desire to avoid a collision with the ocean floor, and the requirement to end an experiment to meet dive time constraints.
- **Tether Management:** The longest run ended when tether tension exceeded the thrust output of the ROV. In this sense, the problem reflects a limitation of the system hardware configuration and not a problem with the system software described by this dissertation.
- **Occlusion by Squid Ink:** This problem reflects a fundamental limitation of the vision sensing strategy. The visual sensor cannot penetrate turbid water; such conditions result when squid ink diffuses into the viewing cone and occludes line of sight to the target animal.
- **Target Disintegration:** Larvacean houses are so fragile that they disintegrate rapidly in the presence of a large ROV. This problem occurs even when human pilots attempt to track a larvacean house. (Sinking houses, such as those pursued for extended periods by the automated jelly-tracking system, are more robust to hydrodynamic disturbances than free floating larvacean houses.)

As a general observation, run termination statistics demonstrate a marked improvement in performance through time. Early dives, not described by Table 6.3, terminated regularly because of failures to segment the gelatinous animal target. On subsequent dives, most test runs terminated after control related failures. As many as 58% of runs, on 10/23/01, and 67% of runs, on 5/9/02, ended because of a control failure in the range or bearing directions. By comparison, zero control failures occurred after the introduction of the boundary control term on 6/26/02. The boundary control term, along with the shift to parallel stereo, also greatly reduced the number of immediate abort failures not related to a bad vision profile, from 13% on 10/23/01 and 11% on 5/9/02 down to 0% on 6/26/02 and subsequent dates. At the conclusion of the experimental dive series, recognition related failures (including bad recognition, bad false positives and immediate aborts due to a bad vision profile) remained as the major culprits limiting the length of jelly-tracking runs, particularly during operations among the dense squid population observed on 10/11/02. Although rec-

ognition-related failures appear to be the major bottleneck in achieving longer tracking periods, the present tracking system nonetheless succeeded in achieving several long duration tracking runs without encountering a recognition issue. In fact, as shown by Table 6.2, only one of the four longest runs ended on account of a vision failure.

### 6.4.2 The Study of Gelatinous Animal Subjects

The two longest dives illustrate the utility of the jelly-tracking system for science applications. First, the 34-minute run tracking a sinking larvacean house (6/26/02) demonstrated the capability of the jelly-tracking system to collect new data to extend the results of a previous science experiment. Second, the 89-minute run tracking the hydromedusa *Ptychogena* demonstrated a new quantitative capability to measure three-dimensional motion behaviors over long distances in the ocean. This capability relies on a combination of the jelly-tracking system and a doppler-velocity log (DVL).

#### **Larvacean Study**

First, the larvacean house run repeated a specific experiment previously performed by Hamner and Robison [44]. The larvacean *Bathochordaeus* continuously sheds and rebuilds its feeding filter, known commonly as its "house." When the larvacean abandons its house, the old filter, laden with oversize particulates, descends toward the ocean floor. Hamner and Robison measured sinking rates for larvacean houses and hypothesized that the flux of these houses serves as an important mechanism providing nutrients to bottom dwelling species. Figure 6.23 presents data from a series of eight larvacean tracking runs performed under human-pilot control.

The same figure also plots data from an experiment using the automated jelly-tracking system. The depth trace taken during the automated experiment (average velocity 2.4 km/day) aligns qualitatively with the descent of the fastest of the eight larvacean houses measured by Hamner (average velocity 2.1 km/day). Hamner's paper attributes the speed of the fastest of the eight samples to its "arrow-shaped, streamlined" form, a description which applies equally well to the rapidly descending house observed during the automated tracking experiment.

In effect the automated larvacean experiment demonstrates the ability of the jelly-tracking system to reproduce a science result. The potential for further application of the automated system is enormous; the system could be applied to generate a vast quantity of additional data to generate

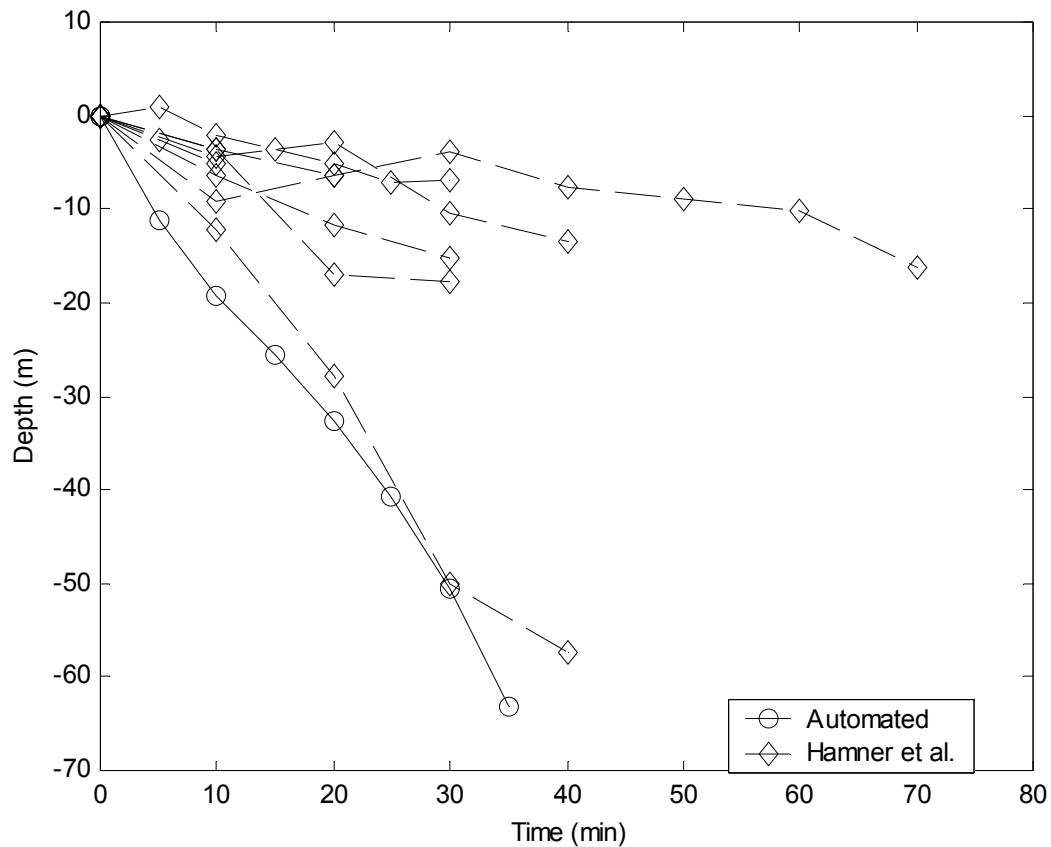


**Figure 6.23 Larvacean Run: Comparison of Automatically Acquired Data to Previous Data**

*Data describe an extended run tracking a sinking larvacean house (6/26/02 DL34). This plot shows depth vs. time for a sinker at 5 minute intervals. The new data, acquired under autonomous control, is compared to published scientific data from Hamner and Robison's paper on Bathochordaeus [44]. This run, at 34 minutes, is the second longest run logged by the automated tracking system. The run was terminated manually when the larvacean house approached the ocean floor.*



more precise statistics about larvacean house sinking rates. The automated system could also be used to study dependence of larvacean house sinking rates as a function of season, nutrient abundance, or shape during descent.

### Medusa Study

The run tracking the medusa *Ptychogena* demonstrates a capability to perform a new class of science experiment studying animal motion behaviors. This experiment exploits a combination of the jelly-tracking sensor, which measures animal motion relative to an ROV, and a DVL sensor, which measures ROV velocities relative to the water or to the ocean floor. The combination enables a quantitative measurement of the motion of a gelatinous specimen relative to its environment.

Figure 6.24 reconstructs the motion of the ptychogena specimen, relative to the ocean floor, using combined DVL and vision sensor measurements. (Figure 6.25 and Figure 6.26 give alternate viewpoints on the same four-DoF data set.) These motion reconstruction plots rely on a bottom-lock DVL measurement which was available only when the altitude of the DVL above the ocean floor was 25 m or less (Figure 6.27, middle plot). The dominant motion displayed by the jelly target during the time of bottom lock is a large translation toward the WNW direction ( $301^\circ$  degrees from North), at a rate of 4.7 m/min. As the jelly was not swimming during this time, the motion appears to be the result of a current moving along the floor of the Monterey Canyon, outward toward the ocean. Underneath the jelly, the ocean floor dropped by more than 22 meters during the time the animal transited 70 meters, making the average angle of the Canyon floor a  $19^\circ$  degree dropoff (Figure 6.27). These changes were significantly larger than the DVL drift rate. The DVL specifications indicate that it accumulates position errors, in the worst case, at no more than 0.12 m/min.

During the jelly's advective transit to the WNW, a significant hydrodynamic structure, possibly a streamwise vortical component of the benthic boundary layer, captured both the animal and the ROV. The first sign of the hydrodynamic event occurred at minute 27, when the tether force rapidly changed direction, pulling to the West (Figure 6.19). At the same time, the pressure-depth signal indicated a slight upwards motion of the jelly, though the animal continued to swim downward. Within five minutes, the vehicle and jelly began moving distinctly to the East. This change appeared to lead into a helical motion with a 20 m diameter, significantly larger than the length

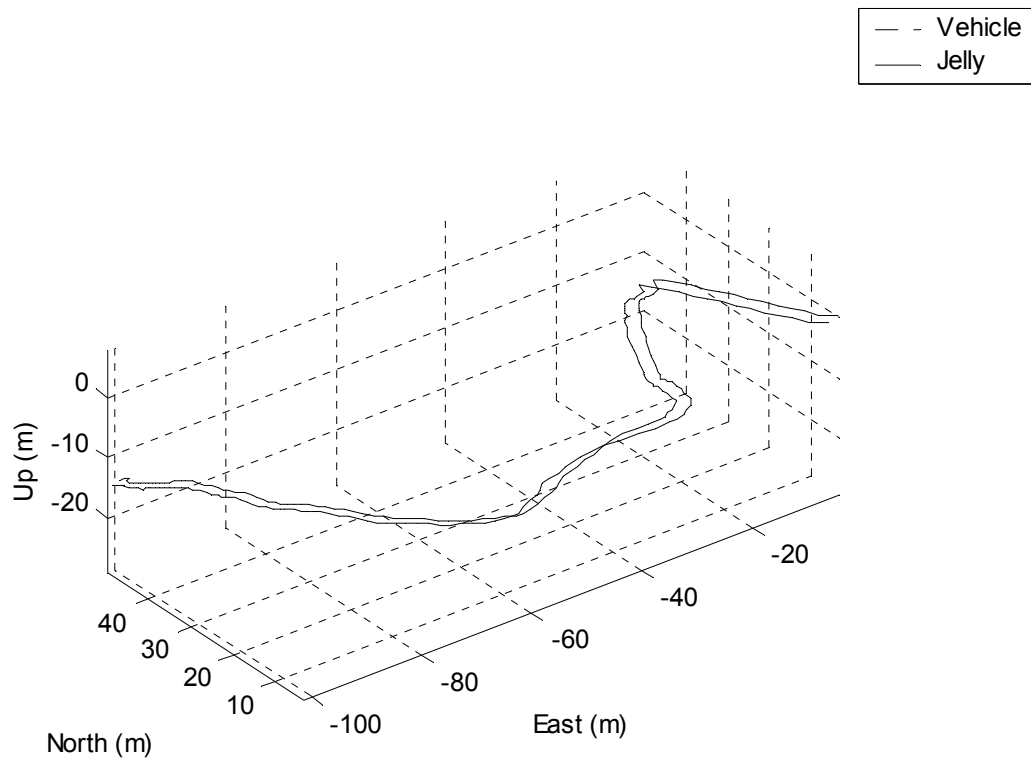


**Figure 6.24 Ptychogena Run 5: Motion of Ptychogena over the Sea Floor**

Data describe the middle 30 minutes of an extended experiment tracking the medusa Ptychogena (9/24/02 DL31). This plot depicts the motion of a Ptychogena over the ocean floor in three-dimensional, world-fixed coordinates. During the period shown (Minutes 35-56), the DVL was able to lock onto the ocean floor and provide world-frame motion measurements. Vehicle and animal positions in the world frame are obtained by combining vision-based measurements with acoustic DVL measurements. Vehicle position is shown as a dashed line; the jelly position, as a solid line. The vehicle shifts in yaw by 180 degrees in the middle of the run. As a result, the ROV switches from a position in front of the animal (facing ENE) to behind the animal (WSW). During this time the animal was not swimming, and was transported entirely by the local current.

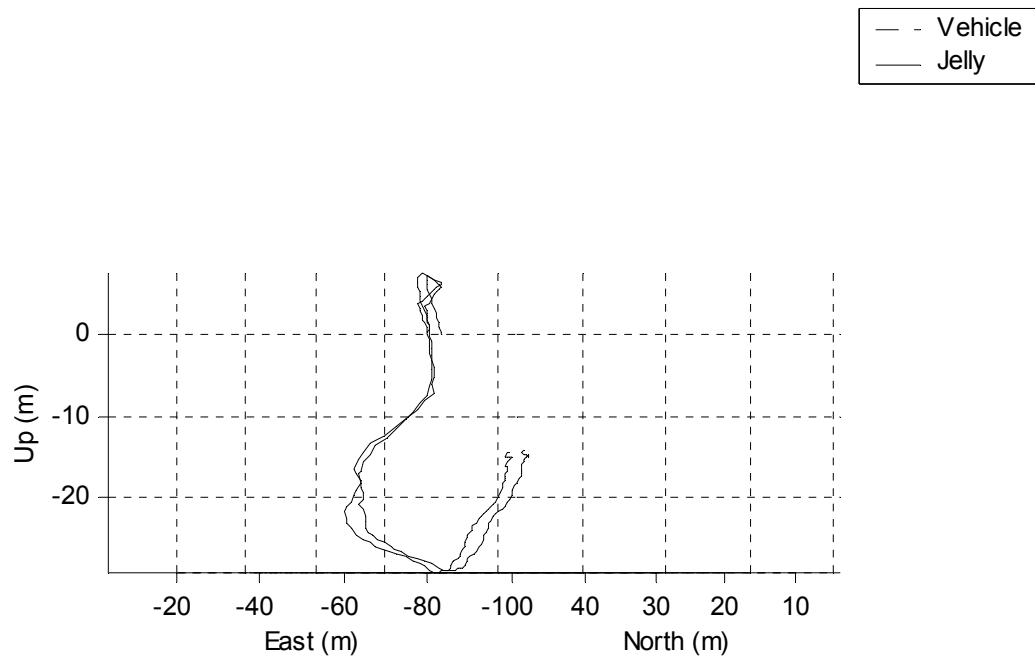


**Figure 6.25 Ptychogena Run 6: Motion of Ptychogena over the Sea Floor, End-on View**

*Data describe the middle 30 minutes of an extended experiment tracking the medusa Ptychogena (9/24/02 DL31). The initial and final progress of the Ptychogena (see Figure 6.24) over the sea floor proceeds out of the page (toward the Northwest). The interruption in the straight line motion occurs due to a significant hydrodynamic event which pulled both ROV and medusa into a helical motion of 20 m in diameter. The ROV and animal completed three-quarters of the helical rotation before resuming straight-line motion toward the Northwest.*

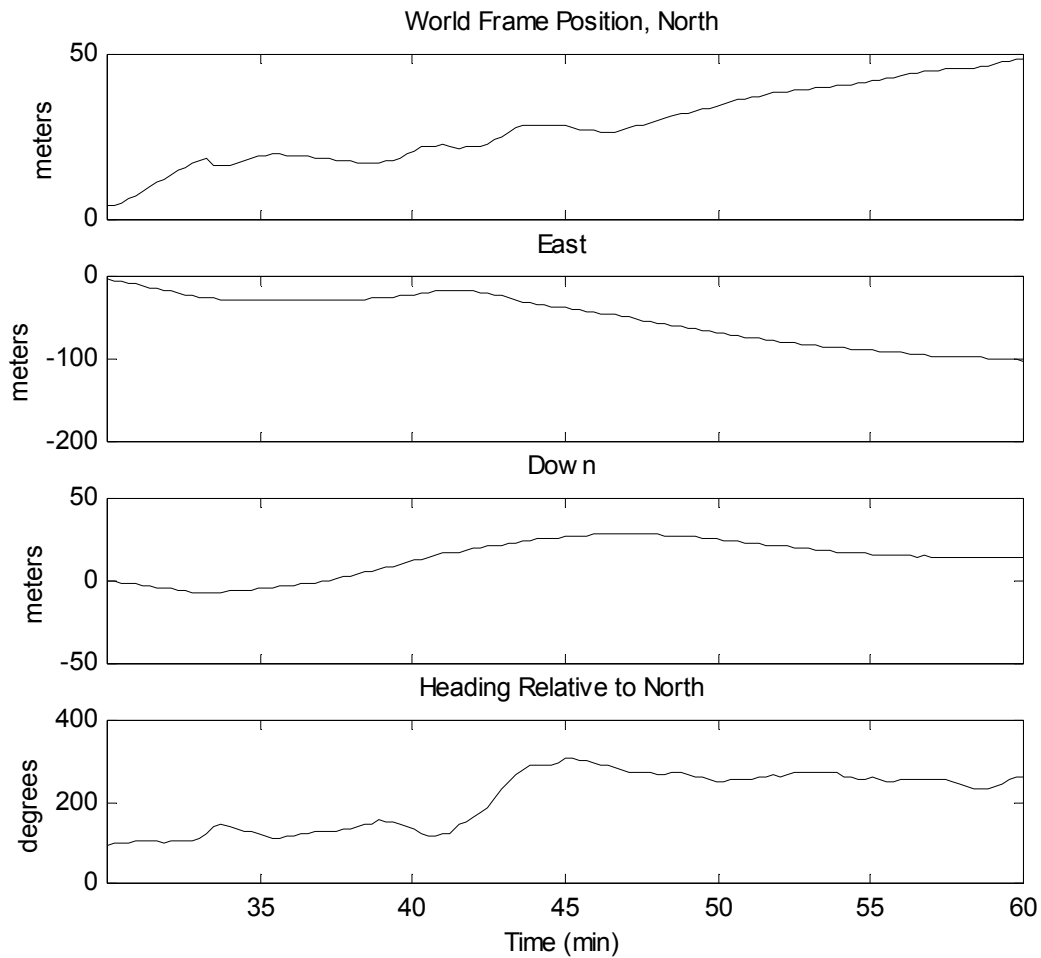


**Figure 6.26 Ptychogena Run 7: Motion of the Ptychogena over the Sea Floor, Time Traces**

*Data describe the middle 30 minutes of an extended experiment tracking the medusa Ptychogena (9/24/02 DL31). The progress of the Ptychogena over the sea floor is plotted in world fixed coordinates. The vehicle rotation is apparent in the heading plot (bottom). Data are undersampled in these plots (plotted at 0.05 Hz rather than 10 Hz). As a consequence, these data appear artificially smooth.*

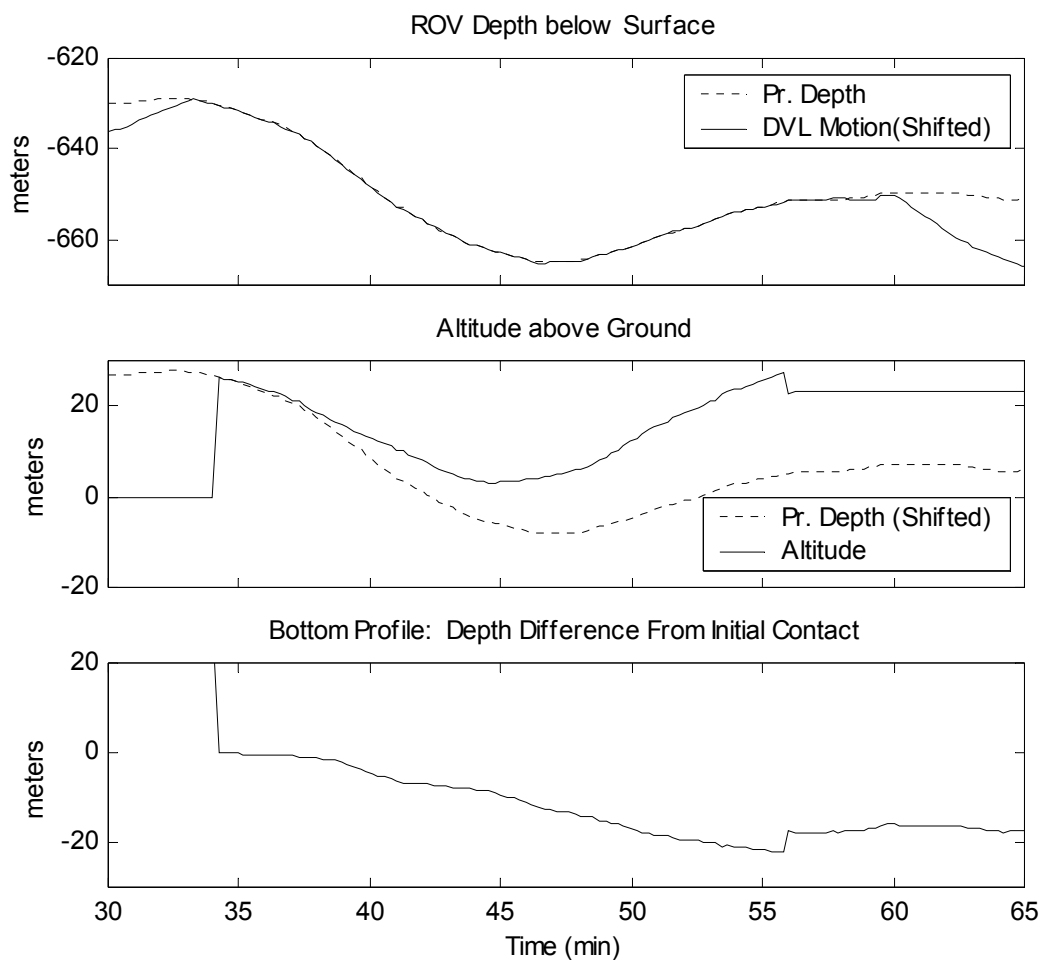


**Figure 6.27 Ptychogena Run 8: Altitude and Depth**

Data describe the middle 30 minutes of an extended experiment tracking the medusa *Ptychogena* (9/24/02 DL31). DVL and Pressure gage measurements are compared during the time the DVL had bottom lock (Minutes 35-56). The top plot shows depth as measured by the pressure gage (dashed line) and by the integration of the DVL signal (solid line). The *ptychogena* specimen ceased swimming just after the DVL acquired bottom lock (at a depth of 629.3 m). As the integrated DVL position is relative, it has been shifted to match the pressure depth at the time of initial bottom lock. The middle plot shows the DVL altitude (time of flight) in comparison with the pressure gage measurement. The pressure depth measurement is shifted to match the altitude measurement at the time of initial bottom lock. The difference between the two signals (bottom) indicates the change in the depth of the seafloor beneath the animal as it moved toward the Northwest.

scale of either the vehicle or the tracked jelly. Viewed from the direction of the current (WNW), this motion progressed three-quarters of the way around the helix axis, as illustrated by Figure 6.25. The second dramatic shift in tether bias force occurred at the nadir of the corkscrew motion, tugging on the vehicle to the East as the ROV began to move to the West of its initial trajectory. At their lowest point, the ROV and the animal subject came within 4 m of the ocean floor.

Thus DVL data describe a large, three-dimensional advective transport of the *Ptychogena* specimen. The capability to measure such motion could be applied to address open questions about horizontal migrations of deep-ocean gelatinous animals (Chapter 2.5.3). As the *Ptychogena* experiment is the first quantitative measurement of long distance, three-dimensional motion for a jellyfish in the deep ocean, more data will be required to assess the ecological significance of this type of large, passive migration. Nonetheless, the potential for future applications of this system to measure both bottom-relative and water-relative animal motions (with the DVL set to water-lock mode) is enormous.

The experiment also touches on open questions about the stimuli used by *Ptychogena* to trigger initiation and termination of diel vertical migration (Chapter 2.5.2). After swimming downward nearly 70 meters, the *Ptychogena* abruptly stopped swimming. The end of swimming motions, at Minute 33, occurred just prior to the start of the large corkscrew motion illustrated in Figure 6.25. Without more data, no reliable connection can be established to link the hydrodynamic event with the end of animal swimming; however, from an evolutionary point of view, the ability to detect benthic boundary layer turbulence could permit a medusa to detect the ocean floor before colliding with it and, in effect, avoid the risk of colliding with the ocean floor or encountering benthic predators. If the animal did stop swimming as the result of an environmental trigger, it seems likely that the trigger involved pressure sensitivity. The pressure depth measured by the ROV reversed just prior to the end of jelly swimming (Figure 6.19). During the reversal, the jelly apparently moved more than 1 m upward toward the ocean surface, even though the jelly continued to swim directly downward during this time. Many hydromedusae appear to sense both gravity direction and pressure changes (Chapter 2.7). Thus, it seems possible that the jelly recognized this incongruity between its swimming direction and the reversed pressure signal and, consequently, stopped swimming. Substantially more experimental evidence will be required, however, to support or refute this hypothesis.

The initiation of jelly swimming also raises questions about the stimuli that triggered this change in motion behavior. Because the *ptychogena* began its sustained downward swim within minutes of the approach of the tracking ROV, it seems likely that disturbances produced by the ROV triggered the initiation of swimming. Certainly the ROV affected the environment by adding sources of light, heat, acoustic vibrations, and larger hydrodynamic fluctuations. No evidence exists to tie any one of these disturbances to the initiation of *Ptychogena* motion. Nonetheless, based on the accumulated body of research linking increased ambient lighting to downward swimming among other hydromedusae, it seems likely that the ROV lights triggered a DVM-type motion behavior (Chapter 2.5.2).

This final observation raises very significant questions about the influence of the jelly-tracking instrument on the behavioral phenomena under observation. An important aspect of fielding an automated jelly-tracking platform will involve the assessment of the biological significance of disturbances produced by the tracking vehicle. Based on the *Ptychogena* experiment, and on the apparent attraction of large numbers of squid to the ROV during the 10/11/02 dive, it appears that the ROV's light sources represent the most significant disturbance on the environment introduced by the tracking vehicle. Methods to reduce the lighting level will undoubtedly reduce the tracking vehicle's influence on the animal subject and its environment.

---

## 6.5 Summary

This chapter presented experimental data to demonstrate the function of the components of the jelly-tracker and to validate the overall performance of the complete system. Ocean dives deploying the ROV *Ventana* in Monterey Bay completed three overlapping experimental phases: a vision phase, a control phase, and a biological applications phase. In the vision phase, experiments collected video data used to develop the gradient-based segmentation methods described in Chapter 4. The control phase demonstrated the field control system from Chapter 5 and pinpointed the particular importance of the boundary control term, used to enforce the limits of the camera viewing cone. The final, biology-application phase of experimental testing validated the ability of the automated system to achieve extended-duration tracking. These experiments tracked several animals for extended periods of time, as long as 89 minutes for one *Ptychogena* specimen. The *Ptychogena* run also illustrated the capability of the jelly-tracking system to reconstruct animal motion in three-dimensions and to correspond these motions with behaviors observed in the video data. Evi-

dence suggests that the jelly-tracking platform may have had some impact on behavioral phenomena under observation. Nonetheless, field tests of the automated jelly-tracking system firmly establish the system's utility to enable new scientific experiments.



*In all the hundreds of published papers on vertical migration, no one has ever tracked an individual zooplankter in situ over a 24-h period. Such a study would not only provide data on how zooplankton budget their time between various behaviors, but would allow us to examine behavioral variability between individuals.*

- H.J. Price et al., 1988 [77]

---

This chapter examines jelly tracking for autonomous underwater vehicle (AUV) applications with a constrained energy budget. Scientists desire very long-duration tracking of individual animal specimens, as long as 24 hours or more. For operations with a remotely operated vehicle (ROV) platform, however, the requirement for on-station support by a surface vessel restricts the practicality of animal tracking to only a few hours. The transfer of jelly-tracking technology from an ROV to an AUV platform offers the potential to achieve 24-hour tracking in the future, as AUVs can operate independently with no physical connection to a surface ship. In exchange for this independence, an AUV sacrifices both the high-bandwidth communication link and the steady power supply available through a tether. Consequently, the design of a jelly-tracking AUV must satisfy two major challenges: a reliability requirement, akin to that for ROV operations, and an energy requirement, an added constraint specific to operations with an untethered AUV.

To reduce the power budget for the demonstrated ROV-based jelly-tracking system to a level consistent with the requirements for AUV-based jelly-tracking, this chapter analyzes the major power sink for the experimental system: sensor illumination. Section 7.1 establishes relative energy budgets for the ROV and AUV platforms. Whereas lighting consumes 3.4 kW for the ROV-based jelly-tracking system, the AUV-based system will offer fewer than 20 W for active illumination. To examine means of reducing the sensor illumination power to this level, Section 7.2 employs a radiometric analysis of the lighting system. The analysis indicates that focused spot-lighting and strobed lighting, together, can reduce energy requirements sufficiently to enable AUV-based tracking. The use of strobed lighting, however, introduces a new possibility for disturbing a tracked animal and interfering with observed behaviors. As a consequence, Section 7.3 develops a new light-response model for gelatinous animals and employs it to evaluate the pro-

posed strobe pattern. The model indicates that, in fact, strobed lighting (with light-on periods of less than 20 ms and light-off periods of approximately 1 s) may improve the quality of biological data collection by reducing the effects of artificial lighting on animal behavior. Thus, in the future, strobed lighting may offer benefits for both AUV and ROV operations.

## 7.1 Power Budget for AUV-based Tracking

Comparison of power budgets for AUV and ROV-based jelly tracking establishes the relative power reduction required to deploy the experimentally demonstrated jelly-tracking technology on an energy-constrained AUV platform. This section estimates the power budget for a conceptual jelly-tracking AUV as shown in Table 7.1. The estimated sensor power budget is approximately 20 W. This figure is 200 times smaller than the sensor power budget of the current ROV-based system, which consumes more than 4 kW of continuous power during jelly-tracking operations.

### 7.1.1 Overall AUV Power Budget

The power budget for the jelly-tracking AUV consists of three primary terms: sensor power,  $P_s$ , actuator power,  $P_a$ , and hotel load,  $P_h$ . Whereas the power required to sense the target animal and to actuate position relative to that animal may be optimized through strategic system design, the hotel load represents a fixed overhead. This load comprises the power draw of continuously active components necessary for AUV function (processing, data storage, auxiliary sensing) and is estimated at 10 W. Thus the total power consumed by the vehicle,  $P$ , is

$$P = P_s + P_a + P_h. \quad (7.1)$$

Budget Item (for an AUV of mass 135 kg)	Power
Sensor Power (Lighting, Cameras, Processing)	22 W
Actuator Power - Steady Drag Component	< 0.01 W
Actuator Power	2 W
Hotel Load	10 W
Total Power Available (based on a payload of 15 kg NiCad batteries/day)	34 W

**TABLE 7.1. Summary of the energy budget for a hypothetical jelly-tracking AUV**

This power requirement cannot exceed the total power available given AUV energy storage and mission duration.

$$P = \frac{e \mathcal{M}_e}{T} \quad (7.2)$$

Here  $e$  represents energy density,  $\mathcal{M}_e$  represents mass dedicated to energy storage, and  $T$  represents the total duration of the jelly-tracking mission. Nickel-cadmium batteries are assumed to provide energy storage ( $e = 55$  W-h/kg according to [172]) for a jelly-tracking mission of one-day duration ( $T = 24$  h). Given the hotel load and the total power available from energy storage, the power available for animal sensing,  $P_s$ , depends only on the power consumed by the thrusters.

### 7.1.2 Actuator Power

The actuator power requirement,  $P_a$ , depends on the dynamics of the animal under observation, on the vehicle control law, and on environmental disturbances. These factors contribute both to steady and unsteady forcing by the vehicle actuators.

For the jelly-tracking application, steady thruster forcing does not produce a significant demand for actuator power. Steady thruster forcing need counter only steady animal swimming and any external forces exerted on the AUV. For ROV-based tracking, significant thrust was required to offset steady external forces, caused primarily by tether forcing. In the absence of a tether, animal translational motions dominate the steady actuator power demand. To estimate the power required to pursue a swimming animal, the AUV is modeled as a sphere (isotropic drag coefficient) with neutral buoyancy. The volume of the sphere is

$$V = \frac{\mathcal{M}_e + \mathcal{M}_o}{\rho}. \quad (7.3)$$

Here  $\rho$  is the density of seawater. The total vehicle mass incorporates both the mass dedicated to energy storage,  $\mathcal{M}_e$ , and the mass dedicated to other vehicle components,  $\mathcal{M}_o$ . The frontal area of the same sphere is

$$A = \pi \left( \frac{3V}{4\pi} \right)^{2/3} \quad (7.4)$$

Given this area, the steady actuator power required for pursuit depends on the cube of the tracked animal's velocity,  $v$ . The drag coefficient for the sphere is taken to be 0.5.

$$P_{a, steady} = \frac{1}{4} \rho A \|v\|^3 \quad (7.5)$$

Even for a very rapidly swimming gelatinous animal the steady drag power requirement is small. To provide an example, the drag for a vehicle the size of OTTER, Stanford's experimental AUV testbed [160], can be considered:  $\mathcal{M}_e + \mathcal{M}_o = 150$  kg. Using 30% efficient thrusters and pursuing one of the faster-swimming gelatinous animals, a siphonophore moving at 11 cm/s (Chapter 2.6.4), the steady actuation power requirement for this vehicle, assuming that the target animal swims continually, is  $P_{a, steady} = 0.4$  W. For a more typical animal, moving 90% of the time at a speed of 2 cm/s, the steady power requirement for the same vehicle is a miniscule  $P_{a, steady} = 0.002$  W.

Unsteady actuation, by comparison, may consume a significantly larger amount of power than steady actuation, even for typical circumstances. These power demands result from the AUV's inability to recover energy during vehicle accelerations or decelerations. All variations in the speed of the tracked animal over time thus require the expenditure of energy by the tracking AUV. Assuming negligible drag and perfect tracking (i.e. negligible dynamics associated with vehicle control) the power required for AUV acceleration is

$$P_{a, unsteady} = C_m (\mathcal{M}_e + \mathcal{M}_o) T^{-1} \int_T |\dot{v} \cdot v| dt \quad (7.6)$$

The added mass coefficient,  $C_m$ , accounts for the mass of water accelerated during vehicle acceleration. For a sphere of neutral buoyancy, the added mass coefficient is 1.5. Animal kinematics are modeled approximately as one-dimensional oscillations around a steady velocity in the direction  $\hat{v}$ :

$$v = [\bar{v} + v' \cos(\omega t + \phi)] \hat{v} . \quad (7.7)$$

The oscillations parameters depend strongly on the species of animal tracked (see Chapter 2). For a typical *Mitrocoma cellularia* specimen, for instance, approximate parameters include a mean velocity,  $\bar{v}$  of 0.5 cm/s, a fluctuating velocity,  $v'$ , of approximately 0.5 cm/s and a pulse frequency of 0.5 Hz ( $\omega = 3.1$  rad/s). For a typical *Aequorea victoria* specimen, the approximate parameters are a  $\bar{v}$  of 1.24 cm/s,  $v'$  of 0.5 cm/s and pulse frequency of 1.47 Hz ( $\omega = 9.2$  rad/s) [25]. The averaged unsteady power of (7.6) can be calculated by integrating the kinematics of (7.7) over an integer number of cycles. When  $\bar{v} > v'$ , the direction of motion never reverses, and the formula for time averaged unsteady power, with no energy recovery, is

$$P_{a,unsteady} = C_m(\mathcal{M}_e + \mathcal{M}_o) \frac{2\bar{v}v'\omega^2}{\pi} \quad (7.8)$$

For 30% thruster efficiency, a 150 kg vehicle and continuous swimming, the unsteady power requirement for pursuing the typical *Mitrocoma* is only 0.1 W. The unsteady power requirement for tracking the *Aequorea victoria*, however, is as high as 2.5 W. Moreover, the actual energy expenditure may be even higher, since the 2.5 W estimate does not include extra dynamics introduced by imperfect tracking.

### 7.1.3 Sensor Power

After subtracting off the requirements for the hotel and actuator loads from the total power budget, the remaining available power can supply the jelly-positioning sensor.

$$P_s = \frac{e\mathcal{M}_e}{T} - P_a - P_h \quad (7.9)$$

To obtain an estimate of  $P_s$ , the vehicle is again assumed to have a mass similar to that of Stanford's OTTER vehicle. This experimental AUV has a base mass, without batteries, of approximately  $\mathcal{M}_o = 135$  kg, dry. (The jelly-tracking AUV, unlike OTTER, is assumed not to flood; flooding of internal cavities increases OTTER's mass by an additional 300 kg.) Assuming the jelly-tracking vehicle has a base mass of 135 kg and is following an *Aequorea victoria* specimen, (7.9) becomes

$$P_s = \left( \frac{55}{T} - 0.02 \right) \mathcal{M}_e - 12.3 \text{ W} \quad (7.10)$$

This equation assumes energy storage in the form of nickel-cadmium batteries and a hotel load of 10 W. From the equation, a battery load of 10 kg/day supports a sensor power draw,  $P_s$ , of approximately 11 W. A battery load of 15 kg/day supports a power draw of approximately 22 W. As a reference point, the OTTER vehicle was designed with approximately 14 kg of onboard energy storage.

#### 7.1.4 Comparison of AUV and ROV

Energy budget estimates for the jelly-tracking AUV are listed in Table 7.1. Based on these figures, the jelly-tracking AUV is assumed to require a jelly-tracking sensor with a power demands in the 10-20 W range. Of this requirement, 2-4 W are assumed to go to power the camera and vision-processing DSP components. The remaining power is available for lighting.

Overall, these power requirements are consistent with those of other sensors designed for AUV applications. For instance, Langebrake *et al.* report the test results for several general-purpose AUV sensors including a chemical sensor (6 W), a shadowed particle profiler (70 W), and a laser line-scan bottom profiler (60 W) [170]. Short *et al.* describe a mass spectrometer for AUV applications that consumes less than 100 W power [176]. The RDI Workhorse doppler velocity log (DVL) consumes approximately 30 W.

At 10-20 W total power, the AUV-based jelly-tracking sensor has significantly stricter energy requirements than the ROV-based sensor. The ROV hotel and sensor energy budget is 8 kW, with 3.4 kW dedicated to lighting, 1.1 kW dedicated to systems and 3.5 kW dedicated to science hardware [9]. Although energy systems and science hardware do not generally consume their maximum budgeted power, illumination consumes its full power budget continuously during jelly-tracking operations. To enable AUV-based jelly-tracking requires that this 3.4 kW lighting budget be reduced by a factor of at least 200.

---

## 7.2 Optimizing Lighting Configuration

Several design approaches can reduce the illumination power requirement for jelly tracking. The most benign design change, the optimization of system geometry, cannot alone achieve the 200-

fold reduction in lighting power demanded for AUV operations. Other possible improvements include using low-light cameras and strobing the illumination source.

### 7.2.1 Radiometry

The power savings that result from geometric changes are described with a radiometric analysis. The following equation for irradiance, or power flux, describes propagation losses between the light source and the camera. Equation (7.11) assumes the light source, camera sensor and target animal are arranged as depicted in Figure 7.1.

$$I_0 = I_s(\lambda) \left[ \eta_0 \Gamma(\alpha, {}^s\phi_j, {}^s\theta_j) \frac{d_s^2}{d_c^2} \frac{d_j^2}{\|{}^s q_{\text{ref}}\|^2} e^{-c(\lambda)(\|{}^s q_{\text{ref}}\| + \|{}^0 q_{\text{ref}}\|)} \right]^{-1} \quad (7.11)$$

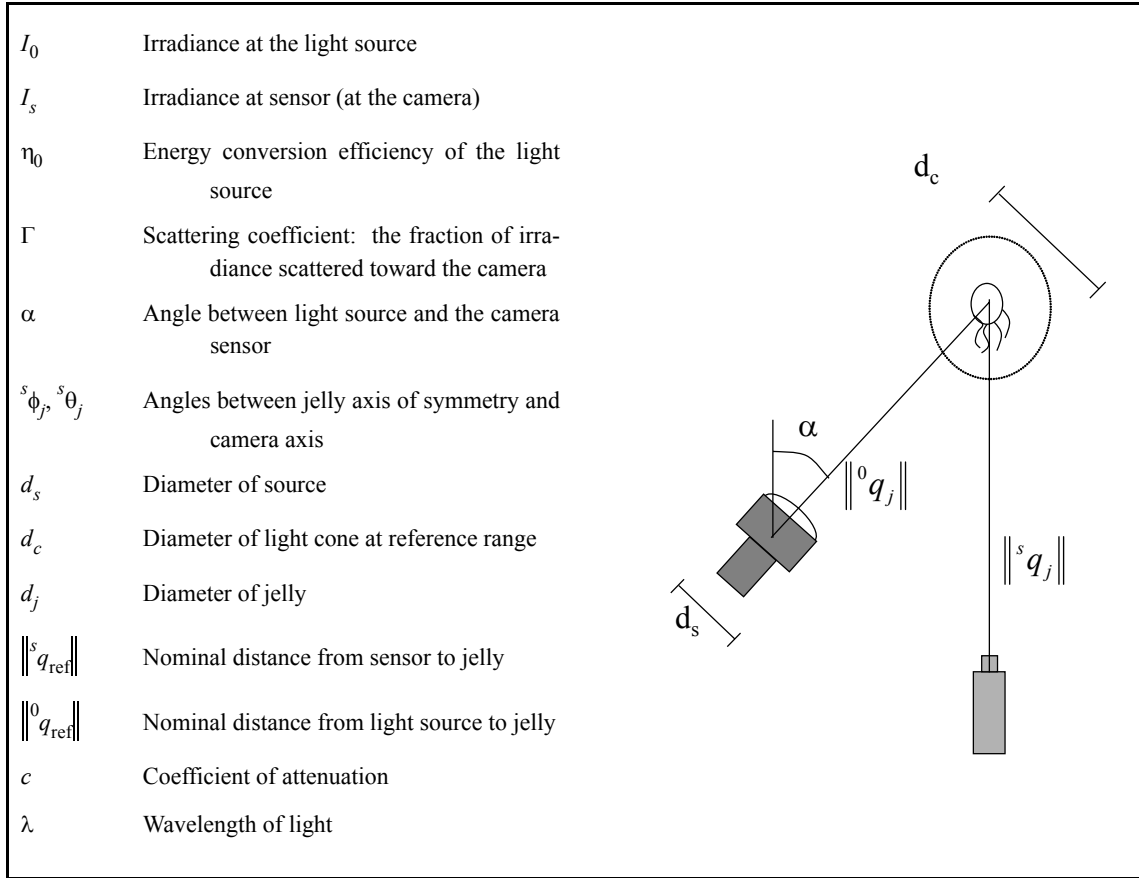


Figure 7.1 Radiometry Definitions

In this equation, four intrinsic parameters describe the light source:  $I_0$ , the irradiance produced by the lamp;  $\eta_0$ , the energy conversion efficiency of the light source;  $d_s$ , the diameter of the light source; and  $d_c$ , the diameter of the illuminated cone at the nominal target range. The latter pair of parameters establish the spreading angle and effective origin of the light source. Only one intrinsic parameter describes the camera sensor:  $I_s$ , the minimum level of irradiance required for target detection, as measured at the camera. The camera field of view does not influence the energy equation (and can be set to the angle of  $2 \operatorname{atan}(d_c / \|q_{\text{ref}}\|)$  for maximum pixel resolution). All other parameters are extrinsic and hence defined by the environment, the target, and the viewing geometry.

Equation (7.11) describes three mechanisms that degrade signal strength: signal spreading, target transmissivity, and absorption. For geometric optimization, the most significant of these loss mechanisms is spreading. Spreading losses result because the energy in an impulsive wave front leaving from a point source spreads evenly over a spherical surface area that grows with the square of the distance the wave has traveled. For an active illumination task, light waves spread twice, first from the light source to the target and again from the target to the camera. In (7.11), the  $d_s^2/d_c^2$  term describes initial spreading from the source to the target, and the  $d_j^2/\|q_{\text{ref}}\|^2$  term describes subsequent scattering from the target to the camera. Although the latter scattering term depends on target range, the initial spreading term, by design, does not. This independence results if the source spreading angle is narrowed to compensate for increased source-to-target range, thus holding  $d_c$  constant.

Transmission of light through the transparent target also reduces signal strength significantly. For jelly-tracking, camera sensors collect light in backscatter. The fraction of impinging light scattered back from the target along the angle of the camera,  $\alpha$ , is described by the scattering coefficient,  $\Gamma(\alpha, {}^s\phi_j, {}^s\theta_j)$ . (Target orientation, in terms of the angles  ${}^s\phi_j$  and  ${}^s\theta_j$ , also affects the scattering coefficient.) Because of their high transparency, jellies transmit most impinging light and scatter only a small fraction in other directions. No data has been published to describe the scattering function of a typical gelatinous animal. Empirical observations suggest, however, that optimal viewing occurs for angles,  $\alpha$ , between 45-90°. Because the lighting angle for the ROV-based system already falls in this range and because target orientation may vary arbitrarily, few opportunities are available to optimize the function  $\Gamma$  in order to reduce target-transmission power loss.



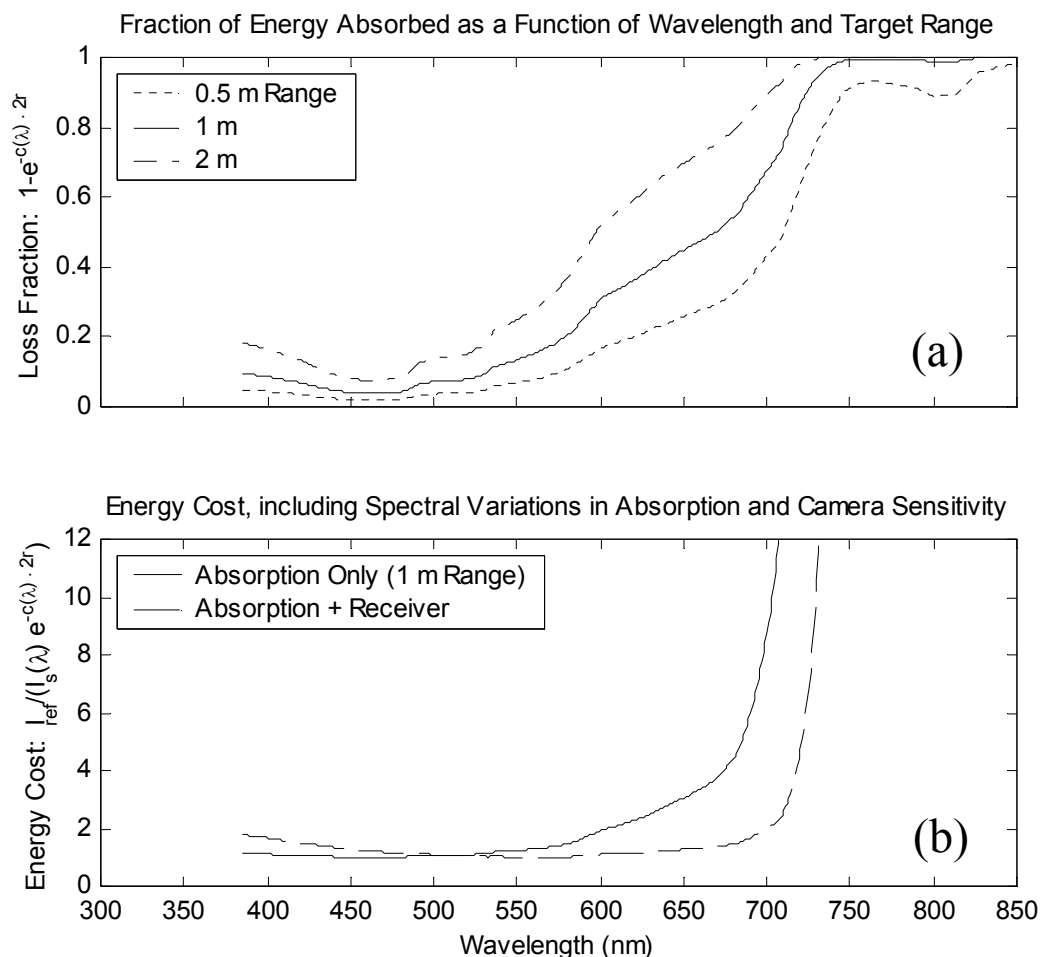


**Figure 7.2 The Spectral Effects of Absorption and Camera Sensitivity**

Plots illustrate that absorption losses are lowest for blue light (~460 nm). Camera sensitivity, however, increases into the near infrared. Given these competing effects, the green wavelengths (~570 nm) minimize system energy costs. **(a):** The fraction of energy lost due to spectral absorption is plotted at three values of target range. Wavelengths in the red and infrared are significantly attenuated by absorption, even at close range. **(b):** Energy costs are plotted as a function of wavelength, with minimum energy normalized to unity. Spectral variations in camera sensitivity balance out increased absorption in the red. Hence, energy requirements are effectively flat (within a factor of two) between 400 and 700 nm. Higher wavelengths (>700 nm) result in exponential increases in energy requirements. Energy costs also rise for lower wavelengths (<400); additionally, lower frequencies are to be avoided as ultraviolet radiation can damage gelatinous animal tissue [53]. Data sources: Attenuation coefficient data from [168], Photodetector data (blue-enhanced silicon photodetector) from [177].

Compared to spreading and target-transmission losses, absorption losses are relatively small when observing an animal at a one-meter range. Physically, the absorption term describes conversion by the water medium of light energy into heat. These losses are difficult to distinguish from scattering losses involving particulates suspended in the water medium. As a consequence, both phenomena are modelled by the exponential absorption term,  $e^{-c(\lambda)(\|q_{\text{ref}}^s\| + \|q_{\text{ref}}^0\|)}$ . Both target range and illumination wavelength affect absorption losses, as illustrated by Figure 7.2(a). The absorption term acts, effectively, as a bandpass filter with a minimum absorption loss near 460 nm. For a nominal target range of 1 m (total path length 2 m), red and infrared wavelengths are significantly attenuated. Spectral variations in camera sensitivity,  $I_s$ , partially offset spectral variations in absorption, however. Figure 7.2(b) shows the spectral effects of absorption and camera sensitivity on the illumination power budget. Overall system power requirements do not vary by more than a factor of 2 between the violet (400 nm) and the red (700 nm) when considering both phenomena together. As a consequence, the choice of illumination wavelength does not significantly affect the AUV energy budget; illumination sources may employ monochromatic or white light, as long as they concentrate illumination power in the 400-700 nm range.

### 7.2.2 Power Optimization

The radiometric propagation equation can be used to optimize the lighting energy budget for the jelly-tracking activity. Equation (7.11) expresses the brightness of the source as an irradiance quantity, with units of power per length-squared. Assuming a circular light source of diameter  $d_s$ , the energy output of the light source is

$$P_0 = \frac{\pi}{4} M^2 I_s(\lambda) \eta_0^{-1} \Gamma^{-1}(\alpha, \phi_j, \theta_j) \|q_{\text{ref}}^s\|^2 e^{c(\lambda)(\|q_{\text{ref}}^s\| + \|q_{\text{ref}}^0\|)}. \quad (7.12)$$

Here the term  $M$  is defined for convenience as the margin ratio, the relative size of the illumination region to the target jellyfish:

$$M = d_c^2 / d_j^2. \quad (7.13)$$

System changes that lower  $P_0$  in effect decrease the energy required to illuminate the target. In this section, three system modifications are considered: changes to system hardware, geometry,

and strobe parameters. A combination of the later two improvements, based on geometry and strobing, are recommended to achieve the desired 200-fold reduction in the lighting energy budget.

### Hardware Improvements

It is difficult to achieve a significant reduction in  $P_0$  by substituting in more efficient light sources or cameras. The current ROV-based jelly-tracking system uses metal halide arclamps as an illumination source (Chapter 3.6.3). These light sources are among the most efficient available for deep-ocean lighting [173]. As such, the  $\eta_0$  parameter cannot effectively be improved for an AUV application.

More flexibility is available to modify the required irradiance at the camera sensor,  $I_s$ . Intensification technologies (such as Silicon Intensifier Target, or SIT, and Intensified-SIT, or ISIT, cameras) offer the capability to significantly boost  $I_s$  above the levels achieved by conventional CCD cameras. By increasing gain at the receiver, rather than the source, significantly less energy is lost due to spherical spreading; in effect, the gain applies only to the solid angle observed by the camera sensor and not to the entire spherical scattering surface around the target jelly.

These significant reductions in illumination energy that result from intensification are accompanied by a highly undesirable side effect, however. The intensification process introduces a high speckle-noise component into the image. High image noise represents a major problem for the jelly-tracking activity. In jelly-tracking, target detection depends on contrast, on the relative measurements of irradiance returned by the jelly target and by the surrounding medium. Because the jelly is transparent and because the jelly scattering function,  $\Gamma$ , is not significantly different from the scattering function for the surrounding ocean, contrast is low regardless of the absolute irradiance level. High signal noise destroys the contrast between target and background for background difference images (see Chapter 4.4.2) and especially for gradient images (Chapter 4.3.3). Consequently, the vision processing methods described in this dissertation do not support the use of intensified cameras for jelly-tracking applications.

### Geometry Improvements

The illumination energy requirement,  $P_0$ , depends on several geometric parameters including the margin ratio,  $M$ ; the camera-to-target distance,  $\|q_{\text{ref}}^s\|$ ; the source-to-target distance,  $\|q_{\text{ref}}^0\|$ ; and the scattering geometry determined by the camera angle,  $\alpha$ , and the target pointing angles,  $(\phi_j, \theta_j)$ . Of these geometric parameters, the margin ratio,  $M$ , offers the greatest potential for

reduction of  $P_0$ . Modification of geometric parameters alone, however, cannot fully achieve the 200-fold reduction in  $P_0$  required for AUV-based jelly tracking.

The margin ratio, which describes the ratio of the minimum diameter of the lighted volume around the animal to the dimension of the animal, is an important parameter both for vision processing and control. The vision processing system depends on contrast between the target and the background to identify the location of the animal specimen (Chapter 4). Effective segmentation requires some margin on all sides of the target animal. To reflect this requirement, a constraint is assumed for the margin ratio parameter, such that  $M \geq M'$  where  $M' = 2$ . Additional vision considerations, such as the desire to recognize approaching animals, and the requirement for aggressive control to avoid target loss outside the viewing boundary (Chapter 5) may require a more conservative constraint on  $M$ . For this analysis, only the contrast-based constraint,  $M \geq 2$ , is considered.

The margin ratio constraint permits  $M$  values significantly smaller than those employed for jelly-tracking trials. At a 1 m range, the ROV lamps give  $d_c$  approximately equal 1 m. Given an approximate target diameter,  $d_j$ , equal 10 cm, the margin ratio for the field-demonstrated jelly-tracking system is  $M = 10$ . Reducing this margin ratio to the minimum required for vision processing results in a 25-fold improvement in the energy budget for illumination, according to (7.12).

Geometry changes other than margin ratio reduction have only a minor effect on the illumination energy budget. The camera-to-target range,  $\|q_{\text{ref}}^s\|$ , for instance, may not be reduced significantly without risking increased hydrodynamic disturbances that might affect the behavior of the tracked target; the impact of hydrodynamic disturbances becomes more severe at short range because the disturbances have less room to dissipate before impinging on the target jelly and because more aggressive actuation is required to keep the target in viewing cone at short ranges. The source-to-target distance,  $\|q_{\text{ref}}^0\|$ , may be shortened somewhat, but these changes only have a small affect on  $I_0$  through the absorption term (see Figure 7.2).

The only remaining geometric parameters are those that affect the scattering function,  $\Gamma^{-1}(\alpha, {}^s\phi_j, {}^s\theta_j)$ . Scattering function dependence on the target orientation angles,  $({}^s\phi_j, {}^s\theta_j)$ , may be reduced significantly by employing multiple light sources at different orientations relative to the camera [171]. The use of multiple light sources, as shown in Figure 7.3, does not otherwise impact the illumination energy budget; however, the use of multiple light sources does provide a

positive benefit for vision processing by improving the uniformity of illumination over the viewing area. It is possible that adjustments to the camera-to-source angle,  $\alpha$ , may permit some illumination reduction. Qualitative empirical evidence suggests that gelatinous animals are more clearly visible when illuminated from the side rather than directly in backscatter (or shadowed in forward scatter). This affect may not be the result of a higher scattering function  $\Gamma$  at angles of  $\alpha$  near  $90^\circ$  so much as an improvement in the contrast between the target and the medium. The intensity of light scattered by the water back toward the camera is given as follows:

$$I_{H_2O} = \tilde{I}_0 n_0 \int_0^\infty \frac{\Gamma_{H_2O}(\alpha(p))}{\|s\|^2 \|q_p\|^2} e^{-c(\lambda)(\|s\| + \|q_p\|)} dp. \quad (7.14)$$

This expression has a form similar to that of (7.12), integrated along a line that extends outward from the camera origin at an angle  $\alpha$ . Position along the line is parameterized by a coordinate,  $p$ . The scattering function of the water,  $\Gamma_{H_2O}(\alpha(p))$ , varies along the length of the line, as do the

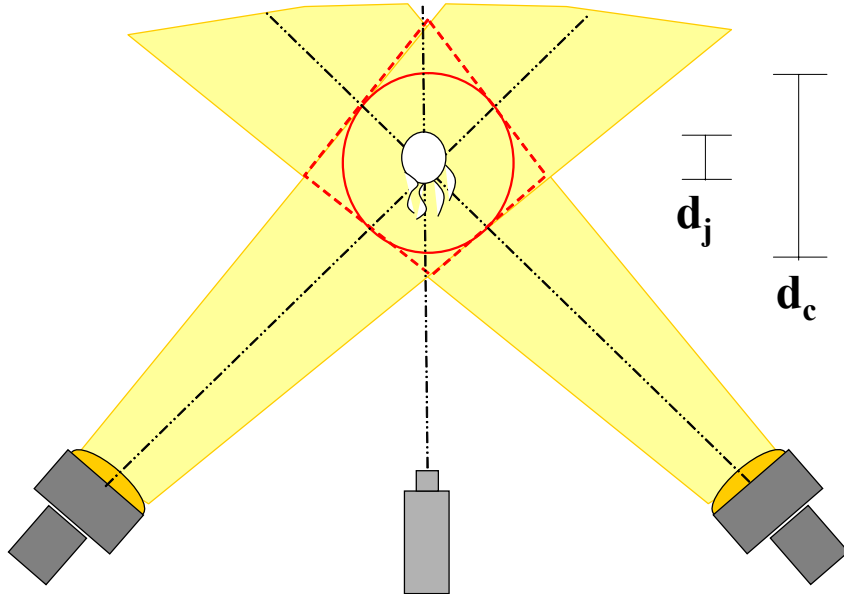
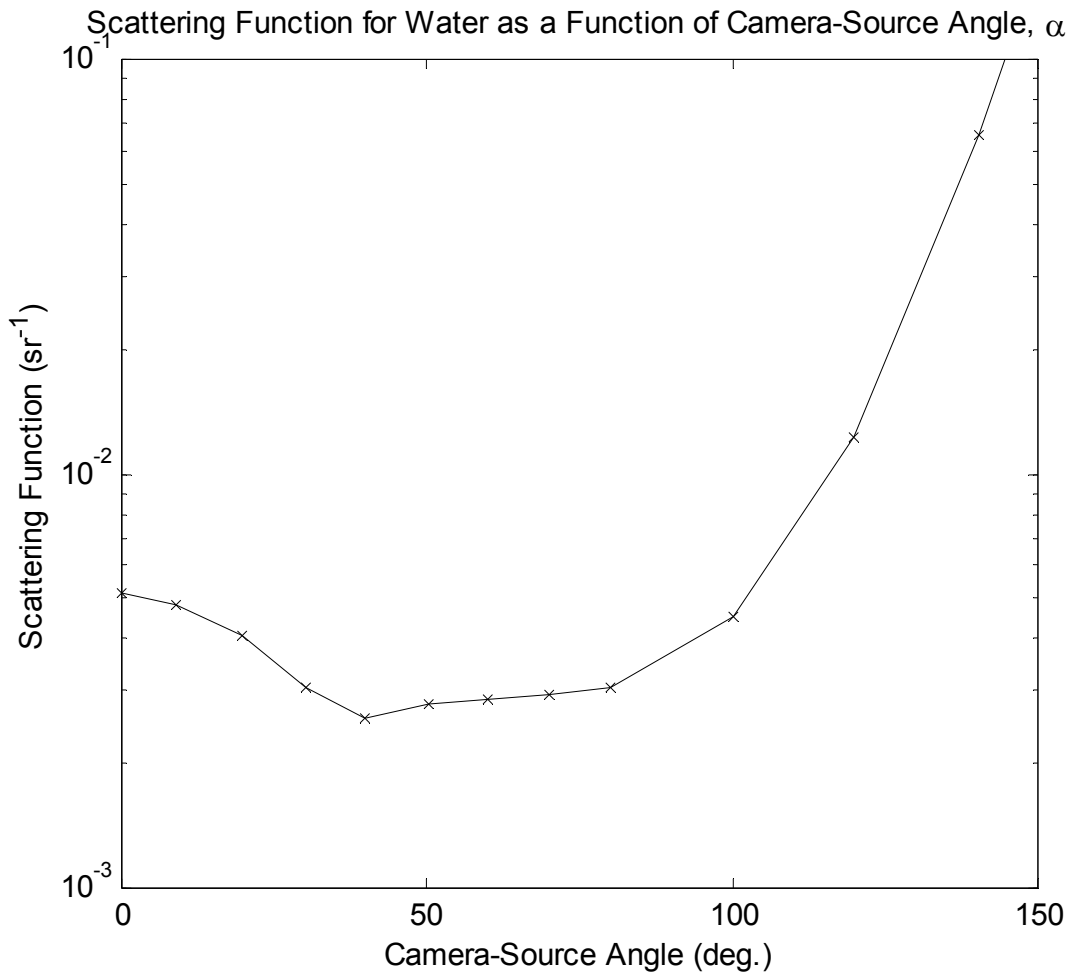


Figure 7.3 Multiple Light Source Geometry

effects of spreading loss and absorption. (The tilde indicates steradian units; thus the scattering function has units of  $\text{sr}^{-1}$  and the source term is expressed as a radiometric intensity with units of  $\text{W}/\text{sr}$ .) The integral (7.14) cannot, in general, be evaluated in closed form. By inspection, however, the magnitude of the signal scattered from the water back toward the camera can be observed to decrease to a minimum near  $\alpha = 90^\circ$ . This phenomenon occurs because the length of the ray along which light is scattered decreases substantially as the angle between the camera and the light source increases toward  $\alpha = 90^\circ$ . Also, the scattering function of water, depicted in Figure 7.4, reaches a minimum value near  $\alpha = 90^\circ$ .



**Figure 7.4 Scattering Function of Water**

*The scattering function of water as reported by [169]. An angle of  $0^\circ$  indicates backscatter, of  $180^\circ$  indicates forward transmission.*

In summary, the major geometric change that improves energy efficiency involves reduction of the margin ratio to its minimum value, as constrained by the requirements of the vision processing system. This change improves the energy budget by a factor of 25. Other geometric changes, such as an increase in the number of light sources spread circumferentially around the camera axis and a shift in the relative camera-source angle toward  $\alpha = 90^\circ$ , improve image quality, but are not expected to have a significant effect on the energy budget.

### Strobed Lighting

The energy equation (7.12) applies to steady lighting; significant improvements in energy efficiency may be achieved by applying unsteady, or strobed, lighting. For the case of a pulsed light source, the modified energy equation is

$$\overline{P}_0 = f_p \tau_d P_0 . \quad (7.15)$$

Here the time-averaged power requirement,  $\overline{P}_0$ , is a function of the pulse frequency,  $f_p$ , and the pulse duration,  $\tau_d$ .

An optimized system could reduce the lighting energy requirement by reducing sample rate below that used for field experiments. The ROV-based jelly-tracking camera sampled at the standard NTSC rate of 60 Hz, with interleaved frames captured alternately at half resolution. With continuous lighting, the pulse duration was approximately  $\tau_d \approx 17$  ms. The pulse duration cannot be significantly reduced (since signal strength is, in fact, proportional to the irradiance at the camera integrated over time). However, the sample frequency could be reduced by a factor of six without otherwise affecting the system, as control commands were issued at a rate of only 10 Hz.

Given a sufficiently robust control strategy, further sampling frequency reduction may be possible. The lowest possible sampling frequency, neglecting control effects, is bounded by the possibility of the target exiting the illuminated viewing area between samples. The acceleration, averaged over one swimming cycle, that carries a jelly from the center to the edge of the illuminated cone (a distance of  $d_c/2$ ) in one sample period is  $a$ :

$$a = d_c f_p^2 . \quad (7.16)$$

This equation may, alternatively, be regarded as a definition for the required cone spreading distance,  $d_c$ . According to (7.16) and (7.13), a proportionality exists between the margin ratio and the minimum sampling rate.

$$M = \frac{a}{d_j f_p^2} \quad (7.17)$$

This relation states that, at very low sample rates, the margin ratio must be increased to compensate for unexpected changes in the target's behavior mode, such as a change from a resting behavior to a swimming behavior. Relationship (7.17) only applies for  $M > M'$ . For faster frequencies, the margin ratio does not shrink smaller than the minimum margin ratio defined by the vision-processing constraint. Thus the margin ratio constraint,  $M'$ , is associated with a critical frequency,  $f_p'$ .

$$f_p' = \sqrt{\frac{a}{M' d_j}} \quad (7.18)$$

As described in Chapter 2, few jellies accelerate faster than one body length in a second ( $a \leq d_j \text{ Hz}^2$ ). Thus an estimate of for the critical frequency is  $f_p' = (M')^{-1/2} = 0.7 \text{ Hz}$ .

The relationship for energy consumption as a function of sample frequency is parameterized by the vision-processing constraint,  $M'$ , and by the critical frequency,  $f_p'$ . The relationship is derived by substituting (7.17) into the time-averaged energy equation, (7.15):

$$\overline{P}_0 \propto f_p M^2 = \begin{cases} f_p M'^2, & f_p \geq f_p' \\ \frac{M'^2 f_p'^4}{f_p^3} & f_p < f_p' \end{cases} \quad (7.19)$$

According to (7.19), decreased sampling frequency actually increases power requirements for frequencies below  $f_p'$ . This phenomenon occurs because the illuminated volume need be increased in size to compensate for unknown target motions over longer sampling intervals. The relationship (7.19) indicates that the minimum energy requirement occurs at  $f_p'$ . Figure 7.5 illustrates this result by plotting the relative power requirements predicted by (7.19).



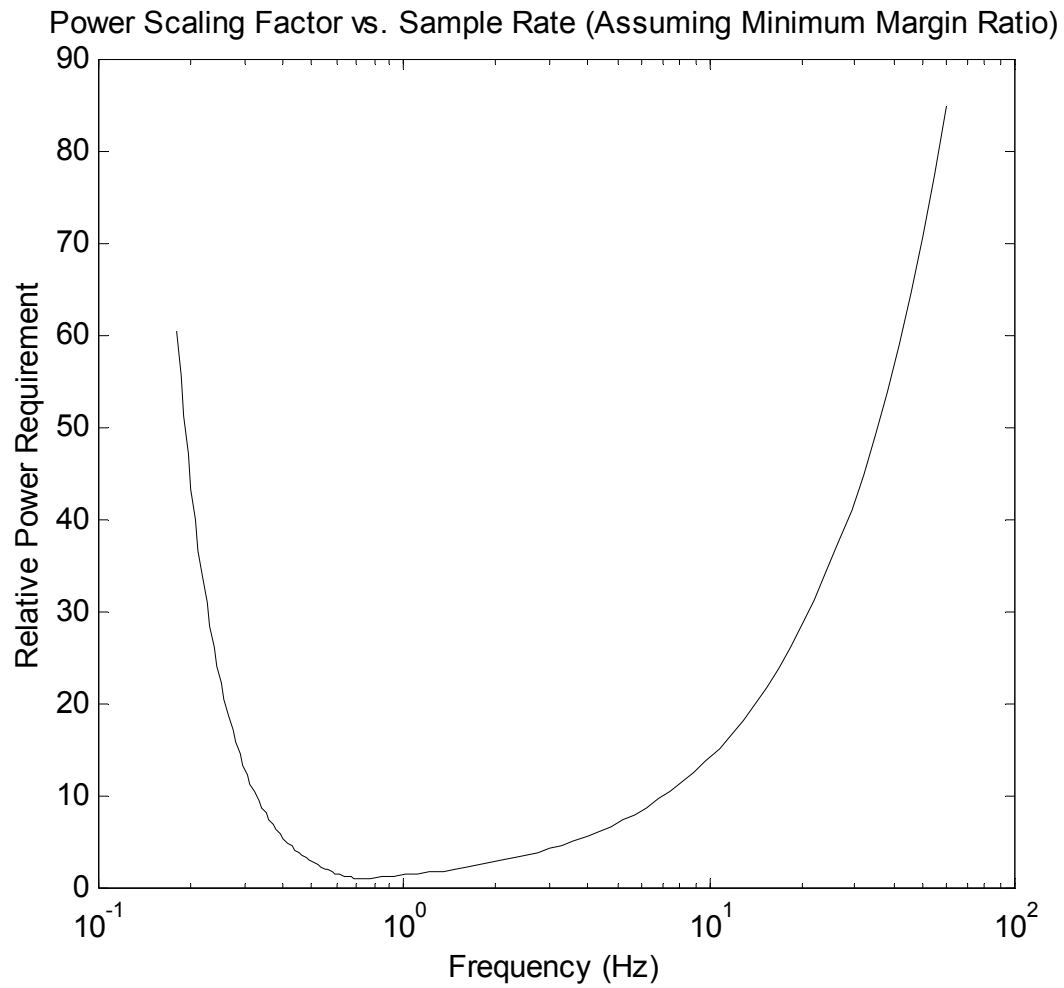


**Figure 7.5 Power Reduction as a Function of Sample Rate**

Power reduction is normalized to unity at the critical frequency,  $f_p'$ . Margin ratio is assumed to be at its minimum value,  $M = M'$  for frequencies above  $f_p'$  and  $M = f_p'^{-2}$  below. In this figure, the critical frequency is estimated to be  $f_p' = 0.7$  Hz and the minimum margin ratio is estimated at  $M' = 2$ .

The figure shows that a reduction in sampling frequency to minimize illumination power can reduce power requirements by a factor of 85. After combining this improvement with the 25-fold improvement possible through geometric optimization, the total illumination energy requirement may be improved by more than a factor of 2000. This factor is much greater than the 200-fold power improvement recommended for AUV-based jelly tracking in Section 7.1. Achieving successful control at low sample rates, however, is a difficult problem, left for future work.

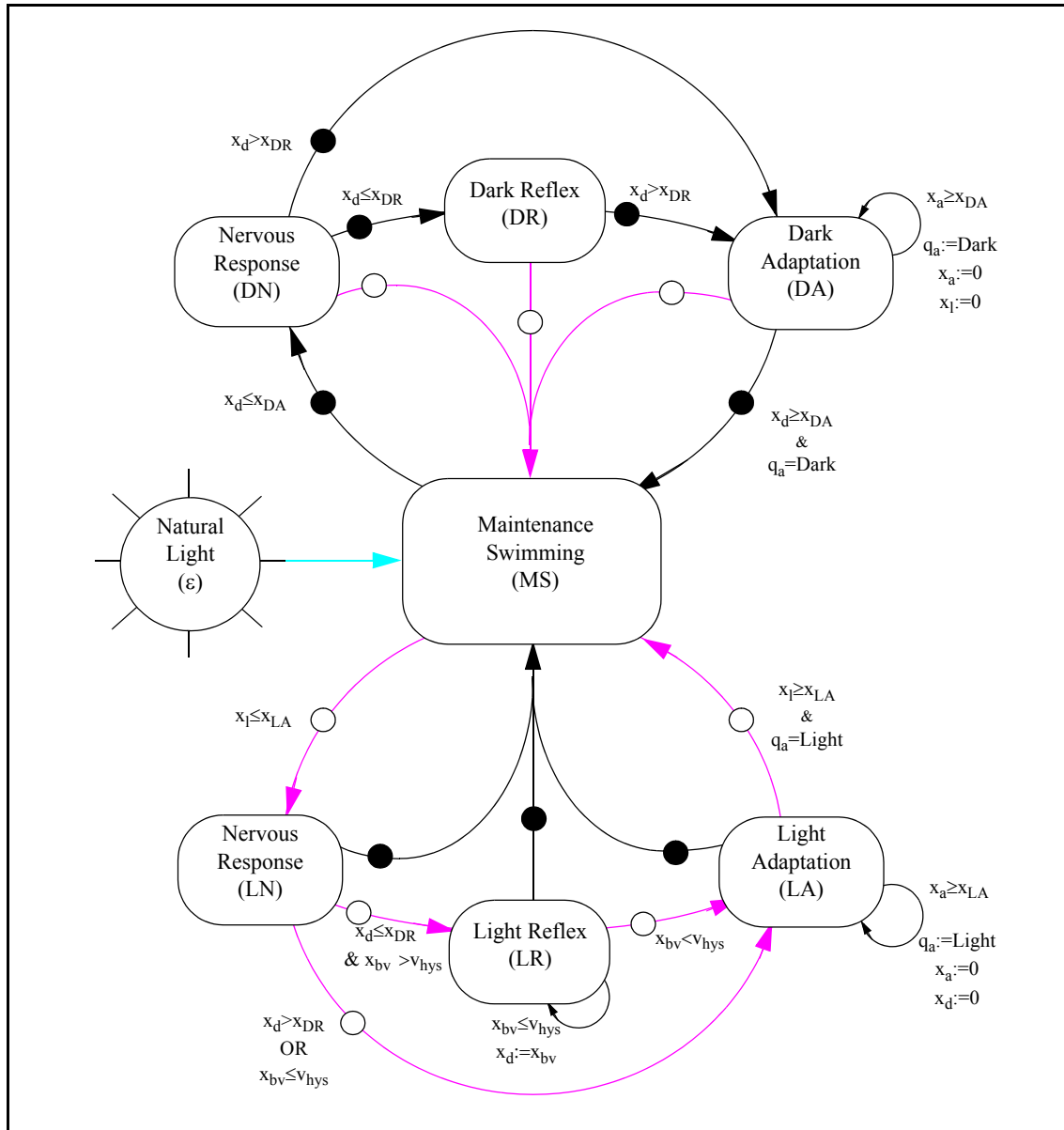
### 7.3 The Impact of Strobed Lighting on Biology Data

As described in Chapter 2, pulsed light stimuli may affect the actions of photosensitive gelatinous animals, both through short-term behaviors, such as the shadow reflex, and through longer-term behaviors, such as diel vertical migration (DVM). In designing a strobed lighting pattern, therefore, it is important to consider the potential impact of the strobe not just on the energy budget of an AUV, but also on the behavioral phenomena under observation. This section constructs a new model for the light response of the medusa *Polyorchis penicillatus*.

Analysis using the model suggests that the proposed low-energy strobe pattern ( $\tau_d \approx 17$  ms and  $f_p \approx 0.7$  Hz) will not trigger repeated artificial reflex actions for a photosensitive medusa. In fact, the strobe pattern, as compared to steady lighting, may actually reduce the impact of lighting disturbances on the observed animal. Whereas steady illumination causes an animal to adapt to an elevated light level, strobed lighting allows the animal to adapt to the darkness and to maintain greater sensitivity to subtle changes in the natural ambient light that are believed to trigger patterns of DVM motion. The use of monochromatic red light ( $\sim 700$  nm) along with the strobe pattern changes the system energy requirements very little and can further decrease the risk of artificially stimulating animal behaviors. Thus these design strategies offers the potential to increase the quality and accuracy of biological data. As a consequence, strobed lighting in the red wavelengths may offer benefits not only for energy-constrained AUV applications, but even for ROV applications.

#### 7.3.1 A Behavioral Response Model for a Photosensitive Medusa

This section introduces a new model to describe light-mediated behavioral responses in a photosensitive medusa. The model provides a means to evaluate a strobed lighting design and to assess



**Control Inputs:**  
 ○ If Strobe On:  $u=1+\epsilon$   
 ● If Strobe Off:  $u=\epsilon$

**2 Discrete-Time ( $q$ ) and 5 Continuous-Time ( $x$ ) States:**  
 Behavioral State:  $q_b \in Q_b$ ,  $Q_b = \{\text{MS}, \text{LN}, \text{LR}, \text{LA}, \text{DN}, \text{DR}, \text{DA}\}$   
 Adaptation State:  $q_a \in Q_a$ ,  $Q_a = \{\text{Dark}, \text{Light}\}$   
 Dark Progress Counter:  $x_d \in \mathbb{R}^+$   
 Light Progress Counter:  $x_l \in \mathbb{R}^+$   
 Adaptation Progress:  $x_a \in \mathbb{R}^+$   
 Motoneuron Potential:  $x_{smn} \in \mathbb{R}$   
 SMN Background Potential:  $x_{bv} \in \mathbb{R}$

Figure 7.6 Definition of Medusa Light Response Model

its potential for stimulating artificial behaviors in an animal under observation. Although the model is hypothesized to apply generally to photosensitive medusa species, model parameters are tuned to the only species for which extensive photoresponse data are available: the shallow-water medusae *Polyorchis penicillatus*.

Figure 7.6 offers a graphical definition of the medusa light-response model. The model is derived from data collected in several research papers including [11,14-16,91]. The hybrid model takes the form of a finite automaton which describes transitions of a discrete behavioral state,  $q_b$ , consisting of seven distinct behavioral modes: the default mode of maintenance swimming, three responses to bright light, and three responses to darkness. In addition to the behavior state, the model includes one other discrete variable, the adaptation state,  $q_a$ , which indicates whether the subject animal is habituated to light or darkness. The model also includes five continuous states: a dark-cycle counter,  $x_d$ ; a light-cycle counter,  $x_l$ ; an adaptation counter,  $x_a$ ; a “base voltage” state,  $x_{bv}$ , describing low level changes in the cell potential of the swimming motor neuron (SMN); and, finally, a total voltage state for the swimming motor neuron,  $x_{smn}$ .

### Behavioral Modes

Changes in the continuous states lead to transition among the seven behavioral modes. The set of seven behavioral modes spans the observed photoresponse behaviors of *P. penicillatus* to impulsive changes in ambient lighting level (Chapter 2.7.4). As illustrated in Figure 7.6, light-stimulated behaviors fall into one of two cycles, a dark cycle or a light cycle. Each cycle traces the physiological pathway from animal photoreceptor (nervous response) to the animal’s muscles (reflex response) and through system-wide habituation (adaptation response). Once fully adapted to a new lighting stimulus, the animal returns to its default swimming state, called maintenance swimming. In this state, spontaneous (i.e. not light-mediated) swimming resumes.

When the light level changes, the model first enters the light nervous (LN) response mode or the dark nervous (DN) response mode, as appropriate. In physiological terms, even very brief light-level changes trigger a response from the medusa’s photosensitive structures, known as ocelli. According to Weber, even light pulses as short as 10 ms trigger an ocellus response which, in turn, triggers a response in the attached optic ganglion [91,92]. This nervous response does not appear, however, to directly affect animal motion behavior.

Responses that do result in visible changes to animal behavior are categorized by the model as light reflex (LR) and dark reflex (DR) responses. The dark reflex, also known as the shadow reflex, involves the complete pathway from the photodetector, through the nervous system, to the swimming muscles. A period of darkness interrupting otherwise bright ambient light triggers the shadow reflex, during which the animal performs a quick burst of one to four swimming pulses, presumably to confound a predator trawling above. The light reflex does not trigger a burst of swimming; rather, the light reflex inhibits a shadow reflex in progress. Effectively, the light reflex stops bursting and resets the shadow reflex so that it may occur again multiple times in rapid succession.

By comparison with reflex responses, which occur for stimuli lasting 100s of milliseconds, adaptation responses occur for much longer periods of light and darkness, which last for 10s or 100s of seconds. During light adaptation (LA) or dark adaptation (DA), the animal habituates to a new light level. In dark adaptation, which generally follows a shadow reflex response, spontaneous swimming is inhibited. In light adaptation, by contrast, spontaneous swimming may occur. This swimming resembles spontaneous swimming in the maintenance swimming (MS) mode, but at an increased pulsing frequency [11]. In the LA mode, as the animal habituates to bright light, its pulse frequency, when swimming, decays gradually back to the base level observed in the MS mode [14]. After habituating to a light or darkness condition, the animal exits the adaptation state and returns to the default mode of maintenance swimming.

Under steady light or darkness, progress generally proceeds circularly around the light or dark cycle (see Figure 7.6) from nervous response to reflex response to adaptation and back to maintenance swimming. On returning to a light or dark cycle after only a brief period of the opposite lighting condition, however, the animal may directly enter the adaptation mode from the nervous response mode, without first triggering an intermediate reflex response.

Progress around each of the two cycles is tracked by a continuous counter variable. The light counter,  $x_l$ , and the dark counter,  $x_d$ , increment or decrement according to the external light stimulus:

$$x_l = \min(x_{LA}, \max(0, f(t_b) + x_l|_{t_b=0})) \quad (7.20)$$

$$x_d = \min(x_{DA}, \max(0, -f(t_b) + x_d|_{t_b=0})) \quad (7.21)$$

Here the time since entering a particular behavioral state is  $t_b$  and the increment/decrement function,  $f(t_b)$ , is controlled by the ambient light input,  $u$ .

$$f(t_b) = \begin{cases} t_b, & u \geq 1 \\ -t_b, & u < 1 \end{cases} \quad (7.22)$$

The ambient light input,  $u$ , takes on the value of the natural lighting during a light-off (or darkness) event:  $u = \varepsilon$ . The artificial lighting level is assigned an intensity of unity and is assumed much stronger than natural lighting level,  $\varepsilon$ , such that  $\varepsilon \ll 1$ . Thus, during a light-on event, the ambient lighting input is effectively that of the artificial light source,  $u = 1 + \varepsilon \approx 1$ .

A third counter, the adaptation counter, tracks the animal's habituation to brightness or darkness:

$$x_a = \begin{cases} \min(x_{DA}, \max(0, -f(t_b) + x_l|_{t_b=0})), & q_a = \text{Light} \\ \min(x_{LA}, \max(0, f(t_b) + x_l|_{t_b=0})), & q_a = \text{Dark} \end{cases} \quad (7.23)$$

When the adaptation counter reaches its maximum value, the model of the animal transitions from light habituation to dark habituation or vice versa.

Transitions between behavioral modes occur based on changes in the progress variables ( $x_l, x_d, x_a$ ) and in the lighting input,  $u$ . If the lighting input does not change, the following transition parameters govern mode transitions as described by Figure 7.6. Transition parameters are selected based on published data for *P. Penicillatus* [11,14-16,91].

$$\begin{aligned} x_{DR} &= 8.0 \text{ s} & v_{\text{hys}} &= 6 \text{ mV} \\ x_{DA} &= 25 \text{ s} & x_{LA} &= 180 \text{ s} \end{aligned} \quad (7.24)$$

If the input signal undergoes a step change, the model immediately transitions out of the current behavioral mode, passes through the MS mode, and enters the opposite light or darkness cycle, starting with a nervous response (LN or DN). The animal is assumed to detect step changes in lighting with a latency of 100 ms.

### Spontaneous and Reflex Swimming

The hybrid model allows for two types of swimming behaviors: reflex swimming, in response to a light stimulus, and natural, or spontaneous, swimming. The model does not account for other spontaneous animal behaviors, such as body and tentacle deformations. A description of the challenges in modeling these diverse spontaneous swimming behaviors for gelatinous animals may be found in [122].

The first type of swimming, spontaneous swimming, occurs only in the LA and MS modes. In these modes, the animal would be expected to alternate between periods of rest and periods of activity. In the MS mode, active periods consist of swimming at a base frequency,  $f_0$ . The spontaneous swimming frequency rises to  $f_{LA}$  when the animal first enters the LA mode and gradually decays back to the base frequency according to the following equation:

$$f = f_0 + (f_{LA} - f_0)e^{-3(x_a/x_{LA})}. \quad (7.25)$$

where  $f_0$  is the maintenance-swimming pulse frequency and where  $f_{LA}$  is the increased pulse frequency observed upon first entering the light-adaptation mode. The ratio of rest and swim activity may change over course of a 24-hour day, to allow the animal to perform large scale vertical migrations based on the natural lighting stimulus,  $\varepsilon$ .

Although the model describes variations in the frequency for spontaneous swimming,  $f$ , it does not explicitly account for individual spontaneous swimming pulses, as they are not correlated with lighting input and are stochastic in nature. The model does, however, explicitly account for individual swim pulses triggered by the shadow reflex.

The model uses two voltage variables to track reflex swimming in the DR mode. The variables describe the cell potential in the swimming motor neuron (SMN), a segment of the *P. penicillatus* nervous system directly responsible for triggering contraction of the muscles used for bell contraction. The first of these states, the base voltage variable,  $x_{bv}$ , tracks low level changes in SMN potential. The base voltage state increases to a threshold,  $v_{max}$ , according to the following rule.

$$x_{bv}(x_d) = \begin{cases} \min(v_{max}, \alpha \cdot (x_d - x_{DN})), & q_b = \{\text{DR}\} \\ \max(0, -\alpha \cdot t_b + x_{bv}|_{t_b=0}), & \text{otherwise} \end{cases} \quad (7.26)$$

When the base voltage reaches a sufficiently excited state ( $x_{bv} = v_{max}$ ), spikes in cell potential, called action potentials occur. Physiologically, action potentials occur when a neuron reaches a high enough cell potential that a flood of charge suddenly rushes through the cell membrane. In effect, this all or nothing signal is a binary voltage spike, generated by the neuron. In the case of the *P. penicillatus* swimming motor neuron, each voltage spike (action potential) triggers a single contraction of the swimming bell.

The second voltage state,  $x_{smn}$ , captures the total voltage for the swimming motor neuron, effectively the sum of the base voltage with an action potential function,  $g(x_d)$ .

$$x_{smn} = x_{bv}(x_d) + g(x_d) \quad (7.27)$$

A typical action potential burst consists of one to four bell contractions in rapid succession. The model action potential function,  $g(x_d)$ , treats the voltage spike cluster as a train of rectangle functions of duration  $\tau$ .

$$g(x_d) = \begin{cases} \gamma \sum_n \text{rect}\left(\frac{1}{\tau}(x_d - t_{nP})\right), & q_b = \{\text{DR}\} \\ 0, & \text{otherwise} \end{cases} \quad (7.28)$$

For simplicity,  $g(x_d)$  is modeled deterministically as a series of only two action potentials occurring at dark cycle times of  $t_{1P}$  and  $t_{2P}$ .

### 7.3.2 Tuning and Validating the Light-Response Model

The light-response model, introduced in the previous section, was tuned and then subsequently validated using two distinct datasets. Each dataset describes the swimming motoneuron voltage,  $x_{smn}$ , over time in response to a binary (light-dark) input signal,  $u$ . Spikes in SMN voltage correspond with swimming pulses: a clear indication of artificial animal behaviors induced by an outside light source.

#### Tuning

The model was tuned based on an initial training dataset, drawn from [86]. Figure 7.7(a) illustrates this training dataset. The training set describes the onset of the shadow reflex in response to



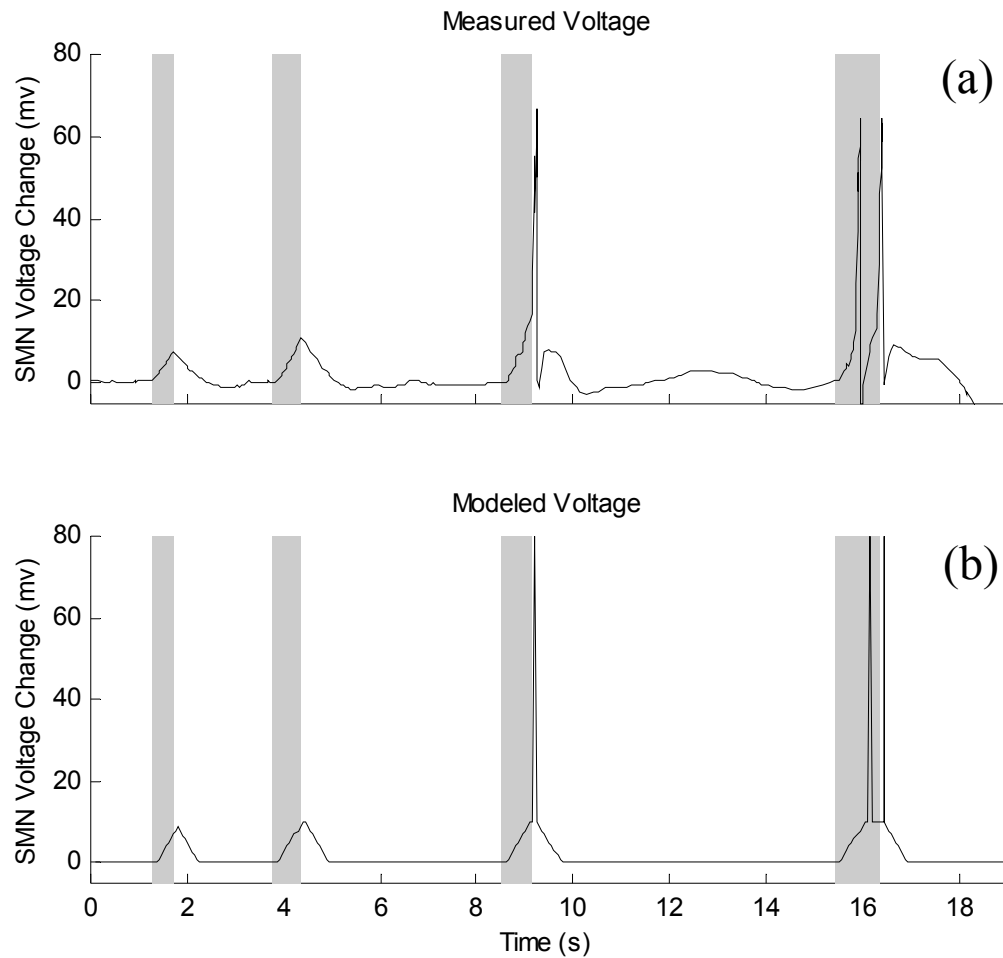


**Figure 7.7 Training a Model for Polyorchis Data**

The light-response model was tuned to match data for a *Polyorchis* specimen. (a) This experimental dataset, reported by [86], depicts the swimming motor neuron (SMN) potential for four light-off events of durations 0.44 s, 0.55 s, 0.64 s, and 0.92 s. Gray regions represent times during which the light stimulus was turned off. Light off events may trigger large spikes in the SMN potential. These spikes are action potentials, all-or-nothing events which trigger a single swimming pulse. Action potentials do not trigger in response to short light-off events (less than 0.55s), but do trigger after longer light-off events (above 0.6 s). (b) The lower plot shows the voltage output of the light-response model to the sequence of four light-off events. Model parameters were tuned to match the experimental data, so that modeled action potentials, like those of the experiments, trigger for pulse durations of 0.6 s and longer.

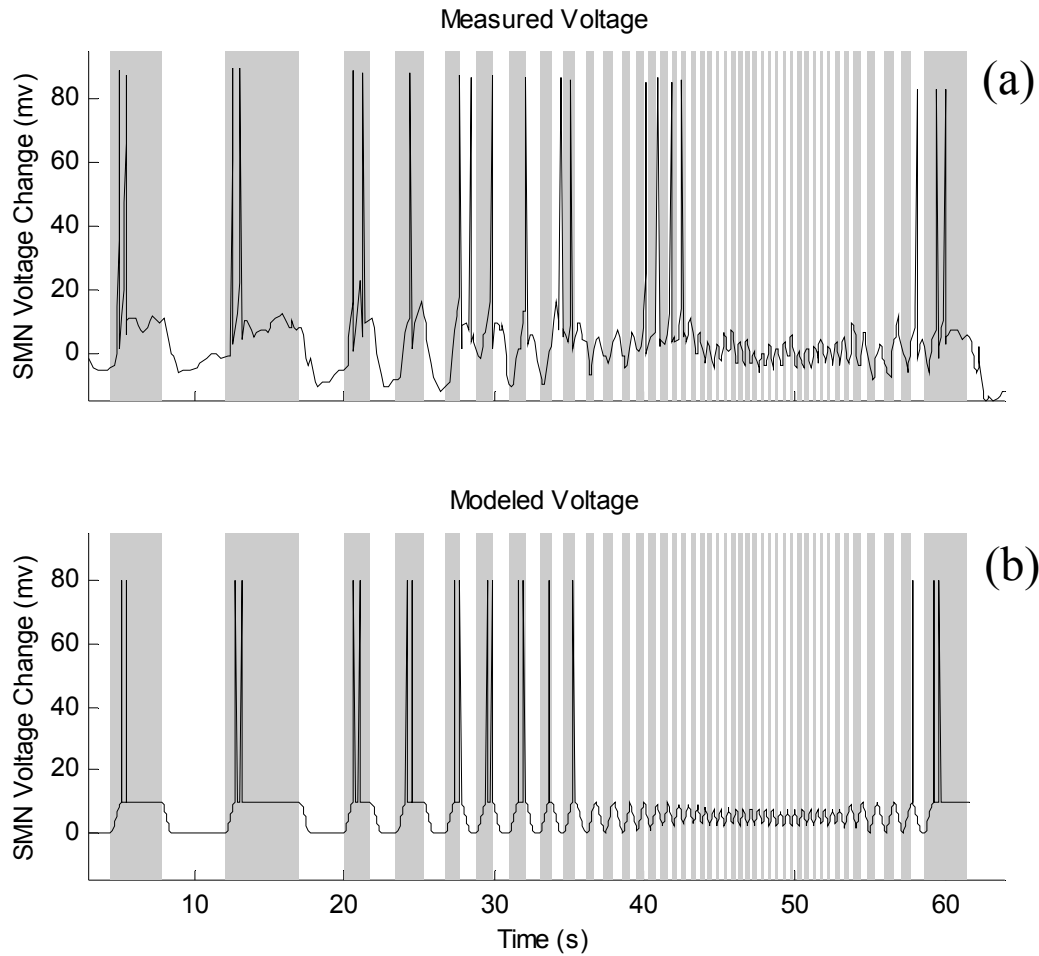


**Figure 7.8 Validating the *Polyorchis* Model in Response to a Train of Light-off Events**

The light response model was validated using a second *Polyorchis* dataset. (a) The second experimental data set is reported by [16] and evaluates jelly response to a train of subsequent light off events. The signal generator controlling the light source performs a square wave sweep from 0.5 Hz to 4 Hz and back. (b) The light-response model captures most of the action potentials observed in the experimental dataset. Significantly, the model misses a rapid sequence of four pulses that occur between seconds 40 and 43, when the pulse frequency reaches 1.25 Hz. These pulses may represent an unmodeled resonance mode. Also, the model missed three pulses which occurred during light-on periods. These pulses may have been spontaneous swimming events unrelated to the optical stimulus.

varying length periods of darkness. The set includes four light-off events, each longer than the last, applied to a light-adapted *P. Penicillatus* specimen. The specimen only reacts to the two light-off events longer than 0.6 seconds. A series of two action potentials was recorded for the light-off event lasting 0.92 seconds.

The parameters of the action potential function,  $g(x_d)$ , were tuned based on this dataset, assuming a 100 ms latency. The resulting parameter selections were as follows.

$$\begin{aligned} v_{max} &= 10 \text{ mV} & \gamma &= 70 \text{ mV} \\ \alpha &= 20 \text{ mV/s} & \tau &= 0.05 \text{ s} \\ t_{1P} &= 0.60 \text{ s} & t_{2P} &= 0.92 \text{ s} \end{aligned} \tag{7.29}$$

The light-response model qualitatively reflects the source data, as shown by Figure 7.7(b). Only small discrepancies are noticeable, such as the oscillations in the SMN voltage after the first action potential, for instance, which result in an increased base voltage and a reduced trigger time for the action potentials associated with the last of the four light-off events. This phenomenon appears to be the result of dynamic behavior of  $x_{smn}$ , which is not captured by the algebraic description of (7.26)-(7.28).

### Validation

In order to evaluate parameter tuning based on the first dataset, a second experimental dataset was used for model validation. The validation dataset, drawn from [16], reports swimming motor neuron voltage,  $x_{smn}$ , for a *Polyorchis penicillatus* specimen subjected to a swept-frequency square wave. The frequency sweep begins at 0.5 Hz, increases to 4 Hz, and then returns back to 1.6 Hz. Figure 7.8(a) plots the experimental data. The plot indicates that the animal subject responds with an apparent shadow reflex for each dark period before the 36th second of the run. Subsequent dark periods, shorter than 0.6 s, do not trigger a shadow reflex, with the exception of an anomalous set of action potentials between seconds 40 and 43. No further SMN action potentials were recorded until the dark period again lengthened beyond 0.6 s (after the 57th second of the experiment).

The model response qualitatively resembled the experimental data. The choice of the model parameters for the ramp slope,  $\alpha$ , and the base-voltage threshold,  $v_{max}$ , appear consistent with the data, as shown by Figure 7.8(b). The spike width,  $\tau$ , and the spike height,  $\gamma$ , also appear consistent with experimental data. Also, the model is seen to repeatedly trigger shadow responses for

multiple successive light-off periods. This fact indicates the LR mode plays a role in resetting the shadow reflex, and that the hysteresis voltage,  $v_{hys}$ , is properly set.

In general, the timing of the first action potential, at  $t_{1p} = 0.6$  s, was also consistent with observed data. Shadow reflex action potentials predicted by the model stopped at the 36th second and resumed after the 57th, as indicated by the experimental data. However, the model did not predict the burst of anomalous spikes between seconds 40 and 43, which occurred during dark periods of only 0.4 s in length. This set of four action potentials may be the result of the chemo-electrodynamics of the cell, which are modeled only with algebraic equations in the model. A more complex dynamic form would be required to capture the observed phenomenon, which appears to have a narrow band resonance peak near 2.5 Hz. As a final observation, the  $t_{2p}$  parameter appears to be longer than 0.92 for the validation dataset. The discrepancy may be attributed to the relative lack of data represented in the training dataset.

In summary, the validation dataset gives confidence that the light-response model can qualitatively predict the reactions of *P. Penicillatus* in response to a sequence of pulsed lighting events. The validation dataset does indicate, however, a warning about model validity for pulsed sequences with a dominant Fourier frequency component near 1.25 Hz. Such sequences may cause resonance of the base voltage and, as a consequence, may result in action potentials not predicted by the light-response model. The proposed light pattern, which runs at 0.7 Hz with a pulse duration of 17 ms, does not have a significant Fourier component near this 1.25 Hz resonance point (as shown by Figure 7.9), and appears, thus, to be a valid input for the light-response model.

### 7.3.3 Applying the Light-Response Model to the Design of a Strobed Lighting System

In minimizing the lighting power budget for an energy-constrained AUV, Section 7.2.2 recommended the use of strobed lighting with a pulse duration of approximately 0.017 s and an inter-pulse spacing of approximately 1.4 s ( $f_p' \approx 0.7$  Hz). Because changes in illumination level may stimulate artificial behaviors in observed gelatinous animals, it is important to consider the potential impact of this strobe pattern on biological observation. The new light-response model offers a means of addressing this concern. The model predicts how a particular species of medusa, *Polychorda penicillatus*, responds to the proposed low-energy strobe pattern. Assuming that other photosensitive gelatinous animal species display neural, reflex, and adaptation reactions over time

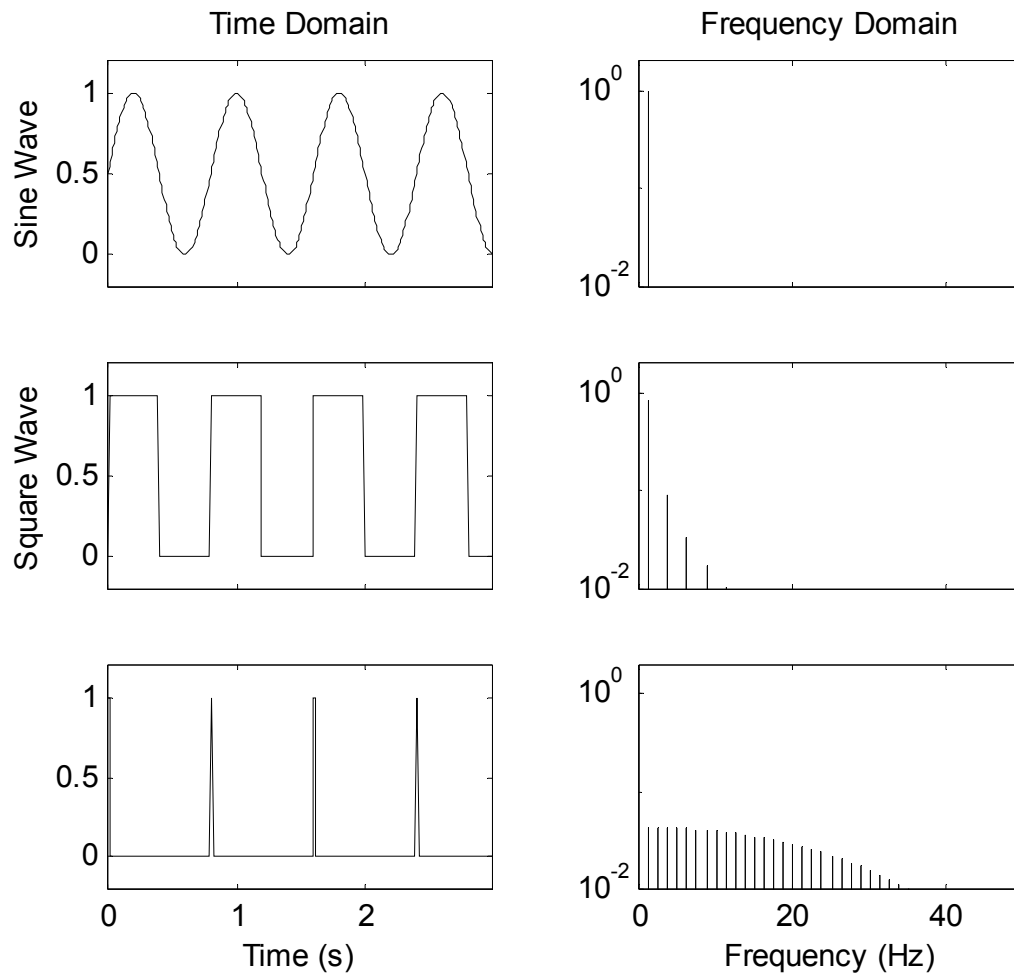


**Figure 7.9 Frequency Domain Description of Pulsed-Light Sequences**

Time and frequency domain representations are shown for three sequences, all of which repeat with a 1.25 Hz frequency. The first sequence is a sine wave, the second a square wave with even light-on and light-off periods, and the third a strobe sequence with very short strobe pulses ( $\tau_d=0.017$  s). Frequency domain plots are shown for each of the three signals, with the DC component stripped and the remaining components normalized such that total signal power was equal to unity. Whereas the sine wave and square wave signals have a very strong power component at 1.25 Hz, the pulsed strobe sequence only has a very small component at 1.25 Hz.

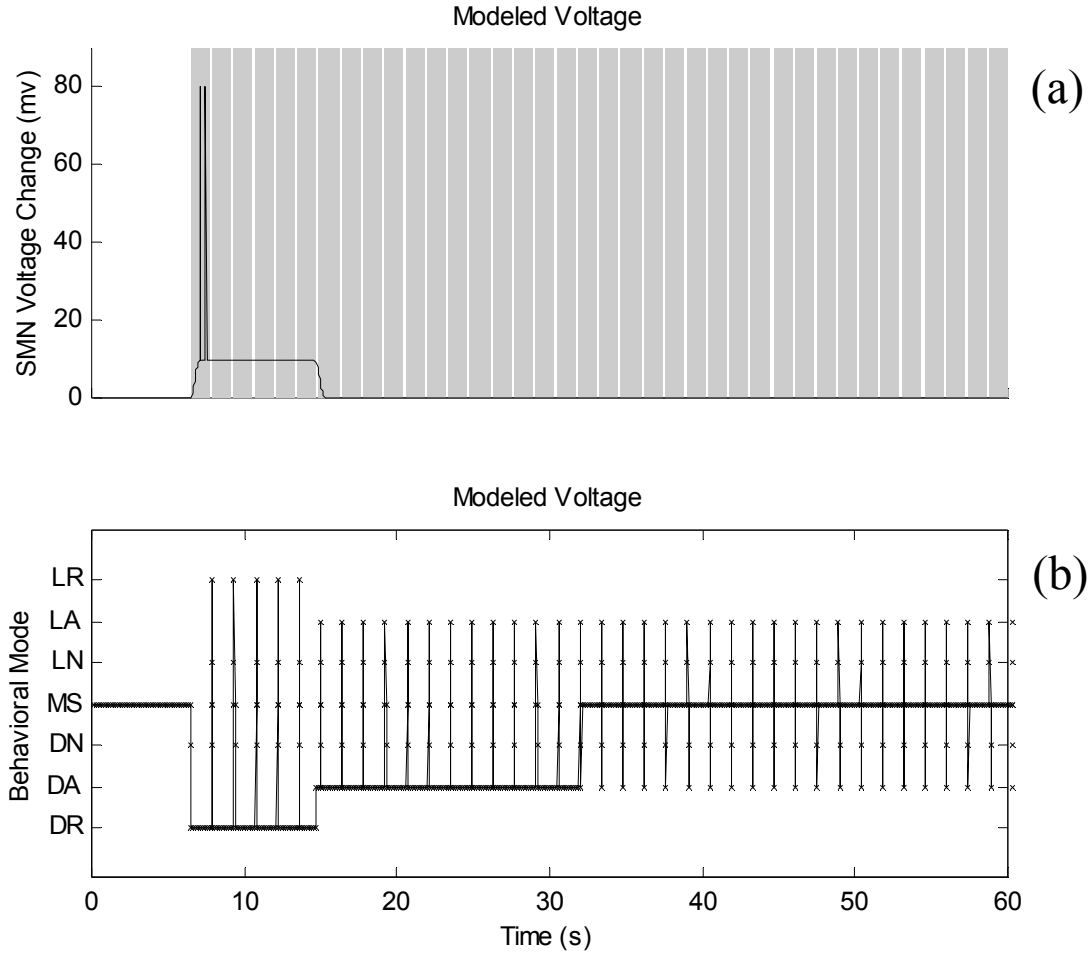


**Figure 7.10 Applying Light-Response Model to Proposed Low-Energy Strobe Pattern**

The low-energy strobe pattern from Section 7.2.2 was used as an input to the light-response model. The model was initialized assuming the subject animal was light adapted,  $q_a = \text{Light}$ . (a) The upper plot shows the time response of the swimming motorneuron voltage as a function of time, subject to a strobe pattern with period 1.4 s and light-on pulse duration of 0.017 s. A shadow reflex is observed when the lighting environment first switches to the strobed pattern. (b) The lower plot shows the behavior mode as a function of time. The dominant behavioral mode switches, at light-off, from maintenance swimming (MS) to the dark reflex mode (DR) to the dark adaptation mode (DA) and finally back to maintenance swimming in the dark-adapted state,  $q_a = \text{Dark}$ .

scales similar to that of *P. penicillatus*, the model enables the evaluation of the proposed lighting pattern to assess its impact on biological observation studies.

Figure 7.10 shows the predicted light-response of the reference medusa to the proposed low-energy strobe pattern. The response is plotted assuming the subject animal is adapted, initially, to bright light. When the strobe sequence begins, the first light-off event triggers an immediate shadow response. The following, 17 ms light-on event does not last long enough to effectively trigger the LR mode to reset the shadow reflex. As such, the dark cycle is permitted to complete the dark reflex (DR), to complete dark adaptation (DA), and to return to the maintenance swimming (MS) mode in the dark adapted state. The model thus converges on the dark-adapted MS mode after a sufficient time interval. The converged state is, in fact, a periodic steady state, with intermittent sweeps through the LN, LA, DN, and DA modes during and after each 17 ms light pulse. The model never enters the reflex states (LR or DR), and hence, no artificial motion behaviors are triggered by the proposed low-energy strobe sequence once the model converges to its periodic steady-state.

Thus, according to the model, the proposed low-energy strobed lighting pattern does not appear to negatively impact the quality of biological observations of photosensitive animals. Although the medusa ocellus may produce a small neural response following each pulsed lighting event, no artificial motions are triggered and the animal's dominant behavior mode remains as dark-adapted maintenance swimming.

Surprisingly, pulsed lighting may actually enable studies not otherwise possible using constant illumination. Under the strobed lighting pattern, the model achieves a dark-adapted periodic steady-state in the MS mode. By comparison, the constant illumination input places the model in a light-adapted steady-state in the MS mode. When adapted to bright lighting, the animal subject may lose its sensitivity to subtle changes in natural lighting level,  $\epsilon$ . Thus constant lighting may interfere with behaviors mediated by subtle changes in lighting level, such as DVM. Because the strobed lighting sequence allows the animal to adapt to darkness, the animal may retain greater sensitivity to changes in natural ambient lighting. In this sense, pulsed lighting may offer benefits not just in terms of energy savings, for AUV applications, but also in terms of the quality of biological observations, a factor relevant both for AUV and ROV applications.

### 7.3.4 Choice of an Illumination Wavelength

Strobed lighting provides one means of reducing illumination disturbances on a tracked animal. The choice of illumination wavelength provides a second means of influencing the lighting disturbance environment [7,167,175]. Selecting an illumination wavelength away from the wavelength of peak photoreceptor sensitivity reduces an animal's ability to perceive artificial lighting stimuli. Figure 2.8, which plots the spectral sensitivity for the ocelli of two representative species, *Sarsia Tubulosa* and *Polyorchis Penicillatus*, suggests that small changes in illumination wavelength can significantly impact an animal's ability to perceive ambient illumination. At 700 nm, these photoreceptors have a sensitivity more than 25 times lower than their peak value. Sensitivity also decreases into the blue, but the potential hazard of radiation damage under ultraviolet light [53] limits the sensitivity reduction achievable at shorter wavelengths.

Although both strobed lighting and wavelength selection can improve the quality of biological data collection by reducing illumination disturbances, they have opposite affects on the system energy budget. While strobed lighting reduces illumination power requirements, wavelength selection increases power requirements. Power increases for wavelength selection over the 400-700 nm band are moderate, less than a factor of two. An elbow in the energy cost curve results in exponential increases in power requirements when lighting at wavelengths above 700 nm, as illustrated by Figure 7.2(b).

Thus red illumination (~700 nm) provides a good compromise between concerns about biological disturbances and concerns about the energy budget for AUV operations. The energy reductions afforded by geometric improvements and strobing more than compensate for the modest (two-fold) increase in energy costs required to illuminate at 700 nm. At the same time, the combination of strobed and red lighting offers the potential for a tremendous reduction in the lighting disturbance environment and a corresponding improvement in the quality of biological data collected. Consequently, such a lighting system may offer benefits not only for AUV-based tracking, but also for ROV applications.

---

## 7.4 Summary

The major challenge in transferring experimentally validated tracking technologies from an ROV platform to an AUV platform involves the reduction of sensing power requirements and, in partic-



ular, the power required for illumination. An energy budget analysis for a conceptual jelly-tracking AUV places the illumination power requirement at approximately 20 W, a 200-fold reduction in power relative to that used by the experimental ROV system. Converting from the diffuse illumination used for ROV operations to focused spotlighting reduces the illumination energy requirement by as much as a factor of 25. The use of strobed lighting (at a sample rate of 0.7 Hz) can further reduce power requirements by a factor of approximately 80. Achieving these low-energy benefits requires accurate modeling of vehicle and target motions so as to permit low-sample rate control. Thus, under the assumption of accurate low-sample rate control, scaling arguments suggest that the combination of spotlighting and strobing, together, can permit the use of the experimentally validated jelly-tracking system for an energy-constrained AUV application.

Prior investigations have demonstrated that alternating patterns of bright light and darkness can trigger reflex swimming in photosensitive medusa. As a means of evaluating the biological impact of the proposed low-energy strobed lighting pattern, this chapter introduced a hybrid model for the light response of a representative medusa. Subject to the 0.7 Hz low-energy strobe pattern, the model quickly reached periodic steady state in the maintenance swimming mode. In this mode, the strobe pattern triggers a small neural response following each light flash but provokes no artificial motion behaviors. Moreover, the strobe pattern allows the subject animal to adapt to the darkness and to retain sensitivity to natural lighting. As subtle variations in natural lighting level may trigger diel vertical migration (DVM), strobed lighting affords a better opportunity to study long-duration behavioral phenomena, like DVM, than steady lighting. Thus strobed lighting appears to have a beneficial effect on jelly observation, rather than the detrimental effect initially suspected.

That strobed illumination may offer not only an energy benefit, but also a reduction in lighting disturbances, implies that pulsed lighting may benefit both AUVs and ROVs. Use of monochromatic red wavelengths ( $\sim 700$  nm), in conjunction with strobing, could further reduce the lighting disturbance environment with little impact on system energy requirements. The resulting strobed, red-light illumination component could thus meet the constrained-energy budget requirements for AUV operations and simultaneously improve the quality of biological data collection for both AUV and ROV applications.



*Long term visual tracking of single individuals seems possible, but obviously will require considerable effort and expense.*

- H.J. Price et al., 1988 [77]

---

The jelly-tracking project has focused on developing new technologies that enable automated robotic tracking of deep-ocean gelatinous animals, both using tethered ROV platforms and untethered AUV platforms. This chapter summarizes the key achievements of the jelly-tracking project. The chapter also proposes directions for engineering development, to assist in transfer of the jelly-tracking technology into regular marine operations, and for future research, to extend the work of this dissertation to tackle other visual tracking applications, to enable tracking in hotspots of biological activity, and to address remaining control challenges in the development of AUV-based jellyfish tracking.

---

## 8.1 Core Research Contributions

The jelly-tracking research project has tackled a new application area at a system level. Previous technologies for observing deep-ocean gelatinous animals over long durations faced two major problems: fatigue of human pilots and cost of infrastructure. Automating robotic jelly-tracking addresses these two problems. Specifically, new techniques introduced in this dissertation enable an ROV-based pilot assist that frees the pilot from the fatiguing burden of servo-level control. These technologies will also serve as key components to enable jelly tracking with AUVs. AUVs, untethered platforms that perform simple, repetitive tasks and require less operational infrastructure than ROVs, will, in the future, reduce research costs and permit very long-duration tracking activities, on the order of 24 hours or more.

Two major research challenges arise in automating a jelly-tracking robot. To perform long-duration biological observation, the system must achieve both (1) high system reliability and, (2)

for AUV-applications, low system energy consumption. The research of this dissertation examines the role played by individual components in achieving these system-level goals. In particular this work emphasizes the first challenge, that of achieving high system-level reliability. To this end, the dissertation has examined the design of custom visual sensing and feedback control software tailored for the jelly-tracking task. Deep-ocean experiments have validated the reliability of this software package as a pilot-assist for ROV-based jelly tracking. Because the field-demonstrated system relies on significant power availability, a final design study complements experimental work and suggests methods to modify sensor illumination to satisfy the low-energy requirement for AUV-based deployment.

### 8.1.1 System Reliability for ROV-Based Tracking

The major contributions of this work involve design and experimental validation of technologies that enable a reliable jelly-tracking pilot assist for ROV operations.

#### **Experimental Contribution: First-Ever Demonstration of Deep-Ocean Animal Tracking**

This work performed the first-ever experiments to demonstrate automated robotic tracking of an animal in the deep-ocean. The duration of uninterrupted tracking served as the primary metric to establish system reliability. Early baseline experiments, deploying off-the-shelf technologies, consistently lost the animal target after fewer than three minutes of tracking. By contrast, the improved jelly-tracking pilot assist pursued a swimming *Ptychogena* specimen for 89 minutes. The improved system also tracked other animals for periods longer than thirty minutes. Of the four longest runs, only one run (tracking a *Solmissus* specimen) ended because of a software failure.

#### **Vision Contribution: Design of Visual Tracking Systems for Natural Scenes**

This dissertation introduced a new design technique to streamline the synthesis of vision-processing methods for jelly-tracking and for other tracking applications in unstructured, natural environments. In these environments the engineer cannot control or modify the visual appearance of the target or the surrounding scene. Previously, the standard design method for new visual tracking applications involved implementing a large number of vision-processing strategies and empirically evaluating them on a reference set of video clips. The new design approach circumvents this time

consuming activity by directly analyzing the information content in a video database and using this analysis to identify a small subset of vision algorithms with filtering and topology processing sub-components that best differentiate targets in a reference dataset. This design method, called the segmentation efficiency method, was applied to a jelly-tracking database consisting of 182 video clips of transparent gelatinous animals imaged under a variety of uneven lighting conditions. The segmentation efficiency analysis focused the design process and, despite the complexity of midwater scenes, enabled jelly-tracking using a relatively simple, computationally efficient algorithm based on a morphological-gradient threshold. In experiments, the vision-processing method consistently and successfully identified tracking targets of varied species under varied illumination conditions with no parameter-tuning by a human operator.

**Control Contribution: Design of a Control Law Tailored for ROV-Based Jelly Tracking**

This dissertation developed a control law that addresses the critical issues associated with visual observation of a gelatinous animal. These issues included (1) the definition of a control objective consistent with the physical camera sensor, (2) the selection of a thruster map to minimize thruster outputs which might disturb the animal target, and (3) the specification of additional control terms that enforce the limits of the camera viewing cone in the face of large disturbances. Since the ROV plant acts, in essence, as a damped second-order system, a classical proportional-derivative (PD) control formed the core of the tracking law. A first modification to the baseline control law accounted for the nature of desired visual science data. Acquiring this data required animal tracking in only three of the system's four degrees of freedom. A decomposition of the vehicle dynamics into two subspaces, one associated with the control objective and the other an orthogonal null space, permitted a precise definition of the control law in terms of the input of the system's visual sensor. A second modification involved the mapping of the control input to the vehicle thrusters. In implementing this map, which incorporated control in both the control-objective and null spaces, the thruster map was optimized to minimize total thrust output in an attempt to reduce hydrodynamic stimuli that could affect animal behavior. A third modification involved the augmentation of the linear control law with two additional control terms to compensate for large disturbance forces. Because the linear control law was designed with low gains, to permit tracking of animal swimming motions without requiring large thruster outputs, the linear control law does not effectively reject large disturbances. The supplementary control terms, an estimator-based distur-

bance-accommodation law and a nonlinear boundary-control law, provided more aggressive thrust to prevent loss of the target from the camera viewing cone in the face of large low and high-frequency environmental forcing.

### 8.1.2 System Energy Consumption for AUV-Based Tracking

This dissertation also analyzed power consumption for sensor illumination and proposed methods for reducing power requirements to a level consistent with AUV-based jellyfish tracking. Illumination for visual sensing was the major power sink for the ROV-based tracking system. Powered via a tether to the surface ship, the experimental ROV drew approximately 4 kW power for lighting and sensing. By comparison, an AUV platform should draw approximately 20 W in order to achieve 24-hour tracking. In addition to energy concerns, the illumination system design must also consider the impact of illumination on the behavioral patterns of photosensitive gelatinous animals. Prior experimental evidence suggests that bright lights and sudden step changes between illumination and darkness may affect the behavior of certain gelatinous animals.

The lighting component analysis introduced in this dissertation considers the design of an illumination system given both the animal-behavior and energy-budget ramifications of lighting design. The first step involved a radiometric analysis that assessed the power reductions possible by varying lighting geometry and strobe parameters. The second step involved modeling the light response of a reference photosensitive medusa (*Polyorchis penicillatus*) and applying this model to evaluate potential animal reactions to the proposed low-energy light pattern. Altogether, the analysis recommended the use of a focused-beam, strobed illumination pattern; based on vision-system constraints, the optimal strobe frequency falls at approximately 0.7 Hz, with a light-on duration of about 20 ms. The light response model suggests that this strobe pattern does not adversely impact observed animal behaviors, and that it may, in fact, preserve the animal's response to subtle environmental lighting changes, such as those associated with DVM.

---

## 8.2 Engineering Development to Support Operational ROV-Based Tracking

Experiments have clearly demonstrated the capability of the new jelly-tracking vision and control software package to enable an ROV-based pilot assist. Minor modifications to the present system

are required, however, to support the transition of the research-oriented system into operational use. Four engineering development activities are identified as requirements prior to deploying the jelly-tracking pilot assist in the field. These modifications address pilot acceptance issues and include (1) improvements to the software interface, (2) changes to the baseline control to address occasional limit cycles, (3) automation of the stereo-geometry calibration and (4) control system modifications to enable bumpless transfer from human control to combined human-computer control in the presence of a significant bias disturbance on the ROV.

### 8.2.1 Interface

The research software used a complex interface that permitted a high degree of on-the-fly customization for field experiments. The lack of a streamlined, user-friendly interface remains the single largest barrier to pilot acceptance of the jelly-tracking system.

### 8.2.2 Limit Cycles

Previous work by Yoerger *et al.* demonstrated that thruster nonlinearities may result in a limit cycle during ROV station-keeping activities [164]. Indeed, occasional limit cycles appeared during jelly-tracking, but only in the absence of significant quasi-steady bias forces (which shift the thruster away from its singularity at zero rotation rate). Although these limit cycles, as described by the plots of Figure 6.6, appear infrequently, they are a nuisance in acquiring presentation video footage. Yoerger recommends the use of sliding-mode control to eliminate ROV thruster-induced limit cycles. Substitution of a sliding mode control law for the linear control block of Figure 5.2c might eliminate the limit-cycle nuisance. The requirement to avoid excessive thruster action during jelly tracking, however, limits the acceptable thrust differential across the sliding-mode boundary layer.

### 8.2.3 Stereo Camera Calibration

Switching to a short-baseline parallel-stereo configuration enhanced the reliability and functionality of the pilot assist, as discussed in Chapter 6. However, obtaining reliable range measurements from the short-baseline configuration requires a careful geometric calibration. The current calibration procedure is labor intensive, requiring several manual steps. Because recalibration should fol-

low any maintenance action that affects the camera mounts, a simpler procedure is required for field operations. Two possible strategies for simplifying the stereo calibration procedure include (1) the construction of a dedicated stereo camera mount, which automatically enforces a precalibrated camera geometry, or (2) the creation of a software calibration tool that automates the calibration procedure given an appropriate set of input images.

#### 8.2.4 Smooth Transfer to Shared Control

The current low-frequency control term enables smooth transfer of the bias offset during transitions from human pilot control to computer-only control. This type of transition, which nulls human pilot commands at system initialization, does not match pilot expectations, as the pilots desire to maintain some manual control capability at all times during the tracking run. Thus a system modification is required to permit transition between human pilot control and shared human-computer control. A problem with this type of shared-control transition arises with the current control system in the presence of large quasi-steady bias forces on the ROV. In this case, the low-frequency control term and the human pilot may both attempt to offset the environmental disturbance. This double compensation may lead to target loss (see Figure 6.8). The key to avoiding double compensation involves interpreting the human pilot command and phasing in the low-frequency control term only as the human pilot eases off the control stick.

---

### 8.3 Topics for Future Research

A number of new research directions have arisen as part of this dissertation effort. This section groups new research topics into three technical areas: vision, control, and biology application.

#### 8.3.1 Vision

Chapter 4 presented research to enable vision-based tracking of gelatinous animals. This work involved both the development of a general design technique for visual tracking in unstructured, natural environments and the application of this technique to the jellyfish-tracking task. Future research opportunities exist to extend both of these contributions: to evaluate the general design strategy for other vision applications and to extend the jelly-tracking vision-processing strategy to extreme conditions and to long-duration AUV applications.



**Extension of the Segmentation Efficiency Design Concept**

The new visual-tracking design strategy, called segmentation efficiency design, was developed with a particular application in mind. Additional insight into the utility of this method would be gained by applying it to new applications.

Further research, moreover, could extend the basic segmentation design strategy to address a wider range of visual tracking applications. The design strategy presented in this dissertation focused on high sample-rate applications. As such, the strategy emphasized segmentation efficiency over recognition quality, under the assumption that recognition features, such as prior target location, are always available for high sample-rate applications. Additional research could provide a recognition efficiency metric, parallel to the segmentation efficiency metric, that would extend the new design strategy to lower sample-rate applications. Unlike segmentation efficiency, however, this new recognition efficiency will depend strongly on sample period, since most recognition features vary weakly over time. The nondimensionalized sample period, or recognition number, as introduced in Chapter 4 may thus play an important role in the future derivation of a recognition efficiency.

Further research could also generalize the segmentation efficiency concept to higher dimensional spaces. The current segmentation efficiency technique queries each processing filter and topology to determine the pair that best distinguishes target and background pixels. A higher dimensional metric, based on machine learning techniques, could extend the analysis to handle groups of filters applied simultaneously to identify targets in extremely noisy environments.

**Recognition Improvements for Hotspots and for Long Duration Tracking**

The analysis of Chapter 4.4.1 described the limitations of the recognition technique used in the jelly-tracking system. These limitations lie in the recognition assumptions of low animal density and high sample rate sensing. Further research is required to make the jelly-tracking system robust to situations in which these assumptions do not hold.

The ROV-based jelly-tracking system uses a high sample rate ( $> 10$  Hz) to image a solitary swimming animal. For certain types of experiment, however, the ROV-based system may be used to track a specimen through a biologically active hotspot. In such regions, the high frequency of animal appearance severely degrades the expected tracking duration. Experimental results confirm this limitation. During the 10/11/2002 dive, several experiments attempted to track a *Solmissus* medusa through a hotspot consisting of a large squid population feeding on an abundance of

krill (Chapter 6.4.1). Several instances of partial target occlusion by squid resulted in system failure, reducing the day's average tracking duration to only 10 minutes.

In addition to enabling hotspot observation tasks, an improved recognition strategy is necessary to implement a low-sample rate AUV-based tracking algorithm. AUV based tracking would be used to extend practical tracking times from a few hours, for ROVs, to 24 hours in duration. In order to meet the energy-budget constraints of long-duration AUV tracking, Chapter 7 proposes an illumination strategy based on low-rate visual sampling ( $< 1$  Hz). Low sample rate and long run duration combine to make reliable recognition a difficult challenge. Figure 4.10 indicates the severe impact of these two factors, combined, on the likelihood of mission success. Whereas the figure indicates an 85% chance of successfully completing a 1.5 hour tracking run for the ROV-based system, the figure indicates only a 0.25% of successfully completing a longer 24 hour tracking run given a slower sampling AUV-based system.

### **Automated Target Acquisition for AUV Tracking**

The ROV-based system relies on initialization by a human pilot. Although an AUV-based tracking system could be launched by an ROV to permit human initialization, further research might also provide new techniques to enable fully automated target acquisition and tracking. From a vision-processing viewpoint, this task requires three new technologies: (1) event detection, (2) target classification, and (3) stabilization in the absence of a vision profile. The event detection capability would involve the detection of possible animal targets from midwater video, cluttered with marine snow and marked by nonuniform illumination. Next, subsequent to detecting a specimen, an automated target acquisition routine would need to classify the target to assess its potential utility as a subject for long duration biological observation.

Finally, an alternative positioning capability is required to support classification. During this classification period, no target profile would be available; without a profile, the visual-tracking algorithm described in this dissertation cannot be initialized. A possible alternative positioning approach involves water-relative position rather than animal-relative positioning. A doppler velocity log (DVL) could be used to acquire this measurement; alternatively, a vision-based tracking technique could be employed calculating a 3D position relative to a moving field of marine snow. In either case, it seems likely that water-based positioning could enable effective tracking during this brief classification and training phase.

### 8.3.2 Control for Low Sample-Rate AUV Tracking

Implementing a control law for AUV-based jelly tracking introduces several new research challenges. These challenges involve control law stability for low-rate sampling, incorporation of low-rate control performance into the AUV energy budget and adaptation of control parameters based on available target information in order to further optimize AUV-energy consumption. The null space thrust map might also be refined to effect further reductions in mechanical disturbances on the tracked target.

#### **Stability for Low Sample Rate Tracking**

Assuming vision sensing at 1 Hz, the sensor sample rate would fall below the Nyquist limit based on the vehicle bandwidth. To achieve stable tracking at this low sample rate would require improved system modeling and/or a new sensor fusion strategy. Better predictive models of AUV motion and of the motion of a target animal would enable improved open-loop maneuvering between vision samples. These vision samples would then serve more to correct an open-loop model than to provide a continuous control signal. Alternatively, dead reckoning sensors, such as acoustic water velocity sensors, compass, depth, or inertial sensors, could be fused with the vision sensor to help provide a smooth, higher rate positioning updates. Of course the power required by these sensors would further factor into the overall system design.

#### **Incorporation of Low Sample Rate into the AUV Actuator Energy Budget**

The energy budget analysis of Chapter 7 made a “perfect tracking” assumption. Drift errors, especially given low-rate visual sampling, could add significantly to the unsteady actuation energy budget. If these actuation energy costs are sufficiently large, the balance between accurate tracking, with lower actuation energy costs, and low-rate sampling, with lower illumination energy costs, provides an opportunity for system optimization.

#### **Adaptive-Parameter Control Using Measurements of Animal Behavior or Morphology**

Chapter 2.6.5 discussed the potential to predict animal behavior based on morphology. Animals of different fineness ratio (length over width), for example, tend to behave differently. Prolate (long) animals tend to pulse infrequently but accelerate rapidly when they do pulse. Oblate (wide) animals tend to pulse continuously but move with slower steady velocity. In this sense, predicted ani-

mal behaviors, based on visual measurements, might be used to adapt control parameters for optimal energy efficiency.

### **Exploiting Nonlinear Dynamics in Designing the Null-Space Thruster Map**

The thruster map of Chapter 5.3.1 did not explicitly take into account the relative angles between the camera sensor and the vehicle actuators. Rather the thruster map was designed to minimize the total actuator output in a global sense. In operational jelly-tracking, however, the riskiest thruster outputs are those pointed directly toward the target animal. Thus the thruster map could be dynamically reconfigured to preferentially use those thrusters pointed away from the target animal. In addition to the linear null space described in Chapter 5.3.1, this dynamically reconfigured thruster map could leverage the nonlinear accelerations associated with the cylindrical dynamic equation for the tracking vehicle (5.18). Specifically, the centripetal acceleration term can be used to increase range through lateral thruster actuation, without requiring any radial thrust toward the target. Such a control law may be achieved by writing a feedback linearization of (5.18) assuming a zero actuation component in the radial direction. In generating these equations, the lateral control input automatically enters the radial dynamic equation through the centripetal acceleration term. Ultimately, the use of a dynamically reconfigured thruster map could further reduce mechanical disturbances on the animal target; alternatively, the dynamic map might also permit tracking at closer ranges to the target, further reducing the energy costs associated with lighting, as discussed in Chapter 7.

### **8.3.3 Biology Applications**

The motivation for the jelly-tracking robot roots, at the deepest level, in a biological application. The most important future research to extend from this dissertation will be the application of the tracking system to collect biology data. Validating the jelly light-response model provides an opportunity for further biology research.

#### **Collection of Biology Data Using Automated Jelly-Tracking Methods**

Automated jelly-tracking technologies have been designed to enable new experiments in behavioral biology. Chapter 6.4.2 offers an experimental demonstration of the capabilities of an ROV-based jelly-tracking system to obtain never-before-acquired quantitative measurements for jelly-

motion studies. This potential will be fully realized by future experimental biology that exploits the new jelly-tracking technologies.

### **Effects of Strobed Illumination**

Chapter 7 used a light response model for *Polyorchis penicillatus* to advance two hypotheses related to strobed illumination. The first hypothesis held that the strobed illumination pattern, proposed for a low-energy AUV application, would not trigger artificial reflex behaviors in photosensitive medusa. The second hypothesis held that strobed illumination might actually provide better quality behavioral data, as strobed lighting, unlike continuous lighting, would permit the specimen to respond to low-level natural ambient light. Further experimental investigations will be necessary to validate the light-response model for other animal species and to verify the two hypotheses based on the model.

---

## **8.4 Summary**

This dissertation has introduced and experimentally validated new technologies to enable automated robotic tracking of deep-ocean jellyfish. These technologies will serve as a springboard for exciting new research opportunities, both of an engineering nature, in the development of improved visual recognition and control technologies to enable 24-hour duration AUV-based tracking, and of a biological nature, in the application of ROV-based and, in the future, AUV-based jelly tracking technologies to make new discoveries about the ecology and behaviors of deep-ocean gelatinous zooplankters.



## Appendix A: ROV Parameters

Two days of the 12-day *Ventana* dive series focused on parameter identification (Chapter 6.1.1). These dives collected step-response data for each of the four axes of ROV motion. Measurements were taken using a correlation-based vision system for benthic (ocean-floor) positioning [107,118]. The disturbance environment was unknown. The dominant disturbance consisted of a strong current moving across the ocean floor. To counteract current and tether disturbances, automatic control was applied on all axes orthogonal to the step-response axis.

Table A.1 summarizes parameter identification results. The assumed form for ROV dynamics was that of an axis-independent inertial mass subject to linear drag.

$${}^b\ddot{p}_v + \tilde{b}\dot{p}_v = \tilde{f}u \quad (\text{A.1})$$

Here the state vector,  ${}^b p_v$ , describes the translation and yaw rotation of the vehicle,  $v$ , relative to the benthic surface,  $b$ . The damping and force-scaling matrices,  $\tilde{b}$  and  $\tilde{f}$ , are assumed diagonal. The control input,  $u$ , is taken to be a floating-point value on a scale of -5 to +5.

Identified Parameters	x-axis (fore/aft)	y-axis (lateral)	z-axis (vertical)	psi-axis (yaw)
$\tilde{f}$	0.024 m/s <sup>2</sup>	0.024 m/s <sup>2</sup>	0.054 m/s <sup>2</sup>	0.016 rad/s <sup>2</sup>
$\tilde{b}$	0.20 1/s	0.24 1/s	0.38 1/s	0.27 1/s
Typical Control Params				
$k_p$	20 1/m	20 1/m	10 1/m	20 (unitless)
$k_d$	10 s/m	10 s/m	5 s/m	10 s
Effective Bandwidth				
$\omega_n$	0.69 rad/s	0.69 rad/s	0.73 rad/s	0.56 rad/s
$f_n$	0.11 Hz	0.11 Hz	0.12 Hz	0.09 Hz

TABLE A.1. Approximate Parameter Values for *Ventana*





## Appendix B: Code Structure

The complete code listing for the jelly-tracking software package is archived with the Aerospace Robotics Lab on the Sun-Valley server (in /apps/arl/cvsroot/MBARI/PrecControl/sensor7). The following table maps sections of this thesis to objects within the C++ project, to provide a rough guide to the layout of the jelly-tracking software.

	Functionality	Thesis Chapter	Sensor7 Code Object::Method
Main Thread	--	--	CAVPEngineThread
Data Logging	--	--	CDataLoggerThread
Vision	Segmentation	Chapter 4.3.3	CStackOut::NextStack
	Recognition Statistics	Chapter 4.3.4	CStackOut::NextList
	Identification of Best Match and Declaration of False-Positives	Chapter 4.3.4	CStackOut::NextMatch
Control	Frame Transformations	Chapter 5.2.2 & Chapter 5.3.1	CGlobalDisplacement::Execute
	Error Formation	Chapter 5.2.2	CErrorCalculation::CalcJellyError
	Control Law	Chapter 5.5	CController::Execute
	Application of Thrust Map	Chapter 5.3	CErrorCalculation::CalcJellyError
	Activation of Boundary	Chapter 5.4.3	CJellyDisp::ProcessMatchData
	Disturbance-Accommodation Estimator	Chapter 5.4.3	CGlobalDisplacement::DecoupledAxisCorrector AND CGlobalDisplacement::DecoupledAxisPredictor
	Disturbance-Accommodation Control	Chapter 5.4.3	CController::Execute

**TABLE B.1. Approximate Parameter Values for *Ventana***



---

## Bibliography

---

### C.1 Introduction and Background

- [1] A.R. Conway. *Autonomous Control of an Unstable Model Helicopter Using Carrier Phase GPS Only*. PhD thesis, Stanford University, Stanford, CA 94305, 1995. Also published as SUDAAR 664.
- [2] S.A. Earle. *Sea Change: A Message of the Oceans*. Ballantine Books, 1995.
- [3] R. Ellis. *Deep Atlantic: Life, Death and Exploration in the Abyss*. The Lyons Press, 1996.
- [4] B.C. Monger, S. Chinniah-Chandy, E. Meir, S. Billings, C.H. Greene, and P.H. Wiebe. Sound scattering by the gelatinous zooplankters *Aequorea victoria* and *Pleurobrachia bachei*. *Deep-Sea Research II*, 45:1255-1271, 1998.
- [5] E. Mutlu. Target strength of the common jellyfish (*Aurelia aurita*): a preliminary experimental study with a dual-beam acoustic system. *ICES Journal of Marine Science*, 53:309-311, 1996.
- [6] J. Rife and S. Rock. A pilot aid for ROV-based tracking of gelatinous animals in the midwater. In *Proceedings of the 2001 OCEANS Conference*, 2:1137-1144, 2001. IEEE/MTS.
- [7] B.H. Robison. Midwater research methods with MBARI's ROV. *Marine Technology Society Journal*, 26(4):32-39, 1992.
- [8] B. Robison. The coevolution of undersea vehicles and deep-sea research. *MTS Journal*, 33(4):65-73, 1999.
- [9] *ROV Ventana*. Retrieved July 30, 2003 from the Monterey Bay Aquarium Research Institute (MBARI) web site: <http://www.mbari.org/dmo/ventana/ventana.html>.

## C.2 Biology

---

- [10] A.L. Alldredge. Discarded appendicularian houses as sources of food, surface habitats, and particulate organic matter in planktonic environments. *Limnology and Oceanography*, 21(1):14-23, 1976.
- [11] P.A.V. Anderson and G.O. Mackie. Electrically coupled, photosensitive neurons control swimming in a jellyfish. *Science*, 197(4299):186-188, 1977.
- [12] M.N. Arai. Behaviour of planktonic coelenterates in temperature and salinity discontinuity layers. In G.O. Mackie, editor, *Coelenterate Ecology and Behavior*, pages 211-218. Plenum Press, 1976.
- [13] M.N. Arai. Attraction of Aurelia and Aequorea to prey. *Hydrobiologia*, 216/217:363-366, 1991.
- [14] S.A. Arkett. The shadow response of a hydromedusan (*Polyorchis penicillatus*): behavioral mechanisms controlling diel and ontogenic vertical migration. *Biological Bulletin*, 169:297-312, 1985.
- [15] S.A. Arkett and A.N. Spencer. Neuronal mechanisms of a hydromedusan shadow reflex: I. Identified reflex components and sequence of events. *Journal of Comparative Physiology A*, 159:201-213, 1986.
- [16] S.A. Arkett and A.N. Spencer. Neuronal mechanisms of a hydromedusan shadow reflex: II. Graded response of reflex components, possible mechanisms of photic integration and functional significance. *Journal of Comparative Physiology A*, 159:215-225, 1986.
- [17] K.M. Bailey and R.S. Batty. A laboratory study of predation by Aurelia aurita on larval herring (*Clupea harengus*): experimental observations compared with model predictions. *Marine Biology*, 72:295-301, 1983.
- [18] U. Bathmann, M.H. Bundy, M.E. Clarke, T.J. Cowles, K. Daly, H.G. Dam, M.M. Dekshe-nieks, P.L. Donaghay, D.M. Gibson, D.J. Gifford, B.W. Hansen, D.K. Hartline, E.J.H. Head, E.E. Hofmann, R.R. Hopcroft, R.A. Jahnke, S.H. Jonasdottir, T. Koirboe, G.S. Kleppel, J.M. Klinck, P.M. Kremer, M.R. Landry, R.F. Lee, P.H. Lenz, L.P. Madin, D.T. Manahan, M.G. Mazzocchi, D.J. McGillicuddy, C.B. Miller, J.R. Nelson, T.R. Osborn, G.-A. Paffen-hofer, R.E. Pieper, I. Prusova, M.R. Roman, S. Schiel, H.E. Seim, S.L. Smith, J.J. Torres, P.G. Verity, S.G. Wakeham, and K.F. Wishner. Future marine zooplankton research: A per-spective. *Marine Ecology Progress Series*, 222:297-308, 2001.

- [19] A. Benovic. Diurnal vertical migration of *Solmisus albescens* (Hydromedusae) in the southern Adriatic. *Marine Biology*, 18:298-301, 1973.
- [20] Q. Bone and G.O. Mackie. Urochordata. In G.A.B. Sheldon, editor, *Electrical Conduction and Behaviour in 'Simple' Invertebrates*, pages 473-535. Oxford University Press, 1982.
- [21] R.D. Brodeur, C.E. Mills, J.E. Overland, G.E. Walters, and J.D. Schumacher. Evidence for a substantial increase in gelatinous zooplankton in the Bering Sea, with possible links to climate change. *Fisheries Oceanography*, 8(4):296-306, 1999.
- [22] D.M. Chapman. Cnidarian histology. In L. Muscatine and H.M. Lenhoff, editors, *Coelenterate Biology*, pages 2-92. Academic Press, 1974.
- [23] M.M. Coates and S.H. Thompson. Vision in a cubozoan jellyfish. *American Zoologist*, 40(6):977, 2000.
- [24] M.M. Coates. Personal Communication. Stanford, 2003.
- [25] S.P. Colin and J.H. Costello. Morphology, swimming performance and propulsive mode of six co-occurring hydromedusae. *The Journal of Experimental Biology*, 205:427-437, 2002.
- [26] J.H. Costello and S.P. Colin. Morphology, fluid motion and predation by the scyphomedusa *Aurelia aurita*. *Marine Biology*, 121:327-334, 1994.
- [27] J.H. Costello and S.P. Colin. Flow and feeding by swimming scyphomedusae. *Marine Biology*, 124:399-406, 1995.
- [28] J.H. Costello, E. Klos and M. Ford. In situ time budgets of the scyphomedusae *Aurelia aurita*, *Cyanea* sp., and *Chrysaora quinquecirrha*. *Journal of Plankton Research*, 20:383-391, 1998.
- [29] T.L. Daniel. Mechanics and energetics of medusan jet propulsion. *Canadian Journal of Zoology*, 61:1406-1420, 1983.
- [30] T.L. Daniel. Cost of locomotion: unsteady medusan swimming. *Journal of Experimental Biology*, 119:149-164, 1985.
- [31] T.L. Daniel. Invertebrate swimming: integrating internal and external mechanics. In C.P. Ellington and T.J. Pedley, editors, *Biological Fluid Dynamics, Symposia of the Society for Experimental Biomechanics*, 49:61-89, 1995.
- [32] M.E. DeMont and J.M. Gosline. Mechanics of jet propulsion in the hydromedusan jellyfish, *Polyorchis penicillatus*, I. mechanical properties of the locomotor structure. *Journal of Experimental Biology*, 134:313-332, 1988.

- [33] M.E. DeMont and J.M. Gosline. Mechanics of jet propulsion in the hydromedusan jellyfish, *Polyorchis penicillatus*, II. energetics of the jet cycle. *Journal of Experimental Biology*, 134:333-345, 1988.
- [34] M.E. DeMont and J.M. Gosline. Mechanics of jet propulsion in the hydromedusan jellyfish, *Polyorchis penicillatus*, III. a natural resonant bell; the presence and importance of a resonant phenomenon in the locomotor structure. *Journal of Experimental Biology*, 134:347-361, 1988.
- [35] S. Donaldson, G.O. Mackie and A. Roberts. Preliminary observations on escape swimming and giant neurons in *Aglantha digitale* (Hydromedusae: Trachylina). *Canadian Journal of Zoology*, 58:549-552, 1980.
- [36] M.D. Ford, J.H. Costello, K.B. Heidelberg and J.E. Purcell. Swimming and feeding by the scyphomedusa *Chrysaora quinquecirrha*. *Marine Biology*, 129:355-362, 1997.
- [37] W.B. Gladfelter. *Swimming in Medusae (Cnidaria: Hydrozoa and Scyphozoa): A Study in Functional Morphology and Behavior*. PhD thesis, Stanford University, Stanford, CA 94305, 1970.
- [38] W.M. Graham, F. Pagès and W.M. Hamner. A physical context for gelatinous zooplankton aggregations: a review. *Hydrobiologia*, 451:199-212, 2001.
- [39] W.M. Hamner, L.P. Madin, A.L. Alldredge, R.W. Gilmer, and P.P. Hamner. Underwater observations of gelatinous zooplankton: Sampling problems, feeding biology, and behavior. *Limnology and Oceanography*, 20(6):907-917, 1975.
- [40] W.M. Hamner and I.R. Hauri. Long-distance horizontal migrations of zooplankton (Scyphomedusae: Mastigias). *Limnology and Oceanography*, 26(3):414-423, 1981.
- [41] W.M. Hamner. The importance of ethology for investigations of marine zooplankton. *Bulletin of Marine Science*, 37(2):414-424, 1985.
- [42] W.M. Hamner, S.W. Strand, G.I. Matsumoto, and P.P. Hamner. Ethological observations on foraging behavior of the ctenophore *leucothea*-sp. in the open sea. *Limnology and Oceanography*, 32(3):645-652, 1987.
- [43] W.M. Hamner. Behavior of plankton and patch formation in pelagic ecosystems. *Bulletin of Marine Science*, 43(3):752-757, 1988.
- [44] W.M. Hamner and B.H. Robison. In situ observations of giant appendicularians in Monterey Bay [California, USA]. *Deep-Sea Research, Part I*, 39(7/8):1299-1313, 1992.

- [45] W.M. Hamner, M.S. Jones, and P.P. Hamner. Swimming, feeding, circulation and vision in the Australian box jellyfish, *Chiroaex fleckeri* (cnidaria, cubozoa). *Marine and Freshwater Research*, 46:985-990, 1995.
- [46] W.M. Hamner. Predation, cover, and convergent evolution in epipelagic oceans. In P.H. Lenz, D.K. Hartline, J.E. Purcell, and D.L. Macmillan, editors, *Zooplankton: Sensory Ecology and Physiology*, pages 17-36. Gordon and Breach, 1996.
- [47] W.M. Hamner. Sensory ecology of scyphomedusae. In P.H. Lenz, D.K. Hartline, J.E. Purcell, and D.L. Macmillan, editors, *Zooplankton: Sensory Ecology and Physiology*, pages 475-492. Gordon and Breach, 1996.
- [48] J. F. Haney. Diel patterns of zooplankton behavior. *Bulletin of Marine Science*, 43(3):583-603, 1988.
- [49] R.R. Hopcroft and B.H. Robison. A new mesopelagic larvacean, *Mesochordaeus erythrocephalus*, sp nov., from Monterey Bay, with a description of its filtering house. *Journal of Plankton Research*, 21(10):1923-1937, 1999.
- [50] G.A. Horridge. Statocysts of medusae and evolution of stereocilia. *Tissue and Cell*, 1(2):341-353, 1969.
- [51] L.H. Hyman. *Phylum Cnidaria*. In *The invertebrates: Protozoa through Ctenophora. Vol.1*, pages 365-661. McGraw-Hill, 1940.
- [52] S. Johnsen and E. Widder. The physical basis of transparency in biological tissue: ultrastructure and minimization of light scattering. *Theoretical Biology*, 199:181-198, 1999.
- [53] S. Johnsen and E. Widder. Ultraviolet absorption in transparent zooplankton and its implications for depth distribution and visual predation. *Marine Biology*, 138:717-730, 2001.
- [54] K. Kanatani. *Geometric Computation for Machine Vision*. Clarendon, 1993.
- [55] R.J. Larson. Costs of transport for the scyphomedusa *Stomolophus meleagris* L. Agassiz. *Canadian Journal of Zoology*, 65:2690-2695, 1987.
- [56] R.J. Larson, C.E. Mills, and G.R. Harbison. In situ foraging and feeding-behavior of narcomedusae (cnidaria, hydrozoa). *Journal of the Marine Biological Association of the United Kingdom*, 69:785-794, 1989.
- [57] R.J. Larson, C.E. Mills, and G.R. Harbison. Western Atlantic midwater hydrozoan and scyphozoan medusae: in situ studies using manned submersibles. *Hydrobiologia*, 216/217:311-317, 1991.

- [58] G.O. Mackie. Locomotion, flotation, and dispersal. In L. Muscatine and H.M. Lenhoff, editors, *Coelenterate Biology*, pages 313-358. Academic Press, 1974.
- [59] G.O. Mackie and C.E. Mills. Use of the Pisces IV submersible for zooplankton studies in coastal waters of British Columbia. *Canadian Journal of Fisheries and Aquatic Sciences*, 40:763-776, 1983.
- [60] G.O. Mackie. Defensive strategies in planktonic coelenterates. In P.H. Lenz, D.K. Hartline, J.E. Purcell, and D.L. Macmillan, editors, *Zooplankton: Sensory Ecology and Physiology*, pages 435-446. Gordon and Breach, 1996.
- [61] L.P. Madin. Feeding behavior of tentaculate predators: in situ observations and a conceptual model. *Bulletin of Marine Science*, 43(3):413-429, 1988.
- [62] J.B. Marliave and C. E. Mills. Piggyback riding by pandalid shrimp larvae on hydromedusae. *Canadian Journal of Zoology*, 71:257-263, 1993.
- [63] V.J. Martin. Photoreceptors of cnidarians. *Canadian Journal of Zoology*, 80:1703-1722, 2002.
- [64] G.I. Matsumoto and W.M. Hamner. Modes of water manipulation by the lobate ctenophore *Leucothea* sp. *Marine Biology*, 97:551-558, 1988.
- [65] G.I. Matsumoto, K.A. Raskoff, and D.J. Lindsay. *Tiburonia granrojo* n. sp., a mesopelagic scyphomedusa from the Pacific Ocean representing the type of a new subfamily (Class: Scyphozoa: order Semaestomeae: family Ulmaridae: subfamily Tiburoniinae subfam. nov.). *Marine Biology*, 143:73-77, 2003.
- [66] P.A. Meglitsch and F.R. Schram. *Invertebrate Zoology*. Oxford University Press, 1991.
- [67] C.E. Mills. Regulation of buoyancy in hydromedusae. *American Zoologist*, 20:820, 1980.
- [68] C.E. Mills. Diversity of swimming behaviors in hydromedusae as related to feeding and utilization of space. *Marine Biology*, 64:185-189, 1981.
- [69] C.E. Mills. Vertical migration and diel activity patterns of hydromedusae: studies in a large tank. *Journal of Plankton Research*, 5:619-635, 1983.
- [70] C.E. Mills. Density is altered in hydromedusae and ctenophores in response to changes in salinity. *Biological Bulletin*, 166(1):206-215, 1984.
- [71] C.E. Mills and R.G. Vogt. Evidence that ion regulation in hydromedusae and ctenophores does not facilitate vertical migration. *Biological Bulletin* 166(1):216-227, 1984.



- [72] C.E. Mills and J. Goy. In situ observations of the behavior of mesopelagic *Solmissus narcomedusae* (Cnidaria, Hydrozoa). *Bulletin of Marine Science*, 43(3):739-751, 1988.
- [73] C.E. Mills. Medusae, siphonophores, and ctenophores as planktivorous predators in changing global ecosystems. *ICES Journal of Marine Science*, 52:575-581, 1995.
- [74] L. Murbach. Some light reactions of the medusa *Gonionemus*. *Biological Bulletin*, 17: 354-368, 1909.
- [75] K. Ohtsu and M. Yoshida. Electrical activities of the anthomedusan, *Spirocodon saltatrix* (Tilesius). *Biological Bulletin*, 145:532-547, 1973.
- [76] L.M. Passano. Scyphozoa and Cubozoa. In G.A.B. Sheldon, editor, *Electrical Conduction and Behaviour in 'Simple' Invertebrates*, pages 149-202. Oxford University Press, 1982.
- [77] H.J. Price, G.A. Paffenhofer, C.M. Boyd, T.J. Cowles, P.L. Donaghay, W.M. Hamner, W. Lampert, L.B. Quetin, R.M. Ross, and J.R. Strickler. Future studies of zooplankton behavior: questions and technological developments. *Bulletin of Marine Science*, 43(3):853-872, 1988.
- [78] J.E. Purcell and M.N. Arai. Interactions of pelagic cnidarians and ctenophores with fish: a review. *Hydrobiologia*, 451:27-44, 2001.
- [79] G.H. Pyke, H.R. Pulliam and E.L. Charnov. Optimal foraging: a selective review of theory and tests. *The Quarterly Review of Biology*, 52(2):137-154, 1977.
- [80] B.H. Robison, K.R. Reisenbichler, R.E. Sherlock, J.M.B. Silguero, and F.P. Chavez. Seasonal abundance of the siphonophore, *Nanomia bijuga*, in Monterey Bay. *Deep-Sea Research, Part II*, 45:1741-1751, 1998.
- [81] Q. Schuyler and B.K. Sullivan. Light responses and diel migration of the scyphomedusa *Chrysaora quinquecirrha* in mesocosms. *Journal of Plankton Research*, 19(10):1417-1428, 1997.
- [82] R.E. Sherlock and B.H. Robison. Personal Communication. MBARI, 2000-2002
- [83] J.M.B. Silguero and B.H. Robison. Seasonal abundance and vertical distribution of mesopelagic calycophoran siphonophores in Monterey Bay, CA. *Journal of Plankton Research*, 22(6):1139-1153, 2000.
- [84] C.L. Singla. Ocelli of Hydromedusae. *Cell Tissue Research*, 149:413-429, 1974.
- [85] C.L. Singla. Statocysts of Hydromedusae. *Cell Tissue Research*, 158:391-407, 1975.

- [86] A.N. Spencer and W.E. Schwab. Hydrozoa. In G.A.B. Sheldon, editor, *Electrical Conduction and Behaviour in 'Simple' Invertebrates*, pages 73-148. Oxford University Press, 1982.
- [87] A.N. Spencer and S.A. Arkett. Radial symmetry and the organization of central neurons in a hydrozoan jellyfish [*Polyorchis penicillatus*]. *Journal of Experimental Biology*, 110:69-90, 1984.
- [88] S.W. Strand and W.M. Hamner. Predatory behavior of *Phacellophora-camtschatica* and size-selection predation upon *Aurelia-aurita* (scyphozoa, cnidaria) in Saanich Inlet, British Columbia. *Marine Biology*, 99:409-414, 1988.
- [89] S.L. Tamm. Ctenophora. In G.A.B. Sheldon, editor, *Electrical Conduction and Behaviour in 'Simple' Invertebrates*, pages 266-358. Oxford University Press, 1982.
- [90] E. Widder. Personal Communication. HBOI, 2002
- [91] C. Weber. Electrical activities of a type of electroretinogram recorded from the ocellus of a jellyfish, *Polyorchis penicillatus* (Hydromedusae). *Journal of Experimental Zoology*, 223:231-243, 1982.
- [92] C. Weber. Electrical activity in response to light of the ocellus of the hydromedusan, *Sarsia tubulosa*. *Biological Bulletin*, 162:413-422, 1982.
- [93] D. Wright and J.E. Purcell. Effect of salinity on ionic shifts in mesohaline scyphomedusae, *Chrysaora quinquecirrha*. *Biological Bulletin*, 192:332-339, 1997.
- [94] D. Wrobel and C. Mills. *Pacific Coast Pelagic Invertebrates: A Guide to the Common Gelatinous Animals*. Monterey Bay Aquarium, 1998.

---

### C.3 Image Processing and Visual Servoing

- [95] O. Amidi, T. Kanade, and R. Miller. Vision-based autonomous helicopter research at Carnegie Mellon Robotics Institute (1991-1998). In M. Vincze and G.D. Hager, editors, *Robust Vision for Vision-Based Control of Motion*, pages 221-232. SPIE Optical Engineering/IEEE Press, 2000.
- [96] P.H. Batavia, D.A. Pomerleau, and C.E. Thorpe. Overtaking Vehicle Detection Using Implicit Optical Flow. In *Proceedings of the IEEE Transportation Systems Conference*, pages 729-734, 1997.

- [97] K.W. Bowyer and J.P. Phillips. Overview of work in empirical evaluation of computer vision algorithms. In K.W. Bowyer and J.P. Phillips, editors, *Empirical Evaluation Techniques in Computer Vision*. IEEE Computer Press, 1998.
- [98] K.W. Bowyer. Experiences with empirical evaluation of computer vision algorithms. In R. Klette, H.S. Stiehl, M.A. Viergever, and K.L. Vincken, editors, *Performance Characterization in Computer Vision*. Kluwer Academic Publishers, 2000.
- [99] W.E. Boyce and R.C. DiPrima. *Elementary Differential Equations and Boundary Value Problems*. Wiley, 2001.
- [100] C.K. Chow and T. Kaneko. Automatic boundary detection of the left ventricle from cineangiograms. *Computers and Biomedical Research*, 5:388-410, 1972.
- [101] P.I. Corke and S.A. Hutchinson. Real-time vision, tracking and control. In *Proceedings of the International Conference on Robotics and Automation*, pages 622-623, 2000. IEEE.
- [102] P. Courtney and N.A. Thacker. Performance characterization in computer vision: the role of statistics in testing and design. In J. Blanc-Talon and D.C. Popescu, editors, *Imaging and Vision Systems: Theory, Assessment and Applications*, pages 109-128. Nova Science Publishers, Inc., 2001.
- [103] S. Dougherty and K.W. Bowyer. Objective evaluation of edge detectors using a formally defined framework. In K.W. Bowyer and J.P. Phillips, editors, *Empirical Evaluation Techniques in Computer Vision*. IEEE Computer Press, 1998.
- [104] Ç.E. Erdem and B. Sankur. Performance evaluation metrics for object-based video segmentation. In *Proceedings of the 10th European Signal Processing Conference*, 2:917-920, 2000.
- [105] Y. Fan and A. Balasuriya. Autonomous target tracking by AUVs using dynamic vision. In *Proceedings of the 2000 International Symposium on Underwater Technology*, pages 187-192, 2000.
- [106] S.D. Fleischer, S.M. Rock, and R. Burton. Global position determination and vehicle path estimation from a vision sensor for real-time video mosaicking and navigation. In *Proceedings of the OCEANS 1997 Conference*, 1:641-647, 1997. IEEE/MTS.
- [107] S.D. Fleischer. *Bounded-Error Vision-Based Navigation of Autonomous Underwater Vehicles*. PhD thesis, Stanford University, Stanford, CA 94305, 2000. Also published as SUDAAR 728.

- [108] R. Garcia, J. Batlle, and X. Cufi. A system to evaluate the accuracy of a visual mosaicking methodology. In *Proceedings of the OCEANS 2001 Conference*, 4:2570-2576, 2001. IEEE/MTS.
- [109] R.C. Gonzalez and R.E. Woods. *Digital Image Processing*. Addison-Wesley Publishing Company, Inc., 1993.
- [110] N. Gracias and J. Santos-Victor. Underwater mosaicking and trajectory reconstruction using global alignment. In *Proceedings of the OCEANS 2001 Conference*, 4:2557-2563, 2001. IEEE/MTS.
- [111] A. Huster, S.D. Fleischer, and S.M. Rock. Demonstration of a vision-based dead-reckoning system for navigation of an underwater vehicle. In *Proceedings of the 1998 World Conference on Autonomous Underwater Vehicles*, pages 185-189, 1998.
- [112] D. Kocak, N. da Vitoria Lobo, and E. Widder. Computer vision techniques for quantifying, tracking, and identifying bioluminescent plankton. *IEEE Journal of Oceanic Engineering*, 24(1):81-95, 1999.
- [113] E. Kristof, A. Chandler, and W.M. Hamner. 3-D as an underwater tool. In *Proceedings of the OCEANS 1988 Conference*, pages 713-718, 1988. IEEE.
- [114] M.B. Leahy, V.W. Milholen, and R. Shipman. Robotic aircraft refueling: a concept demonstration. In *Proceedings of the 1990 Aerospace and Electronics Conference*, 3:1145-1150, 1990.
- [115] J.-F. Lots, D.M. Lane, and E. Trucco. Application of a 2 ½ D visual servoing to underwater vehicle station-keeping. In *Proceedings of the OCEANS 2000 Conference*, 2:1257-1264, 2000. IEEE/MTS.
- [116] J.-F. Lots, D.M. Lane, E. Trucco, and F. Chaumette. A 2D visual servoing for underwater vehicle station keeping. In *Proceedings of the International Conference on Robotics and Automation*, 3:2773-2778, 2001. IEEE.
- [117] R.L. Marks, H.H. Wang, M.J. Lee, and S.M. Rock. Automatic visual station keeping of an underwater robot. In *Proceedings of the OCEANS 1994 Conference*, 2:137-142, 1994. IEEE.
- [118] R.L. Marks. *Experiments in Visual Sensing for Automatic Control of an Underwater Robot*. PhD thesis, Stanford University, Stanford, CA 94305, 1995. Also published as SUDAAR 681.

- [119] M. Minami, J. Agbanhan, and T. Asakura. Manipulator visual servoing and tracking of fish using a genetic algorithm. *Industrial Robot*, 26(4):278-289, 1999.
- [120] S. Negahdaripour and P. Firoozfam. Positioning and photo-mosaicking with long image sequences; comparison of selected methods. In *Proceedings of the OCEANS 2001 Conference*, 4:2584-2592, 2001. IEEE/MTS.
- [121] S. Negahdaripour and Xun Xu. Mosaic-based positioning and improved motion-estimation methods for automatic navigation of submersible vehicles. *IEEE Journal of Oceanic Engineering*, 27(1):79-99, 2002.
- [122] A.M. Plotnik and S.M. Rock. Quantification of cyclic motion of marine animals from computer vision. In *Proceedings of the OCEANS 2002 Conference*, 3:1575-1581, 2002. IEEE/MTS.
- [123] J. Rife and S. Rock. Visual tracking of jellyfish *in situ*. In *Proceedings of the International Conference on Image Processing*, 1:289-292, 2001. IEEE.
- [124] C. Roman and H. Singh. Estimation of error in large area underwater photomosaics using vehicle navigation data. In *Proceedings of the OCEANS 2001 Conference*, 3:1849-1853, 2001. IEEE/MTS.
- [125] S. Samson, T. Hopkins, A. Remsen, L. Langebrake, T. Sutton, and J. Patten. A system for high-resolution zooplankton imaging. *IEEE Journal of Oceanic Engineering*, 26(4):671-676, 2001.
- [126] C. Silpa-Anan, T. Brinsmead, S. Abdallah and A. Zelinsky. Preliminary experiments in visual servo control for autonomous underwater vehicle. In *Proceedings of the International Conference on Intelligent Robots and Systems*, pages 1824-1829, 2001.
- [127] H. Singh, C. Roman, L. Whitcomb, and D. Yoerger. Advances in fusion of high resolution underwater optical and acoustic data. In *Proceedings of the 2000 International Symposium on Underwater Technology*, pages 206-211, 2000.
- [128] X. Tang and W.K. Stewart. Plankton image classification using novel parallel-training learning vector quantization network. In *Proceedings of the 1996 OCEANS Conference*, 3:1227-1236, 1996. IEEE/MTS.
- [129] X. Tang, W.K. Stewart, L. Vincent, H. Huang, M. Marra, S.M. Gallager and C.S. Davis. Automatic plankton image recognition. *Artificial Intelligence Review*, 12:177-199, 1998.

- [130] R.A. Tidd and J. Wilder. Fish detection and classification system. *Journal of Electronic Imaging*, 10(6):283-288, 2001.
- [131] S. van der Zwaan and J. Santos-Victor. Real-time vision-based station keeping for underwater robots. In *Proceedings of the OCEANS 2001 Conference*, 2:1058-1065, 2001. IEEE/MTS.
- [132] P. Villegas, X. Marichal and A. Salcedo. Objective evaluation of segmentation masks in video sequences. In *Proceedings of the 1999 Workshop on Image Analysis for Multimedia Interactive Services*, pages 85-88, 1999.
- [133] M. Vincze and G.D. Hager, Ed. *Robust Vision for Vision-Based Control of Motion*, SPIE Optical Engineering/IEEE Press, 2000.
- [134] L.B. Wolff. Applications of polarization camera technology. *IEEE Expert*, 10(5):30-38, 1995.
- [135] Y.J Zhang. A survey on evaluation methods for image segmentation. *Pattern Recognition*, 29(8):1335-1346, 1996.

---

## C.4 Control

- [136] G. Antonelli, F. Caccavale, S. Chiaverini, and L. Villani. An output feedback algorithm for position and attitude tracking control of underwater vehicles. In *Proceedings of the IEEE Conference on Decision and Control*, pages 4567-4572, 1998.
- [137] G. Antonelli, S. Chiaverini, N. Sarkar, and M. West. Adaptive control of an autonomous underwater vehicle: experimental results on ODIN. *IEEE Transactions on Control Systems Technology*, 9(5):756-765, 2001.
- [138] R. Bachmayer and L.L. Whitcomb. An open loop nonlinear model based thruster controller for marine thrusters. In *Proceedings of the International Conference on Intelligent Robots and Systems*, pages 1817-1823, 2001. IEEE.
- [139] G. Campa, M. Innocenti, and F. Nasuti. Robust control of underwater vehicles: sliding mode control vs.  $\mu$  synthesis. In *Proceedings of the OCEANS 1998 Conference*, 3:1640-1644, 1998. IEEE/MTS.
- [140] G. Conte and A. Serrani. Global robust tracking with disturbance attenuation for unmanned underwater vehicles. In *Proceedings of the International Conference on Control Applications*, pages 1094-1098, 1998. IEEE.

- [141] G. Conte, A. Serrani, A.M. Perdon. Rejecting the disturbances due to the umbilical's traction in the ROV's control. In *Proceedings of the OCEANS 1998 Conference*, 3:1245-1249, 1998. IEEE/MTS.
- [142] P.I. Corke and S.A. Hutchinson. A new partitioned approach to image-based visual servo control. *IEEE Transactions on Robotics and Automation*, 17(4):507-515, 2001.
- [143] M.L. Corradini and G. Orlando. A discrete adaptive variable-structure controller for MIMO systems, and its application to an underwater ROV. *IEEE Transactions on Control Systems Technology*, 5(3):349-359, 1997.
- [144] J.P.V.S. da Cunha, R.R. Costa, and L. Hsu. Design of a high performance variable structure position control of ROVs. *IEEE Journal of Oceanic Engineering*, 20(1):42-55, 1995.
- [145] F. Driscoll, R. Lueck, and M. Nahon. The motion of a deep-sea remotely operated vehicle system. *Ocean Engineering*, 27(1):29-56, 2000.
- [146] C. Edwards and S.K. Spurgeon. Section 3.3: existence of solution and equivalent control. *Sliding Mode Control: Theory and Applications*. Taylor and Francis, 1998.
- [147] T.I. Fossen. *Guidance and Control of Ocean Vehicles*. John Wiley & Sons, 1994.
- [148] G.F. Franklin, J.D. Powell and A. Emami-Naeini. Section 7.8.3: disturbance rejection by disturbance estimation. *Feedback Control Systems*. Addison Wesley, 1994.
- [149] J.C. Gerdes and E.J. Rossetter. A unified approach to driver assistance systems based on artificial potential fields. *Journal of Dynamic Systems, Measurement and Control*, 123:431-438, 2001.
- [150] K.R. Goheen and E.R. Jefferys. Multivariable self-tuning autopilots for autonomously and remotely operated underwater vehicles. *IEEE Journal of Oceanic Engineering*, 15(3):144-151, 1990.
- [151] A.J. Healey and D. Lienard. Multivariable sliding-mode control for autonomous diving and steering of unmanned underwater vehicles. *IEEE Journal of Oceanic Engineering*, 18(3):327-339, 1993.
- [152] A.J. Healey, S.M. Rock, S. Cody, D. Miles, and J.P. Brown. Toward an improved understanding of thruster dynamics for underwater vehicles. *IEEE Journal of Oceanic Engineering*, 20(4):354-361, 1995.
- [153] K. Leabourne, S.M. Rock, and S.D. Fleischer. Station keeping of an ROV using vision technology. In *Proceedings of the OCEANS 1997 Conference*, 1:634-640, 1997. IEEE/MTS.

- [154] T.W. McLain and S.M. Rock. Experimental measurement of ROV tether tension. In *Proceedings of ROV '92*, 1992.
- [155] Y. Mezouar and F. Chaumette. Path planning in image space for robust visual servoing. In *Proceedings of the International Conference on Robotics and Automation*, pages 2759-2764, 2000. IEEE.
- [156] J. Rife and S. Rock. Field experiments in the control of a jellyfish tracking ROV. In *Proceedings of the 2002 OCEANS Conference*, 4:2031-2038, 2002. IEEE/MTS.
- [157] P. Rives and J.-J. Borrelly. Underwater pipe inspection task using visual servoing techniques. In *Proceedings of the International Conference on Intelligent Robots and Systems*, pages 1:63-68, 1997. IEEE.
- [158] N. Sarkar, T.K. Podder, and G. Antonelli. Fault-accomodating thruster force allocation of an AUV considering thruster redundancy and saturation. *IEEE Transactions on Robotics and Automation*, 18(2):223-233, 2002.
- [159] D.A. Smallwood and L.L. Whitcomb. The effect of model accuracy and thruster saturation on tracking performance of model based controllers for underwater robotic vehicles: experimental results. In *Proceedings of the International Conference on Robotics and Automation*, pages 1081-1087, 2002. IEEE.
- [160] H.H. Wang. *Experiments in Intervention Autonomous Underwater Vehicles*. PhD thesis, Stanford University, Stanford, CA 94305, 1996. Also published as SUDAAR 683.
- [161] L.L. Whitcomb and D.R. Yoerger. Development, comparison, and preliminary experimental validation of nonlinear dynamic thruster models. *IEEE Journal of Oceanic Engineering*, 24(4):481-494, 1999.
- [162] L.L. Whitcomb and D.R. Yoerger. Preliminary experiments in model-based thruster control for underwater vehicle positioning. *IEEE Journal of Oceanic Engineering*, 24(4):495-506, 1999.
- [163] D.R. Yoerger, J.B. Newman, and J.-J.E. Slotine. Supervisory control system for the JASON ROV. *IEEE Journal of Oceanic Engineering*, 11(3):392-400, 1986.
- [164] D.R. Yoerger, J.G. Cooke, and J.-J.E. Slotine. The influence of thruster dynamics on underwater vehicle behavior and their incorporation into control system design. *IEEE Journal of Oceanic Engineering*, 15(3):167-178, 1990.



- [165] J. Yuh, J. Nie and C.S.G. Lee. Experimental study on adaptive control of underwater robots. In *Proceedings of the International Conference on Robotics and Automation*, pages 393-398, 1999. IEEE.
- [166] S. Zhao, J. Yuh, and H.T. Choi. Adaptive DOB control of underwater robotic vehicles. In *Proceedings of the OCEANS 2001 Conference*, 1:397-402, 2001. IEEE/MTS.

---

## C.5 AUV Lighting Design

- [167] P.J. Auster, D.H. Good, S.C. LaRosa, and H.J. Sprunk. Observing animal behavior with ROVs: minimizing impacts with red light. In *Proceedings of ROV '90*, pages 185-190, 1990. MTS.
- [168] G. Dietrich, K. Kalle, W. Krauss, and G. Siedler. *General Oceanography*. John Wiley and Sons (Wiley-Interscience), 1980.
- [169] H. Gordon. Modeling and simulating radiative transfer in the ocean. In R. Spinrad, K. Carder, and M. Perry, editors, *Ocean Optics*, pages 3-39. Oxford University Press, 1994.
- [170] L. Langebrake, S. Samson, E. Kaltenbacher, E. Steimle, J. Patten, and C. Lembke. Sensor development: progress towards systems for AUVs/UUVs. In *Proceedings of the OCEANS 2000 Conference*, 1:617-621, 2000. IEEE/MTS.
- [171] L. Mertens. *In-Water Photography: Theory and Practice*. Wiley-Interscience, 1970.
- [172] J. Mooney, chair, Committee on Undersea Vehicles and National Needs. *Undersea Vehicles and National Needs*, page 27. National Academy Press, 1996.
- [173] M. Olsson, D. Rimer, and S. Parker. ROV lighting with metal halide. White paper. Deep Sea Power & Light, 2000.
- [174] J. Rife and S. Rock. A low energy sensor for AUV-based jellyfish tracking. In *Proceedings of the 12th International Symposium on Unmanned Untethered Submersible Technology*, 2001.
- [175] B.H. Robison. Midwater biological research with the WASP ADS. *Marine Technology Society Journal*, 17:21-27, 1983.
- [176] R. Short, D. Fries, M. Kerr, and R. Byrne. *In-situ* chemical analysis using mass spectrometry on unmanned underwater vehicles. In *Proceedings of the OCEANS 2000 Conference*, 1:605-609, 2000. IEEE/MTS.

- [177] *Silicon Photodiode, Blue Enhanced Photoconductive Quadrant Type PDB-C204*. Retrieved May 20, 2001 from the Photonic Detectors, Inc. web site: <http://www.photonicdetectors.com/pdf/pdbc204.pdf>.